PHOTONIC BANDGAP ANALYSIS AND FABRICATION OF MACROPOROUS SILICON BY ELECTROCHEMICAL ETCHING

Trifon Teodorov Trifonov

ISBN: 978-84-693-6270-9
Dipòsit Legal: T.1376-2010

ADVERTIMENT. La consulta d'aquesta tesi queda condicionada a l'acceptació de les següents condicions d'ús: La difusió d'aquesta tesi per mitjà del servei TDX (www.tesisenxarxa.net) ha estat autoritzada pels titulars dels drets de propietat intel·lectual únicament per a usos privats emmarcats en activitats d'investigació i docència. No s'autoritza la seva reproducció amb finalitats de lucre ni la seva difusió i posada a disposició des d'un lloc aliè al servei TDX. No s'autoritza la presentació del seu contingut en una finestra o marc aliè a TDX (framing). Aquesta reserva de drets afecta tant al resum de presentació de la tesi com als seus continguts. En la utilització o cita de parts de la tesi és obligat indicar el nom de la persona autora.

ADVERTENCIA. La consulta de esta tesis queda condicionada a la aceptación de las siguientes condiciones de uso: La difusión de esta tesis por medio del servicio TDR (www.tesisenred.net) ha sido autorizada por los titulares de los derechos de propiedad intelectual únicamente para usos privados enmarcados en actividades de investigación y docencia. No se autoriza su reproducción con finalidades de lucro ni su difusión y puesta a disposición desde un sitio ajeno al servicio TDR. No se autoriza la presentación de su contenido en una ventana o marco ajeno a TDR (framing). Esta reserva de derechos afecta tanto al resumen de presentación de la tesis como a sus contenidos. En la utilización o cita de partes de la tesis es obligado indicar el nombre de la persona autora.

WARNING. On having consulted this thesis you're accepting the following use conditions: Spreading this thesis by the TDX (www.tesisenxarxa.net) service has been authorized by the titular of the intellectual property rights only for private uses placed in investigation and teaching activities. Reproduction with lucrative aims is not authorized neither its spreading and availability from a site foreign to the TDX service. Introducing its content in a window or frame foreign to the TDX service is not authorized (framing). This rights affect to the presentation summary of the thesis as well as to its contents. In the using or citation of parts of the thesis it's obliged to indicate the name of the author.

UNIVERSITAT ROVIRA I VIRGILI
PHOTONIC BANDGAP ANALYSIS AND FABRICATION OF MACROPOROUS SILICON BY ELECTROCHEMICAL ETCHING
Trifon Todorov Tirfonov
ISBN:978-84-693-6270-9/DL:T-1376-2010

UNIVERSITAT ROVIRA I VIRGILI
Departament d'Enginyeria Electrònica, Elèctrica i Automàtica
Avda. Països Catalans 26, Campus Sescelades, 43007 Tarragona, SPAIN

Photonic bandgap analysis and fabrication of macroporous silicon by electrochemical etching

Thesis presented for the qualification of Ph.D.

by

Trifon Trifonov

Directors:
Dr. Lluís F. Marsal
Dr. Ángel Rodríguez

Tarragona 2004

UNIVERSITAT ROVIRA I VIRGILI
PHOTONIC BANDGAP ANALYSIS AND FABRICATION OF MACROPOROUS SILICON BY ELECTROCHEMICAL ETCHING
Trifon Todorov Tirfonov
ISBN:978-84-693-6270-9/DL:T-1376-2010

ISBN:978-84-693-6270-9/DL:T-1376-2010

The work described in this thesis was made possible thanks to the collaboration of Grupo de Dispositivos Semiconductores (GDS), Departament d'Enginyeria Electrònica (DEE), Universitat Politècnica de Catalunya (UPC). It has been funded by the Research Scholarship from the Departament d'Enginyeria Electrònica, Elèctrica i Automàtica (DEEEA), Universitat Rovira i Virgili (URV) and Consejo Interinstitucional de Ciencia y Technologia (CICYT) under Grant No. TIC2002-04184-C02. It was also supported in part by Centre de Supercomputació de Catalunya (CESCA), through an allocation of a computer time.

ISBN:978-84-693-6270-9/DL:T-1376-2010

If we knew what it was we were doing,
it would not be called research,
would it?

Albert Einstein

UNIVERSITAT ROVIRA I VIRGILI
PHOTONIC BANDGAP ANALYSIS AND FABRICATION OF MACROPOROUS SILICON BY
ELECTROCHEMICAL ETCHING
Trifon Todorov Tirfonov
ISBN:978-84-693-6270-9/DL:T-1376-2010

ISBN:978-84-693-6270-9/DL:T-1376-2010

Contents

Acknowledgements v

Preface vii

1. Introduction to photonic crystals 1
- 1.1. Basic concepts: photonic crystal and photonic band gap 3
- 1.2. Defects in photonic crystals 11
- 1.3. Methods for calculating photonic band structure and other physical quantities 15
  - 1.3.1. Maxwell's equations 16
  - 1.3.2. Reciprocal lattice 19
  - 1.3.3. The plane wave method 22
  - 1.3.4. The finite difference time domain (FDTD) method 26
  - 1.3.5. Other methods 30
- 1.4. Technologies for fabricating 2D photonic crystals. State of the art 31
  - 1.4.1. Lithography 32
  - 1.4.2. Dry etching 33
  - 1.4.3. Soft lithography 34
  - 1.4.4. Glass capillary plate 35
  - 1.4.5. Anodization techniques 35

2. Photonic bands of 2D photonic crystals. Bandgap engineering 39
- 2.1. Photonic bands in two dimensions 40
- 2.2. The general rule of thumb 42
- 2.3. Symmetry reduction 45
- 2.4. Effects of symmetry reduction in 2D square and triangular lattices 49
  - 2.4.1. Lattice description and numerical method 49
  - 2.4.2. Results and discussion 52
  - 2.4.3. Summary 65
- 2.5. Conclusions 67

3. Photonic crystals with three dielectric components 69
- 3.1. Introduction 69
- 3.2. Lattice description and numerical method 72
- 3.3. Results and discussion 74

ISBN:978-84-693-6270-9/DL:T-1376-2010

3.3.1. Triangular lattice 74
3.3.2. Honeycomb lattice 79
3.4. Conclusions 87

4. Electrochemical etching of silicon. Experimental 89
4.1. Introduction and historical overview of porous silicon 89
4.2. Electrochemical etching of silicon 93
4.3. Electrochemical dissolution reaction 98
4.4. The physics of macropore formation in n-type silicon 100
4.5. Experimental 106
4.5.1. Set-up 106
4.5.2. Sample preparation 111

5. Fabrication of 2D photonic crystals based on macroporous silicon. Technological aspects 117
5.1. Pore morphology and process parameters 118
5.1.1. Random macropore formation in n-type silicon 118
5.1.2. Ordered macropore growth in n-type silicon 130
5.2. Microporous silicon covering the pore walls 142
5.3. Conical pores. Rules for improving pore uniformity 146
5.3.1. Nitrogen bubbling of the electrolyte 148
5.3.2. Etching at lower temperatures 149
5.3.3. Compensation of pore conicity by increasing etching current 152
5.4. Effects of surfactants on macropore growth 154
5.5. Conclusions 164

6. Applications of macroporous silicon 167
6.1. Brief overview 167
6.2. Silicon dioxide pillars 171
6.3. Optical short-pass filters 178
6.4. Ratchet-type macropores 182
6.5. Summary 187

7. Summary and conclusions 189
Outlook 191

Appendixes 193
Appendix A. Electrochemical etching set-up 194

UNIVERSITAT ROVIRA I VIRGILI
PHOTONIC BANDGAP ANALYSIS AND FABRICATION OF MACROPOROUS SILICON BY ELECTROCHEMICAL ETCHING
Trifon Todorov Tirfonov
ISBN:978-84-693-6270-9/DL:T-1376-2010

Appendix B. Specifications of the lithographic masks employed for the macroporous silicon fabrication 196
Appendix C. Porosity as a function of the pore diameter to pore pitch ratio for different pore shapes and patterns 198

References 201

Publications related to this thesis 217

UNIVERSITAT ROVIRA I VIRGILI
PHOTONIC BANDGAP ANALYSIS AND FABRICATION OF MACROPOROUS SILICON BY ELECTROCHEMICAL ETCHING
Trifon Todorov Tirfonov
ISBN:978-84-693-6270-9/DL:T-1376-2010

ISBN:978-84-693-6270-9/DL:T-1376-2010

Acknowledgements

This thesis would not have been possible without the collaboration, the help and the work of a number of people from various universities and research centers. Hereby, I would like to express my gratitude to all of them.

First of all I wish to thank my supervisors, Dr. Lluís F. Marsal at University Rovira i Virgili and Dr. Ángel Rodríguez at Technical University of Catalonia, for their guidance, constant support and their friendship. Lluís, all my simulations would resemble simply numbers without your advices and your insights into the field. Ángel, I could not say anything better than – Master, I am proud to be your apprentice! To both of you my sincere thanks.

I thoroughly acknowledge Dr. Josep Pallarès at University Rovira i Virgili for the encouragement, the wise hints and for his help to make a progress in the simulations. My special thanks go to Dr. Ramón Alcubilla at Technical University of Catalonia. I was and I continue being impressed how a badly written manuscript converts into a good article after his revision. His suggestions, the discussions with him have always been invaluable, showing me to search for the physics and to answer the "Why?".

I am grateful to Yago Rosselló for his help with the mask design and also to Jorge Amirola for leading my first steps in the Clean Room. I will always be in debt with Miguel García Molina and his technician team – Xavier and Juan Carlos – for their professionalism and ability to solve any problem with the clean room equipment no matter how complex it could be. Without their great work there would be no electrochemical set-up. I am also very grateful to Mercè Moncusí who taught and trained me to work unaided with the SEM equipment. Without her help I could not "see" my samples.

I would like to thank my colleagues and good friends - Mikhail and Ivan - for sharing with me their impressive knowledge in FDTD programming and for the fruitful discussions that helped me a lot to make band structure simulations. Special thanks go to Mikhail, who always had cigarettes to give me when I was in need. I am indebted to Mariona for teaching me and shedding light on such obscure topics for me, like "concentrations", "pH", "surfactants", etc. I wish to thank Raúl for helping me in LabVIEW programming and for being my friend. I am grateful to all Ph.D. students at

ISBN:978-84-693-6270-9/DL:T-1376-2010

the University Rovira i Virgili for being such excellent colleagues. Special thanks for my friends: Edgar, Hamdy and Mohamed.

I wish to thanks Dosi, Mikhaela and Miguel Ángel who have made may stay in Spain enjoyable over all these years. No gratitude would be sufficient to repay their unconditional support and their friendship. I hope I will see you someday somewhere…

The research scholarship from the University Rovira i Virgili is gratefully acknowledged.

I would like to express my gratitude to all my teachers from the Faculty of Physics, Sofia University “St. Kliment Ohridski” for giving me a solid base in physics. I am also very grateful to all my former colleagues – Toni, Plamen, Boyan, Boiko, Ivan, Orlin, Rosen - at the Institute of Electronics, Bulgarian Academy of Sciences for teaching me how to work in a team.

I thank my parents for their love, understanding and their cares for me.

Finally, the most kindly thanks go to my wife Mariana for giving me her love, for being at my side and for her great patience with my “thesis writing” stress.

ISBN:978-84-693-6270-9/DL:T-1376-2010

Preface

Photonic crystals are artificially created materials that can do to photons what an ordinary semiconductor does to electrons: that is to say, they can exhibit a *photonic band gap*, a situation in which photons with certain energies cannot propagate inside the crystal, regardless of polarization and propagation direction. The photonic band gap is therefore likely to be the true optical analog of the fundamental gap of a semiconductor. The possible benefits of this analogy can be compared only with the impact of the transistor revolution. Since they were invented in 1987, photonic crystals have triggered considerable interest because of their unusual optical properties. The unique properties of photonic crystals also mean that they are now recognized as a new and major field of optoelectronics.

Macroporous silicon, with its high dielectric contrast, very high aspect ratios and full compatibility with the silicon microelectronic industry is an excellent model system for studying the optical properties of two-dimensional and even three-dimensional photonic crystals. Besides, macroporous silicon has been shown to have several unique uses in many other fields, like electronics, micromachining, gas sensing and biotechnology. Research into macroporous silicon is continuously growing, prompted by its enormous potential for applications.

This thesis focuses on the development of the electrochemical etching technique for fabricating macroporous silicon structures that can be used as two-dimensional photonic crystals. Macropore arrays with square, triangular and honeycomb arrangements, and pore lengths and diameters up to 150 μm and 2 μm, respectively, were fabricated using this technique. Our study aimed to optimize the etching parameters in order to reduce structural inhomogeneities in the macropore arrays. Any imperfections in the periodic structure, generated by the fabrication process itself, can have detrimental effects on the properties of the photonic crystal. Extensive photonic band structure simulations were performed in order to find the optimal dielectric configurations that yield substantial absolute photonic gaps. By modifying the photonic lattice, we searched for such optimal configurations that also relax the fabrication requirements.

The thesis is organized as follows:

ISBN:978-84-693-6270-9/DL:T-1376-2010

Chapter 1 gives a brief introduction to photonic crystals and the underlying theory that governs their unusual optical properties. It also describes some of the widely used numerical methods for calculating several physical quantities related to photonic crystals. Various techniques that are currently being used to fabricate these materials are briefly reviewed.

Chapter 2 deals with the photonic bandgap formation in 2D photonic crystals comprising air rods drilled in silicon. Photonic lattices of different configurations with rods of various shapes, orientations and sizes are studied in an attempt to determine an absolute photonic band gap and to maximize its width as a function of the geometrical parameters of the 2D photonic crystal. The results are also described in terms of the relative difficulty of fabricating these optimized structures.

Chapter 3 discusses the photonic bandgap properties of 2D photonic crystals consisting of rods covered with a thin interfacial layer. The interfacial layer may be an unwanted result of the fabrication process itself or added intentionally. We study how this layer affects the properties of the absolute band gap for two complementary configurations: air rods drilled in silicon or silicon pillars embedded in air.

Chapter 4 introduces the experimental technique for fabricating macroporous structures by light-assisted electrochemical etching of n-type silicon. The physics of macropore formation and the properties of electrochemically etched macropore arrays are outlined. The phenomenological model describing how the experimental parameters influence the pore formation is discussed. The electrochemical etching set-up developed for macroporous silicon fabrication is described in this chapter. The main process sequence for sample preparation is also detailed.

Chapter 5 is devoted to the fabrication of macroporous silicon structures suitable for applications as 2D infrared photonic crystals. A preliminary study was made to acquire a basic understanding of the etching process and the influence of the process parameters. Special attention is paid to the most important etching parameters that have to be taken into account in order to obtain large-area macropore arrays with high aspect ratios and good structural characteristics. Some critical effects accompanying the etching process that act as sources of imperfections in the perfect pore pattern are discussed. Several ordered macroporous structures, fabricated after the etching parameters are optimized, are presented.

Chapter 6 describes some of the applications of macroporous silicon which are not related to photonic crystals. New structures fabricated by means of electrochemical etching are given. Our first steps towards three-dimensional microstructures are

UNIVERSITAT ROVIRA I VIRGILI
PHOTONIC BANDGAP ANALYSIS AND FABRICATION OF MACROPOROUS SILICON BY ELECTROCHEMICAL ETCHING
Trifon Todorov Tirfonov
ISBN:978-84-693-6270-9/DL:T-1376-2010

presented.

Chapter 7 presents the conclusions of our work and outlines possible future studies.

UNIVERSITAT ROVIRA I VIRGILI
PHOTONIC BANDGAP ANALYSIS AND FABRICATION OF MACROPOROUS SILICON BY
ELECTROCHEMICAL ETCHING
Trifon Todorov Tirfonov
ISBN:978-84-693-6270-9/DL:T-1376-2010

ISBN:978-84-693-6270-9/DL:T-1376-2010

Chapter 1

Introduction to photonic crystals

Since the invention of the first transistor in 1947 [1], electronics technology has permeated through almost every sphere of our lives. Advances in this field have allowed scientists to miniaturize and integrate millions of transistors onto a single chip, which has ushered in the Information Age. Today such chips are important parts of devices as diverse as computers, video cameras, cellular phones, copy machines, jumbo jets, modern automobiles, manufacturing equipment, electronic scoreboards and video games. Without the transistor there would be no Internet and no space travel. However, even though some of the aforementioned devices have reached tremendous levels of sophistication, they are nothing out of the ordinary in the way in which they transfer, process and store information. Basically, electrons are assumed to be the carriers involved in information processing and our modern information technology is still based on this assumption.

Photonics, the technology of photons (as electronics is the technology of electrons), promises to be the new century's driving force in the advancement of, mainly but not only, information technology, such as communications and computing. Photonics technology arose out of the advent of lasers and the optical fibers, which are the best choice as source and channel of the information carrier: light particles (or photons). Photons have several advantages over electrons. They travel in a dielectric material at much higher speeds than electrons in a metallic wire. Photons can also carry

UNIVERSITAT ROVIRA I VIRGILI
PHOTONIC BANDGAP ANALYSIS AND FABRICATION OF MACROPOROUS SILICON BY ELECTROCHEMICAL ETCHING
Trifon Todorov Tirfonov
ISBN:978-84-693-6270-9/DL:T-1376-2010

a larger amount of information per second. The bandwidth of dielectric material is significantly larger than that of metals: for fiber-optic systems it is typically in the order of one terahertz, while for electronic systems (e.g. telephone) it is only a few hundred kilohertz. Furthermore, photons are not as strongly interacting as electrons, which helps to reduce energy losses. The advantages of replacing electrons by photons in the transport of information are more than evident. The fiber-optic cables that today span the oceans have revolutionized our communications, but they are not only useful for long hauls. Nowadays, optical interconnects through optical fibers are already used to connect different computers. It is predicted that optical interconnects will be used to connect computer boards in five years, while the use of optical links within the chip is being investigated and will probably become a reality in 10-15 years [2]. The integration of optical links within the electronic chips is important because the continuing exponential reduction in feature sizes on the chip has already raised some barriers related to fundamental material and processing aspects [3]. An important example is that of the limitations in the operating speed of microelectronic devices due to the electrical interconnects. As the transistor size scales-down, the operating frequency of the circuit is no longer dictated by the transistor switching time but by the wiring delay. In addition, as integration progresses, the interconnects on a single chip get longer and longer. All these facts have prompted a considerable amount of research on the integration of different optoelectronic components on the same (silicon) substrate [4]. And this has given rise to a new technology: silicon microphotonics [5,6], the optical equivalent of microelectronics for integrated circuits. This technology requires new multipurpose optical components to be designed that are analogous to the electronic transistor, in which optical switching, wavelength dispersion and even wavelength conversion can take place. In other words, the incorporation of light as information carrier should be realized not only in the transport section of this technology but also, and principally, in the logic section: signal processing.

A new class of optical materials, known as photonic crystals (PCs) or photonic band gap (PBG) materials [7], promises to meet many of these demands. It is believed that photonic crystals may hold the key to an all-optical integrated circuit: that is, a photonic microchip. Indeed, scientists have begun to imagine photonic microchips which resemble microscopic metropolises on a micrometer scale, with photonic crystal buildings that house bundles of light, and highways and bridges that guide light along narrow channels and around tight corners. The overwhelming impact that these photonic devices would have on our society could be compared only with the impact of the transistor revolution.

UNIVERSITAT ROVIRA I VIRGILI
PHOTONIC BANDGAP ANALYSIS AND FABRICATION OF MACROPOROUS SILICON BY
ELECTROCHEMICAL ETCHING
Trifon Todorov Tirfonov
ISBN:978-84-693-6270-9/DL:T-1376-2010

This chapter gives a brief introduction to photonic crystals and to the underlying theory that governs their unusual optical properties. It also describes some of the widely used numerical methods for calculating several physical quantities related to photonic crystals. Various techniques that are currently used to fabricate these materials are briefly summarized. However, the chapter is by no means a complete and exhaustive review of all of the work that has been done so far in this rapidly growing field of photonics. Informative reviews of the most significant work in this area can be found in Ref. [8-12], while an excellent introduction to the field is given in Ref. 13.

1.1. Basic concepts: photonic crystal and photonic band gap

Photonic crystals are artificial materials with a spatial periodicity of their dielectric constant on a wavelength scale. The history of PCs has its origin in two articles by Yablonovitch [14] and John [15], published almost simultaneously in 1987. The basic idea consists of designing materials that can affect the properties of photons in much the same way that ordinary semiconductors affect the properties of electrons.

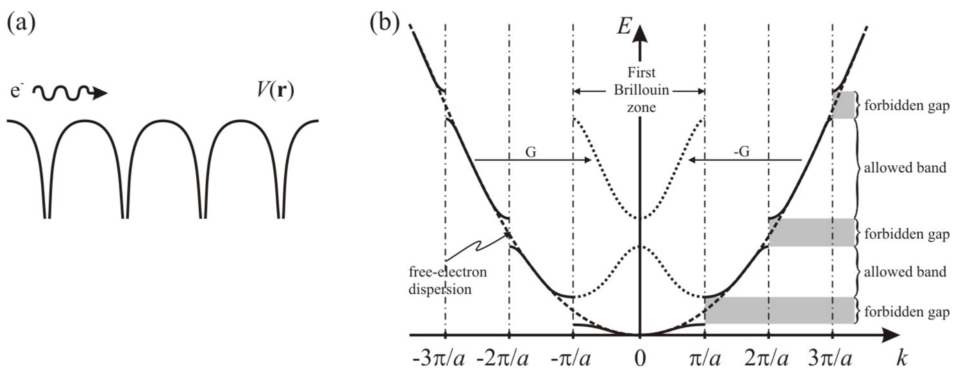

Fig. 1.1. (a) Schematic illustration of an electron wave propagating in a one-dimensional periodic potential caused by equally spaced atoms in the crystal; (b) Dispersion relation $E(\mathbf{k})$ (the energy of an electron as a function of its wave vector) in a one-dimensional periodic lattice with lattice period a [16]. The energy parabola $E = \hbar^2 k^2 / 2m$ of the free electron is given by a dashed line. The energy states of the electron (solid lines) split off at $\mathbf{k}=\pm\pi/a$, $\pm 2\pi/a$, … (where the Bragg reflection condition is met) and a forbidden gap in the spectrum of one-electron states is opened. Because of periodicity in **k**-space the dispersion relation can be restricted for practical reasons to the first Brillouin zone ($k=\pm\pi/a$): a region of reciprocal space closer to the origin than to any other reciprocal lattice points. This is schematically depicted by dotted lines, which represent the energy dispersion folded back into the first Brillouin zone by subtracting some reciprocal lattice vector **G**.

ISBN:978-84-693-6270-9/DL:T-1376-2010

A conduction electron, propagating in the periodic potential (Fig. 1.1a) caused by the atomic lattice, behaves like a wave that suffers reflections from different lattice planes, so called Bragg reflections [16]. The existence of a periodic potential, causing Bragg reflections, leads to the formation of energy bands, which are separated by energy gaps (*band gaps*) (Fig. 1.1b). Electrons with energies inside the gaps cannot propagate in certain directions in the crystal. These gaps arise because the electron waves reflected from the neighboring atoms interfere constructively with the original wave of the home atom. When this one-dimensional case is extended to the three dimensional one, the periodicity of the real crystal could give rise to a *complete energy gap*, in which electrons cannot propagate in any direction. This sort of gap is, for example, the fundamental band gap between the valence and the conduction bands of the semiconductors, and determines most of their lucrative properties.

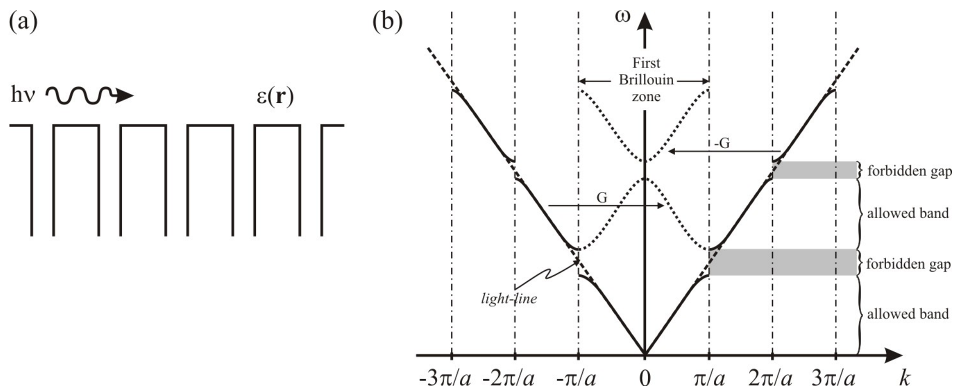

Fig. 1.2. (a) Schematic illustration of the propagation of an electromagnetic wave in a one-dimensional structure with periodic variation of dielectric constant ε(**r**); (b) Dispersion relation ω(**k**) (the frequency of light as a function of its wave vector) in such a periodic structure with lattice period *a* [17]. The dispersion relation of light $\omega = \frac{c}{\sqrt{\varepsilon}}k$ in a homogeneous material is given by a dashed line (the so called *light-line*). By analogy with the propagation of an electron in a one-dimensional periodic potential, the originally degenerated photon states at **k**=±π/*a*, ±2π/*a*, … split off and a forbidden gap in the electromagnetic spectrum is opened. The allowed bands are folded back inside the first Brillouin zone taking into account the identity of the wave vectors **k**, which differ from each other by a multiple of the reciprocal lattice vector **G**.

The familiar behavior of electrons in a semiconductor and its description by Bloch wave functions, reciprocal space, Brillouin zones and dispersion relations can be carried over to the electromagnetic case. Figure 1.2 illustrates the propagation of an electromagnetic wave in a one-dimensional structure with periodic variation of the

UNIVERSITAT ROVIRA I VIRGILI
PHOTONIC BANDGAP ANALYSIS AND FABRICATION OF MACROPOROUS SILICON BY ELECTROCHEMICAL ETCHING
Trifon Todorov Tirfonov
ISBN:978-84-693-6270-9/DL:T-1376-2010

dielectric constant and the corresponding photon dispersion relation. It can be seen that the propagation of light bears a strong similarity to the propagation of a conduction electron in a crystalline solid. For electromagnetic radiation, the periodic variation in the dielectric constant (or refractive index) of the material plays the same role as the atomic periodic potential does for the electrons. The high-dielectric parts of the structure (Fig. 1.2a) act as strong scatterers. For certain wavelengths and directions, the interference of electromagnetic waves scattered by different lattice planes is constructive. Waves with these wavelengths are Bragg reflected and cannot propagate inside the structure in the direction of the Bragg reflection. The Bragg reflection is therefore associated with the appearance of frequency *stop gaps*: a range of forbidden frequencies in the dispersion relation (Fig. 1.2b). For wave vectors **k** at and near $\mathbf{k}=\pm\pi/a$, $\pm 2\pi/a$, … the Bragg reflection condition is met and the dispersion relation splits into two branches separated by a stop gap. Inside the gap, all wave vectors **k** are complex and correspond to evanescent waves which decay in the structure. The width of these stop gaps increases with increasing the dielectric contrast ($\varepsilon_{high}/\varepsilon_{low}$) of the constituent media. When the periodicity extends over all three dimensions and if the dielectric contrast is high enough, the stop gaps in all directions can overlap to form a complete *photonic band gap* (PBG): that is, a range of frequencies for which light propagation is forbidden, irrespective of the direction of propagation. The photonic band gap may therefore be the true optical analogue of the fundamental band gap of a semiconductor.

The absence of allowed states for light inside a photonic band gap is conceptually a very important point and its implications go beyond classical optics. Although the photonic band gap makes it possible for photonic crystals to act as optical passive devices (e.g. mirrors or filters), photonic crystals were vigorously studied mainly because of their ability to manipulate the radiation dynamics of the active materials embedded in them. As was first put forward by Yablonovitch [14], the photonic band gap may completely inhibit spontaneous emission. Excited atoms inside a photonic crystal with their transition frequencies tuned to the band gap cannot emit photons, because inside the gap there are no quantum mechanical states available into which photons can go. It has been demonstrated that spontaneous emission is inhibited in a microwave region by surrounding the atoms with a pair of metal plates [18]. Below the cut-off frequency of this waveguide-like structure there are no electromagnetic modes available and spontaneous emission is "turned off". However, the problem of metal waveguides is that they do not scale well into optical frequencies, because at optical frequencies metals present high dissipative losses. The advantage of dielectric

UNIVERSITAT ROVIRA I VIRGILI
PHOTONIC BANDGAP ANALYSIS AND FABRICATION OF MACROPOROUS SILICON BY ELECTROCHEMICAL ETCHING
Trifon Todorov Tirfonov
ISBN:978-84-693-6270-9/DL:T-1376-2010

structures is that they can, at least in principle, be lossless, even all the way up to optical frequencies. The inhibition of spontaneous emission in a photonic crystal was first observed in 1990 by Martorell and Lawandy [19].

John [15] had a completely different viewpoint on the use of photonic band gap materials. He suggested that if a three-dimensional periodic dielectric structure is disordered in such a way that it remains periodic on average, it may be easier to observe a strong localization of light (the so-called *Anderson localization*). The concept of Anderson localization was initially proposed for the possible phenomenon of disorder-induced metal-insulator transition in electronic systems [20]. To make it simple, Anderson localization refers to situations in which electrons, when released in a random medium which could be, for instance, a free space with random potential, may stay close to the initial place. The envelope of the electron wave function is subsequently revealed as an exponential decay in any direction from the point of emission [21]. The mechanism behind the Anderson localization of electrons has been attributed purely to the multiple scattering of electrons by the random potential: a feature of the wave nature of electrons. Multiple scattering and interference of the scattered electromagnetic waves, when the average distance between the scattering events is similar to that of the wavelength of light, are the mechanisms behind the Anderson localization of light, not electrons. Therefore, it is the wave nature of light and electrons the property that binds semiconductors with photonic crystals, and electron with optical localization. These analogies can be generalized to many other wave phenomena [22]. For example, acoustic band gap materials, also known as *phononic crystals*, were introduced shortly after photonic band gap materials. Phononic crystals are periodic arrangements of materials with different densities and therefore with different sound velocities, which can be designed to exhibit a band gap for sound, instead of light [23-28].

Photonic crystals are classified mainly into three categories: that is, one-dimensional (1D), two-dimensional (2D) and three-dimensional (3D) crystals depending on whether the periodic variation of the dielectric constant is created in one, two or three dimensions (Fig. 1.3). The one-dimensional photonic crystal is the familiar dielectric multilayer, or *Bragg stack*, which consists of alternating layers of two different dielectric materials. The optical properties of such dielectric multilayers are well-known and were being used long before the concept of photonic crystals was introduced [29]. The applications of the dielectric multilayer structures are widespread (e.g. as stop-band filters, high-reflection mirrors, antireflection coatings, cavities for distributed feedback lasers, etc.). However, these applications are rather limited because 1D PCs exhibit photonic gap only for light traveling at normal incidence. As we move

UNIVERSITAT ROVIRA I VIRGILI
PHOTONIC BANDGAP ANALYSIS AND FABRICATION OF MACROPOROUS SILICON BY ELECTROCHEMICAL ETCHING
Trifon Todorov Tirfonov
ISBN:978-84-693-6270-9/DL:T-1376-2010

away from the normal incidence, the band gap quickly disappears.

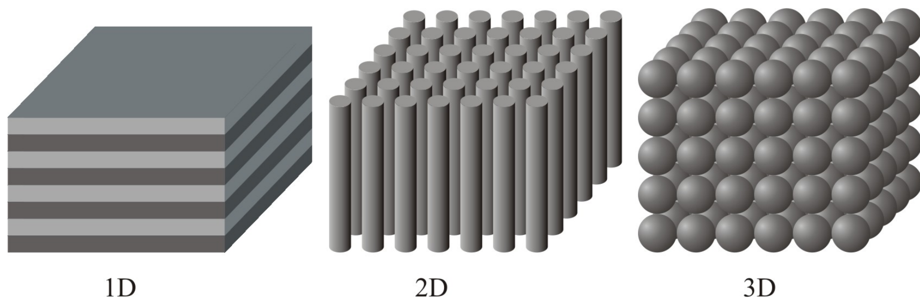

Fig. 1.3. Schematic illustration of one-dimensional (1D), two-dimensional (2D) and three-dimensional (3D) photonic crystals

Two- and three-dimensional PCs have received much more attention because they offer a rich variety of new optical phenomena. One example is the complete photonic band gap that can be realized in certain 3D crystals. Shortly after the theoretical prediction [30], the existence of complete 3D PBG has been demonstrated for the diamond structure [31]. An artificial 3D crystal (later termed "Yablonovite", after its inventor) was created by using conventional machine tools, i.e. by drilling an array of holes into high-refractive-index material. This crystal showed a stop-band for the transmission of microwave radiation between 13 and 15 GHz, irrespective of the direction of propagation, which confirmed the soundness of the basic ideas. Subsequent experimental efforts to develop so-called woodpile structures [32-34] as well as inverse opals [35,36] successfully demonstrated complete 3D PBG in the λ=1.5 μm window. Other 3D PBG structures have also been proposed and have been tried to fabricate, i.e. the spiral crystal [37,38] and the crystal consisting of multilayers and holes [39,40]. However, the fabrication of useful 3D PCs at optical and near-IR length scales is still far from being a trivial task. Each of the fabrication techniques proposed so far has several drawbacks. For example, the above mentioned woodpile structures are created by an elaborate sequence of carefully aligning, stacking, and fusing separate 2D layers, the so-called *layer-by-layer technique*. The number of well-stacked 2D layers is limited by the accumulation of alignment faults and also, by the extraordinarily long time the fabrication takes. The inverse opals, created by the self-assembly of small colloidal spheres and then taking the high-index replica of the formed template, provide a solution to the problem of the size (it is easy to make full 3D structures with a thickness of a hundred of microns). However, the drawback of inverse opals is the lack of control over the crystal symmetry. The self-assembling gives rise to a face-centered cubic (*fcc*)

UNIVERSITAT ROVIRA I VIRGILI
PHOTONIC BANDGAP ANALYSIS AND FABRICATION OF MACROPOROUS SILICON BY ELECTROCHEMICAL ETCHING
Trifon Todorov Tirfonov
ISBN:978-84-693-6270-9/DL:T-1376-2010

arrangement. The *fcc* geometry does not favor the creation of a complete photonic band gap as much as the diamond geometry of the layer-by-layer structures.

Two-dimensional PCs seem to be less attractive than 3D PCs, since the photonic band gap only exists for a propagation of light in the plane of periodicity. However, 2D PCs have made much greater headway mainly because they are more amenable to fabrication, in particular if the tools developed for the silicon microchip industry are used. Lower dimensionality also implies easier manipulation of the photonic lattice to increase functionality, such as deliberate inclusion of defects, as will be shown in the next section, or interfacing with standard optical elements, such as waveguides, fibers, light sources and detectors. In addition, many of the fabrication techniques developed to produce 2D structures can be successfully extended to fabricate 3D photonic crystals [41-43]. The earliest theoretical analysis of the 2D photonic band structure was made by Plihal *et al.* [44]. The 2D structure studied consisted of a periodic array of circular dielectric rods in a square arrangement, embedded in a background medium of different dielectric constant. The band structure analysis showed the existence of photonic band gaps for different polarizations of the electromagnetic waves, i.e. *H*- and *E-polarization* depending on whether the magnetic *H* or the electric field *E* was polarized along the rods. As in the case of 3D, the existence of photonic band gaps in 2D structures was experimentally confirmed first for the microwave region [45,46]. The 2D photonic crystal, reported in Ref. 45, consisted of alumina rods with a diameter of 0.74 mm ordered in a square lattice with a period of 1.87 mm. The measurements showed that although a large gap opened up for electromagnetic waves of *E-polarization*, no gap was observed for *H-polarization*. Further experiments with an array of air holes with a diameter 0.992 cm drilled in a dielectric host to form a triangular lattice with a lattice constant of 1.044 cm [46] showed a *complete band gap* between 13 and 15.5 GHz. A complete PBG in the context of 2D structures means a direction- and polarization-independent band gap for propagation that is confined to the plane of periodicity. Many different configurations have since been studied in an attempt to find 2D structures that have a large complete PBG. Examples include square [47], triangular [48], honeycomb [49], and interstitial [50,51] lattices coupled with square [47,52], diamond [51-53], hexagonal [52,54], elliptic [55] and triangular [52,54] shaped rods. Considerable progress has also been made in the fabrication of 2D structures. Many workers have fabricated 2D photonic crystals on micron and sub-micron length scales. Gourley *et al.* [56] and Krauss *et al.* [57] fabricated 2D structures on GaAs-based semiconductors, using electron beam lithography and dry etching techniques. Inoue *et al.* [58] reported a 2D photonic crystal fabricated from a fiber plate.

UNIVERSITAT ROVIRA I VIRGILI
PHOTONIC BANDGAP ANALYSIS AND FABRICATION OF MACROPOROUS SILICON BY ELECTROCHEMICAL ETCHING
Trifon Todorov Tirfonov
ISBN:978-84-693-6270-9/DL:T-1376-2010

A bundle of PbO-clad glass fibers arranged in a triangular lattice was heated and drawn in order to reduce the fiber diameter to the desired lattice constant (1.17 μm). The fiber core was then selectively dissolved, leaving behind a triangular pattern of air holes in a glass matrix. This method makes it possible the formation of hole arrays with an almost infinite aspect ratio (the ratio of hole diameter to hole depth), which cannot be achieved by means of dry etching techniques. Because of the low dielectric contrast (about 2.6) the crystal did not have a complete band gap for either polarization. Grüning *et al.* [59] demonstrated a 2D photonic crystal having holes with a very high aspect ratio, produced by the light-assisted electrochemical etching of silicon [60]. In this technique, the preservation of the shape of an initial pattern through hundreds of micrometers in depth is guaranteed by the fact that the electrochemical etching proceeds upon provision of optically generated positive carriers (holes) that promote the dissolution of the silicon preferentially at the tip of the pores. The fabricated 2D photonic crystal (a triangular array of macropores with a lattice constant of 2.3 μm and a pore diameter of 2.13 μm) showed a complete photonic band gap in the infrared region centered at 4.9 μm. Later, the lattice constant was successfully downscaled to below a micrometer to create a complete PBG for a wavelength of λ=1.3 μm [61]. Much smaller structures that can display photonic band gaps in the visible regime have been produced by a related technique of anodic growth of alumina pores. The pores were grown by anodic oxidation of aluminum, whose surface was previously embossed with regular arrays of shallow concave depressions that acted as seeds for the pore growth. Impressive aspect ratios (over 150) for pores, with diameters as small as 70 nm and periodicities of 100 nm, were reported by Masuda *et al.* [62].

The aforementioned experimental research primarily focused on achieving high aspect ratios when creating the 2D structures. High aspect ratios are required in order for a PBG effects to be seen that fits the calculated results for the 2D plane, in which light propagates forward and expands into both the upper and lower space (the third dimension). An ideal 2D PC extends infinitely into the third dimension, a situation that cannot be reproduced experimentally. Nevertheless, numerical approximations show that the ideal 2D PC can be approximated by structures with aspect ratios that are larger than 20 times the lattice constant. Despite the lack of confinement in the third dimension, light can still be contained in 2D structures by means of total internal reflection. One example is the structure that consists of a high-refractive-index film (a semiconductor, for example) perforated with a 2D photonic lattice and sandwiched between low-index media (air) (Fig. 1.4a). In this structure, known as a *photonic crystal slab*, light is controlled vertically by total internal reflection (due to the refractive index

UNIVERSITAT ROVIRA I VIRGILI
PHOTONIC BANDGAP ANALYSIS AND FABRICATION OF MACROPOROUS SILICON BY ELECTROCHEMICAL ETCHING
Trifon Todorov Tirfonov
ISBN:978-84-693-6270-9/DL:T-1376-2010

contrast of the high-index core and the low-index cladding), and laterally by distributed Bragg reflection due to the presence of the 2D photonic lattice. The photonic crystal slab has been extensively studied because it generates a pseudo-PBG that covers almost all of the 3D angles and it is easily processed [63-69]. Another example is the photonic crystal slab fabricated on a SOI (*silicon-on-insulator*) substrate (Fig. 1.4b) [70-73]. The SOI substrate itself is intrinsically a slab waveguide structure that is very effective at confining light. Photonic crystal slabs made from SOI wafers are extremely promising because they make use of commercially available high-quality wafers (SOI wafers are now being used for the most advanced microprocessor units) and mature Si nanofabrication technology. Also, the SOI PC slab fabrication process is relatively easy and compatible with the current device fabrication process, which makes these structures suitable for the realization of photonic integrated circuits. The techniques developed for the fabrication of 2D PCs will be discussed in greater detail in Section 1.4 of this chapter.

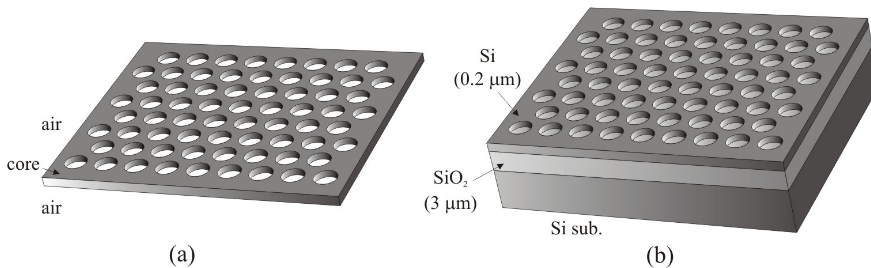

Fig. 1.4. Schematic illustration of a photonic crystal slab (a) and an SOI (*silicon-on-insulator)* photonic crystal (b). A dielectric slab of high-index material (Si) with a perforated 2D photonic lattice is sandwiched between low-index media (air, SiO_2). Light is confined vertically by means of total internal reflection.

The lack of a complete 3D PBG does not mean that 2D photonic crystals are not useful. Several applications have been found for them: semiconductor lasers [74] and light-emitting diodes [75], optical fibers [76], low-loss waveguides and bends [63-73], polarizers [77], channel drop filters [78,79], and so on. Remarkable examples of 2D photonic crystals can even be found in nature. Recently, scientists have discovered that the spine of the marine worm ("sea mouse") [80] consists of an array of regularly arranged hollow cylinders, and this simple structure gives rise to spectacular iridescence. The 2D photonic crystals are still being actively researched and developed in an attempt to find novel ideas and optical devices that can be implemented at a technological level. This thesis only deals with 2D photonic crystals.

UNIVERSITAT ROVIRA I VIRGILI
PHOTONIC BANDGAP ANALYSIS AND FABRICATION OF MACROPOROUS SILICON BY ELECTROCHEMICAL ETCHING
Trifon Todorov Tirfonov
ISBN:978-84-693-6270-9/DL:T-1376-2010

1.2. Defects in photonic crystals

Once the band gap is created, the physics can be further enriched by creating defects in the otherwise perfect photonic crystal. As John suggests [15], light can be strongly localized near the photonic band gap when randomness is introduced into the periodic arrangement. A more microscopic disorder, such as a defect or mistake in the photonic lattice, can lead to the formation of allowed photonic modes, whose frequencies lie within the photonic band gap, and the associated electromagnetic fields are localized in the vicinity of the defect [81]. This approach is reminiscent of semiconductor physics, where a defect in the otherwise perfect solid crystal introduces a defect state in the gap with a localized wavefunction. By analogy with semiconductors, the creation of defect states inside the gap can be interpreted as the "doping" of photonic crystals. This analogy extends as far as the type of "dopant". Adding extra dielectric material to the photonic lattice leads to a "donor"-type defect (i.e. a state near the "conduction" band of the crystal band structure) and removing dielectric material results in an "acceptor" state near the "valence" band [82]. We shall discuss this in greater detail here.

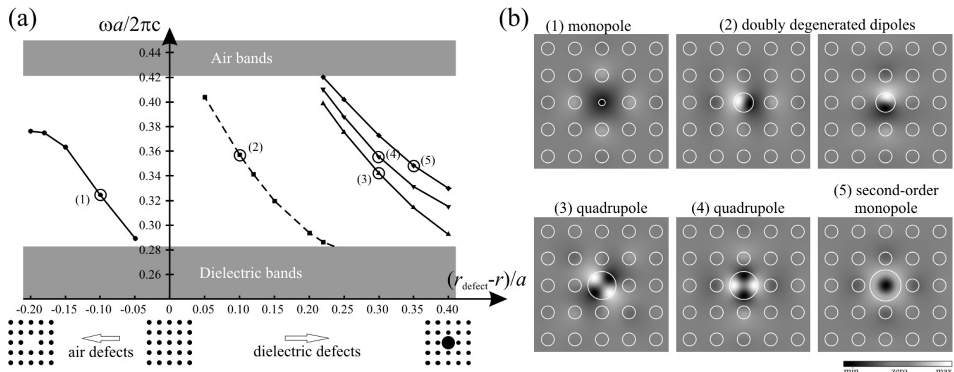

Fig. 1.5. (a) Localized states (the solid and dashed lines) inside the photonic band gap (*E-polarization*) for a square lattice of infinitely long dielectric rods (ε=12) with radius r=0.2a embedded in air. The defect is formed by varying the radius r_{defect} of a single rod. The states on the left correspond to defects formed by decreasing the radius of a single rod (the case of vacancy is $(r_{defect} - r)/a = -0.2$), while the states on the right are formed by increasing the radius of a single rod. The shaded regions represent the edges of the band gap. (b) Electric field pattern (Ez component) associated with selected defect states. Different defect modes exhibit different symmetries. The dashed line denotes modes that are doubly degenerated: two modes have the same frequency.*

* The defect states were computed by using a freely available MIT software package [84].

UNIVERSITAT ROVIRA I VIRGILI
PHOTONIC BANDGAP ANALYSIS AND FABRICATION OF MACROPOROUS SILICON BY ELECTROCHEMICAL ETCHING
Trifon Todorov Tirfonov
ISBN:978-84-693-6270-9/DL:T-1376-2010

Figure 1.5 illustrates an example of the formation of point defect states within the photonic band gap. The photonic crystal is a square lattice with lattice constant a, consisting of infinitely long dielectric rods (ε=12) with radius r=0.2a embedded in air. The shaded regions represent the extended photonic states for an electromagnetic wave of *E-polarization* (electric field polarized along the rods) propagating in the plane of periodicity. The states below the photonic band gap are called "dielectric bands" and the states above it are called "air bands". These terms are used because of the physical origin of the photonic band gap [83]. The modes of the "dielectric bands" have their energies concentrated in the regions of high dielectric constant (in this case, the dielectric rods). Clearly, the frequency of light for a given wavelength is lower in dielectric material than in air. Hence, the bands that lie below the gap at lower frequencies are called "dielectric bands". The "air band" modes also tend to concentrate their energies in high-ε regions so their frequencies are lower. However, the orthogonallity requirement (Ref. 13, Chapter 2) imposes them to have a node (site of zero field) inside the rods, expelling some of the field from the dielectric region. Thus, the "air band" modes concentrate their energies partly in the air regions and should therefore lie at higher frequencies. This results in large band splitting (band gap opening) between the "dielectric" and the "air" bands.

Turning back to our discussion of defect modes, we can make a single defect in the photonic crystal by changing the dielectric medium in one local region, deep within the bulk. This can be done in many ways: for example, by modifying the dielectric constant of a single rod, varying its size or removing it from the crystal. Figure 1.5a shows the effect of varying the radius of a single rod. The frequencies of the defect states (in normalized units ωa/2πc, c=velocity of light in free space) are plotted against the difference $\Delta r = \left(r_{defect} - r\right)/a$ between the radius r_{defect} of the defect rod and the radius r of non-modified rods. Thus, when the defect-rod radius is increased or decreased, Δr has positive or negative values, respectively. A vacancy is created when $\Delta r = -0.2$. Examining the left-hand side of the graphic, we see that when the size of a single rod is reduced below a particular critical value, an allowed state (defect state) is created within the photonic band gap. This state is pushed up into the gap from the dielectric band and sweeps upward across the gap as the radius of the dielectric rod is further reduced. Similarly, an increase in the size of the defect rod also leads to the formation of a defect state within the gap, but in this case it drops down from the air band. In both cases the frequency of the defect state can be tuned by simply adjusting the size of the rod. Reducing the size of the rod involves removing of dielectric material (i.e. we can speak about "air" defects as in the case of vacancy), while increasing the

UNIVERSITAT ROVIRA I VIRGILI
PHOTONIC BANDGAP ANALYSIS AND FABRICATION OF MACROPOROUS SILICON BY ELECTROCHEMICAL ETCHING
Trifon Todorov Tirfonov
ISBN:978-84-693-6270-9/DL:T-1376-2010

size involves adding dielectric material ("dielectric" defects). The analogy with semiconductors, alluded to at the beginning of this section is now clearer. That is, the creation of dielectric defects is analogous to doping the crystal with donor impurities, while the formation of "air" defects resembles doping with acceptor impurities.

The electric field pattern associated with a given defect state (Fig. 1.5b) reveals that light is strongly localized in the vicinity of defects. The electric field, polarized along the rods, decays rapidly (strictly speaking exponentially) away from the defect. The point defect (for example, the removal of a single rod) resembles a microcavity with perfectly reflecting walls. Light of a particular frequency cannot penetrate the bulk crystal because of the photonic band gap, it impinges on the walls and is reflected back into the cavity. Obviously, in the 2D case light can still escape in the third direction but for the real 3D case light will remain trapped within the cavity "forever". There is a notable difference between the air and the dielectric defect states. While an air defect creates a single well-defined mode in the gap, a dielectric defect introduces a number of defect modes in the gap, the lowest of which is doubly degenerated. *Doubly degenerated* means that there are two modes with different field patterns that happen to have the same frequency. Usually the symmetry of the photonic structure is responsible for the degeneration of the modes. The electric field distribution is different for the different defect states: that is to say, different defect states have different symmetries. The modes are labeled according to the number of nodes that can have the field in the azimuthal direction. For example, for the "air defect" modes (left-hand side of the graph), the electric field does not have a node in the plane. Consequently, these modes are labeled as monopoles. Likewise, the modes that have two nodes in the plane are labeled dipoles, those that have four nodes – quadrupoles, etc [85]. Therefore, not only it is possible to control the frequency, but the symmetry of the states can also be controlled to a certain extent. The flexibility in tuning the frequency, localization and symmetry properties of defects makes photonic crystals a very attractive medium for designing novel type optical devices [8,9,79,81,85-88].

Instead of creating a point defect to trap light, one can also create a *linear defect* that guides light from one location to another. Figure 1.6 shows a linear defect formed by removing a single column of rods in the square lattice of dielectric rods embedded in air. The photonic band structure (the shaded regions) of the unperturbed square lattice is projected onto the first Brillouin zone of the line defect. We have removed the rods in such a way that the line defect created is aligned with one of the translational vectors of the crystal. The crystal retains the translational symmetry along the defect line, so we can classify the defect modes with a wave vector **k** (shown in the

UNIVERSITAT ROVIRA I VIRGILI
PHOTONIC BANDGAP ANALYSIS AND FABRICATION OF MACROPOROUS SILICON BY ELECTROCHEMICAL ETCHING
Trifon Todorov Tirfonov
ISBN:978-84-693-6270-9/DL:T-1376-2010

inset), which characterizes the phase variation along the defect. Perpendicular to the defect line, the translational symmetry of the crystal is disrupted and we can no longer describe the electromagnetic modes with a wave-vector "quantum number". We therefore have to plot all the bands of the bulk crystal versus the conserved wave-vector quantum number **k**, and **k** is conserved in the direction of the defect line. This process is called *projecting the band structure of the unperturbed crystal onto the Brillouin zone of the line defect* and results in a continuum of bulk states plus discrete guided bands. More information about this approach can be found in Ref. 13 and 89. The states of the bulk crystal, shown in Fig. 1.6 with shaded patches, correspond to electromagnetic waves that can propagate through the crystal. The solid line inside the gap corresponds to guided modes, which can travel freely within the waveguide channel (defect line). For the particular configuration given, there is only one guided band. Since it lies within the photonic band gap, the states in this band extend along the defect line, but decay exponentially into the bulk of photonic crystal. This is seen on the right side of Fig. 1.6, which shows the electric field distribution for a given guided mode. Light is confined within and directed along the defect line through a conceptually new mechanism for light guiding.

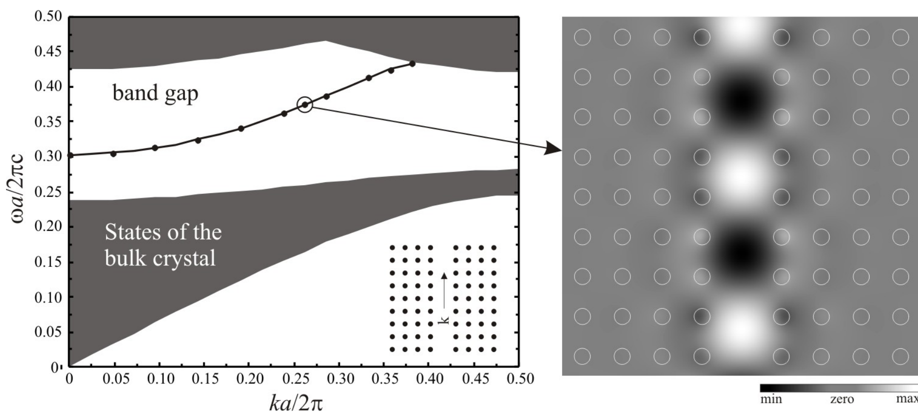

Fig. 1.6. Projected photonic band structure (*E-polarization*) for a linear defect in a square lattice of dielectric rods (ε=12) with radius *r*=0.2*a* (*a*=lattice constant) embedded in air. The frequencies (in normalized units $\omega a/2\pi c$) are plotted versus the wave vector *k* (also in normalized units $ka/2\pi$) along the direction of the defect. The line defect is formed by removing a single column of rods from the otherwise perfect photonic lattice. The shaded regions represent the continuum of extended states of the bulk crystal, separated by a photonic band gap. The solid line within the photonic band gap denotes the band of guided modes propagating through the line defect. The electrical field distribution for a guided mode is given on the right and shows that the mode extends along the defect but decays rapidly inside the crystal.*

* The numerical simulations were performed using a freely available MIT software package [84].

UNIVERSITAT ROVIRA I VIRGILI
PHOTONIC BANDGAP ANALYSIS AND FABRICATION OF MACROPOROUS SILICON BY ELECTROCHEMICAL ETCHING
Trifon Todorov Tirfonov
ISBN:978-84-693-6270-9/DL:T-1376-2010

Traditionally, light is guided in an optical fiber, one of the principal components of today's optical communication technology, by means of total internal reflection. Light propagating in the high-refractive-index fiber core is totally reflected at the interface with a low-index cladding. However, if the fiber is bent or distorted on a microscopic scale, light can easily escape into the background electromagnetic modes of the empty space, because the angle of incidence is too large for total internal reflection to occur. Similar considerations apply to the other principal elements of today's optical communication technology such as high-index waveguiding structures. On the other hand, in PC waveguide structures, light cannot radiate out of the guide because there are no background electromagnetic modes available due to the photonic band gap. This suggests that photonic crystals can be used to guide light efficiently, even around tight corners. Indeed, the guiding of light around sharp bends was first demonstrated theoretically by Mekis *at al.* [90] and then experimentally by Lin *et al.* [91] in the microwave region. Consequently, light propagation in waveguides with bends was observed for wavelength λ=1.5 μm by Baba *et al*. [67].

The deliberate formation of defects, such as the aforementioned microcavities and waveguides, considerably enhances the functionality of the photonic crystals and enables the miniaturization of optoelectronic components and circuits. New applications emerge constantly, but there seems to be no particular aspect of photonic crystals that yields quick and easily applicable results. It has only been in the last few years that real research has begun to test the theories about the practical applications of photonic crystals with embedded defects and many problems still need to be resolved. One example is the large scattering loss, which is mostly due to imperfections in the fabrication process. Therefore, an important question in the near future is how to decrease scattering losses by improving fabrication. If, for example, a PC waveguide is to be produced and used in high-density circuits, a small bend, a branch, a cross, a low-loss coupler, a wide transmission band, and an efficient coupling with external light must also be developed. Recent reviews of the most significant work that has been done so far in this area can be found in Ref. [12, 88, 92-94].

1.3. Methods for calculating photonic band structure and other physical quantities

All of the new physical phenomena related to PCs were first theoretically predicted, and then, some of them were confirmed experimentally. What is more, the photonic crystals themselves were initially the result of theoretical research. The

UNIVERSITAT ROVIRA I VIRGILI
PHOTONIC BANDGAP ANALYSIS AND FABRICATION OF MACROPOROUS SILICON BY ELECTROCHEMICAL ETCHING
Trifon Todorov Tirfonov
ISBN:978-84-693-6270-9/DL:T-1376-2010

development of methods for analyzing the photonic crystals is essential, if we want to understand their fundamental properties and be able to master the technology of making them. Any experimental exploration or technological exploitation of PCs must be accompanied by a quantitative theoretical analysis so that the most interesting cases can be identified, the experimental measurements interpreted, and stable designs for successfully operating devices be found. This section provides an outline of the most widely used numerical techniques that make it possible to determine the optical properties of PCs both qualitatively and quantitatively.

1.3.1. Maxwell's equations

All electromagnetic phenomena are governed by Maxwell's four macroscopic equations, which, written in the CGS-unit system, are [95]:

$$\vec{\nabla}\cdot\vec{D} = 4\pi\rho \tag{1.1}$$

$$\vec{\nabla}\times\vec{H} - \frac{1}{c}\frac{\partial\vec{D}}{\partial t} = \frac{4\pi}{c}\vec{J} \tag{1.2}$$

$$\vec{\nabla}\times\vec{E} + \frac{1}{c}\frac{\partial\vec{B}}{\partial t} = 0 \tag{1.3}$$

$$\vec{\nabla}\cdot\vec{B} = 0 \tag{1.4}$$

where (respectively) $\vec{E}$ and $\vec{H}$ are the electric and magnetic field vectors, $\vec{D}$ and $\vec{B}$ are the electric displacement and magnetic induction vectors, and ρ and $\vec{J}$ are the free charge and current densities; all of these quantities are potentially functions of both position $\vec{r}$ and time t.

In our particular case (i.e. light propagation in periodic dielectric media), some assumptions can be made so that Maxwell's equations can be cast in a simpler form. Since the nonhomogeneous equations (1.1) and (1.2) contain the charges and currents (which represent the influence of matter), the influence of matter can be attributed to the vectors $\vec{D}$ and $\vec{H}$, in which the electric and magnetic polarizabilities of the medium are taken into account. For a linear* and isotropic medium, the electric displacement $\vec{D}$

* Polarization $\vec{P}$ of a dielectric medium induced by an electric field $\vec{E}$ is usually written as the following power series: $P(E) = \varepsilon_0\left(\chi_1 E + \chi_2 E^2 + \chi_3 E^3 + ...\right)$ where the coefficients χ are tensors. For example, the Kerr tensor is χ_2. The medium is linear, if the coefficients χ_2, χ_3, … can be neglected.

UNIVERSITAT ROVIRA I VIRGILI
PHOTONIC BANDGAP ANALYSIS AND FABRICATION OF MACROPOROUS SILICON BY ELECTROCHEMICAL ETCHING
Trifon Todorov Tirfonov
ISBN:978-84-693-6370-9/DL:T-1376-2010

and magnetic field $\vec{H}$ are proportional to $\vec{E}$ and $\vec{B}$ as:

$$\vec{D}(\vec{r},t) = \varepsilon(\vec{r},\omega)\vec{E}(\vec{r},t) \quad (1.5)$$

$$\vec{H}(\vec{r},t) = \frac{1}{\mu(\vec{r})}\vec{B}(\vec{r},t) \quad (1.6)$$

where the dielectric constant (or permittivity) $\varepsilon(\vec{r},\omega)$ and magnetic permeability $\mu(\vec{r})$ are scalar functions.* We can assume that the medium is free of any absorption (low-loss dielectric) so the dielectric constant ε can be treated as purely real.† We also assume that the dielectric constant ε is independent of frequency, which is reasonable for the relatively narrow frequency ranges that are of interest in photonic crystals. We do not deal with magnetic materials so we may assume $\mu = 1$, which holds for most dielectric materials of interest. Finally, since we are interested only in the modes of propagating electromagnetic field and not in light-matter interaction (i.e. light propagates within the crystal but there are no sources of light), we can assume that free charges and electric currents are absent from the medium and set $\rho = \vec{J} = 0$. Taking all these assumption into account, Maxwell's equations become:

$$\vec{\nabla}\cdot\varepsilon(\vec{r})\vec{E}(\vec{r},t) = 0 \quad (1.7)$$

$$\vec{\nabla}\times\vec{H}(\vec{r},t) - \frac{\varepsilon(\vec{r})}{c}\frac{\partial\vec{E}(\vec{r},t)}{\partial t} = 0 \quad (1.8)$$

$$\vec{\nabla}\times\vec{E}(\vec{r},t) + \frac{1}{c}\frac{\partial\vec{H}(\vec{r},t)}{\partial t} = 0 \quad (1.9)$$

$$\vec{\nabla}\cdot\vec{H}(\vec{r},t) = 0 \quad (1.10)$$

Next, we look for time-harmonic solutions whose time dependence is $e^{i\omega t}$ for some angular frequency ω (all possible solutions can be expressed in this form since Maxwell's equations are linear):

$$\vec{E}(\vec{r},t) = \vec{E}(\vec{r})\cdot e^{i\omega t} \quad (1.11)$$

$$\vec{H}(\vec{r},t) = \vec{H}(\vec{r})\cdot e^{i\omega t} \quad (1.12)$$

Substituting (1.11) and (1.12) in (1.8), (1.9) we find:

---

* This formalism is generalized to an anisotropic media, where ε_{ij} and μ_{ij} are tensors.

† Complex dielectric constants are used to account for absorption [95].

$$\vec{\nabla} \times \vec{H}(\vec{r}) - \frac{i\omega}{c}\varepsilon(\vec{r})\vec{E}(\vec{r}) = 0 \quad (1.13)$$

$$\vec{\nabla} \times \vec{E}(\vec{r}) + \frac{i\omega}{c}\vec{H}(\vec{r}) = 0 \quad (1.14)$$

After eliminating $\vec{E}(\vec{r})$ or $\vec{H}(\vec{r})$ in (1.13) and (1.14), we obtain the following wave equations

$$\vec{\nabla} \times \left(\frac{1}{\varepsilon(\vec{r})} \vec{\nabla} \times \vec{H}(\vec{r}) \right) - \left(\frac{\omega}{c} \right)^2 \vec{H}(\vec{r}) = 0 \quad (1.15)$$

$$\frac{1}{\varepsilon(\vec{r})} \vec{\nabla} \times \left(\vec{\nabla} \times \vec{E}(\vec{r}) \right) - \left(\frac{\omega}{c} \right)^2 \vec{E}(\vec{r}) = 0 \quad (1.16)$$

which are treated as eigenvalue problems* in their operational form with eigenfunctions $\vec{H}(\vec{r})$ and $\vec{E}(\vec{r})$, and eigenvalues $(\omega/c)^2$.

When the crystal is homogeneous in all spatial directions (i.e. we can set $\varepsilon(\vec{r}) = \varepsilon$), the above eigenvalue equations produce a continuum spectrum of eigenfrequencies ω. Indeed, we can expand the fields $\vec{E}(\vec{r})$ and $\vec{H}(\vec{r})$ in terms of plane waves $e^{i\vec{k}\cdot\vec{r}}$ and after substituting in (1.15) or in (1.16) we get:

$$\frac{(\vec{k})^2}{\varepsilon} = \left(\frac{\omega}{c} \right)^2 \quad \text{or} \quad \omega(\vec{k}) = \frac{c}{\sqrt{\varepsilon}} \left| \vec{k} \right| \quad (1.17)$$

which is the *dispersion relation of light* propagating in a homogeneous dielectric, the so-called *light line*. In comparison to the propagation of light in vacuum ($\varepsilon = 1$) this means that in a medium with a dielectric constant ε, the speed of light c is reduced by a factor of $1/n$, where $n = \sqrt{\varepsilon}$ is the medium refractive index.

By definition, the photonic crystal is a periodic arrangement of different dielectric materials so the dielectric constant $\varepsilon(\vec{r})$ will be a periodic function of the

---

* It is worth pointing out that the Maxwell's operator acting on the $\vec{H}(\vec{r})$ field $\left(\Theta = \nabla \times \frac{1}{\varepsilon(\vec{r})} \nabla \times \right)$ in Eq. (1.15) is Hermitian, and as a consequence, its eigenvalues are real and positive. The operator $\left(\Theta = \frac{1}{\varepsilon(\vec{r})} \nabla \times (\nabla \times \right)$ acting on $\vec{E}(\vec{r})$ in Eq. (1.16) is not Hermitian, however. But, with a little manipulation, the Eq. (1.16) can be transformed into generalized eigenvalue equation, which involves only Hermitian operators [13].

UNIVERSITAT ROVIRA I VIRGILI
PHOTONIC BANDGAP ANALYSIS AND FABRICATION OF MACROPOROUS SILICON BY ELECTROCHEMICAL ETCHING
Trifon Todorov Tirfonov
ISBN:978-84-693-6370-9/DL:T-1376-2010

position $\vec{r}$. The role of the periodic dielectric function $\varepsilon(\vec{r})$ is analogous to that of the periodic atomic potential $V(\vec{r})$ from quantum mechanics. Indeed, the equation (1.15) bears a close resemblance to the stationary Schrödinger equation with Maxwell's operator $\left(\Theta = \nabla \times \frac{1}{\varepsilon(\vec{r})} \nabla \times\right)$ being analogous to Schrödinger's $\left(H = -\frac{\hbar^2}{2m}\nabla^2 + V(\vec{r})\right)$ operator [16] and the function $\frac{1}{\varepsilon(\vec{r})}$ analogous to the potential function $V(\vec{r})$. These analogies are far-reaching, and make it possible for us to think of photonic crystals in terms of solid state physics. In the sections below, we shall demonstrate how concepts such as reciprocal lattice, Bravais lattice, Brillouin zone, etc. can be carried over the PC case. However, we should point out some important differences. One is the vectorial nature of electromagnetic field, which means that scalar wave approximations (as is the case for electrons) will be insufficient. Calculations of photonic band structure based on scalar wave approximation have predicted a large complete PBG for a 3D *fcc* lattice of air spheres [96,97]. Later, a more rigorous study took into account the vector characteristics of light and demonstrated the incomplete formation of a PBG for the same lattice caused by band degeneracy of light with different polarizations [30,98]. Another important property of the equations (1.15) and (1.16), and of Maxwell's equations in general, is that they are scale-independent. If we downscale all the dimensions by a factor *s*, the solutions are exactly the same except that the frequencies must be multiplied by *s*. This means that we can solve the equations once and then apply the same results to problems at all length scales and frequencies. Because of this scale invariance, it is advisable to express distance and time in dimensionless units. Distances are usually represented as multiples of *a* (*a*=lattice constant), and all angular frequencies in units $2\pi c/a$, which is equivalent to a/λ (λ=vacuum wavelength).

1.3.2. Reciprocal lattice

The building blocks of a solid crystal are atoms, ordered periodically in a perfect crystal lattice. The building blocks of a photonic crystal are *photonic atoms* - dielectric scatterers (layers, rods, holes, spheres, etc.), ordered in a periodic *photonic lattice*. It is important to note that the size of *photonic atoms* is comparable to the wavelength of light, at which the photonic crystal is designed to operate. An infinite photonic crystal can be correctly described with the formalism of *Bravais lattices*, familiar from solid-state physics [16]. The *Bravais lattice* summarizes only the

UNIVERSITAT ROVIRA I VIRGILI
PHOTONIC BANDGAP ANALYSIS AND FABRICATION OF MACROPOROUS SILICON BY
ELECTROCHEMICAL ETCHING
Trifon Todorov Tirfonov
ISBN:978-84-693-6270-9/DL:T-1376-2010

geometry of the underlying periodic structure, regardless of what the actual structural units may be. Indeed, if we forget for a moment the shape and the structure of photonic atoms and regard them as points, then the photonic lattice can be generated entirely through the translation:

$$\vec{R} = n_1\vec{a}_1 + n_2\vec{a}_2 + n_3\vec{a}_3 \qquad (1.18)$$

where $\vec{a}_1$, $\vec{a}_2$ and $\vec{a}_3$ are the three *primitive lattice vectors* and n_1, n_2 and n_3 range through all the integral values. The *primitive unit cell* (or *Wigner-Seitz cell**) can also be defined as a volume of space that, when translated through all the primitive vectors, just fills all of the space. The primitive cell may contain one or more photonic atoms (as is the case for the honeycomb and hybrid lattices discussed in Chapter 2), surrounded by a piece of the background material. The calculations, usually photonic band structure calculations, are then performed over the computational domain that consists of one unit cell by applying periodic boundary conditions to update the fields at the cell boundaries.

Instead of using the real space lattice to perform the calculations, it is usually useful to use its associated *reciprocal lattice*. The reciprocal lattice is generated by the primitive vectors $\vec{b}_1$, $\vec{b}_2$ and $\vec{b}_3$ through

$$\vec{G} = h_1\vec{b}_1 + h_2\vec{b}_2 + h_3\vec{b}_3 \qquad (1.19)$$

where h_i, i=1,2,3 are arbitrary integers and $\vec{b}_i$ is related to the real space primitive vectors $\vec{a}_i$ according to:

$$\vec{b}_1 = 2\pi\frac{\vec{a}_2\times\vec{a}_3}{\vec{a}_1\cdot(\vec{a}_2\times\vec{a}_3)}, \quad \vec{b}_2 = 2\pi\frac{\vec{a}_3\times\vec{a}_1}{\vec{a}_1\cdot(\vec{a}_2\times\vec{a}_3)}, \quad \vec{b}_3 = 2\pi\frac{\vec{a}_1\times\vec{a}_2}{\vec{a}_1\cdot(\vec{a}_2\times\vec{a}_3)} \qquad (1.20)$$

where $\Omega = \vec{a}_1\cdot(\vec{a}_2\times\vec{a}_3)$ is the volume of the primitive unit cell. The above relations can also be written as $\vec{a}_i\cdot\vec{b}_j = 2\pi\delta_{ij}$, with δ_{ij} denoting the Kronecker symbol.

The reciprocal lattice works in the wavevector space. It is a set of all wavevectors $\vec{k}$ that yield plane waves $e^{i\vec{k}.\vec{r}}$ with the periodicity of the real space lattice. Then, the Wigner-Seitz cell of the reciprocal lattice will be just the first Brillouin zone that encloses the set of all nonredundant wavectors $\vec{k}$, to which the problem of solving the eigenvalue equation can be restricted. As was shown previously (Section 1.1),

* The Wigner-Seitz cell about a lattice point is defined as the region of space that is closer to that point than to any other lattice point. It is a primitive cell that keeps the full symmetry of the Bravais lattice.

UNIVERSITAT ROVIRA I VIRGILI
PHOTONIC BANDGAP ANALYSIS AND FABRICATION OF MACROPOROUS SILICON BY ELECTROCHEMICAL ETCHING
Trifon Todorov Tirfonov
ISBN:978-84-693-6370-9/DL:T-1376-2010

owing to the translational symmetry the photonic dispersion relation is usually plotted against the wavevector $\vec{k}$, confined in a finite range (e.g., $-\frac{\pi}{a}\cdots\frac{\pi}{a}$) called the first Brillouin zone. In fact, since the lattice generally possesses additional symmetries, for example some kind of rotational symmetry, the range of unique wavectors is further reduced. One then looks for solutions to the eigenvalue problem only for $\vec{k}$-vectors inside this symmetry-reduced region, known as the *irreducible Brillouin zone*.

Fig. 1.7. Two-dimensional example of a hexagonal real space photonic lattice (left) and its corresponding reciprocal lattice concept (right). The photonic crystal consists of infinitely long dielectric cylinders with a dielectric constant ε_r embedded in a background material of $\varepsilon_b \neq \varepsilon_r$. The center-to-center distance *a* between the cylinders is the *lattice constant*. The primitive real space vectors $\vec{a}_1$ and $\vec{a}_2$ are chosen so that $|\vec{a}_1| = |\vec{a}_2| = a$. Different choices of the primitive unit cell are indicated (the regions enclosed by a solid line). The reciprocal vectors of the associated reciprocal lattice are $\vec{b}_1$ and $\vec{b}_2$ with $|\vec{b}_1| = |\vec{b}_2| = 4\pi/\sqrt{3}a$ and $\vec{a}_i \cdot \vec{b}_j = 2\pi\delta_{ij}$. The first Brillouin zone (a hexagon) is located in the reciprocal lattice and the irreducible Brillouin zone is shown as a shaded triangular wedge with the high symmetry points Γ, X and J indicated.

Figure 1.7 gives an illustrative example of the real space photonic lattice together with its corresponding reciprocal lattice, and also of all the abovementioned terms of solid state physics. For the sake of simplicity, however, they have been reduced to the 2D case. The formalism of the reciprocal lattice is used to the fullest extent in the *plane wave method* for photonic band structure calculations, with which we shall continue our discussion.

UNIVERSITAT ROVIRA I VIRGILI
PHOTONIC BANDGAP ANALYSIS AND FABRICATION OF MACROPOROUS SILICON BY ELECTROCHEMICAL ETCHING
Trifon Todorov Tirfonov
ISBN:978-84-693-6270-9/DL:T-1376-2010

1.3.3. The plane wave method

The simplest but by no means the only way to calculate photonic band structures is to adapt the methods of electronic band structure calculations to the case of photonic crystals. The *plane wave expansion method* can be classified as one of the numerical techniques borrowed from solid state physics. However, it had to undergo various adjustments before it could be carried over to the photonic case. These adjustments reflect the differences between photonic and conventional crystals, such as the fact that the electromagnetic field is inherently vectorial by nature or that the "scattering potentials" of photonic atoms are known beforehand and do not have to be determined self-consistently. In the following, we shall outline how the widely used plane wave method can be applied to the problem of photonic band structure calculations.

All structural and material information of the photonic crystal is fully contained in the dielectric constant $\varepsilon(\vec{r})$, which is periodic $\varepsilon(\vec{r}+\vec{R})=\varepsilon(\vec{r})$ to the set of all lattice vector $\vec{R}$ (Eq. 1.18) generated by the real space primitive translations $\vec{a}_i$, i=1,2,3. The photonic band structure can be obtained straightforwardly by considering the wave equation (1.15)* in the reciprocal space: that is, in the space of the wavevectors $\vec{k}$. To this end, the inverse of the periodic dielectric function should be expanded in a Fourier series on the reciprocal lattice $\vec{G}$ [17]:

$$\frac{1}{\varepsilon(\vec{r})}=\sum_{\vec{G}}\kappa(\vec{G})e^{i\vec{G}\cdot\vec{r}} \tag{1.21}$$

where the Fourier coefficients $\kappa(\vec{G})$ are obtained through an integration over the primitive unit cell, whose volume we have designated by Ω, as follows:

$$\kappa(\vec{G})=\frac{1}{\Omega}\int_{\Omega}d^3r\frac{1}{\varepsilon(\vec{r})}e^{-i\vec{G}\cdot\vec{r}} \tag{1.22}$$

We can apply the Bloch-Flouquet theorem [16], which tells us that the solutions to a Hermitian eigenvalue problem can always be chosen to have the form of a plane wave $e^{i\vec{k}\cdot\vec{r}}$ times a function $\vec{u}(\vec{r})$ with the periodicity of the Bravais lattice $\vec{u}(\vec{r}+\vec{R})=\vec{u}(\vec{r})$. In other words, the solutions to Eq. (1.15) are plane waves modulated by a lattice periodic function. Because of the discrete translational symmetry of the

---

* Similar considerations also apply for the wave equation (1.16).

UNIVERSITAT ROVIRA I VIRGILI
PHOTONIC BANDGAP ANALYSIS AND FABRICATION OF MACROPOROUS SILICON BY ELECTROCHEMICAL ETCHING
Trifon Todorov Tirfonov
ISBN:978-84-693-6270-9/DL:T-1376-2010

lattice, the solutions are labeled by wavevector $\vec{k}$, which is confined in the first Brillouin zone. As a consequence, the dispersion relation $\omega_n(\vec{k})$ in an infinitely extended $\vec{k}$-vector space is folded back onto the first Brillouin zone, introducing a discrete band index *n*. Therefore, the eigenstates $\vec{H}(\vec{r})$ are characterized by a wavevector $\vec{k}$ and a band index *n* and are expressed as

$$\vec{H}(\vec{r}) \overset{B.F.\,theorem}{\equiv} \vec{H}_{\vec{k}n}(\vec{r}) = e^{i\vec{k}\cdot\vec{r}} \cdot \vec{u}_{\vec{k}n}(\vec{r}) \tag{1.23}$$

The eigenfunctions (1.23) can be expanded in Fourier series like the inverse of the dielectric function $\varepsilon^{-1}(\vec{r})$ in (1.21). The Fourier expansion leads to the following form of the eigenfunctions:

$$\vec{H}_{\vec{k}n}(\vec{r}) = \sum_{\vec{G}} \vec{H}_{\vec{k}n}(\vec{G}) e^{i(\vec{k}+\vec{G})\cdot\vec{r}} \tag{1.24}$$

Substituting (1.21) and (1.24) in (1.15), we obtain the following eigenvalue equation for the expansion coefficients $\vec{H}_{\vec{k}n}(\vec{G})$

$$-\sum_{\vec{G}'} \kappa(\vec{G}-\vec{G}')(\vec{k}+\vec{G})\times(\vec{k}+\vec{G}')\times\vec{H}_{\vec{k}n}(\vec{G}') = \left(\frac{\omega_{\vec{k}n}}{c}\right)^2 \vec{H}_{\vec{k}n}(\vec{G}) \tag{1.25}$$

where $\omega_{\vec{k}n}$ denotes the eigenfrequency of the eigenmodes $\vec{H}_{\vec{k}n}(\vec{r})$. If this equation is solved numerically, the dispersion relation of the eigenmodes, or the photonic band structure, can be obtained. To be solved numerically, however, the summation in equations (1.21) and (1.24) should be calculated up to a finite, but sufficiently large number *N* of vectors $\vec{G}'$, which is called the *number of the plane waves* used in the expansion. The eigenvalue problem is solved for each $\vec{k}$ and it is equivalent to the diagonalization of the matrix defined by the left-hand side of Eq. (1.25). The dimension* of the matrix is 2*N*×2*N* for $\vec{H}_{\vec{k}n}(\vec{G})$, since $\vec{H}_{\vec{k}n}(\vec{G})$ should be perpendicular to the vector $\vec{k}+\vec{G}$ in accordance with the requirement of transversality from the Maxwell's

* The divergence-free nature of the magnetic field, $\nabla\cdot\vec{H}(\vec{r})=0$, allows us to restrict the number of expansion coefficients to only two transverse polarizations for any given plane wave. For a total number of plane waves *N*, this leads to a 2*N*×2*N* matrix problem, instead of the 3*N*×3*N* matrix problem that results from applying the plane wave method to the Eq. (1.16) for the electric field. The eigenvalue equation for the magnetic field is preferred also because of the continuity of the magnetic field $\vec{H}(\vec{r})$, which reduces the number of plane waves necessary for obtaining converged results.

ISBN:978-84-693-6270-9/DL:T-1376-2010

fourth equation (1.10). Indeed, $\vec{H}_{\vec{k}n}(\vec{G})$ can be expressed by a linear combination $\vec{H}_{\vec{k}n}(\vec{G}) = h_{\vec{k}n}^{\vec{G}1}\vec{e}_{\vec{G}1} + h_{\vec{k}n}^{\vec{G}2}\vec{e}_{\vec{G}2}$ of two orthogonal normal vectors $\vec{e}_{\vec{G}1}$ and $\vec{e}_{\vec{G}2}$ so that the unity vectors $\vec{e}_{\vec{G}1}$, $\vec{e}_{\vec{G}2}$ and $(\vec{k}+\vec{G})/|\vec{k}+\vec{G}|$ form an orthogonal triad. Then, the Eq. (1.25) converts into:

$$\sum_{\vec{G}'}\sum_{j=1}^{2} M_{\vec{k}}^{ij}(\vec{G},\vec{G}')h_{\vec{k}n}^{\vec{G}'j} = \left(\frac{\omega_{\vec{k}n}}{c}\right)^2 h_{\vec{k}n}^{\vec{G}i} \tag{1.26}$$

where the matrix elements $M_{\vec{k}}(\vec{G},\vec{G}')$ are given by:

$$M_{\vec{k}}(\vec{G},\vec{G}') = |\vec{k}+\vec{G}||\vec{k}+\vec{G}'|\kappa(\vec{G}-\vec{G}')\begin{pmatrix} \vec{e}_{\vec{G}2}\cdot\vec{e}_{\vec{G}'2} & -\vec{e}_{\vec{G}2}\cdot\vec{e}_{\vec{G}'1} \\ -\vec{e}_{\vec{G}1}\cdot\vec{e}_{\vec{G}'2} & \vec{e}_{\vec{G}1}\cdot\vec{e}_{\vec{G}'1} \end{pmatrix} \tag{1.27}$$

The Eq. (1.26) can be solved numerically by the standard numerical techniques for matrix diagonalization (see for example Ref. 99). However, we first have to generate the matrix elements $M_{\vec{k}}(\vec{G},\vec{G}')$ and to do this we need to calculate the coefficients $\kappa(\vec{G})$ in the Fourier expansion of the dielectric function (Eq. 1.22). In general, these are evaluated numerically, but if the shapes of the photonic atoms in the unit cell are simple enough, the integral in Eq. (1.22) can be solved analytically. For example, for the 2D photonic crystal given in Section 1.3.2, consisting of infinitely long cylinders with radius r_a and dielectric constant ε_r, which are embedded in background dielectric (ε_b) and are arranged in a hexagonal lattice, the Fourier coefficients $\kappa(\vec{G})$ are then given by

$$\kappa(\vec{G}) = \begin{cases} \frac{1}{\varepsilon_r}f + \frac{1}{\varepsilon_b}(1-f) & |\vec{G}| = 0 \\ \left(\frac{1}{\varepsilon_r} - \frac{1}{\varepsilon_b}\right) f \frac{2J_1(Gr_a)}{Gr_a} & |\vec{G}| \neq 0 \end{cases} \tag{1.28}$$

where J_1 is the first-order Bessel function of the first kind and $f = 2\pi/\sqrt{3}\,(r_a/a)^2$ is the *filling fraction* of the rod, defined as the area of the rod πr^2 divided by the area of the unit cell $\frac{\sqrt{3}}{2}a^2$.

It is worth pointing out that all information pertaining to the geometry of the lattice is contained in the matrix of the coefficients $\kappa(\vec{G})$. The formulation (1.26) provides a very convenient solving routine, since the bulk of the solution "machinery"

UNIVERSITAT ROVIRA I VIRGILI
PHOTONIC BANDGAP ANALYSIS AND FABRICATION OF MACROPOROUS SILICON BY ELECTROCHEMICAL ETCHING
Trifon Todorov Tirfonov
ISBN:978-84-693-6270-9/DL:T-1376-2010

can remain in place, while only the $\kappa(\vec{G})$ coefficients change with different crystal structures. Reference 100 provides the analytical expressions (like Eq. 1.28) of these coefficients for 2D crystal structures with a variety of arrangements and shapes of the scatterers.

The value of the dielectric function tends to contain many sharp steps throughout the photonic crystal, so the question remains of whether these discontinuities are accurately represented within the plane wave method and, as a consequence, the convergence properties of the plane wave method have been carefully investigated [101,102]. The convergence properties of the plane wave method based on the magnetic field, which is what has been described so far, are much better than those of the same approach based on the electric or displacement field. The plane wave method involves computing the matrix of Fourier coefficients of the inverse of the dielectric constant (Eq. 1.21). This Fourier transforming can be done in two ways. The Fourier coefficients can be calculated by directly Fourier transforming the inverse dielectric constant $\varepsilon^{-1}(\vec{r})$. This is known as the direct method. Alternatively, we can take the Fourier transform of the function $\varepsilon(\vec{r})$ and invert the resulting matrix. This is known as the Ho-Chan-Soukoulis method [30]. Since the operations of taking the Fourier transform and inversion commute on the complete set of plane waves, the results for both methods in an infinite system must coincide exactly. However, we are numerically restricted to operating on a finite dimensional subspace of the full reciprocal lattice. This leads to dramatically different rates of convergence for the two methods as the subspace (i.e. the number of plane waves) increases. Detailed investigations have clearly demonstrated the superior convergence properties of the Ho-Chan-Soukoulis method [102].

Owing to its simplicity and flexibility in handling practically any geometry of the unit cell, the plane wave method has become a powerful and widely used tool for most investigations into photonic band structures. With a little additional work the plane wave method can also be used to calculate other physical quantities, which play a fundamental role in the understanding of photonic crystal properties. For example, the spontaneous emission rate of an excited atom or molecule is proportional to the photonic density of states, which is defined by "counting" all allowed states with a given frequency ω and can be expressed by the sum of all bands and an integral over the first Brillouin zone of a Dirac-δ function $\delta(\omega-\omega_n(\vec{k}))$ [103]. The group velocity and group velocity dispersion are necessary for understanding the pulse propagation and optical response in linear and nonlinear photonic crystals. They can be calculated through a simple numerical differentiation of the band structure. However, great care

UNIVERSITAT ROVIRA I VIRGILI
PHOTONIC BANDGAP ANALYSIS AND FABRICATION OF MACROPOROUS SILICON BY ELECTROCHEMICAL ETCHING
Trifon Todorov Tirfonov
ISBN:978-84-693-6270-9/DL:T-1376-2010

should be taken to avoid numerical instabilities. Methods for evaluating group velocity more accurately, which are also based on band structure calculations by the plane wave method, can be found in Ref. 17 and 104. The plane wave method has also been used to numerically calculate the transmittance and Bragg reflectivity of 2D photonic crystals [105, 106 or 17]. By redefining the unit cell and constructing the so-called *supercell*, the plane wave method is used to calculate defect structures, as was shown by the examples in Section 1.2. In the supercell, a set of several photonic crystal periods are placed around the defect. It is assumed that such a supercell is repeated infinitely in space. Since the wave functions are localized around the defect, the modes of adjacent defects hardly overlap each other when the supercell is sufficiently large, and can be calculated almost without ambiguity. However, the number of defect problems that can be treated by supercells within the plane wave method is limited to relatively simple structures, because a considerable number of plane waves are needed, and the computational time must therefore be long, if calculations are to be accurate. The real-space methods (i.e. the *finite difference time domain method* (FDTD)) are more efficient in this respect, giving high accuracy with a low computational time.

1.3.4. The finite difference time domain (FDTD) method

The plane wave method became the first method that was seriously used to study photonic crystals, because it is easy to understand and computationally very straightforward to implement. However, it has some serious limitations which restrict its usefulness. First, the method fixes the wave vector $\vec{k}$ and then determines the eigenfrequencies for this $\vec{k}$, so the method runs into difficulties if the dielectric constant is itself a function of frequency. Hence, structures that include metallic or other dispersive materials are beyond the scope of the plane wave method. Second, the key step in the method is the matrix diagonalization, so the computer time required scales like N^3, where N is the number of plane waves used in the expansion. This scaling law is inefficient and renders the calculations impossibly time consuming when a large number of plane waves is required for more complex structures. Therefore the PWM method is limited to treating only simple photonic crystals, unless a supercomputer is available.

The *finite difference time domain* approach for photonic band structure calculations overcomes all these drawbacks of the plane wave method. It was first described by Yee in 1966 [107] and so has been known to the electrical engineering

UNIVERSITAT ROVIRA I VIRGILI
PHOTONIC BANDGAP ANALYSIS AND FABRICATION OF MACROPOROUS SILICON BY ELECTROCHEMICAL ETCHING
Trifon Todorov Tirfonov
ISBN:978-84-693-6270-9/DL:T-1376-2010

community for more than 30 years. It was not applied to photonic band structure calculations until 1995 when Chan *et al.* [108] developed the so-called *Order-N method*, using a FDTD computational scheme that scales linearly with the system size. Below, we shall outline only the main ideas. The methodology and computational schemes for a variety of photonic problems can be found in the excellent book by Taflove [109].

The FDTD method is a general method for numerically solving the time-dependent Maxwell's equations in real space, approximating the space and time derivatives with finite differences. For the FDTD simulations of photonic crystals, a number of "building blocks" need to be defined. These are a set of geometrical and material boundary conditions, the initial field configuration(s) and several tools for extracting and calculating the relevant physical quantities [110]. These four parts (i.e. the core algorithm, the boundary conditions, the material and electromagnetic field setup and the data extraction) constitute the FDTD simulation. The basis of the simulation is the core algorithm, which calculates the temporal evolvement of the electromagnetic fields. The Maxwell's equations

$$\frac{1}{c}\frac{\partial}{\partial t}\vec{H}(\vec{r},t) = -\nabla\times\vec{E}(\vec{r},t) \tag{1.29}$$

$$\frac{\varepsilon(\vec{r})}{c}\frac{\partial}{\partial t}\vec{E}(\vec{r},t) = \nabla\times\vec{H}(\vec{r},t) \tag{1.30}$$

are discretized on a simple cubic lattice* where space-time points are separated by fixed units of time δt and distance δs. The spatial derivatives are approximated at each lattice point by a corresponding centered difference, which gives rise to finite-difference equations. For example, the difference form of the x component of the electric field $\vec{E}$ in the Eq. (1.30) can be written as

$$\frac{E_x\Big|^{m+\frac{1}{2}}_{i+\frac{1}{2},j,k} - E_x\Big|^{m-\frac{1}{2}}_{i+\frac{1}{2},j,k}}{\delta t} = \frac{c}{\varepsilon\Big|_{i+\frac{1}{2},j,k}}\left[\frac{\left(H_z\Big|^{m}_{i+\frac{1}{2},j+\frac{1}{2},k} - H_z\Big|^{m}_{i+\frac{1}{2},j-\frac{1}{2},k}\right)}{\delta s} - \frac{\left(H_y\Big|^{m}_{i+\frac{1}{2},j,k+\frac{1}{2}} - H_y\Big|^{m}_{i+\frac{1}{2},j,k-\frac{1}{2}}\right)}{\delta s}\right] \tag{1.31}$$

where the upper indices of the fields represent the time step and the lower triple indices the point in space. The other five equations are of similar form. For the electric $\vec{E}$ and magnetic field $\vec{H}$, the algorithm is essentially leapfrog [110] – it leaps in time from $\vec{H}$

---

* Here, the simple cubic mesh, as originally developed by Yee [107] is adopted only for simplicity. The FDTD method has also been implemented on non-orthogonal and non-uniform meshes [111].

ISBN:978-84-693-6270-9/DL:T-1376-2010

at t to $\vec{E}$ at $t+0.5\delta t$ to $\vec{H}$ at $t+\delta t$, and so forth. To ensure sufficient accuracy the size of the cubic cell δs should be set to less than 1/12th of the smallest wavelength (in the highest index material), so the field values do not change too much from one grid point to another. Besides, the time step δt must also be bounded to ensure numerical stability – it is proportional to the spatial resolution δs [109].

Because the computational domain is of finite size, special considerations should be given to the boundaries. The fields are updated by using appropriate boundary conditions, because information outside the computational domain is not available. The choice of boundary conditions depends on the system under investigation. To calculate the fields in an infinitely extended periodic system, Bloch periodic boundary conditions are applied to reduce the computational domain to just one primitive unit cell of the crystal. In this case, the fields at nodes outside the domain are related to the fields inside by the condition $\vec{E}(\vec{r}+\vec{a},t)=e^{i\vec{k}.\vec{a}}\vec{E}(\vec{r},t)$ where $\vec{a}$ is a lattice vector. If defects are present or introduced, the fundamental periodicity is no longer available and one has to resort to absorbing boundary conditions. These conditions must not reflect outgoing energy back into the inner region of the simulation. Several approaches have been developed, among which Mur's boundary conditions and the *perfectly matched layer* (PML) are the most popular [109].

The next serious question connected with the FDTD implementation is the initial field source. The nature and kind of initial conditions or the source used to excite the electromagnetic eigenmodes in the system also depend on the problem that is considered. The initial source might be an impulse (rather short to cover the frequency range of interest and not to intersect with outgoing radiation), a bundle of plane waves or a Gaussian-shaped field distribution. The initial field must be divergence-free: if not, it will contain some constantly operating sources, which will violate the reflection-transmission calculations. For photonic band structure simulations, the initial source given in the original work by Chan *et al.* [108] has proven to work well. It is represented as a sum of plane waves for the magnetic field $\vec{H}$ of the form

$$\begin{aligned}\vec{H}(\vec{r},t=0) &= \sum_{\vec{G}}(\vec{v}\times(\vec{k}+\vec{G}))e^{i(\vec{k}+\vec{G})\cdot\vec{r}} \\ \vec{E}(\vec{r},t=0) &= 0\end{aligned} \tag{1.32}$$

where $\vec{v}$ is an arbitrary vector so that $\nabla\cdot\vec{H}=0$ is satisfied. The appropriate choice of $\vec{v}$ is critical, because it selects eigenmodes with a certain symmetry. Those eigenmodes may not always couple to eigenmodes of different symmetries and results may therefore

ISBN:978-84-693-6270-9/DL:T-1376-2010

be incomplete. However, this selective coupling of the initial conditions to particular eigenmodes may be exploited, for example, to selectively calculate different polarizations.

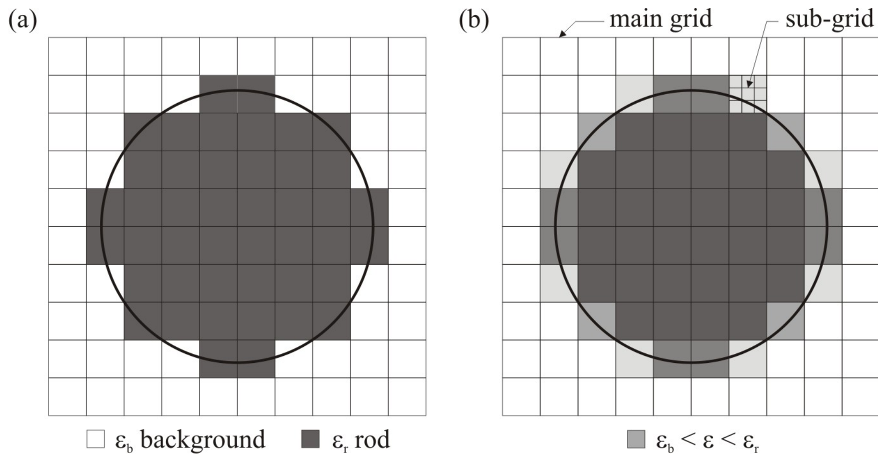

Fig. 1.8. Two ways of assigning values of the dielectric constant to the discrete numerical cells for a cylinder (rod) in two dimensions. Parameters ε_r and ε_b denote the dielectric constants of the rod and the background material, respectively. (a) The cells are set either to ε_r or ε_b depending on which material occupies most of the cell. (b) The dielectric constant ε assigned to the cell is found by averaging over some sub-mesh, so that $\varepsilon_b < \varepsilon < \varepsilon_r$. After [110].

At this point we would like to emphasize the practical aspect of modeling a curved surface on the discrete grid, because it strongly influences on the convergence properties of the band structure simulation. Figure 1.8 illustrates two ways of assigning values of the dielectric constant to the discrete numerical cells for a cylinder (rod) in two dimensions. In the left-hand picture, the cells are set either to ε_b (dielectric constant of the background material) or ε_r (dielectric constant of the rod), depending on which material occupies most of the cell. This scheme is known as the *staircase method*. In the right-hand picture, the cell-value is set as a geometrical average over the cell by using some sub-mesh, so the cells at the border of the cylinder have values somewhere between ε_b and ε_r. This scheme for assignation is sometimes referred to as the *fuzzy-cell method* [110]. Smoothing of the material parameters in the vicinity of the object borders leads to a faster convergence in band structure calculations [108].

When everything is done and set, the simulation starts and proceeds with a progressive marching in time for a certain number of time steps. If the eigenfrequencies are to be extracted, during the simulation the field components must be stored at some

UNIVERSITAT ROVIRA I VIRGILI
PHOTONIC BANDGAP ANALYSIS AND FABRICATION OF MACROPOROUS SILICON BY ELECTROCHEMICAL ETCHING
Trifon Todorov Tirfonov
ISBN:978-84-693-6270-9/DL:T-1376-2010

grid-points for each time step, thus constructing a time series of the fields. These time series are then Fourier transformed. The resulting spectrum consists of a discrete set of peaks, where each peak corresponds to an eigenfrequency. This procedure should be repeated for a number of $\vec{k}$ -vectors throughout the Brillouin zone (or the irreducible Brillouin zone) so that the band structure diagram can be drawn. In principle it would be sufficient to analyze the spectrum at one grid-point. However, if the point chosen happens to be in the node of an eigenmode, a peak in the spectrum will be missed, giving rise to a missing state in the band diagram. In practice, recording the fields at a number of randomly chosen grid-points avoids this problem. The resolution in frequency space is proportional to the number of time steps calculated in the simulation and therefore to the computation time. To extract the field-distribution of a certain eigenmode, the calculation must be repeated, and a narrow-band filter-function (for example a discrete Fourier transform for the eigenfrequency ω) applied to the whole space-grid.

The unique advantage of the FDTD method is that it enables the time domain simulations of pulses propagating through and interacting with complex defect structures. This method has been instrumental in the development of numerous designs of functional elements for optical communications devices, such as waveguide bends [90], junctions [112], channel drop filters [78,79], etc. The main shortcoming of the FDTD method is its computational requirements. It requires enormous computational resources, large amounts of memory and fast execution. However, because of the remarkable progress in computer technology, a standard personal computer can now calculate models that could formerly only be handled by supercomputers.

1.3.5. Other methods

Both the FDTD and plane wave methods have become mainstream methods for simulating photonic crystals. They are regularly used for band structure calculations. Many other methods have also been developed, which can be applied for solving general or more specific physical problems related to photonic crystals. Here, we shall very briefly describe two of them.

The *scattering matrix method* (SMM) [113,114] is used to characterize systems composed of a finite set of parallel dielectric cylinders in homogeneous medium, giving a precise static solution in a short time. In the SMM method, the source wave and the scattering objects are initially defined. The electromagnetic field at an arbitrary position

UNIVERSITAT ROVIRA I VIRGILI
PHOTONIC BANDGAP ANALYSIS AND FABRICATION OF MACROPOROUS SILICON BY ELECTROCHEMICAL ETCHING
Trifon Todorov Tirfonov
ISBN:978-84-693-6270-9/DL:T-1376-2010

is subsequently calculated from the summation of two waves: the wave arriving directly from the source and the wave that is scattered by an object. Every scattered wave is represented in terms of cylindrical function expansion. The amplitude of each degree of cylindrical function, which is excited by waves from the source positions, is represented by the scattering matrix. The source position, the scattering matrix, and the scattered wave are related to each other in simultaneous equations, and the excited amplitudes are found by solving a linear system, which immediately gives the electromagnetic field distribution at arbitrary positions. The main limitations of the method are: it can only be used with 2D crystals; the calculation examples are restricted to circular objects because the calculation task is much simpler since analytical scattering matrix solutions are available for circular figures; only static solutions of electromagnetic fields can be obtained, and the time response cannot.

The *transfer matrix method* (TMM) developed by Pendry and MacKinnon [115] is a combination of FDTD analysis and multilayer analysis methods. The TMM method works with discretized Maxwell's equations. However, the initial excitation is supposed to be monochromatic, and the basic structural unit is a layer of grid cells. The structure under consideration is divided into a set of layers with the same number of grid points in each layer. Using the discretized Maxwell's equations, the fields in adjacent layers are connected via the layer-to-layer transfer matrix. The output field is then calculated from the input field by the transfer matrix of the structure, which is a product of all individual layer-to-layer transfer matrices. The TMM method is less universal, but it is more computationally effective than the FDTD method. Nevertheless, it suffers the same problem that the computational resources required increase drastically when dealing with 3D problems, especially with fields localized within defects. The method can be used to model infinite periodic structures, and to find the eigenmodes and eigenfrequencies, as well as the transmission and reflection coefficients.

1.4. Technologies for fabricating 2D photonic crystals. State of the art

In Section 1.1 we pointed out that the fabrication of 3D and even 2D photonic crystals for the wavelength range of interest is still far from being a trivial task. The key number here is λ=1.5 μm, since this is the typical wavelength of light used by the optoelectronic industry. Of course, we would like to be able to fabricate photonic crystals that also operate in the visible and near-infrared spectrum, where they may find

their most promising applications. Almost all of the applications proposed for photonic crystals rely on the existence of the photonic band gap. However, the frequency at which the band gap occurs is directly related to the size of the scattering elements that make up the photonic lattice. Specifically, the size of the features must be of the order λ/2, where λ is the wavelength of light at which the gap occurs. Therefore, to achieve a band gap in the visible region we should be able to fabricate lattice elements in the order of 1/4 μm. Moreover, we should be able to fabricate precisely small elements with roughly ten lattice periods in each direction. Any deviations in the size or in the period may affect the properties of the photonic crystal and reduce the band gap significantly. Perhaps for this reason, the fabrication of 2D photonic crystals has developed the most, mainly because the fabrication requirements are relaxed because of the lower dimensionality, and because mature techniques are available, borrowed from the microelectronics industry. Most research also focuses on the use of semiconductor materials* because of their high dielectric constant required for achieving a wide photonic band gap. Below, we shall review the techniques that are most widely used in 2D photonic crystal fabrication.

1.4.1. Lithography

Generally, lithography is used to pattern the substrate for 2D photonic crystals. Considering the small size of the lattice (periodicity between 0.2 and 0.7 μm, with sub-0.1 nm control of feature size desirable) for a PBG in optical range, standard photolithography techniques cannot be used. The most popular alternative is *electron-beam lithography* (EBL), in which the photons for resist exposure are replaced by electrons. Since the wavelength of an electron is far smaller than that of a photon, diffraction is not a limit to the resolution. Although projection and proximity EBL systems exist, the most popular are the direct writing systems, in which a focused electron beam is scanned across the surface to generate the pattern. The resolution of this process tends to be limited by the resist and substrate used. Although the beam can be focused to less than 2 nm, feature sizes are typically a minimum of 10-20 nm because of electron scattering in the resist and electron backscattering from the substrate. EBL has been used by a variety of groups to generate patterns that can be applied in the visible [116] to near-IR [57,117] ranges. Although its resolution is higher, EBL is more expensive and gives lower yields than conventional photolithography.

---

* One exception are the photonic crystal fibers which basically use 2D PBG as fiber cladding. However, they are beyond the scope of the present review.

UNIVERSITAT ROVIRA I VIRGILI
PHOTONIC BANDGAP ANALYSIS AND FABRICATION OF MACROPOROUS SILICON BY ELECTROCHEMICAL ETCHING
Trifon Todorov Tirfonov
ISBN:978-84-693-6270-8/DL:T-1376-2010

Several workers have also succeeded in using interference lithography to generate the hexagonal pattern. The method was first proposed and implemented by Berger *et al.* [118] to fabricate 2D hexagonal patterns in a photosensitive polymer, which subsequently served as an etch mask for transfer to a high-index silicon substrate. The 2D interference pattern with hexagonal symmetry was produced by diffracting a laser beam from a single optical element consisting of three diffraction gratings at an angle of 120° to one another. The diameter and pitch of the high- and low-intensity regions of the interference pattern are determined by the laser wavelength and the angle of the first-order diffracted beams with respect to the incoming beam. Later, this approach was extended [119,120] to create low index contrast 3D structures with face- or body-centered cubic like symmetry. The interference lithography methods, however, can create only defect-free photonic structures.

1.4.2. Dry etching

Dry etching, together with e-beam lithography, is commonly used in the semiconductor technology. There are various versions of dry-etching processes, which have rather obscure acronyms, like RIE, DRIE, RIBE, CAIBE, etc. Clearly, a comprehensive review of all these techniques, which are used to fabricate planar semiconductor devices, would be very complicated and lengthy. We shall restrict ourselves to a short description of the basic physical process involved. Generally, dry etching covers a family of methods by which a solid surface is etched in the gas or vapor phase, physically by ion bombardment, chemically by a chemical reaction through a reactive species at the surface, or by combined physical and chemical mechanisms. Most dry etching techniques are plasma-assisted. They are commonly divided into three groups: (1) *chemical plasma etching* (PE), (2) synergetic *reactive ion etching* (RIE), and (3) physical *ion-beam etching* (IBE). For groups (1) and (2), the basic principle of etching involves generating chemically reactive neutrals (e.g., F, Cl) and ions (e.g., SF_x^+) that, under the effect of an electric or magnetic field, accelerate towards the target substrate. The reactive species (neutrals or ions) are formed by the collision of molecules in a reactant gas (e.g., SF_6, CF_4, Cl_2, etc.) with a cloud of energetic electrons excited by a radiofrequency (RF) field. When the etching process is purely chemical, powered by the spontaneous reaction of neutrals with the target, it is known as *chemical plasma etching*. But if ion bombardment of the substrate surface plays a synergistic role in the chemical reactions, the etching process is known as *reactive ion etching* (RIE). The processes in group (3) are based on a purely physical

UNIVERSITAT ROVIRA I VIRGILI
PHOTONIC BANDGAP ANALYSIS AND FABRICATION OF MACROPOROUS SILICON BY ELECTROCHEMICAL ETCHING
Trifon Todorov Tirfonov
ISBN:978-84-693-6270-9/DL:T-1376-2010

etching mechanism, i.e. accelerated ions (e.g. Ar^+) impinge on the surface and physically remove material from the substrate. Reactive species are not added. The etching techniques in group (2) use both chemical and physical etching mechanisms.

Chemically assisted ion beam etching (CAIBE) is probably the most widely used dry etching technique for fabricating 2D planar photonic crystals, PC waveguides and microcavities [57,68,93,71,121]. In this technique, reactive species are introduced into the process independently of the etching ion beam, and in this way make it possible to control the physical and chemical parameters separately. The aspect ratios (hole diameter : etch depth) achieved by CAIBE are in the order of 20 : 1 (120 nm holes etched at a depth of 2.5 μm in the GaAs/AlGaAs structure [121]). With more conventional RIE, the typical aspect ratios are 6-8 : 1 [93].

III-V compound semiconductors are necessary to fabricate light emitting devices. Although aspect ratios are high for the GaAs system when the CAIBE technique is used, the internal efficiency of light emission decreases in the photonic crystal because of the large surface recombination of GaAs. The InP system is more difficult to process but its recombination velocity is lower than that of the GaAs. The ideal etching characteristic for the InP system is being proven by i*nductively coupled plasma reactive ion etching* (ICP-RIE) [122]. Briefly, this technique provides further excitation to the electron cloud and to the reactive ions by means of an externally applied RF magnetic field. It increases the density of ions and neutrals, which results in higher etching rates.

1.4.3. Soft lithography

Soft lithography, extensively reviewed by Xia and Whitesides [123], is a non-photolithographic technique based on self-assembly and replica molding for micro- and nanofabrication. An elastomeric stamp with patterned relief structures on its surface is used to generate patterns and structures with feature sizes ranging from 30 nm to 100 μm. Several techniques have been developed: micro-contact printing, replica molding, micro-transfer molding, micro-molding in capillaries, solvent assisted micro-molding, etc. In nanoimprinting, a pattern recorded in a mold is press transferred to a thermoplastic polymer thin film, where ridges and trenches with a minimum size of 25 nm and a depth of 100 nm are created [41]. Further processing may be applied to record the transferred pattern into the substrate for large scale replication. Although it is a 2D technique, it can be extended and used to build 3D structures by iterative

UNIVERSITAT ROVIRA I VIRGILI
PHOTONIC BANDGAP ANALYSIS AND FABRICATION OF MACROPOROUS SILICON BY ELECTROCHEMICAL ETCHING
Trifon Todorov Tirfonov
ISBN:978-84-693-6270-8/DL:T-1376-2010

processing [41].

1.4.4. Glass capillary plate

The capillary plate is the first material used to successfully produce a 2D photonic crystal in both the near-IR and visible wavelength region [58]. The method consists basically of drawing a bundle of optical fibers, in which core (SiO_2) and cladding (PbO) can be selectively dissolved. Hundreds of glass fibers are bundled together to form a hexagonal lattice (close-packed arrangement). The bundle is then heated and drawn out to reach the desired lattice parameter. Next, the core is selectively dissolved to leave a hexagonal lattice of air holes in glass. A glass capillary, which provides this fabrication process with its name, with holes of an almost infinite aspect ratio can be fabricated. The filling fraction of the air holes can be adjusted through the initial core/cladding radii ratio. Although structures with a hole periodicity of about 0.2 μm [124] have been made, there are still problems such as the generation of cracks caused by the strain that occurs during the core etching for such small hole periods.

1.4.5. Anodization techniques

Anodization techniques are wet etching techniques that use selective etching phenomena, which depend on the semiconductor crystal direction. Unlike dry etching methods, in which the anisotropy of the etching process is controlled by the plasma conditions, the anodic etching of single crystal semiconductors, formed from Si, InP, GaAs, is a selective etching process, and the selectivity depends on the nature of the crystal direction. By this technique 2D photonic crystals formed of very high-aspect-ratio hole arrays in a semiconductor can be fabricated.

The anodization of Si in acid solutions (usually HF solutions, although organic etchants have also been used) gives rise to macroporous silicon [60]. Because of the generally “macroscopic” (1-50 μm) feature size of the etched holes, the material produced by this technique is termed “macroporous” silicon, in contrast to its “microscopic” relative. The etching process proceeds upon provision of positive carriers (holes), which takes part in the chemical dissolution reaction. In p-type Si, the holes are majority carriers, while in n-type Si they must be generated by illumination. The sample characteristics (doping level, orientation), the applied voltage and the etching current are the main etching parameters that control the pore size and morphology. As in n-type

Si the holes are photo-generated, the etching current and applied voltage decouple, thus allowing better control of the process and also making it possible to modulate the pore diameter in depth by varying the current. For this reason, and also because of the lack of a reliable model with a "predictive power" on the pore geometry, the anodic etching of p-type Si is somewhat less developed than the etching of n-type Si. Such a model does exist for n-Si and fits well with the experimental results [125]. The sample is first patterned by means of photolithography, oxidation and subsequent wet anisotropic etching (KOH, TMAH) to make a series of indentations on the silicon surface. When the sample is immersed in the HF etchant and backside illuminated, the photo-holes concentrate around the sharp curvature at the bottom of the indentations, where the pore formation begins. As the pores grow, the tips of the pores etch preferentially, which leads to very deep, straight pores.

Initially Grüning et al. [126] reported a 2D photonic crystal, which exhibited individual gaps for both polarizations in the infrared region between 20 and 40 μm. The fabricated crystal consisted of a square array of macropores etched in silicon, with a pore diameter of 6.2 μm and a pore depth of 340 μm. This constitutes an aspect ratio of $> 50 : 1$ and compares favorably with the ratios $< 10 : 1$ that are typically achieved by dry etching. Macroporous silicon with feature sizes in the sub-micron range has been demonstrated [61,127], showing a 2D polarization-independent PBG for wavelengths 1.3-1.5 μm. Starting from the macroporous silicon fabrication, it is also possible to reverse the photonic structure, i.e. to make silicon pillars in air, instead of air pores in silicon [128]. The high-aspect-ratio hole array structure by anodic etching has also been reported in compound semiconductors like InP and GaAs [129-131].

An alternative approach for producing 2D structures that can display band gaps in the visible is the anodic growth of porous alumina. After the anodic oxidation of alumina in an acid solution, a porous oxide film of vertical holes is formed on the surface. This covering film, known as anodic porous alumina, is the result of the formation of a regular structure, in which an amorphous state of alumina grows via self-organization, independent of the crystal direction. A combined technique, using an aluminum texturing process and the self-organization channel formation, has been developed as a method for fabricating anodic porous alumina with an ideal fine hole arrangement [62]. Before the anodic oxidation, the aluminum surface is textured by a molding process using a master with hexagonally arranged convexes. The master is made of durable SiC wafer on which the convex structure is arranged regularly by e-beam lithography and, consequently, can be used repeatedly. The master is placed on the aluminum and mechanically pressed to form a regular arrangement of shallow

UNIVERSITAT ROVIRA I VIRGILI
PHOTONIC BANDGAP ANALYSIS AND FABRICATION OF MACROPOROUS SILICON BY ELECTROCHEMICAL ETCHING
Trifon Todorov Tirfonov
ISBN:978-84-693-6270-0/DL:T-1376-2010

concave depressions onto the aluminum surface. The formed in this way predetermined pattern acts as initiation points and guide the growth of channels during the anodic oxidation. Holes with diameters as small as 70 nm and aspect ratios of 150 : 1 were reported by Masuda *et al.* [62]. A measured sample, fabricated by this technique showed a stopband in the transmission characteristic around 600 nm [132].

To conclude, we would like to point out that the experimental techniques outlined here are by no means all of the research that has been undertaken in the fabrication of 2D photonic crystals. We have already mentioned that some of these 2D techniques are being developed to make 3D photonic crystals. However, the opposite is also true – many of the techniques that are currently used for 3D PC fabrication can also be used for 2D photonic crystals. The border between 2D and 3D fabrication is sometimes rather diffuse, so clearly differentiating between them is not only difficult but unnecessary.

UNIVERSITAT ROVIRA I VIRGILI
PHOTONIC BANDGAP ANALYSIS AND FABRICATION OF MACROPOROUS SILICON BY ELECTROCHEMICAL ETCHING
Trifon Todorov Tirfonov
ISBN:978-84-693-6270-9/DL:T-1376-2010

ISBN:978-84-693-6270-9/DL:T-1376-2010

Chapter 2

Photonic bands of 2D photonic crystals. Band-gap engineering

This chapter is devoted to the photonic band-gap formation in 2D photonic crystals. Photonic lattices of different configurations that comprise dielectric scatterers of various shapes, orientations and sizes are studied in view of the existence of an absolute PBG and the maximization of its width as a function of the geometrical parameters of 2D photonic crystal. The absolute PBG in the context of 2D photonic crystals is understood as a forbidden frequency region in the photonic band structure, where no propagation is possible for any direction in the plane of periodicity and for any polarization of the incident light. Since the photonic band gap is one of the major features of the photonic crystals, the search for 2D structures that possess large and robust absolute PBG has motivated a lot of research. We address hereafter more systematically the fundamental question of the existence of an absolute PBG for a wide choice of photonic lattices. We also examine how changes in the topology, lattice symmetry and shape of the scatterers influence the properties of photonic band gap and give the optimum parameters that yield a maximal gap width for a given structure. Our results are also detailed in terms of the relative difficulty of fabrication by giving the smallest feature size for each of these optimized photonic lattices.

ISBN:978-84-693-6270-0/DL:T-1276-2010

2.1. Photonic bands in two dimensions

We shall begin our discussion by using an example in order to introduce the main concepts we shall work with from this point forward. Let us consider the photonic crystal shown in Fig. 1.7 from Chapter 1. It consists of infinitely long dielectric cylinders with dielectric constant ε_r embedded in a dielectric background (ε_b) and ordered periodically to form a 2D hexagonal lattice. We assume that the dielectric constant of the cylinders is ε_r=1 (air) and that of the background material is ε_b=12.096 (Si at wavelength λ=1.55 μm [7]). The considered photonic crystal becomes then formed of cylindrical air holes etched deeply (infinitely) in a silicon host matrix. This photonic lattice has been extensively studied both theoretically [13,48,52,117,133] and experimentally [46,59,61,132,134] and now, it is widely accepted that the hexagonal arrangement of circular air rods in a dielectric host gives rise to the largest absolute PBG among the known 2D photonic crystals. Due to the translational symmetry in two dimensions, to calculate the photon dispersion relation $\omega(\vec{k})$ we can restrict our attention only for wavevectors $\vec{k}$ inside the first Brillouin zone, given in Fig. 1.7b. Besides the translational symmetry, the hexagonal lattice possesses some rotational and mirror symmetries, which allow us to further restrict the set of non-redundant wavevectors $\vec{k}$ within the irreducible Brillouin zone (shown as a shaded triangular wedge in Fig. 1.7b). Indeed, we can easily see that the given structure is invariant when it is rotated by multiples of 60 degrees. All the symmetry operations that transform the lattice into itself are known to constitute a *space group*. Besides the translation symmetry operations, the space group contains proper or improper rotations[*] which also leave the lattice unchanged. The rotational parts of the space group symmetry elements constitute a group which is called the *point group* of the lattice. The shown hexagonal lattice belongs to C_{6v} point group[†] [17]. Detailed information on the symmetry properties of square and hexagonal lattices, as well as the basics of the group theory can be found in Ref. 17 Chapter 3, Ref 135 Chapters 1 and 2, or Ref 136.

Besides the above symmetry operations, if we restrict ourselves to consider only the propagation of light confined in the plane of periodicity (the plane

---

[*] The rotations are described by 3x3 orthogonal matrices in the three dimensional Euclidean space. A proper rotation is an ordinary rotation, whose matrix has determinant of +1. An improper rotation has a determinant of -1. The improper rotations can be described as a combination of an ordinary rotation followed by an inversion [136].

[†] The symmetry group $C_{6\upsilon}$ consists of rotations of $\pi/3$ and mirror operations. C_n generally means rotation by $2\pi/n$ radian [136].

UNIVERSITAT ROVIRA I VIRGILI
PHOTONIC BANDGAP ANALYSIS AND FABRICATION OF MACROPOROUS SILICON BY ELECTROCHEMICAL ETCHING
Trifon Todorov Tirfonov
ISBN:978-84-693-6270-9/DL:T-1376-2010

perpendicular to the axis of the cylinders), the crystal becomes then invariant under reflections through this plane. This mirror symmetry allows us to classify the modes by separating them into two distinct polarizations: either *TE* (transverse-electric) or *TM* (transverse-magnetic) modes [13]. For the former, the only non-zero components of the electromagnetic field are (E_x, E_y, H_z), i.e. the electric field $\vec{E}$ is confined in the plane of periodicity while the magnetic field $\vec{H}$ is polarized along the axis z of the cylinders. For the latter the reverse is true: (H_x, H_y, E_z) with the magnetic field $\vec{H}$ confined in the plane and the electric field $\vec{E}$ parallel to the cylinders. In the literature sometimes the following notation can be found: *E-polarization* which corresponds to *TM* modes and *H-polarization* corresponding to *TE* modes. For the rest of the text we will adopt the notation with *TE* and *TM* polarization modes. The shown separation of the modes into two polarizations is a unique property of every 2D photonic crystal.

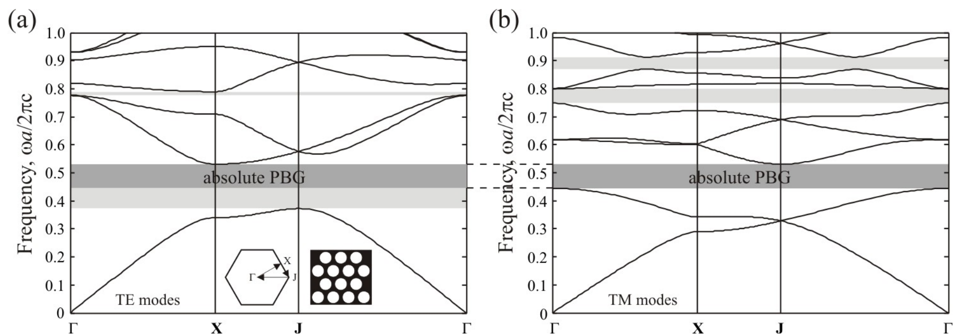

Fig. 2.1. Photonic band structure of 2D photonic crystals consisting of air holes (ε=1) drilled into silicon matrix (ε=12.096) and arranged in a triangular lattice (shown in the right inset). The radius of the air holes is r=0.48a (a=lattice constant). The photonic bands are calculated separately for (a) the *TE* and (b) the *TM* polarization modes along the Γ-X-J-Γ path of the irreducible Brillouin zone (shown in the left inset). The *TE1-2* and *TM2-3* polarization gaps overlap and form an absolute PBG. It has a normalized width of $\Delta\omega/\omega_g$=17%.

Therefore, the photonic bands for the present 2D photonic crystal should be calculated separately for *TE* and *TM* polarization modes and for wavevectors $\vec{k}$ going along the edges of the irreducible Brillouin zone. In Fig. 2.1 we plot the photonic bands along the **Γ-X-J-Γ** path considering that the radius r of the air holes is r=0.48a. It can be seen that the band structures for *TE* and *TM* modes are completely different. There can be photonic band gaps for one polarization and not for the other. In our particular case, there are band gaps for both polarization modes. In addition, the *TE1-2* (i.e. the gap

ISBN:978-84-693-6270-0/DL:T-1276-2010

between the first and the second photonic bands) and the *TM2-3* polarization gaps overlap in the frequency region 0.44448÷0.53078 (in units 2πc/*a*). The absolute PBG formed in this way has a frequency width of $\Delta\omega$=0.086 (2πc/*a*). It is sometimes useful to express the absolute PBG width in dimensionless units, which are independent of the scale of the crystal. This can be done by defining the quantity *gap-midgap ratio* (or normalized gap width) as the frequency width $\Delta\omega$ of the gap divided by the frequency ω_g at the middle of the gap: that is, $\Delta\omega/\omega_g$ [13]. In this way, if the system is scaled up or down, all the frequencies scales accordingly, but this quantity stays unchanged. For the given dielectric contrast and size of the rods the absolute PBG has a gap-midgap ratio $\Delta\omega/\omega_g$=17%.

What are the real dimensions of the air holes and the lattice if the photonic crystals should operate in the λ=1.55 μm window? To calculate this we need to center the gap at wavelength λ=1.55 μm. From the Fig. 2.1 we can see that the mid-gap frequency is about ω_g=0.488 (2πc/*a*). Then, from the relation

$$\frac{\omega a}{2\pi c} = \frac{a}{\lambda} = 0.488 \qquad (2.1)$$

we obtain for the lattice constant *a*=0.756 μm. The radius of the air holes should therefore be *r*=0.363 μm. As in this case the lattice constant *a* is the center-to-center distance between the holes, the thickness of the dielectric wall which separates two neighbor holes will therefore be $(a-2r)$ ≈0.030 μm. The fabrication of such elements with so small size (30 nm) is really a difficult task and requires state-of-the-art e-beam lithography and dry etching techniques. For all structures studied in this chapter we have evaluated the relative difficulty of fabrication by centering the gap at λ=1.55 μm (Table 2.1).

2.2. The general rule of thumb

Can we predict if a particular 2D structure will have an absolute photonic band gap? Clearly, the dielectric contrast plays a fundamental role in the band-gap opening because it determines the strength of the scattering. For example, for the triangular lattice examined above the minimum index contrast between the dielectric materials must be 2.66 so as to an absolute PBG open up [133]. There are also other factors that have a fundamental role to play for the existence of photonic band gaps. One of these factors is the lattice type since it controls the shape of the first Brillouin zone and so the

UNIVERSITAT ROVIRA I VIRGILI
PHOTONIC BANDGAP ANALYSIS AND FABRICATION OF MACROPOROUS SILICON BY ELECTROCHEMICAL ETCHING
Trifon Todorov Tirfonov
ISBN:978-84-693-6270-9/DL:T-1376-2010

likelihood of achieving a gap in all directions. Very important factor is also the crystal topology. In general, we can have two kinds of topologies: a cermet topology, for which the crystal consists of isolated dielectric blocks embedded in a host matrix of second dielectric, or a network topology where both materials forms connected structures. The first photonic crystal (*Yablonovite* structure [31]) falls into the group of crystals with network topology and has a sizable band gap. Other 3D crystals, such as woodpile structures [32-34], inverse opals [35,36], the proposed spiral crystal [37,38] and even the simple cubic structure despite of its unfavorable crystal symmetry (dielectric rods with either square or circular cross-sections arranged in a cubic lattice [137]) exhibit sizable gaps because all they are networks. This turns out to be a general conclusion: the network topology is more favorable for the development of large gaps than the cermet [22].

The above conclusion also holds for the 2D photonic crystals. The wide-spread opinion is that the structure of air holes in a dielectric host is most likely to produce large absolute gaps than dielectric rods embedded in air. Based on the difference of the filling factors between the dielectric band and the air band (related to the distribution of the displacement field $\vec{D}$), a general rule of thumb has been drawn [13]: *TM band gaps are favored in a lattice of isolated high-ε regions, and TE band gaps are favored in a connected lattice.*

In fact, we have already discussed this notion in Chapter 1 where the reasons for the large frequency jump between the air and dielectric bands were explained [83]. For example, the square lattice of dielectric rods in air (that is, isolated high-ε regions) exhibits large gaps for the *TM* modes, whilst the *TE* modes have no gaps at all. The displacement field $\vec{D}$ at the top of the dielectric band is mostly concentrated in the dielectric rods (for the *TM* modes the $\vec{D}$ field is parallel to the rods and so it is discontinuous across the boundary). The modes at the bottom of the air band also tend to concentrate their energies in the dielectric rods but the orthogonality requirement forces them to have a $\vec{D}$ field expelled to some extent into the air regions. So the modes at the top of the gap will have higher energies and will therefore lie at higher frequencies. For the *TE* modes the situation is different as these modes have $\vec{D}$ perpendicular to the rods. The mode at the bottom of the gap tries to concentrate the field within the rods but the condition of field discontinuity at the boundaries enforces the field to have lines penetrating into the air. The mode at the top of the gap is much the same. Thus, there is no large band gap between the modes of the dielectric and air bands. If we consider now a structure formed of air holes in a dielectric host (connected

UNIVERSITAT ROVIRA I VIRGILI
PHOTONIC BANDGAP ANALYSIS AND FABRICATION OF MACROPOROUS SILICON BY ELECTROCHEMICAL ETCHING
Trifon Todorov Tirfonov
ISBN:978-84-693-6270-9/DL:T-1276-2010

structure), the *TE* modes will then have larger gaps. The lines of the displacement field $\vec{D}$ of the *TE* modes at the bottom of the gap run along the dielectric channels (the veins) between the air rods in order to avoid the air. The upper modes must have the $\vec{D}$ field orthogonal, it is expelled into the air rods and large gap opens up. The *TM* modes have $\vec{D}$ concentrated in the dielectric regions: for the lower modes it is mostly concentrated in the intersections between the dielectric veins and for the upper modes it is located inside the veins. Thus, there is no large frequency jump between the lower and upper *TM* modes and no gap is open up.

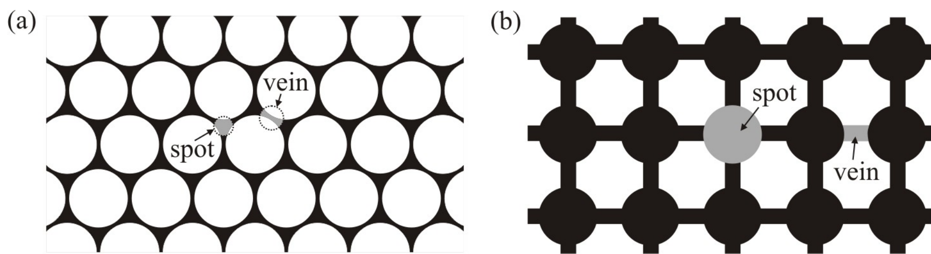

Fig. 2.2. (a) Photonic crystal formed of air holes in a dielectric matrix arranged in a hexagonal lattice [13]. (b) Photonic crystal formed of dielectric rods in air, which are connected by narrow dielectric veins [138]. The figure illustrates the general rule of thumb, which holds that an absolute PBG is favored in structures formed of high-ε regions that are both practically isolated and linked by narrow veins.

In order to obtain an absolute PBG which in 2D photonic crystals is formed of the overlap between both *TE* and *TM* polarization gaps we should therefore look for a compromise structure: it must be formed of high-ε regions which are both practically isolated and linked by narrow veins. One example is the well-known triangular (or hexagonal) structure (Fig. 2.2a). As was shown, when the radius of air holes is large enough this structure does exhibit an absolute PBG. The spots between the air columns look like localized regions of high-ε material which are connected through the narrow veins between the columns. Another example of 2D structure with network topology is the square lattice studied by Qiu and He [138]. In this structure, an absolute photonic band gap is obtained by optimally connecting the dielectric rods in a square lattice with narrow dielectric veins (Fig. 2.2b).

It is worth pointing out that the general rule of thumb can be used to explain the band gaps particularly at low frequencies. However, due to the complication of the differential operators in Maxwell's equations (different field components are coupled to

UNIVERSITAT ROVIRA I VIRGILI
PHOTONIC BANDGAP ANALYSIS AND FABRICATION OF MACROPOROUS SILICON BY ELECTROCHEMICAL ETCHING
Trifon Todorov Tirfonov
ISBN:978-84-693-6270-9/DL:T-1376-2010

each other even if the dielectric function $\varepsilon(\vec{r})$ can be separated), it is difficult to obtain analytical (even approximate) solutions for the distribution of the displacement field at high frequencies. Many 2D photonic crystals with large absolute PBG [49,139-141] can not be explained or found by this general rule of thumb.

2.3. Symmetry reduction

Degeneracy lifting is another explanation for the opening of an absolute PBG and even a method for creating band gaps. It is well known that the symmetry plays an important role in the opening of absolute PBGs [49]. Often, severe restrictions to the absolute PBG formation are due to the symmetry-induced degeneracies of photonic bands at high symmetry points in the Brillouin zone. These degeneracies give rise to overlapping bands and thus, they prevent photonic gaps from opening up. In some cases the band degeneracy can be lifted by symmetry breaking. We have already said that in the 3D case the *fcc geometry* is less favorable for creating a band gap than the *diamond geometry*. Consider, for example, the 3D *fcc* crystal, which does not possess an absolute PBG. By decreasing its symmetry through the introduction of a two-point basis set (which produces the diamond structure), the degeneracy in the bands is lifted and an absolute PBG is obtained [30].

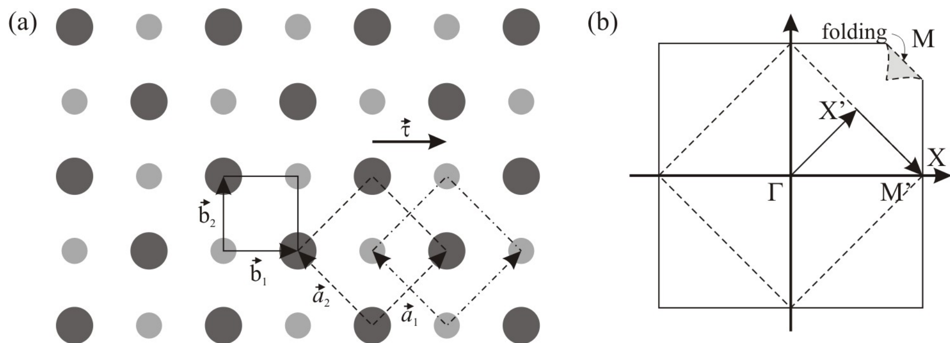

Fig. 2.3. Square lattice with inclusion of additional rod at the center of the unit cell (a) and its Brillouin zone (b). The unit cell and the Brillouin zone of the direct lattice (where the rods are identical) are shown by solid lines, while for the perturbed lattice (rods of different size) they are denoted by dashed lines. The structure can also be represented by two simple interpenetrating square lattices (dashed and dash-dotted lines) which are shifted with respect to each other by a vector τ. The folded corner in the Brillouin zone of the direct lattice schematically suggests the folding required to achieve the Brillouin zone of the perturbed lattice. After [142].

UNIVERSITAT ROVIRA I VIRGILI
PHOTONIC BANDGAP ANALYSIS AND FABRICATION OF MACROPOROUS SILICON BY ELECTROCHEMICAL ETCHING
Trifon Todorov Tirfonov
ISBN:978-84-693-6270-0/DL:T-1276-2010

Quite similar to this 3D case, is the degeneracy lifting by the introduction of a two-point basis set in the simple square 2D lattice, first studied by Anderson and Giapis [50]. In order to illustrate the mentioned concepts we shall proceed with an example of the square lattice of dielectric rods embedded in air. Consider the structure shown in Fig. 2.3a. It is a face-centered square lattice with a basis including two different rods. We can represent this lattice as two interpenetrating simple square lattices whose generating primitive vectors are denoted by dashed and dash-dotted arrows, respectively. The two sub-lattices consist of rods with two different sizes and are shifted with respect to each other by a vector $\vec{\tau} = a(1,0)$. We can define the unit cell of the structure (shown by dashed line in Fig. 2.3a) by the vectors $\vec{a}_1 = a(1,1)$ and $\vec{a}_2 = a(-1,1)$. The unit cell consists of four rods with radius r_1 placed at the corners of the cell and an included rod of radius $r_2<r_1$ placed at the center of the cell. We notice that such inclusion of additional rod does not change the point group symmetry of the lattice (it belongs to the same point group* $C_{4\upsilon}$ as the simple square lattice). The translation group symmetry does not change either. Thus the space group symmetry of the structure does not change at all although the smallest unit cell must include two rods after the smaller rod is added.

When all rods are identical then the structure is described by an unit cell (represented with solid line), generated by the primitive vectors $\vec{b}_1 = a(1,0)$ and $\vec{b}_2 = a(0,1)$. We will refer to the lattice of identical rods as a *direct lattice.* The structure where the rods have different sizes will be referred to as a *perturbed lattice* [142]. Note that the area of the unit cell for the direct lattice is less then twice the area of the unit cell for the perturbed lattice. Consequently, the Brillouin zone for the direct lattice will be twice bigger than the Brillouin zone for the perturbed lattice. The Brillouin zones of both lattices are shown in Fig. 2.3b, where the representation adopted is just the same as the one, used for the primitive unit cells. The periodic "potential" of the structure $\varepsilon(\vec{r})$ can be treated as a sum of the potential associated with the simple square lattice of identical rods plus a perturbative potential related to the difference in the rod size. The inclusion of perturbative potential results in a doubling of the period and in a complete nesting of the Brillouin zone of the direct lattice into the Brillouin zone of the perturbed lattice. The folding of Brillouin zone of the direct lattice required to achieve the Brillouin zone of the perturbed lattice is schematically depicted in Fig. 2.3b. We can see that the points **Γ** and **M** associated with the direct lattice will be combined in one point

* The point group $C_{4\upsilon}$ contains all symmetry operations that transform a square into itself [136].

UNIVERSITAT ROVIRA I VIRGILI
PHOTONIC BANDGAP ANALYSIS AND FABRICATION OF MACROPOROUS SILICON BY
ELECTROCHEMICAL ETCHING
Trifon Todorov Tirfonov
ISBN:978-84-693-6270-9/DL:T-1376-2010

Γ' associated with the perturbed lattice. The point **X** of the direct lattice becomes point **M'** in the perturbed lattice.

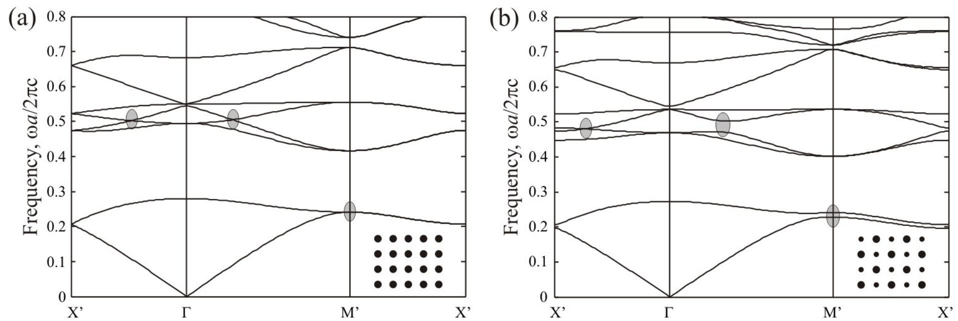

Fig. 2.4. Photonic band structure (*TM* modes) of the square lattice with a two point basis set (shown in Fig. 2.3) for ε_r=12.096 (Si) and ε_b=1 (air). (a) Band structure of the direct lattice (identical rods with radii $r_1=r_2=0.2a$) drawn for the twice folded Brillouin zone of the perturbed lattice. (b) Band structure of the perturbed lattice (rods of different sizes, with $r_1=0.2a$ and $r_2=0.22a$). In both cases, the picture insets denote the lattice under consideration. Numerous band degeneracies can be observed in the band spectrum of the direct lattice (some of them are marked by shaded ellipses). However, in the spectrum of the perturbed lattice when the rods differ in size some of these band degeneracies are lifted. Further increasing of the difference between the rods can even give rise to band gap opening between the fourth and fifth photonic bands.

The photonic band structure for the square lattice with two-point basis set is shown in Fig. 2.4 for the *TM* modes. The dielectric constant of the rods is assumed to be that of Si (ε_r=12.096), while the background material is supposed to be air (ε_b=1). Figure 2.4a shows the band spectrum for the direct lattice, i.e. the case of identical rods with equal radii $r_1=r_2=0.2a$. Figure 2.4b shows the spectrum of the perturbed lattice comprising rods of different sizes, i.e. $r_1=0.2a$ and $r_2=0.22a$. The spectrum is drawn for the twice folded Brillouin zone of the perturbed lattice. In the perturbed lattice, the spectrum along the **Γ-M'** direction will be folded from the spectrum of the direct lattice along **Γ-X** and **M-X** directions, while the spectrum along the **Γ-X'** direction will be folded from two branches in the direct-lattice spectrum: from point (0,0) to $\pi/2a(1,1)$ and from point $\pi/a(1,1)$ to $\pi/2a(1,1)$. We can see that numerous band degeneracies exist in the spectrum of the direct lattice. Some of them are labeled by shaded ellipses. The labeled band degeneracies are lifted in the spectrum of the perturbed lattice. The fourth and fifth photonic bands which intersect along **Γ-M'** and **Γ-X'** directions are related to the two different alternating layers of rods perpendicular to the (11) direction. In the direct lattice these layers are identical and the bands have the same energy. However, in

ISBN:978-84-693-6270-0/DL:T-1276-2010

the perturbed lattice the layers are different (rods of different size) and these two bands have to split. The greater the difference between dielectric rods, the greater is the energy splitting, which finally results in band gap opening between the fourth and fifth photonic bands. Similarly, all bands along the **M'-X'** direction in the direct-lattice spectrum are identical. The vector **M'X'** in the reciprocal space corresponds to the planes {11} which are identical in the direct lattice but are of different kind in the perturbed lattice. This is why the bands along the **M'-X'** direction have to split in the spectrum of the perturbed lattice. It is worth mentioning that not all band degeneracies can be lifted by such a perturbation. The inclusion of an additional rod at the center of the unit cell still keeps the symmetry of the simple square lattice. That is why some degeneracies at the high symmetry points of the Brillouin zone are conserved also in the perturbed lattice. More detailed discussion of applying the described *perturbative approach* to the analysis of complex square lattices can be found in Ref. 142. Similar perturbative approach has been also used in Ref. 49 to explain the gap opening in 2D honeycomb and graphite structures.

We have seen that band degeneracies can be lifted by the inclusion of an additional rod even though the space symmetry of the lattice is not disrupted. There are, however, several other ways in which one can reduce the symmetry. One example is the complex structure studied by Anderson and Giapis [140] where the square lattice combines two different rod sizes, with a total of six rods added in each primitive unit cell. It has been shown that this structure possesses large absolute PBG for the configuration of dielectric rods embedded in air. Degeneracy lifting can be also achieved by using anisotropic dielectric materials [141]. In such materials, the *TE* and *TM* polarization modes see different refractive index contrasts (due to the different ordinary n_o and extraordinary n_e refractive indexes of the material), which enables the optimal overlapping between the both polarization gaps and thus, the achieving of large complete PBG. Many other approaches have been applied to obtain large photonic band gap: inserting a third component into the existing photonic crystal [143], using non-circular rods [52,55] and subsequently rotating the non-circular rods [51,144], using the effect of the magnetic permeability [145], using metallodielectric rods [146,147], deforming the lattice by applying a shear strain [148], placing rods of various shapes on different lattice configurations such as square [44,47], triangular [48,52,54], honeycomb or graphite structures [49,149], *kagome* structures [150], etc. Each of these approaches has its own limitations and applicable situations. In the next section we will show that while the inclusion of additional rods and the rotation of non-circular rods can be successfully applied to enlarge the absolute PBG in square lattices, both approaches

UNIVERSITAT ROVIRA I VIRGILI
PHOTONIC BANDGAP ANALYSIS AND FABRICATION OF MACROPOROUS SILICON BY ELECTROCHEMICAL ETCHING
Trifon Todorov Tirfonov
ISBN:978-84-693-6270-9/DL:T-1370-2010

have dramatic effects on the absolute PBG in triangular lattices, leading to a considerable reduction of the gap width.

2.4. Effects of symmetry reduction in 2D square and triangular lattices

In the previous section we have explored some approaches for systematically identifying new photonic crystal structures. The general rule of thumb and the perturbative approach have been used to explain and to predict the occurrence of photonic band gaps. Another approach of explaining or creating photonic band gaps not mentioned hitherto is the degeneracy analysis by making use of supercells. Wu *et al.* [151] have studied the degeneracies in the photonic band structure associated with a supercell of a photonic crystal. These band degeneracies can be lifted by changing the translation group symmetry (the point group symmetry may remain unchanged), which consequently changes the transform matrix between the supercell and the primitive unit cell of the crystal. Some 2D structures with large band gaps have been found through the use of this approach. However, all these approaches fell short of providing physical rules for selecting the optimal structure. We lack an *a priori* understanding as to what "degree" the symmetry should be broken in order to optimize the photonic gaps. Indeed, these methods do not give a quantitative connection between the degree of symmetry reduction and the size of the photonic gaps and do not allow one to exactly determine the ideal structure starting from the desired gap properties. Instead, one must first propose a structure and then calculate its photonic band spectrum to determine if the gap has been optimized or not. So, hard calculations are indispensable if one needs to find the best structure and also the optimal crystal parameters that yield a large absolute PBG. In this section we will show how the symmetry reduction, accomplished by including additional rods, rotating non-circular scatters or a combination of both influence the properties of photonic gaps in 2D square and triangular lattices. Our analysis will be closely related to the practical technological realization of the proposed optimal structures, estimating the relative difficulty of fabrication by centering the gap at wavelength λ=1.55 μm.

2.4.1. Lattice description and numerical method

The patterns of 2D structures under consideration are depicted in Fig. 2.5, as follows: (a) and (b) are basic square lattices of circular and square air rods, respectively;

UNIVERSITAT ROVIRA I VIRGILI
PHOTONIC BANDGAP ANALYSIS AND FABRICATION OF MACROPOROUS SILICON BY ELECTROCHEMICAL ETCHING
Trifon Todorov Tirfonov
ISBN:978-84-693-6270-9/DL:T-1376-2010

(c) and (d) are basic triangular lattices of circular and square air rods; (e), (f) and (g) represent the modified square lattices formed by inclusion of an additional circular or square-shaped rod at the center of the unit cell; (h) and (i) are the modified triangular lattices formed by inclusion of two additional circular rods at the middle of each triangle. For brevity, the structures of [Fig. 2.5a-d] will be referred to as *basic lattices*, while their modified structures [Fig. 2.5e-i] will be referred to as *interstitial lattices*.

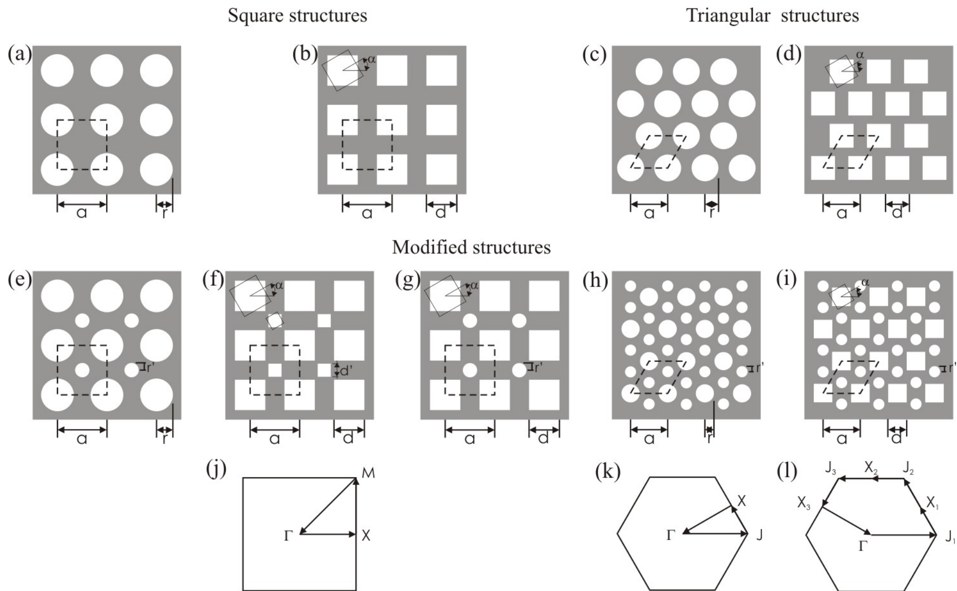

Fig. 2.5. Patterns of the structures under consideration: (a) square-circles (*lattice-scatterers*); (b) square-squares; (c) triangular-circles; (d) triangular-squares; (e) square-circles with a circular included rod; (f) square-squares with a square included rod; (g) square-squares with a circular included rod; (h) triangular-circles with two circular included rods; (i) triangular-squares with two circular included rods; (j) first Brillouin zone for the square structures; (k) and (l) first Brillouin zone for the triangular structures of circular and square rods, respectively. For all structures the lattice unit cell is indicated by a dashed line. Parameters *a*, *r* and *d* denote the lattice constant, the radius (in case of circular rods) and the size (in case of square rods) of the basic rods, respectively. Parameters *r*' and *d*' denote the radius and the size of the included rods (if present). α is the rotation angle of the square rods defined as the angle between axes of the square cross section and the lattice axes.

For all structures the parameters *a, d* and *r* denote the lattice constant, the size of basic square rods and the radius of basic circular rods, respectively. The angle of rotation α of square rods is defined as the angle between axes of the square cross section and the lattice axes. Parameters *d'* and *r'* denote the size and the radius of the

UNIVERSITAT ROVIRA I VIRGILI
PHOTONIC BANDGAP ANALYSIS AND FABRICATION OF MACROPOROUS SILICON BY ELECTROCHEMICAL ETCHING
Trifon Todorov Tirfonov
ISBN:978-84-693-6270-9/DL:T-1376-2010

included square and circular rods, if they are present. For the sake of simplicity, the size of the included elements can be related to the size of the basic rods by introducing a new parameter β, which is defined as: $\beta = r'/r$ for the interstitial structures in [Fig. 2.5e and h]; $\beta = d'/d$ for the structure in Fig. 2.5f and $\beta = 2r'/d$ for the interstitial structures in [Fig. 2.5g and i]. Thus, for the case of interstitial lattices additional degrees of freedom are introduced into the calculations.

The photonic bands of 2D photonic crystals were calculated using the finite difference time domain (FDTD) method, also known as the *OrdernN* method [108,111]. We assumed that all rods were made of the same material (air with relative dielectric constant $\varepsilon_r=1$) and embedded in a background dielectric (silicon with $\varepsilon=12.096$ at $\lambda=1.55$ µm). The bands for both polarization modes were calculated: *TE* modes (*H*-polarization) and *TM* modes (*E*-polarization). When the square lattices were considered, the **Γ**, **M** and **X** points in the Brillouin zone were included in the calculation (Fig. 2.5j) and the photonic bands were traced along the **M-Γ-X-M** path. For the triangular lattices of circular rods, the calculations were performed along the **J-Γ-X-J** path (Fig. 2.5k). In the case of triangular lattices of square rods, the C_3 and C_6 rotational symmetries are lifted [17]. Indeed, it is easy to see that any rotations at 60 or 120 degrees (or their powers) will not leave the lattice unchanged. For square rods arranged in a triangular lattice the point group symmetry is reduced from $C_{6\upsilon}$ to $C_{2\upsilon}$[*]. It is therefore sufficient to perform the calculations along the $\mathbf{X_2}$-**Γ**-$\mathbf{J_1}$-$\mathbf{X_1}$-$\mathbf{J_2}$-$\mathbf{X_2}$ path. However, the rotation of square rods lifts all rotational and mirror symmetries of the lattice. For this reason, the photonic bands of the triangular structure with rotated square rods were traced along the $\mathbf{X_3}$-**Γ**-$\mathbf{J_1}$-$\mathbf{X_1}$-$\mathbf{J_2}$-$\mathbf{X_2}$-$\mathbf{J_3}$-$\mathbf{X_3}$ path of the Brillouin zone, as shown in (Fig. 2.5l). The computational domain for photonic band structure calculations was limited to one primitive unit cell (shown in Fig. 2.5 by a dashed line) by applying periodic boundary conditions to update the fields outside of the cell boundaries. The lattice unit cell was defined over a discrete mesh consisting of 64×64 grid points. To achieve faster convergence, each grid cell was actually regarded as a 100×100 sub-grid points over which the dielectric constant was averaged[†]. This grid size was found to be sufficient for achieving a satisfactory accuracy. The calculation error was estimated to be less than 2% for frequencies below 1.0 (in 2πc/*a* units).

---

[*] The point group $C_{2\upsilon}$ consists of rotations through 180° and two mirror reflections through planes perpendicular to one another. This is the group of operations in a plane that sends a general rectangle into itself [136].

[†] This is the so-called *fuzzy-cell method* already discussed in Chapter 1. See also Fig. 1.8.

UNIVERSITAT ROVIRA I VIRGILI
PHOTONIC BANDGAP ANALYSIS AND FABRICATION OF MACROPOROUS SILICON BY
ELECTROCHEMICAL ETCHING
Trifon Todorov Tirfonov
ISBN:978-84-693-6270-9/DL:T-1276-2010

2.4.2. Results and discussion

- Square lattices

We shall begin our discussion with the basic square structures shown in [Fig. 2.5a and b]. For the given dielectric contrast, the square structure of circular air rods presents an absolute photonic band gap resulting from the overlap between the *TE2-3* and the *TM3-4* polarization gaps across all symmetry points. This absolute PBG has a maximum normalized width of about $\Delta\omega/\omega_g$=3.4% for radius of the rods r=0.492a. In case of square structure with square rod profile, no absolute PBG exists for refractive indexes below 3.51 [47]. In particular, this is valid only when the square rods are not rotated. We will demonstrate that the rotation of square rods leads to a larger absolute PBG that extends over a wide range of rod dimensions and rotation angles. The width of the absolute PBG for both basic square structures can be further improved by including an additional rod in the lattice unit cell.

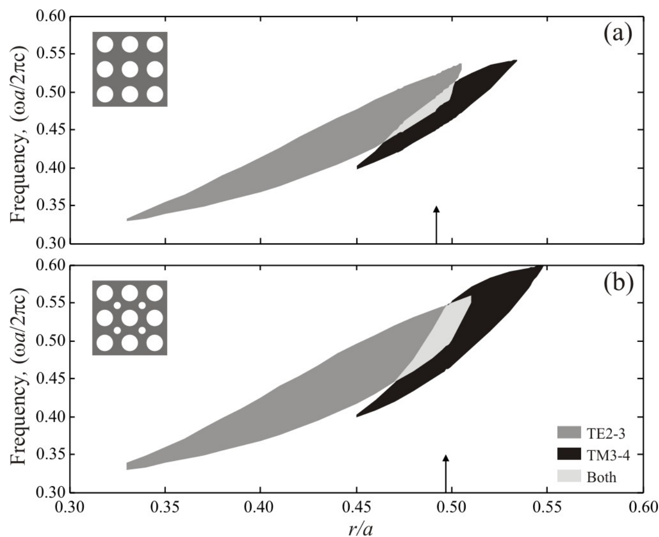

Fig. 2.6. Photonic gap map for (a) the basic square structure of circular air rods and (b) its modified structure formed by including and additional circular rod at the center of the unit cell. The positions of maximal absolute PBG width are indicated by arrows. The figure insets depict the structure under consideration. Only the *TE2-3* and *TM3-4* polarization gaps that form the absolute PBG are shown.

In Fig. 2.6 the dimensionless frequencies of gap boundaries are drawn as

UNIVERSITAT ROVIRA I VIRGILI
PHOTONIC BANDGAP ANALYSIS AND FABRICATION OF MACROPOROUS SILICON BY
ELECTROCHEMICAL ETCHING
Trifon Todorov Tirfonov
ISBN:978-84-693-6270-9/DL:T-1376-2010

functions of r/a for (a) the square lattice of circular rods and (b) its modified lattice with a circular rod included at the center of the unit cell. Here, only the *TE2-3* and *TM3-4* polarization gaps, which form the absolute PBG, are shown. The gap map of the square structure of circular rods (Fig. 2.6a) shows that the maximum width of the absolute PBG appears for rods of radius r=0.492a. We can estimate the relative difficulty of fabrication by centering the gap at wavelength λ=1.55 μm. The mid-gap frequency for this rod radius is ω_g=0.48598 (2πc/a). The lattice constant and the radius of the rods should therefore be a=0.753 μm and r=0.371 μm, respectively. This means that the absolute width of the dielectric walls between adjacent rods should be about 12 nm thick. Although realistic, it is obviously difficult to fabricate this structure. As can be seen, the *TE2-3* polarization gap reduces sharply and closes the absolute PBG as the rod radius nears the close-packed condition. The close-packed condition is reached when adjacent rods begin to touch. For the given configuration it is r_{cp}=0.5a. Band structure analysis shows that second and third *TE* bands are degenerated at point **M** of the Brillouin zone. For the modified structure in Fig. 2.5e, this band degeneracy is lifted. We notice that this modified structure formed after inclusion of an additional rod at the center of the square unit cell is identical to the structure already discussed in Section 2.3 (see Fig. 2.3a). The lattice unit cell comprises two rods of different sizes. Only the dielectric configuration is different. Instead of dielectric rods in air we consider here air rods embedded in a dielectric matrix.

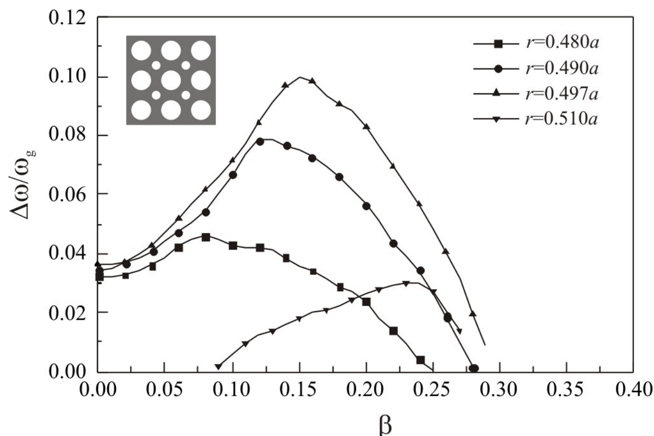

Fig. 2.7. Dependence of the normalized absolute PBG width ($\Delta\omega/\omega_g$) on the parameter $\beta=r'/r$ for the modified square structure with a circular included rod (picture inset) for four different radii r of the basic rods. The maximum absolute PBG appears for r=0.497a and β=0.15 and has a magnitude $\Delta\omega/\omega_g$=10%.

We have performed extensive band calculations varying the radius of the included rod. Figure 2.7 shows the normalized width of the absolute PBG as a function of the parameter $\beta=r'/r$, which is the ratio between the radii of the included r' and the basic r rods. The overall tendency is clearly seen: for small values of β the absolute PBG width is greater than in the case without inclusion (β=0). In addition, the absolute band gap, closed at r=0.51a in the case without inclusion, opens up for values of β between 0.10 and 0.27. The improvement in the absolute PBG width is maximal for β=0.15 and r=0.497a with a magnitude of $\Delta\omega/\omega_g$=10%. This result is slightly different from the one in Ref. 50 because the dielectric contrast and computational method used are different. The gap map for the optimum value of β=0.15 is shown in Fig. 2.6b. As a result of the lifted degeneracy, the overlap between the two polarization gaps is extended. The absolute PBG is nearly *three times* larger than the best one for the basic square lattice. Although including an additional rod improves the absolute PBG size, the fabrication of this structure becomes more difficult. The rod radius for the optimum absolute PBG nears too much the close-packed condition. For the given geometrical parameters and gap centered at λ=1.55 μm the radius of the basic rods is r=0.4 μm, while the radius of the included rod is r'=0.06 μm. Thus, the smallest elements in the structure will be the dielectric walls between adjacent basic rods, which should have a thickness of about 5 nm.

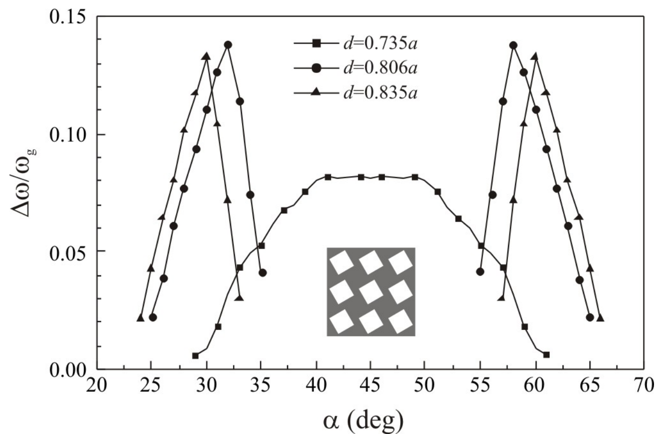

Fig. 2.8. Dependence of the absolute PBG width ($\Delta\omega/\omega_g$) on the rotation angle α for the square structure of square air rods (picture inset) for three different values of square size d. The maximum absolute PBG appears for d=0.806a and α=32° (58°) with a magnitude $\Delta\omega/\omega_g$=13.8%. All gaps exhibit a symmetry with respect to rotation angle α=45° owing to the inverse symmetry of the crystal.

UNIVERSITAT ROVIRA I VIRGILI
PHOTONIC BANDGAP ANALYSIS AND FABRICATION OF MACROPOROUS SILICON BY ELECTROCHEMICAL ETCHING
Trifon Todorov Tirfonov
ISBN:978-84-693-6270-0/DL:T-1376-2010

Next, the square structure of square rods and its corresponding modified structures designed by the inclusion of either square (Fig. 2.5f) or circular (Fig. 2.5g) air rods are considered. As mentioned before, the basic square structure of square rods does not exhibit an absolute PBG for any value of square length d. Band structure analysis indicates that the non-touching second and third *TE* bands overlap, which prevents the *TE2-3* gap from opening up. In addition, the third and fourth *TM* bands are degenerated at the Γ point of the Brillouin zone and no *TM3-4* gap exists for values of $d<0.77a$. This band degeneracy can be lifted by rotating the square rods with respect to the lattice axes, which in turn gives rise to an absolute PBG, formed from the overlapping the *TE2-3* and *TM3-4* polarization gaps. To explain this, one can rely on the general rule of thumb [13] which we have discussed in Section 2.2. The square lattice of square air rods is mainly a connected structure made up of high-index veins. The *TE* gaps are favored in connected structures, while the *TM* gaps are favored in structures of isolated high-index regions (spots). Rotating the square rods leads to a structure of isolated high-index spots that are linked by narrow veins. Suitable dielectric configurations for opening of an absolute PBG can therefore be formed.

Figure 2.8 shows the dependence of the absolute PBG width on the rotation angle α for different values of the square size d. The band gaps exhibit a symmetry with respect to rotation angle $\alpha=45°$ due to the inverse symmetry of the crystal. We notice that the rotation with $\alpha=45°$ transforms this structure in the chessboard lattice studied by Agio and Andreani [53]. The absolute PBG reaches a maximum width of $\Delta\omega/\omega_g=13.8\%$ for $\alpha=32°$ and $d=0.806a$. This absolute PBG is roughly four times larger than the one for the basic square structure of circular air rods. In Fig. 2.9a the positions of the *TE2-3* and *TM3-4* polarization gaps are drawn as functions of the square length d. From geometrical considerations we can obtain that the close-packed condition for square rods rotated at angle α is expressed as $d_{cp} = a\cos\alpha$. Obviously, for non-rotated square rods the close-packed condition is $d_{cp}=a$. The relative width Δx of the dielectric veins between adjacent air rods of size d could be obtained from the relation $\Delta x = \dfrac{a}{\cos\alpha}(d_{cp} - d)$. For rotation angle $\alpha=32°$ we have $d_{cp}=0.848a$, so the smallest width of the narrow veins when $d=0.806a$ (i.e. for parameters that yield maximum gap width) will be $0.050a$. By centering the gap at wavelength $\lambda=1.55$ µm, we obtain that the veins should be approximately 33 nm thick. This result is more encouraging than the previous one in view of the fabrication.

ISBN:978-84-693-6270-9/DL:T-1276-2010

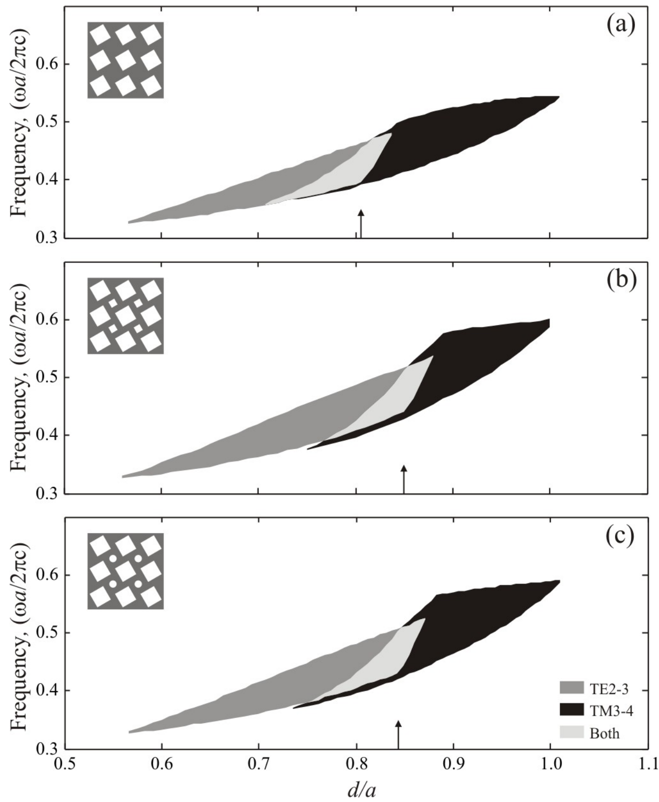

Fig. 2.9. Positions of *TE2-3* and *TM3-4* polarization gaps as functions of square length *d/a* for: (a) the square structure of square rods rotated at angle α=32°; (b) the modified structure with a square rod added at the center of the lattice unit cell for angle of rotation α=27° and size of the included rod β=0.15; (c) the modified structure with a circular rod added at the center of the unit cell for α=28° and β=0.15. The picture insets show the structure under consideration. The positions of the maximal absolute PBG width are indicated by arrows. Only gaps that form the absolute PBG are plotted.

Having discussed the square structure of rotated square rods, we now turn to the effects on the photonic band gaps after an additional rod is included at the center of the lattice unit cell. For the modified square structure in Fig. 2.5f a square rod is added at the center of the unit cell, and for the modified lattice in Fig. 2.5g a circular rod is added. Besides the rotation angle α of the squares, a new degree of freedom is now introduced into our calculations: a parameter β defined as the ratio between the lengths of the added *d*' and the basic rods *d* ($\beta = d'/d$) for the modified structure in Fig. 2.5f, and the ratio between the diameter 2*r*' of the added rod and the length *d* of the basic rods ($\beta = 2r'/d$) for the modified structure in Fig. 2.5g. The size of the included rod is

ISBN:978-84-693-6270-9/DL:T-1370-2010

therefore related to the size of the basic rods in dimensionless units. First, we consider the modified structure with a square rod (Fig. 2.5f). Numerical calculations for α=0° and different values of the parameter β have shown that there is no absolute PBG if the square rods are not rotated. Therefore, including an additional rod is not sufficient to open the absolute PBG for the square lattice of square air rods, at least for the given dielectric contrast.

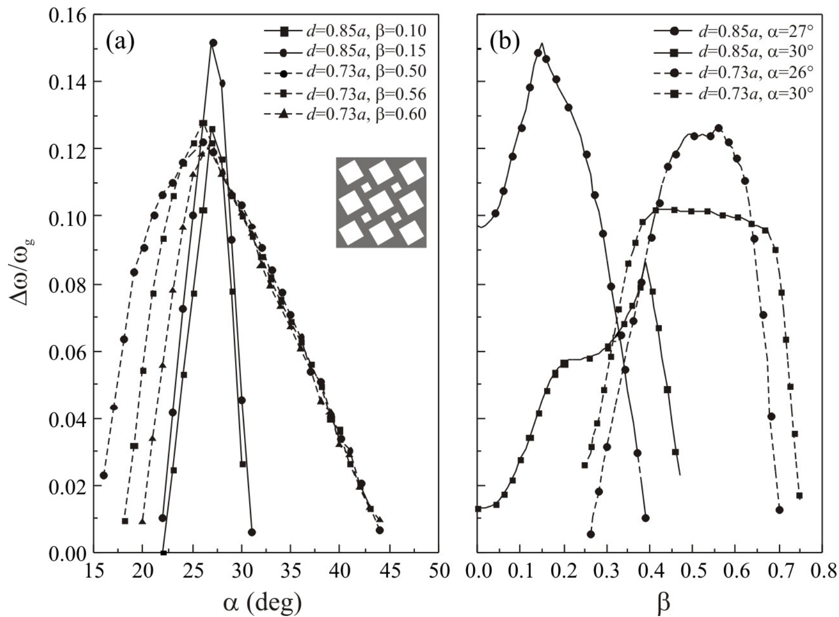

Fig. 2.10. Dependence of the absolute PBG width ($\Delta\omega/\omega_g$) on: (a) the rotation angle α for fixed values of the size β of the included rod and the size d of the basic rods; (b) the parameter $\beta=d'/d$ for fixed values of the rotation angle α and the size d of the basic rods. The figure inset depicts the structure under consideration. The solid lines denote the width of the absolute PBG formed by the overlapping *TE2-3* and *TM3-4* polarization gaps. The dashed lines denote the width of the absolute PBG from the overlap between *TE2-3* and *TM4-5* polarization gaps.

Figure 2.10a shows the dependence of the absolute PBG width on the rotation angle α for fixed values of the parameter β and the square length d. Figure 2.10b shows the dependence of the absolute PBG width on the parameter β for fixed values of α and d. There is no easy way to find the optimum parametric environment (d, β, α) that maximizes the absolute PBG width. For instance, one can fix the rotation angle α and find the values of β and d that yield maximum width of the absolute PBG. The next step, logically, is to perform the calculations by fixing these values and varying α to

UNIVERSITAT ROVIRA I VIRGILI
PHOTONIC BANDGAP ANALYSIS AND FABRICATION OF MACROPOROUS SILICON BY ELECTROCHEMICAL ETCHING
Trifon Todorov Tirfonov
ISBN:978-84-693-6270-9/DL:T-1376-2010

find the optimum angle. However, this does not always lead to the optimum absolute PBG for the structure because for the new optimum angle there will be a new set of β and d. So, hard calculations are needed taking into account all possible values of α, β and d. From Fig. 2.10 we can see that the absolute PBG width ($\Delta\omega/\omega_g$=15.2%) reaches a maximum when α=27°, β=0.15 and d=0.85a. The positions of the *TE2-3* and *TM3-4* polarization gaps as functions of the square size d/a are drawn in Fig. 2.9b. Including an additional rod does improve the absolute PBG width, but we also need to estimate the relative difficulty of fabrication for this improvement. Since the size of the included rod is small, the expression of the close-packed condition will be the same as for the case of non-modified square structure. For a rotation angle α=27°, the close-packed condition is d_{cp}=0.891a. The size of the included rod is d'=0.128a for β=0.15 and d=0.85a. So, the dielectric walls between adjacent basic rods will have the smallest relative width of about 0.046a. For a gap centered at λ=1.55 μm, the absolute width of the dielectric walls should be approximately 34 nm. Therefore, the fabrication of this structure is no more complicated than in the case without inclusion. The absolute PBG, however, is improved.

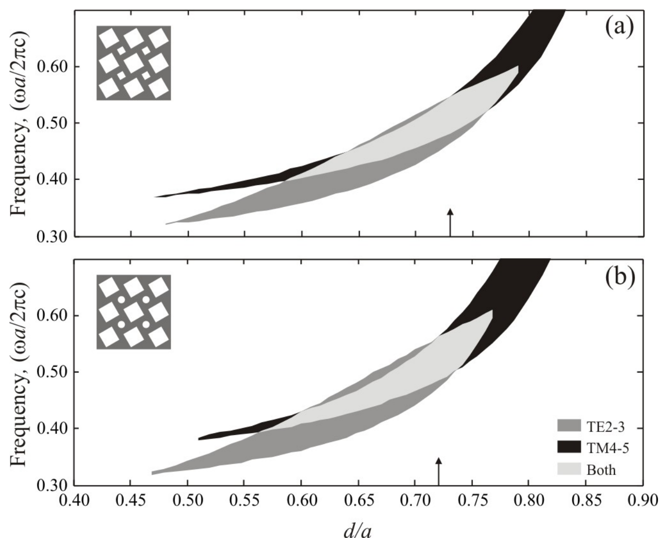

Fig. 2.11. Positions of the *TE2-3* and *TM4-5* polarization gaps as functions of the square length d/a for the modified square structure with an additional rod placed at the center of the unit cell. The included rod has either a square shape (a) or circular shape (b). The rotation angle α and the size of the included rod β are as follows: (a) α=26° and β=0.56; (b) α=31° and β=0.71. The position of the maximum PBG width for both cases is denoted by arrows. The structure is depicted in the figure insets.

UNIVERSITAT ROVIRA I VIRGILI
PHOTONIC BANDGAP ANALYSIS AND FABRICATION OF MACROPOROUS SILICON BY ELECTROCHEMICAL ETCHING
Trifon Todorov Tirfonov
ISBN:978-84-693-6270-9/DL:T-1376-2010

Our numerical calculations show that a new absolute PBG appears when the size of the included rod is increased. This is the result of overlapping between the *TE2-3* and *TM4-5* polarization gaps rather than the overlapping between the *TE2-3* and *TM3-4* gaps. Figure 2.10 shows the width of this absolute PBG as a function of rotation angle α and parameter β, respectively. We can see that the width of this absolute PBG is smaller than that of the absolute PBG formed by the overlap between the *TE2-3* and *TM3-4* gaps. The main advantage, however, is that it extends over a wide range of square lengths d/a far away from the close-packed condition. This is in vast favor for the fabrication. For example, the maximum width of the absolute PBG formed by the overlapping of the *TE2-3* and *TM4-5* polarization gaps is $\Delta\omega/\omega_g$=12.8% when α=26°, β=0.56 and d=0.73a. The close-packed condition for this angle is d_{cp}=0.899a. Under this conditions the included rod will have a relative width of d'=0.409a. The relative width of the dielectric walls between adjacent basic rods is 0.188a, but now the thinnest elements, with a width of 0.099a, are the walls between the basic and the included rods. For gap centered at λ=1.55 µm, the absolute width should be approximately 79 nm. Figure 2.11a shows the positions of the *TE2-3* and *TM4-5* polarization gaps as functions of square length d/a. The absolute PBG exceeds 5% within $0.63 < d/a < 0.78$, which means that the smallest width of dielectric walls ranges between 117 and 54 nm. The angular dependence of the *TE2-3* and *TM4-5* gaps is shown in Fig. 2.12a for d=0.73a and β=0.56. The absolute PBG exceeds 5% within $20° < \alpha < 37°$. As a comparison, for these rotation angles the smallest width of dielectric walls would range between 57 and 67 nm. Although this is not the best absolute PBG for this structure, it seems to be better from the fabrication point of view.

Finally, we studied the modified square structure for which a circular rod is placed at the center of the lattice unit cell (Fig. 2.5g). Our discussion is similar to that for the previous structure, so here we will only provide the main results. In this case, parameter β is defined as the ratio between the diameter $2r'$ of the included rod and the size d of the basic square rods. Figure 2.9c shows the positions of the *TE2-3* and *TM3-4* polarization gaps as functions of d/a. The optimum absolute PBG has a width of $\Delta\omega/\omega_g$=15.6% for d=0.843a, β=0.15 and α=28°. For small values of β there is no significant difference between the modified structure with a circular rod included and the previously discussed structure with a square rod included. The size of the included rod is too small for β=0.15 so there is no significant change in the total filling fraction, if the included rod is square or circular. This is not the case for values of β>0.5, which generate an absolute PBG from the overlapping between the *TE2-3* and *TM4-5* polarization gaps. Figures 2.11b and 2.12b show the positions of the *TE2-3* and *TM4-5*

UNIVERSITAT ROVIRA I VIRGILI
PHOTONIC BANDGAP ANALYSIS AND FABRICATION OF MACROPOROUS SILICON BY ELECTROCHEMICAL ETCHING
Trifon Todorov Tirfonov
ISBN:978-84-693-6270-9/DL:T-1376-2010

polarization gaps as functions of d/a for β=0.71, α=31° and as functions of α for d=0.721a, β=0.71, respectively. The maximum width of the absolute PBG is $\Delta\omega/\omega_g$=14.8%, which is 2% greater than in the case of the interstitial lattice with a square rod included. For these physical parameters the smallest feature size is 57 nm. With this structure, therefore, we gain in absolute PBG width without harming the fabrication.

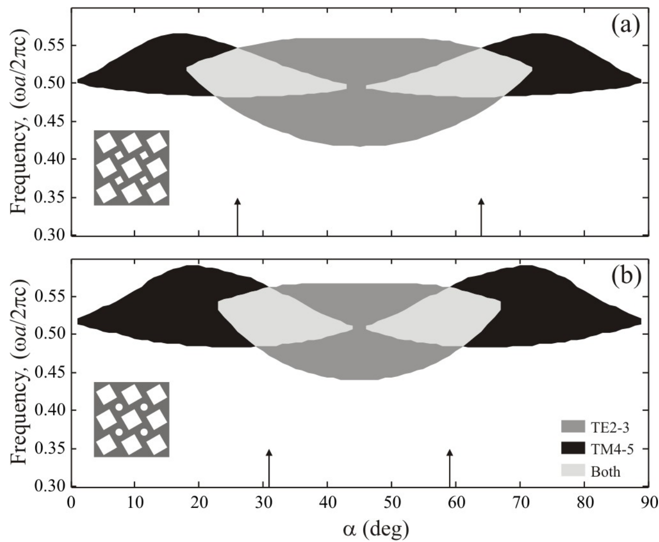

Fig. 2.12. Positions of the *TE2-3* and *TM*4-5 polarization gaps as functions of the rotation angle α for (a) the square structure with a square added rod with β=0.56 and d=0.73a and (b) the square structure with a circular added rod with β=0.71 and d=0.72a. The insets depict the structure under consideration. The positions of maximal absolute PBG widths are indicated by arrows.

- Triangular lattices

In this section we consider the triangular lattices of circular air rods (Fig. 2.5c) and square air rods (Fig 2.5d) and their modified structures (Fig. 2.5h), and 2.5i). The triangular structure of circular air rods is known to present the greatest absolute PBG among the studied 2D photonic crystals. The minimum refractive index contrast required for the opening of an absolute PBG is 2.66 for a filling fraction of the air rods of about 66% [47]. The absolute PBG is the result of the overlap between the *TE1-2* and *TM2-3* polarizations gaps. Figure 2.13a shows the photonic band map for this structure. For the given dielectric contrast (ε_b=12.096 and ε_r=1), the absolute PBG reaches a

ISBN:978-84-693-6270-9/DL:T-1376-2010

maximum width of $\Delta\omega/\omega_g$=17% when the radius of the rods is r=0.478a. The closed-packed condition for this configuration is r_{cp}=0.5a. When the gap is centered at λ=1.55 µm, the dielectric walls between adjacent rods must be 33 nm. This result is similar to that for the square lattices. We tried to apply the same approach, i.e. to optimize the absolute PBG by reducing the lattice symmetry achieved either by inserting additional rods or by using noncircular scatterers.

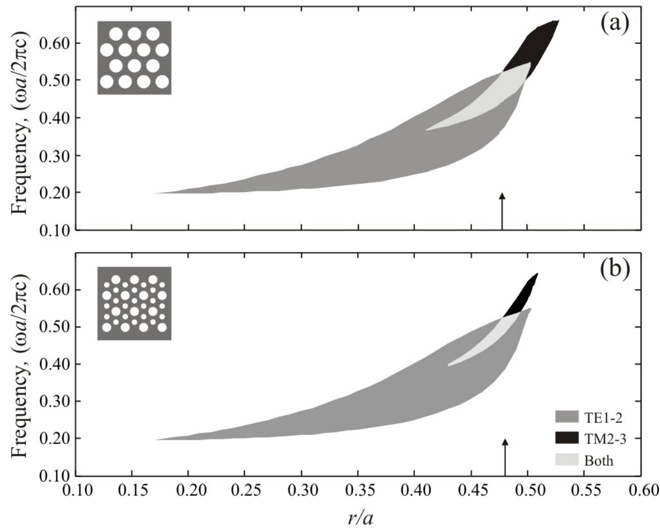

Fig. 2.13. Positions of the *TE1-2* and *TM2-3* polarization gaps as functions of the basic rod size r/a for (a) the basic triangular lattice of circular rods and (b) its modified structure with a circular rod added at the center of each triangle of the lattice unit cell. The size of the included rod is β=r'/r=0.1. The positions of the maximal absolute PBG widths are indicated by arrows. Only gaps that form the absolute PBG are shown.

First we studied the interstitial triangular structure (Fig. 2.5h) in which two additional rods are introduced into the lattice unit cell. The included rods are located at the midpoint between three basic rods of the triangular lattice. In this way, the primitive unit cell comprises three rods with two different radii. It is worth pointing out that such inclusion does not change the point group symmetry of the lattice $C_{6\upsilon}$. Indeed, if we fix the coordinate system at some basic rod the lattice is transformed into itself under rotations of 60, 120, 180, 240 degrees. The six reflection symmetries through planes which are spaced 60° apart are also preserved (see Apendix A). It is therefore enough to consider the irreducible Brillouin zone limited by the points **Γ**, **J** and **X** as shown in Fig. 2.5k. For the triangular structure the parameter β=r'/r is defined as the ratio

UNIVERSITAT ROVIRA I VIRGILI
PHOTONIC BANDGAP ANALYSIS AND FABRICATION OF MACROPOROUS SILICON BY ELECTROCHEMICAL ETCHING
Trifon Todorov Tirfonov
ISBN:978-84-693-6270-9/DL:T-1376-2010

between the radii of included *r*' and basic *r* rods. The dependence of the absolute PBG width on the parameter β for some fixed values of the radius of basic rods *r* is shown in Fig. 2.14a. For the case without inclusion (β=0), the structure switches to the basic triangular lattice of circular rods. Although the included rods are very small, their presence leads to a decrease in the absolute PBG width and, for values of β greater than 0.15, to complete closure of the gap. Figure 2.13b shows the positions of the *TE1-2* and *TM2-3* polarization gaps as functions of *r*/*a* for β=0.1. The maximum absolute PBG width is $\Delta\omega/\omega_g$=8.6% when *r*=0.48*a*. We can see that the *TM2-3* polarization gap is strongly reduced. The inclusion of the interstitial air rods at the midpoint of each triangle disrupts the useful arrangement of the dielectric in isolated and linked regions. Isolated islands of high-index material do not yet exist. Therefore, TM gaps tend to disappear in this structure.

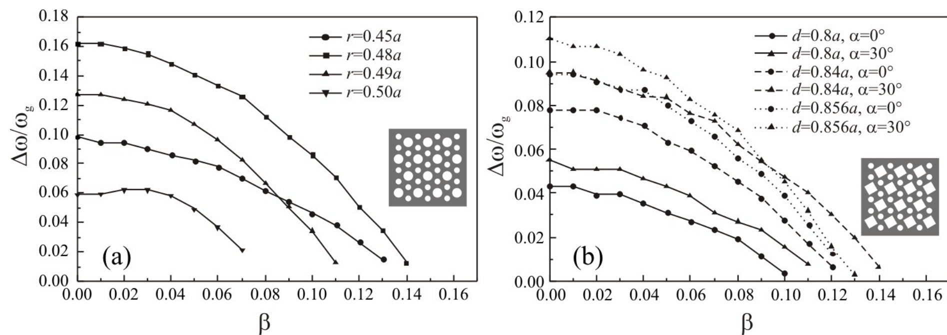

Fig. 2.14. Dependence of the absolute PBG width ($\Delta\omega/\omega_g$) on the parameter β for: (a) the modified triangular structure of circular basic rods and a circular rod placed at the midpoint of each triangle formed of three basic rods; (b) the modified triangular structure of square basic rods and a circular rod placed at the midpoint of each triangle. The gap is plotted for different values of the rod radius *r*, square size *d* and rotation angle α.

To continue our study on symmetry reduction we also examined the triangular lattice of square air rods (Fig. 2.5d). Since the symmetry of the lattice is reduced, we must now consider all the directions of the new irreducible Brillouin zone, as shown in Fig. 2.5l. For this structure there is an absolute photonic gap, which is result from the overlapping *TE1-2* and *TM2-3* polarization gaps, as in the case of triangular structure of circular air rods. Their positions as functions of square size *d*/*a* are plotted in Fig. 2.15a. The absolute PBG has a maximum width of $\Delta\omega/\omega_g$=9.5% for *d*=0.854*a*. The dielectric walls should therefore have a relative width of 0.012*a* and should be about 9 nm thin for the gap centered at λ=1.55 μm. In addition to the smaller absolute PBG with respect to

UNIVERSITAT ROVIRA I VIRGILI
PHOTONIC BANDGAP ANALYSIS AND FABRICATION OF MACROPOROUS SILICON BY ELECTROCHEMICAL ETCHING
Trifon Todorov Tirfonov
ISBN:978-84-693-6270-9/DL:T-1376-2010

the basic triangular lattice of circular rods, this structure would therefore require very stringent technological capabilities.

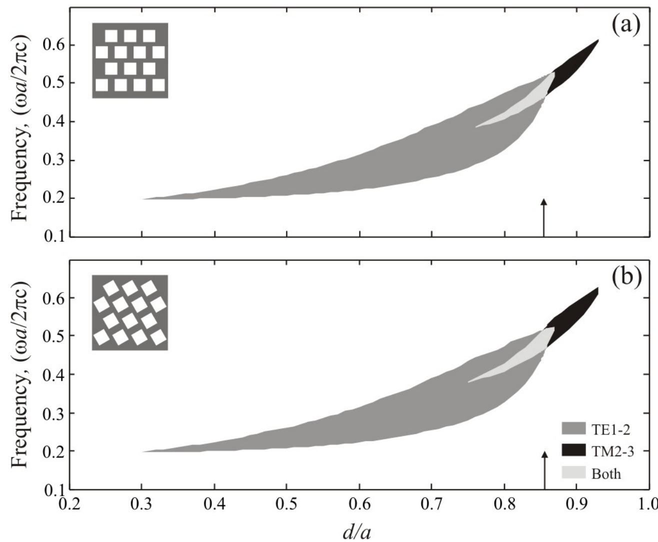

Fig. 2.15. Positions of the *TE1-2* and *TM2-3* polarization gaps as functions of square size *d/a* for a triangular structure of square rods rotated at (a) α=0° and (b) α=30° with respect to the lattice axes. The positions of maximum absolute PBG width are indicated by arrows.

In the case of square structures, the rotation of square rods was an effective way to enlarge the absolute PBG. In the case of triangular lattices we go one step further and apply the same approach. As it was mentioned before, the rotation of the square rods lifts all inversion and rotation symmetries of the lattice. To illustrate this, we show in Fig. 2.16 the photonic band structure for two rotation angles of the square rods, i.e. α=0° (Fig. 2.16a) and α=15° (Fig. 2.16b). In the case of non-rotated rods, we can see that some symmetry directions are redundant because the spectrum keeps the same. For example, the point $\mathbf{X_3}$ of the Brillouin zone is equivalent to point $\mathbf{X_1}$, but point $\mathbf{X_2}$ is different. Similar considerations apply for the points **J**. That is way it is sufficient to perform the calculations only along the $\mathbf{X_2}$-$\mathbf{\Gamma}$-$\mathbf{J_1}$-$\mathbf{X_1}$-$\mathbf{J_2}$-$\mathbf{X_2}$ path as suggested in Ref. 52. However, if the square rods are rotated points $\mathbf{X_3}$ and $\mathbf{X_1}$ become no longer equivalent. For this particular angle (α=15°) the points $\mathbf{X_1}$ and $\mathbf{X_2}$ keep the same symmetry because the lattice is still invariant under reflections through two perpendicular planes rotated at 60° with respect to the lattice axes. Any other angle of rotation, which is not multiple of 15 would break all mirror symmetries of the crystal. For this reason, the calculations

UNIVERSITAT ROVIRA I VIRGILI
PHOTONIC BANDGAP ANALYSIS AND FABRICATION OF MACROPOROUS SILICON BY
ELECTROCHEMICAL ETCHING
Trifon Todorov Tirfonov
ISBN:978-84-693-6270-9/DL:T-1276-2010

were performed taking into account all symmetry points shown in Fig. 2.5l and also in the inset of Fig. 2.16a.

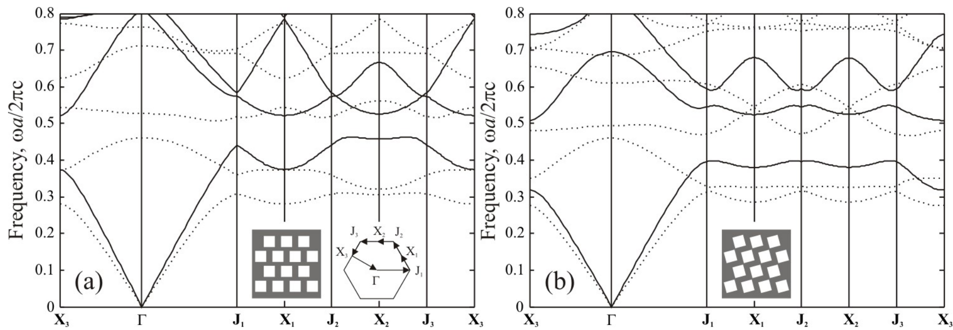

Fig. 2.16. Photonic band structure for the triangular lattice of square air rods in a dielectric background for rotation angles (a) α=0° and (b) α=15°. The rod size in both cases is d=0.854a. The insets depict the structure under consideration. The spectrum is traced along X_3-Γ-J_1-X_1-J_2-X_2-J_3-X_3 path as shown on the right inset. For the case of non-rotated square rods some symmetry directions are redundant.

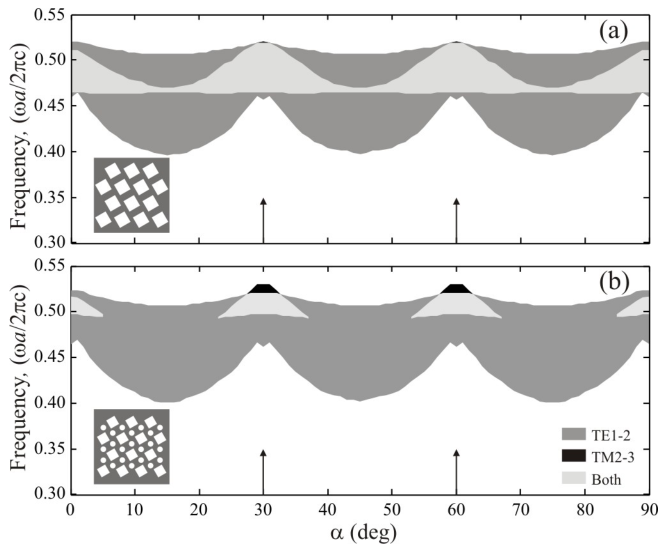

Fig. 2.17. Positions of the *TE1-2* and *TM2-3* polarization gaps as functions of the rotation angle α for (a) the basic triangular structure of square rods with d=0.856a and (b) its modified structure for which two circular rods are introduced into the unit cell with d=0.856a and β=0.1. The figure insets depict the structure under consideration. The positions of maximum absolute PBG widths are indicated by arrows.

UNIVERSITAT ROVIRA I VIRGILI
PHOTONIC BANDGAP ANALYSIS AND FABRICATION OF MACROPOROUS SILICON BY ELECTROCHEMICAL ETCHING
Trifon Todorov Tirfonov
ISBN:978-84-693-6270-9/DL:T-1376-2010

Figure 2.17 plots the positions of the *TE1-2* and *TM2-3* polarization gaps as functions of the rotation angle α for square size d=0.856a. Because of the mirror symmetries of the lattice, the gaps are symmetrical with respect to rotation angles α=30° and α=60°. Therefore, the only non-redundant rotations are those between 0° and 30°. The optimum rotation angle, which provided the best improvement in the absolute PBG, was α=30°. The positions of the *TE1-2* and *TM2-3* polarization gaps as functions of square size d/a are plotted in Fig. 2.15b for this optimum angle. The absolute PBG has a maximum width of $\Delta\omega/\omega_g$=11% for d=0.856a. If we bear in mind that the close-packed condition for α=30° is d_{cp}=0.866a, the relative width of the dielectric walls should be 0.010a. For the gap centered at λ=1.55 μm, this results in an absolute width of approximately 8 nm. Rotating square rods in a triangular structure therefore does not, as it did in the case of square structures, significantly improve the absolute PBG.

By considering the modified triangular structure, which is formed after adding two circular rods in the unit cell (Fig. 2.5i), we have studied the effects of symmetry reduction achieved both by rotating noncircular scatterers and including additional elements. As with the modified triangular lattice of circular rods, including additional rods considerably shrinks the absolute PBG. We found no improvement in the absolute PBG width for any rotation angle α of the square basic rods or for different values of the size β of the included rods. Parameter β in this case is defined as $\beta=2r'/d$. Moreover, again for values of β greater than 0.15 the absolute PBG completely disappears (Fig. 2.14b). For triangular structures, therefore, symmetry reduction based on the inclusion of additional rods does not lead to a larger absolute PBG. The inclusion favorably increases the “air” filling fraction but disrupts the useful arrangement of high-index media in isolated and linked regions. From Fig. 2.17b we can see that, due to the inclusion, the *TM2-3* polarization gap shrinks considerably, which decreases the absolute PBG width.

2.4.3. Summary

Our results on the optimization of the absolute PBG are summarized in Table 2.1 together with the optimal physical parameters that yield a maximum gap width for the proposed structures. We can see that sizable absolute PBGs open up for the triangular lattice of circular air rods and the interstitial square lattice of rotated square rods. Concerning the fabrication difficulty, it is clear that the dielectric walls of all these photonic crystals composed of air rods in a dielectric media should be

UNIVERSITAT ROVIRA I VIRGILI
PHOTONIC BANDGAP ANALYSIS AND FABRICATION OF MACROPOROUS SILICON BY ELECTROCHEMICAL ETCHING
Trifon Todorov Tirfonov
ISBN:978-84-693-6270-0/DL:T-1276-2010

extremely thin. To fabricate such crystals for telecommunication wavelengths, we need highly developed technologies such as e-beam lithography and dry-etching techniques. Such efforts are however rewarded by the large absolute PBG.

TABLE 2.1. Maximum absolute PBG width for the considered structures. The table shows the physical parameters for which the optimum absolute PBG can be obtained. The relative and absolute sizes of the smallest elements are also shown.

Lattice-scatterer	$\Delta\omega/\omega_g$	Physical parameters	Size of the smallest element	
			relative	absolute*
1. Square structures				
a. square-circles	3.4%	r=0.492a	0.016a	10 nm
b. square-circles with an additional circular rod	10%	r=0.497a; β=0.15	0.006a	5 nm
c. square-squares	no absolute PBG exists			
d. square-rotated squares	13.8%	d=0.806a; α=32°	0.050a	33 nm
e. square-rotated squares with an additional square rod	15.2% 12.8%	d=0.85a, α=27°, β=0.15† d=0.73a, α=26°, β=0.56‡	0.046a 0.099a	34 nm 79 nm
f. square-rotated squares with an additional circular rod	15.6% 14.8%	d=0.843a, α=28°, β=0.15† d=0.721a, α=31°, β=0.71‡	0.045a 0.070a	33 nm 57 nm
2. Triangular structures				
a. triangular-circles	17%	r=0.478a	0.044a	33 nm
b. triangular-circles with two additional circular rods	there is no improvement in the absolute PBG size			
c. triangular-squares	9.5%	d=0.854a	0.012a	9 nm
d. triangular-rotated squares	11%	d=0.856a; α=30°	0.010a	8 nm
e. triangular-rotated squares with two additional circular rods	there is no improvement in the absolute PBG size			

* absolute size for gap centered at λ=1.55 μm

† absolute PBG formed from the overlapping *TE2-3* and *TM3-4* polarization gaps

‡ absolute PBG formed from the overlapping *TE2-3* and *TM4-5* polarization gaps

UNIVERSITAT ROVIRA I VIRGILI
PHOTONIC BANDGAP ANALYSIS AND FABRICATION OF MACROPOROUS SILICON BY ELECTROCHEMICAL ETCHING
Trifon Todorov Tirfonov
ISBN:978-84-693-6270-9/DL:T-1376-2010

2.5. Conclusions

To conclude, we have performed a detailed numerical analysis of the photonic band structure of square and triangular lattices with circular and square rod profiles using the FDTD method. Specifically, we have examined how symmetry reduction, achieved by adding small rods to the lattice unit cell or by reorienting the square rods affects the properties of the absolute photonic gap. In short, for square lattices the symmetry reduction approach has been successfully applied to maximize the absolute PBG width. In the case of square lattice of circular rods, the inclusion of an additional rod leads to an absolute PBG, which is about three times larger than the one without inclusion. The rotation of the square rods is critical for opening the absolute PBG in the square structure of square rods. The most significant improvement in the size of the absolute PBG is provided by a combination of including an additional rod and rotating the square rods. Moreover, a new absolute PBG is generated that persists over a wide range of rotation angles and filling fractions far away from the closed-packed condition, and therefore greatly favors the fabrication of photonic crystals.

The largest absolute PBG is the one for the triangular structure of circular air rods. Our results show that modifying the crystal structure by adding interstitial rods or using square rods is not a good way for achieving larger absolute PBG, at least for the special case of air/silicon structures. Adding more rods in the lattice unit cell cannot further enlarge the absolute PBG width. Moreover, the absolute PBG shrinks dramatically because of disrupted islands of high-index material. The use of square scatterers in the triangular lattice considerably reduces the absolute PBG width.

It should be noted that most of the photonic lattices discussed in this chapter have been studied so far mainly by using the plane wave method for photonic band structure calculations. To the author knowledge some of these structures, specifically the interstitial lattices, have not been implemented for the FDTD simulation. There should be no essential difference in the results obtained by the PWE or the FDTD methods. The advantage of the FDTD method is however that it can be easily adapted to calculate quantities that are important for the optical characterization, e.g. transmission and reflection coefficients. It is also interesting to compare the accuracy of both methods when they are employed to study such complex lattices.

The results are also discussed in terms of the practical technological feasibility of the presented photonic crystals. In most of the published studies such discussion is absent. Moreover, the results are presented with respect to the *filling fraction* of the elements (because it is the natural parameter involved in the plane wave expansion) and

UNIVERSITAT ROVIRA I VIRGILI
PHOTONIC BANDGAP ANALYSIS AND FABRICATION OF MACROPOROUS SILICON BY ELECTROCHEMICAL ETCHING
Trifon Todorov Tirfonov
ISBN:978-84-693-6270-9/DL:T-1376-2010

not with respect to their real dimensions. Although for less complex structures, e.g. single-rod lattices with circular or square rods, the real dimensions (square size, rod radius, separation, etc.) can be easily extracted from the optimum filling fraction, for more complex structures that have two or more rods in the unit cell, or rotated non-circular rods such representation based only on the filling fraction becomes unclear and difficult to handle from practical view point.

There are not published studies, at least to the author knowledge, on the interstitial triangular lattices with included rods and rotated square rods.

UNIVERSITAT ROVIRA I VIRGILI
PHOTONIC BANDGAP ANALYSIS AND FABRICATION OF MACROPOROUS SILICON BY ELECTROCHEMICAL ETCHING
Trifon Todorov Tirfonov
ISBN:978-84-693-6270-9/DL:T-1376-2010

Chapter 3

Photonic crystals with three dielectric components

In this chapter, the photonic band gap formation in 2D photonic crystals with three dielectric materials is analyzed. The photonic lattice of such 2D crystals comprises elements that have three different dielectric constants, i.e. apart from the background material with dielectric constant ε_b and the basic rods with dielectric constant ε_r, the lattice may also contain inclusions with dielectric constant $\varepsilon_s \neq \varepsilon_r \neq \varepsilon_b$. Specifically, we assume that the third dielectric component is included as a thin cladding layer covering the basic rods. We calculate the photonic dispersion and analyze the effects of such an inclusion on the absolute PBG size as a function of the cladding material and thickness. We discuss here that the existence of a dielectric cladding has in general a negative effect on the absolute photonic gap, reducing its width. However, we found situations in which the existence of dielectric cladding could be advantageous and larger absolute PBGs could be achieved.

3.1. Introduction

Unlike the numerous studies of 2D PC's with diverse arrangements and scatterers, to our knowledge few authors have studied how the inclusion of third

UNIVERSITAT ROVIRA I VIRGILI
PHOTONIC BANDGAP ANALYSIS AND FABRICATION OF MACROPOROUS SILICON BY ELECTROCHEMICAL ETCHING
Trifon Todorov Tirfonov
ISBN:978-84-693-6270-9/DL:T-1376-2010

dielectric component affects the properties of photonic gaps in 2D crystals. Let us say that such an inclusion does not resemble the creation of local defects in the photonic lattice. As we have discussed in Chapter 1, point (or linear) defects can be created by varying the size of a single rod (or column of rods), or by changing its dielectric constant. Here, we consider that the third dielectric component is not added locally but extends infinitely and periodically in space. So, the third material is part of the primitive unit cell and may keep or not the symmetry of the lattice. Consider, for example, the square lattice with two-point basis set shown in Fig. 2.3. We have already discussed that the inclusion of an additional rod with different size in the unit cell of simple square lattice can lift the symmetry-induced band degeneracies at high symmetry points of Brillouin zone. The same effect can be achieved if we include a rod of different dielectric constant, instead of different size [142]. The lattice unit cell in this case comprises two rods which are identical in size but are made up of different dielectric materials. Exactly the same structure has been also studied by Kim and Lee [152], who investigated how the photonic gaps evolve when the dielectric constant of the included rod is varied between that of the background material (air) and that of the basic rods (alumina). We consider, however, that such a structure with rods of different materials is in a sense abstractive. Indeed, it is difficult for us to imagine how this photonic crystal can be fabricated. If it is currently a challenge to fabricate 2D structures at sub-micron length scales by the state-of-the-art dry etching techniques, what we would say for the fabrication of structure where a third material is involved, which must have a specific dielectric constant and more importantly, which must be arranged in the same small-length-scale periodic fashion. Probably, the easiest way is to etch holes in some material used only as a template, for example silicon. After etching, the holes can be selectively filled with the desired dielectric materials. After removing the silicon we can then obtain the described so far structure consisting of rods of different materials and embedded in air.

We can find situation in which the third dielectric component is not intentionally added in the photonic lattice but is an unwanted result of the fabrication process itself. For example, a promising technique for the fabrication of 2D PC's for the near-IR spectrum is the electrochemical etching of silicon in acid solutions [59, 60]. Macroporous silicon formed by this technique exhibits uniform pores with a diameter of less than one micrometer and an aspect ratio of several hundreds of micrometers. After etching, the macropores are covered by a thin microporous layer [125] that can be treated as an interfacial layer between the pores (air rods) and background medium. The effective refractive index of this interfacial layer is less than the refractive index of

UNIVERSITAT ROVIRA I VIRGILI
PHOTONIC BANDGAP ANALYSIS AND FABRICATION OF MACROPOROUS SILICON BY ELECTROCHEMICAL ETCHING
Trifon Todorov Tirfonov
ISBN:978-84-693-6270-9/DL:T-1376-2010

silicon and depends on the sample characteristics and etching conditions. In this case, the photonic lattice will therefore comprise rods which are surrounded by thin cladding layer of different dielectric constant. Very recently, Pan and Li [153] have studied the effects of the etching interfacial layers on the absolute PBG in 2D triangular structure. They pointed out that the etching process could result in a rough and porous interface between the (air) rods and background matrix, which could be described by an effective dielectric medium. After calculating the photonic spectrum for different values of the effective dielectric constant of this interfacial layer, they concluded that the existence of such layer would always reduce the absolute PBG width. However, they did not consider the inverse structure - namely, dielectric rods in air. It is well known that the honeycomb lattice formed of dielectric rods in air does exhibit absolute PBG's [49]. These absolute PBG's arise for filling fractions far from the close-packed condition and therefore greatly favor the fabrication of 2D photonic crystals. In addition, when the aim is the fabrication of semiconductor active devices, the use of dielectric rods in air instead of holes in dielectric media is advantageous [154]. An important loss mechanism in these active devices is the nonradiative surface recombination at the sidewalls of the active media. A common strategy for reducing the surface recombination is passivating the semiconductor surfaces by a thin dielectric film. Therefore, the interfacial layer in this case is a requirement and it should be intentionally formed.

In this context, we think that it is also important to study how the existence of such dielectric cladding affects the PBG formation in 2D photonic crystals of both complementary arrangements: air rods in dielectric media and dielectric rods in air. In this chapter we shall analyze the absolute PBG formation for triangular and honeycomb photonic structures consisting either of air rods (holes) in silicon or silicon rods in air. We assume that the rod surface, in the case of silicon rods, and hole walls, in the case of air rods, are covered with an interfacial layer of varied thickness. The rod and the surrounding interfacial layer can be treated as a single rod having a core and cladding regions. We consider here three different materials for the dielectric cladding: silicon dioxide (SiO_2), silicon nitride (Si_3N_4) or germanium (Ge). They are chosen for the following reasons. The SiO_2 and Si_3N_4 are commonly used as passivating materials in the silicon industry. A fully-established technique for growing SiO_2 or Si_3N_4 layers exists, that permits fine control of the layer thickness. Besides, the refractive indexes of SiO_2 and Si_3N_4 are less than that of silicon and cover in part the refractive-index range of microporous silicon mentioned above. Thereby, the results considering etched pores "covered" with SiO_2 or Si_3N_4 layer will be also valid for the case of pores walls covered

UNIVERSITAT ROVIRA I VIRGILI
PHOTONIC BANDGAP ANALYSIS AND FABRICATION OF MACROPOROUS SILICON BY ELECTROCHEMICAL ETCHING
Trifon Todorov Tirfonov
ISBN:978-84-693-6270-9/DL:T-1376-2010

with microporous silicon. Germanium is chosen mainly because it has a refractive index greater than that of silicon. Thus, we are not restricted to study only lower-refractive-index materials because deposition of Ge interfacial layer is also possible, for instance by plasma-enhanced chemical vapor deposition (PCVD) technique.

3.2. Lattice description and numerical method

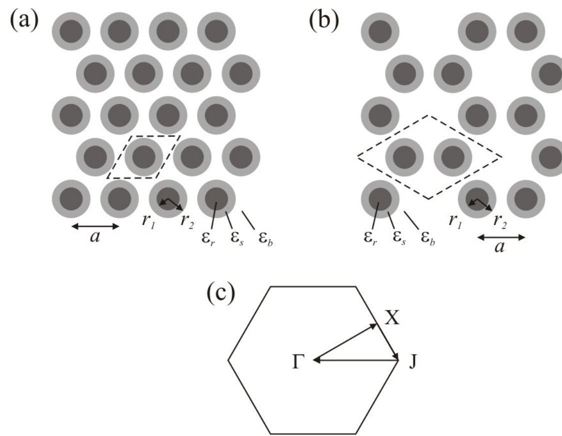

Fig. 3.1. Schematic representation of the studied structures: (a) triangular lattice of circular rods; (b) honeycomb lattice of circular rods; (c) irreducible Brillouin zone of the structure with the high symmetry points indicated. The rods are covered by a shell layer with dielectric constant ε_s different from the dielectric constant of the rods ε_r and that of the background media ε_b. The lattice unit cell is indicated by a dashed line.

The two structures under consideration are depicted in Fig. 3.1, where (a) is a triangular lattice of inner rods and outer interfacial (shell) layer and (b) is the honeycomb lattice of inner rods and outer shell layer. Parameters ε_r, ε_s and ε_b denote the dielectric constants of the inner rod, shell layer and background medium, respectively. When air holes in silicon are considered the dielectric constants of the inner rods and background medium are fixed to be ε_r=1 and ε_b=12.096 (silicon at wavelength λ=1.55 μm [7]). For silicon rods in air, the values of the parameters are reversed, namely ε_r=12.096 and ε_b=1. The shell-layer dielectric constant ε_s for the three different materials considered here is: (1) ε_s=3.9 for SiO_2, (2) ε_s=7.5 for Si_3N_4 and (3) ε_s=16 for Ge [155]. The dielectric constant of the shell layer is therefore fixed to be less than the dielectric constant of silicon for the first two cases and greater than the dielectric constant of silicon for the third case. Parameter a is the distance between the centers of

UNIVERSITAT ROVIRA I VIRGILI
PHOTONIC BANDGAP ANALYSIS AND FABRICATION OF MACROPOROUS SILICON BY ELECTROCHEMICAL ETCHING
Trifon Todorov Tirfonov
ISBN:978-84-693-6270-9/DL:T-1370-2010

two nearest-neighbor rods. For the triangular structure, the lattice constant is equal to *a*, whereas for honeycomb structure the lattice constant is equal to $\sqrt{3}a$. The primitive unit cell of the honeycomb lattice comprises two rods. Parameters r_1 and r_2 denote the radius of the inner rods and the outer radius of the shell layer, respectively. The thickness of the shell layer is then r_2-r_1. We prefer to describe the shell-layer thickness by introducing a new parameter β, defined as the ratio between r_2-r_1 and the outer radius r_2, i.e. $\beta = (r_2 - r_1)/r_2$. Parameter β can range between 0 and 1. We notice that β=0 yields rods without shell layer, while β=1 yields rods made of the shell material only, i.e. there are no inner rods.

The photonic bands of 2D photonic crystals were calculated using the *Order*(*N*) method [108,111] for both *TE* and *TM* polarization modes. We notice that such an inclusion of interfacial layer does not change the point group symmetry of the corresponding lattice. All rotational and mirror symmetries are kept the same as for the shell-less structure, i.e. $C_{6\upsilon}$ point group for the triangular and D_{6h} for the honeycomb lattices [135]. The point group D_{6h} is the group of the hexagonal prism. It can be considered as the direct product of groups D_6 and C_i. Group D_6 contains rotations at 60, 120 and 180 degrees. Group C_i consists of the identity and the inversion operations. In addition to the operation of D_6 and C_i, the point group D_{6h} contains reflections and the symmetry operations S_3 and S_6*. More detailed information can be found in Ref. [135,136]. The Brillouin zones of both lattices are hexagons. The photonic band structure calculations were performed along the **Γ-X-J-Γ** edges of the irreducible Brillouin zone (Fig. 3.1c). The computational domain for the FDTD calculations consisted of one lattice unit cell, repeated infinitely by applying Bloch periodic boundary conditions. The lattice unit cell was divided up into 64×64 discretization grid points. The dielectric constant at each grid point was defined by taking the average of the dielectric constant over 10×10 sub-grid points, ensuring in this way faster convergence [108]. The convergence and numerical stability of the calculations were tested by increasing the grid-size, i.e. using a grid of up to 100×100 points (the number of sub-grid points was kept the same). The deviations in the band frequencies were found to be less than 1% for the lowest ten photonic bands. As a comparison, several tests with smaller grid-size (32×32 points) did not meet the 1% accuracy condition, showing band deviations greater than 3% especially when very thin interfacial layers

---

* S_n denote a rotation of $2\pi/n$ followed by a reflection in a plane perpendicular to the axis of rotation and therefore it is an improper rotation. S_2 and the inversion operator are equivalent [136].

UNIVERSITAT ROVIRA I VIRGILI
PHOTONIC BANDGAP ANALYSIS AND FABRICATION OF MACROPOROUS SILICON BY ELECTROCHEMICAL ETCHING
Trifon Todorov Tirfonov
ISBN:978-84-693-6270-9/DL:T-1376-2010

(β=0.01) were considered. Thus, the results of the gap widths are believed to be accurate to within at least 1% of their true values.

3.3. Results and discussion

3.3.1. Triangular lattice

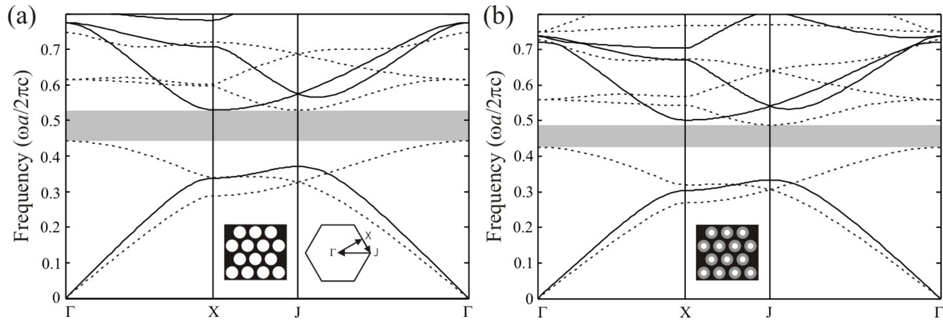

Fig. 3.2. Photonic bands for (a) triangular structure of air holes in silicon at r_1=0.48a and (b) triangular structure of air holes in silicon with an interstitial layer of SiO_2 (ε_s=3.9) at r_1=0.432a and layer thickness β=0.1. The solid and dashed lines denote *TE* and *TM* polarization modes, respectively. The picture insets depict the structures under consideration and the irreducible Brillouin zone for the calculations. The absolute PBG is indicated by shaded area.

We shall begin our discussion with the triangular structure consisting of air holes drilled in silicon (Fig. 3.1a). First, we consider the case when β=0, i.e. there is no interfacial layer. As it was already mentioned, the triangular structure of circular air rods is believed to have the greatest absolute PBG among the studied 2D photonic crystals. Figure 3.2a shows the photonic band structure for the optimum rod radius r_1=0.48a, for which the absolute PBG reaches its maximum normalized width of $\Delta\omega/\omega_g$=17.5%. The absolute PBG is formed from the overlap between the *TE1-2* (i.e. the gap between the first and second photonic bands) and the *TM2-3* polarization gaps. Now let us consider that a shell layer exists between the air rods and the background dielectric, i.e. β>0. Figure 3.2b shows the dispersion curves for r_1=0.432a and β=0.1 considering that the shell layer is made of SiO_2 (ε_s=3.9). For these geometrical parameters the outer radius r_2 of the rods covered with a shell layer is exactly r_2=0.48a and it is equal to the optimum rod radius for the shell-less case. We should expect that the bands decay in frequency because of the reduced air filling fraction. Indeed, the photonic bands tend to bunch towards lower frequencies. This effect is more

UNIVERSITAT ROVIRA I VIRGILI
PHOTONIC BANDGAP ANALYSIS AND FABRICATION OF MACROPOROUS SILICON BY ELECTROCHEMICAL ETCHING
Trifon Todorov Tirfonov
ISBN:978-84-693-6270-9/DL:T-1376-2010

pronounced for the higher bands, which finally leads to a decrease in the absolute PBG width. The absolute PBG width in this case is $\Delta\omega/\omega_g$=13.7%.

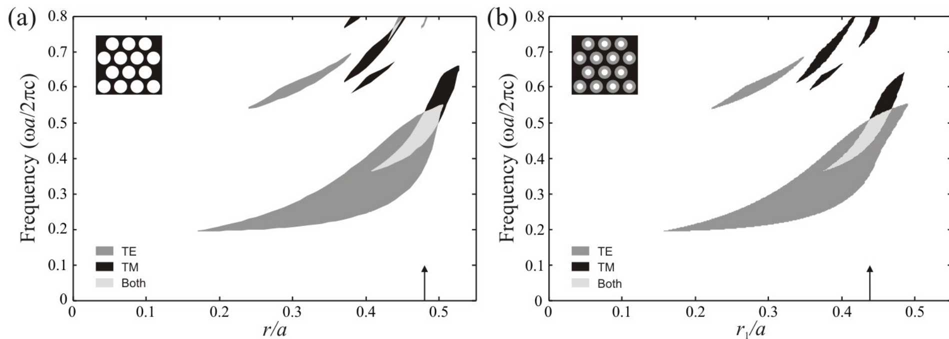

Fig. 3.3. Photonic gap map (normalized frequency $\omega a/2\pi c$ versus relative radius r/a) for the triangular structure of air rods without an interfacial layer (a) and with a SiO_2 interfacial layer of thickness β=0.1 (b). The absolute PBG in the case of shell layer has a maximum width of $\Delta\omega/\omega_g$=15.2% for r_1=0.438a (indicated by arrow). The insets depict the structure under consideration.

The photonic gap map in the case of rods covered with SiO_2 shell layer of thickness β=0.1 is shown in Fig. 3.3b, where the dimensionless frequencies are plotted against the rod radius r_1/a. If we compare this map with the well-known gap map for the ideal triangular structure (plotted in Fig. 3.3a for purposes of comparison) we can see that the gaps lie at lower frequencies. The shift of gap positions towards lower values of the inner rod radius r_1 accounts for the given definition of β. The outer radius r_2 of the rods with shell layer can be calculated from $r_2 = r_1/(1-\beta)$. It can be seen that the *TE1-2* polarization gap is not closed for rod radii above the close-packed condition. Here, the close-packed condition is defined as the value of outer radius r_2 for which the rods covered with a shell layer begin to touch. This is always r_2=0.5a. The value of the inner rod radius r_1 (air rod radius) for which close-packing occurs will then depend on the shell layer thickness β. For example, for β=0.1 the rods begin to touch when r_1=0.45a. The *TE1-2* polarization gap is still opened for r_1>0.45a because the triangular lattice remains connected through the overlapping shell layers of the neighbor rods. The *TM2-3* polarization gap has a smaller width than for the ideal case leading to narrower absolute photonic gap. The largest gap-midgap ratio for this structure is $\Delta\omega/\omega_g$=15.2% reached for r_1=0.438a.

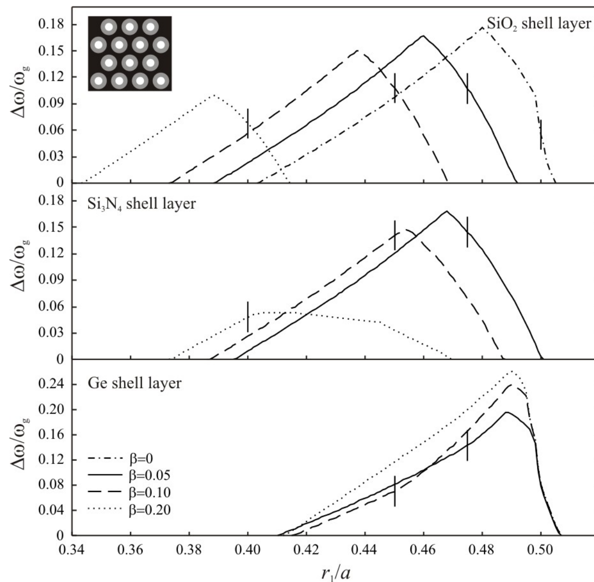

Fig. 3.4. Width $\Delta\omega/\omega_g$ of the absolute PBG as a function of the rod radius r_1 for the triangular structures of air rods covered with SiO_2, Si_3N_4 or Ge shell layers of different thicknesses β. The vertical bar marker indicates the close-packed condition, which is r_{1cp}=0.5, 0.475, 0.45 and 0.4 for β=0, 0.05, 0.1, and 0.2, respectively.

Note that for r_1=0.438a and β=0.1, the thickness of the shell layer is approximately 0.049a, so the outer diameter r_2 of the air rods, "covered" with SiO_2 is r_2=0.487a. It seems that the maximum absolute PBG occurs for almost the same rod diameter as when there is no shell layer. This is because for lower values of β and for shell layers of low dielectric constant, for instance SiO_2, the effective dielectric constant remains almost unchanged. However, for higher values of β and for shell layers of high dielectric constant, the effects of the interfacial layer on the absolute PBG cannot be trivially deduced. The dependence of the absolute PBG on the thickness β and the dielectric material ε_s of the shell layer can be traced from the next two figures. In Fig. 3.4 the normalized width of the absolute PBG is plotted against the radius r_1 of the air rods for several values of the parameter β and for the three shell materials considered here. The case without shell layer (β=0) is also shown for the purposes of comparison. For the case of SiO_2 shell layer, it can be seen that as the thickness of the layer increases, the position of maximum absolute PBG shifts towards lower values of the rod radius r_1. The absolute PBG reaches its maximum for values of r_1 below the close-packed condition (indicated by a short vertical bar). Unlike the inner rod radius r_1, the value of outer rod radius r_2 which gives the largest absolute PBG remains close to

UNIVERSITAT ROVIRA I VIRGILI
PHOTONIC BANDGAP ANALYSIS AND FABRICATION OF MACROPOROUS SILICON BY
ELECTROCHEMICAL ETCHING
Trifon Todorov Tirfonov
ISBN:978-84-693-6270-9/DL:T-1376-2010

0.48*a*, as for the shell-less case. Figure 3.5 shows the dependence of the maximum gap width on the shell layer thickness β. For the case of SiO_2 layer, the maximum width of the absolute PBG decreases for values of β>0, and for β>0.33 the absolute gap completely disappears. For greater values of β, the air rods have a thick SiO_2 cladding, so the structure resembles now a triangular structure formed mostly of SiO_2 rods embedded in silicon. This structure does not exhibit an absolute PBG because of the low dielectric contrast $\varepsilon_b/\varepsilon_s$.

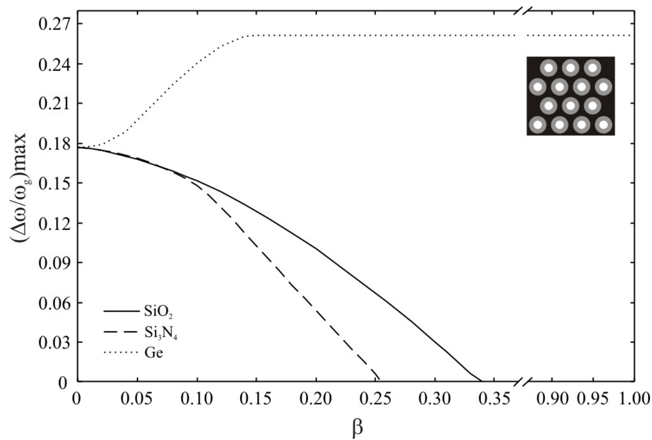

Fig. 3.5. Maximum width of the absolute PBG as a function of the shell-layer thickness β for the triangular lattice of air rods "covered" with SiO_2 (ε_s=3.9), Si_3N_4 (ε_s=7.5) or Ge (ε_s=16) shell layer. The abscissa is truncated for the sake of clarity.

The overall behavior of the absolute PBG in the case of Si_3N_4 shell layer (ε_s=7.5) is similar to the previous case. The existence of a shell layer always leads to a smaller absolute gap (Fig. 3.5). However, the absolute PBG width decreases more rapidly and, for values of β>0.25, it is almost zero. The position of the maximum absolute PBG is no longer as predictable as it was for the SiO_2 shell layer. For example, in the case of the SiO_2 shell layer, it was found that the absolute PBG reached its maximum width for outer radius r_2 near 0.48*a*, regardless of the shell layer thickness β. In the case of Si_3N_4, however, the absolute PBG does not follow the same rule. For β=0.1, the absolute PBG has a maximum when r_1=0.454*a*, so the outer radius should be r_2=0.504*a*. The outer radius r_2 becomes greater than the close-packed condition and the shell layers of adjacent rods should therefore overlap. The critical value of the shell layer thickness β, for which the maximum absolute PBG width appears at the close-packed condition, is β=0.09. For β>0.09, the absolute PBG decreases sharply because

ISBN:978-84-693-6270-9/DL:T-1376-2010

the optimum outer radius r_2 already approaches the filling-space condition. The filling-space condition is defined as the radius for which the rods entirely fill the area of the unit cell. For the triangular structure, this is r_2=0.577a. For shell layer thickness greater than 0.09, the optimum gap is reached when the rods actually overlap. Therefore, the photonic structure consisting of Si_3N_4-clad air rods embedded in silicon background becomes a structure comprising air rods embedded in Si_3N_4 background, instead of silicon. Because of the low dielectric contrast, the triangular lattice of air rods in Si_3N_4 presents a very small absolute PBG width of about $\Delta\omega/\omega_g$=2.8%.

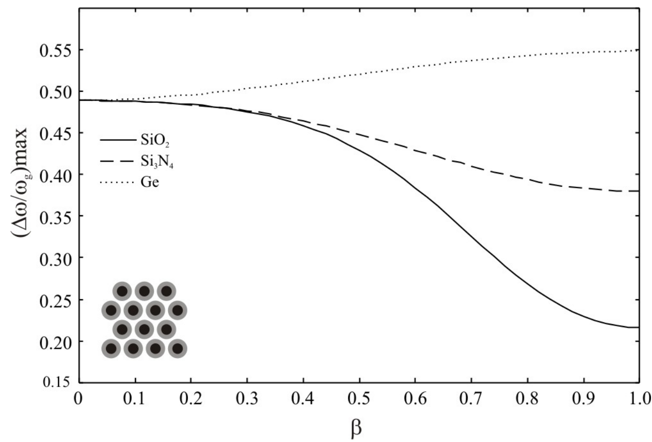

Fig. 3.6. Maximum width of the *TM1-2* polarization gap as a function of the shell layer thickness β for the triangular structure of silicon rods in air. The picture inset depicts the structure under consideration.

The behavior of the absolute PBG drastically changes when the air rods are covered with Ge (ε_s=16) shell layer. The dielectric constant of the shell layer is now greater than that of background material. It should be expected that the existence of an interstitial layer would improve the absolute PBG because of higher dielectric contrast ($\varepsilon_s/\varepsilon_r$) at the air-rod interface. Indeed, the absolute PBG has greater magnitudes than in the shell-less case (β=0) (Fig. 3.5). The gap width increases as the shell layer gets thicker. For example, for β=0.2 the maximum absolute PBG width is $\Delta\omega/\omega_g$=26.2% at r_1=0.49a. However, the optimum absolute PBG always happens to occur above the close-packed condition. Moreover, when β>0.15 it occurs for rod radii above the filling-space condition, so the structure we actually investigate is a triangular structure of air rods embedded in Ge background matrix. For radius r_1 far from the close-packed condition, the width of the absolute PBG is always less than its width in the shell-less

UNIVERSITAT ROVIRA I VIRGILI
PHOTONIC BANDGAP ANALYSIS AND FABRICATION OF MACROPOROUS SILICON BY ELECTROCHEMICAL ETCHING
Trifon Todorov Tirfonov
ISBN:978-84-693-6270-9/DL:T-1376-2010

case.

Having discussed the triangular structure of air rods covered with a shell layer and embedded in silicon, we shall now study the inverse arrangement, i.e. silicon rods covered with a shell layer and embedded in air. For the shell-less silicon rods (β=0), it is well known that the triangular structure does not exhibit any absolute PBG because of disrupted lattice connectivity [13]. Neither does the existence of a shell layer (β>0) contribute to the opening of an absolute PBG. We can use the general rule of thumb, which holds that the connectivity of high-ε regions is conducive to *TE* gaps, and that isolated islands of high-ε material lead to *TM* gaps. Then there is no reason for the absolute PBG opening because the shell layer does not form any connected structure. We think it would be interesting to see how the shell layer affects the properties of the first *TM* polarization gap (*TM1-2*), which is about $\Delta\omega/\omega_g$=48.9% for the shell-less triangular structure. Figure 3.6 shows how the maximum width of the *TM1-2* gap depends on the shell layer thickness β for the three dielectric materials considered. We can see that if the dielectric constant of the shell material is less than that of silicon, the gap diminishes when the thickness of the shell layer increases. For germanium, whose dielectric constant is greater than that of silicon, the reverse is true: the gap widens as β increases. For β=1, the silicon rods covered with a shell layer are transformed into rods made of the corresponding shell material. Therefore, for the triangular structure of dielectric rods with a shell layer, the width of the *TM1-2* polarization gap always ranges between its values for β=0 (shell-less rods) and β=1 (rods entirely replaced by the shell layer).

These results suggest that the gap behavior is governed by the dielectric contrast at the shell layer/air interface. Covering the rods with materials of low dielectric constant will reduce the width of the gap, while high-dielectric claddings will improve the gap size. However, for the triangular structure of air rods in dielectric media, this improvement is fictitious because it appears for infeasible rod diameters. Any interfacial layers for this arrangement should be therefore avoided.

3.3.2. Honeycomb lattice

We turn now to study the honeycomb lattice consisting of rods covered with a shell layer. In the ideal case (shell-less rods), the honeycomb arrangement of air holes in dielectric media exhibits a narrow absolute PBG due to the weak overlap between *TE5-6* and *TM6-7* polarization gaps (see, for example, Fig. 2 of Ref. 149). In the

UNIVERSITAT ROVIRA I VIRGILI
PHOTONIC BANDGAP ANALYSIS AND FABRICATION OF MACROPOROUS SILICON BY ELECTROCHEMICAL ETCHING
Trifon Todorov Tirfonov
ISBN:978-84-693-0270-9/DL:T-1376-2010

particular case of air rods embedded in silicon background, this absolute PBG has an optimum width of $\Delta\omega/\omega_g$=4.4% for r_1=0.484a, which is very close to the close-packed condition. The evolution of this absolute PBG, when an interfacial layer is present between the air rods and the background silicon, is rather strange. Figure 3.7 shows its optimal width as a function of the shell layer thickness for the three shell materials considered. It can be seen that shell layers of lower dielectric constants, i.e. SiO_2 and Si_3N_4, yield an improvement in the absolute PBG size, whereas shell layers of higher dielectric constants, i.e. Ge, reduce the gap width. This gap behavior is just opposite to the already discussed one for the triangular lattice of air rods in silicon. We notice that the observed improvement in the absolute PBG size always occurs for rod radii above the close-packed condition (r_2=0.5a). Near the close-packed condition, the honeycomb lattice of air rods in dielectric resembles a triangular structure with lattice constant $\sqrt{3}a$ formed by dielectric rods of noncircular cross section and embedded in air [149]. Therefore, for rod radii above the close-packed condition we actually examine the triangular structure comprising noncircular dielectric rods in air. The unfeasible rod diameters and the really small width of the absolute PBG, make the honeycomb lattice of air rods in dielectric worthless for practical realization.

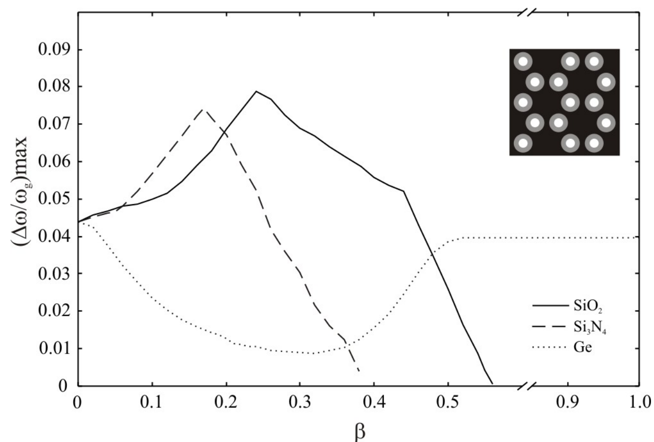

Fig. 3.7. Optimal width of the absolute PBG as a function of the shell layer thickness β for the honeycomb lattice of air rods embedded in silicon. The abscissa is truncated for the sake of clarity.

The most prominent feature of the honeycomb structure is that, in the case of dielectric rods embedded in air, it exhibits an absolute PBG, so in a sense it is complementary to the triangular structure discussed in the previous section. Also, the

UNIVERSITAT ROVIRA I VIRGILI
PHOTONIC BANDGAP ANALYSIS AND FABRICATION OF MACROPOROUS SILICON BY ELECTROCHEMICAL ETCHING
Trifon Todorov Tirfonov
ISBN:978-84-693-6270-9/DL:T-1376-2010

absolute PBG occurs at filling fractions that are far from the close-packed condition, which makes the fabrication of such 2D photonic crystal less formidable. In Fig. 3.8a we plot the dispersion relation for the shell-less honeycomb lattice at r_1=0.247a. An absolute photonic gap opens up from the overlap between *TE5-6* and *TM7-8* polarization gaps. For the given rod radius, this absolute PBG has a maximum normalized width of $\Delta\omega/\omega_g$=10%. Let us cover now the silicon rods by SiO_2 of thickness β=0.1, so that the outer radius r_2 of the rods with a shell layer remains r_2=0.247a. Figure 3.8b plots the dispersion relation for this case and we can see that the bands go to higher frequencies since the effective dielectric constant is reduced. The gap width ($\Delta\omega/\omega_g$=9.4%) is slightly decreased compared to the ideal (shell-less) structure.

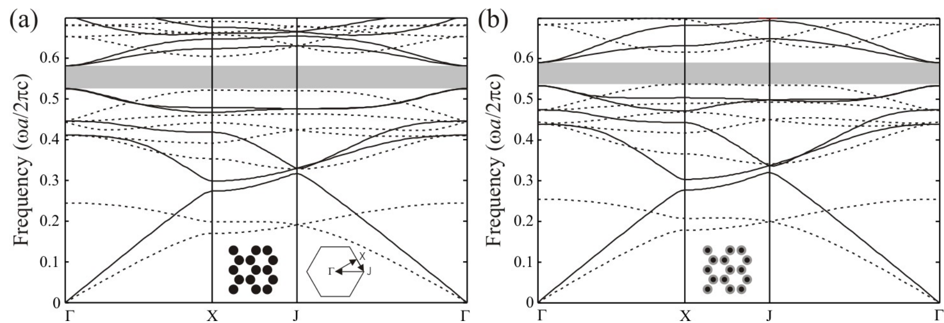

Fig. 3.8. Photonic band structures for the honeycomb lattice of silicon rods in air: (a) shell-less rods with radius r_1=0.247a and (b) rods with inner radius r_1=0.222a (outer radius r_2=0.247a) covered by SiO_2 with thickness β=0.1. The solid and dashed lines represent the *TE* and *TM* modes, respectively. The frequency range of the absolute PBG is indicated by a shaded patch.

Figure 3.9 shows the photonic gap map for the honeycomb lattice of silicon rods in air (Fig. 3.9a) and its modified structure considering that the rods are covered with SiO_2 layer of thickness β=0.1. As for the shell-less honeycomb lattice, three absolute photonic gaps are present, which appear and have their maxima for different rod dimensions. The highest absolute PBG is formed from the overlapping *TE5-6* and *TM7-8* polarization gaps. Hereafter, to avoid ambiguity and repetition, we will refer to this absolute PBG as the G1 gap. The lowest one is due to the overlap between *TE3-4* and *TM6-7* gaps. It will be referred to as the G2 gap. Finally, the overlapping *TE5-6* and *TM6-7* polarization gaps give rise to a small absolute PBG, which will be referred to as the G3 gap. In addition to these three absolute PBG a weak overlap can be seen between the *TE1-2* and *TM2-3* polarization gaps (Fig. 3.9b), which is not observed in the gap map of the ideal honeycomb structure. However, the gap size of this new absolute PBG

is too small to be used, so we do not concern ourselves with this band-gap region. The largest absolute photonic gap for the present case is the G1 gap, which reaches its maximum width of $\Delta\omega/\omega_g$=9.6% for r_1=0.234a. Therefore, it seems that the existence of an interfacial layer surrounding the silicon rods reduces the size of the largest absolute PBG for the studied structure. But, we will show that the interfacial layer could favor the other absolute PBG's, increasing their initially smaller magnitudes, and could even give rise to larger gaps compared to the shell-less structure. We have studied how the three substantial absolute PBG's (G1, G2 and G3) for the structure shown in Fig. 3.1b evolve with respect to the material and thickness of the shell layer covering the silicon rods.

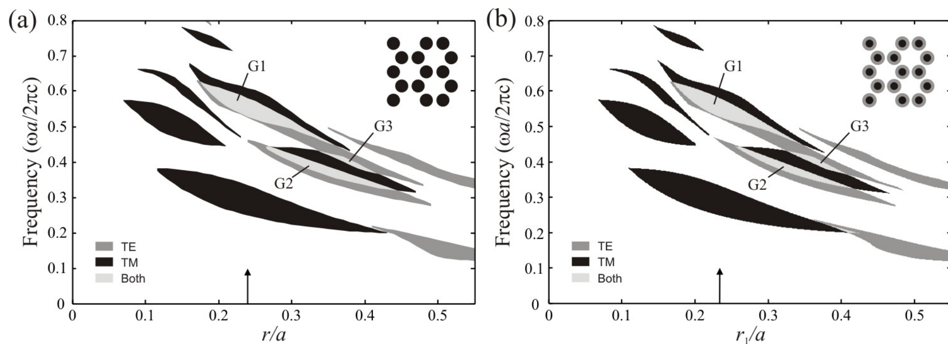

Fig. 3.9. Photonic gap map for the honeycomb lattice of silicon rods in air for (a) rods without a shell layer and (b) rods covered with SiO_2 layer of thickness β=0.1. Three absolute PBG's are observed, denoted as G1, G2 and G3 absolute gaps. The arrow indicates the position r=0.247a (r_1=0.234a) of the largest absolute PBG with a maximum width of $\Delta\omega/\omega_g$=10% ($\Delta\omega/\omega_g$=9.6%) for the shell-less (SiO_2-cladding) cases. The insets illustrate the structure under consideration.

Figure 3.10 shows the normalized widths of these absolute PBG's as functions of the rod radius r_1 for three different thicknesses of the shell layer made of SiO_2. Again, the case without shell layer (β=0) is also shown for purposes of comparison. The G1 gap decreases slightly with increasing the shell layer thickness β, whereas the other two gaps G2 and G3 are more strongly affected. This is particularly due to the variations in the filling fraction for different radii r_1. From the definition of parameter β, according to whether the inner rod radius r_1 is small or high, the shell layer will be thinner or thicker for fixed value of β. Since the G2 and G3 gaps arise for higher values of r_1, the introduced amount of the shell material is greater than in case of smaller r_1, so these gaps appear to be more sensitive to changes in β. Nevertheless, the overall tendency for the G1 and G2 gaps is the same. These gaps shrink when a shell layer is present,

ISBN:978-84-693-6270-9/DL:T-1376-2010

whereas the G3 gap widens. It should be noted that in the present case the close-packed condition (r_2=0.5a) is never reached.

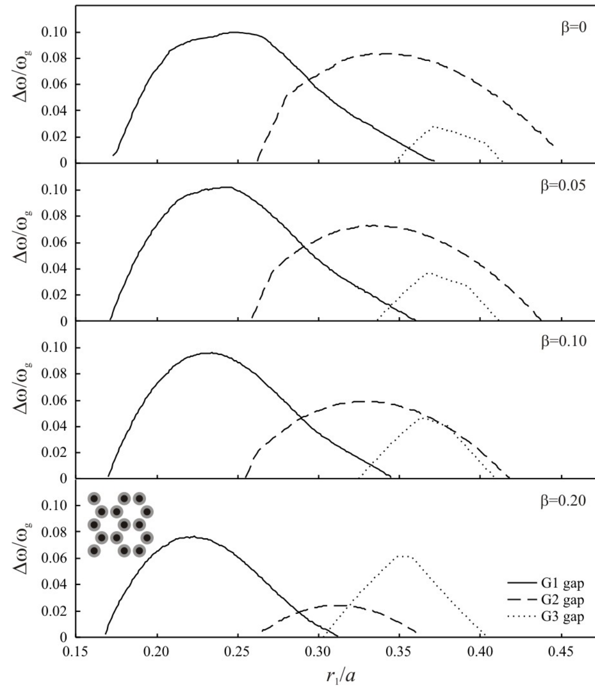

Fig. 3.10. Normalized widths of the three absolute PBG's (G1, G2 and G3) for the honeycomb lattice plotted against the inner rod radius r_1 for three shell layer thicknesses β=0.05, 0.10 and 0.20. The considered shell layer material is SiO_2 (ε_s=3.9). The shell-less case (β=0) is shown for purposes of comparison.

Almost the same happens in the evolution of the gaps when a shell layer of Si_3N_4 is considered (Fig. 3.11). We will discuss here only the main differences in gap behavior with respect to the previous case. The G1 and G2 absolute gaps are much less affected by the thickness of the shell layer and decrease slightly as β increases. The increase in the G3 gap, however, is lower than in the case of SiO_2 shell layer. The maximum width reached for β=0.2 is $\Delta\omega/\omega_g$=5.3%, compared to $\Delta\omega/\omega_g$=6.1% in the case of SiO_2.

UNIVERSITAT ROVIRA I VIRGILI
PHOTONIC BANDGAP ANALYSIS AND FABRICATION OF MACROPOROUS SILICON BY ELECTROCHEMICAL ETCHING
Trifon Todorov Tirfonov
ISBN:978-84-693-6270-9/DL:T-1376-2010

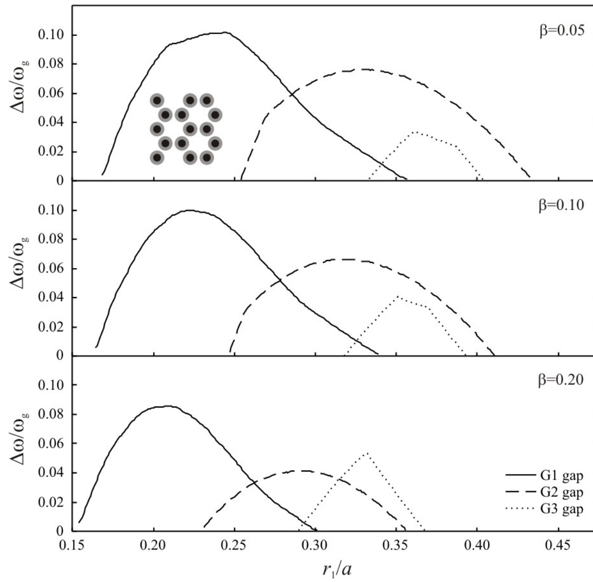

Fig. 3.11. Normalized widths of the three absolute PBG's (G1, G2 and G3) for the honeycomb lattice plotted against the rod radius r_1 for three shell layer thicknesses β. The shell layer material studied is Si_3N_4 (ε_s=7.5).

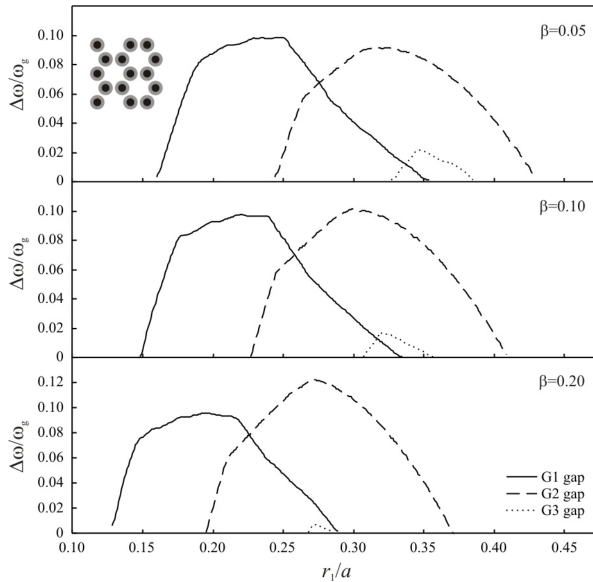

Fig. 3.12. Normalized widths of the G1, G2 and G3 absolute gaps for the honeycomb lattice plotted against the rod radius r_1 for three shell layer thicknesses β. The shell layer material studied is Ge (ε_s=16).

UNIVERSITAT ROVIRA I VIRGILI
PHOTONIC BANDGAP ANALYSIS AND FABRICATION OF MACROPOROUS SILICON BY ELECTROCHEMICAL ETCHING
Trifon Todorov Tirfonov
ISBN:978-84-693-6270-9/DL:T-1376-2010

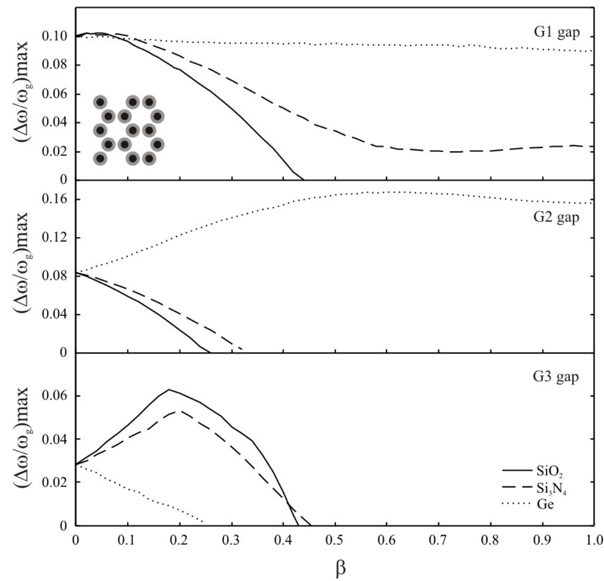

Fig. 3.13. Optimal widths of the G1, G2 and G3 absolute photonic gaps as functions of shell layer thickness β for the three dielectric materials considered SiO_2, Si_3N_4 and Ge. The lower β=0 and upper β=1 limits represent the shell-less honeycomb lattice with rods made of silicon or of the shell dielectric, respectively.

If the shell layer is made of Ge, whose dielectric constant is greater than that of silicon rods, the absolute PBG's evolve in a completely different way (Fig. 3.12). For example, the G3 gap is disappointingly small and for values of β>0.24 it becomes fully suppressed. Fortunately, the G1 gap which was the largest one for the shell-less honeycomb lattice, is not altered at all by the thickness of the shell layer. Even at β=0.2, its width $\Delta\omega/\omega_g$=9.6% remains almost the same as for the shell-less case. Moreover, the G2 gap now shows a relative width $\Delta\omega/\omega_g$=12.2% and so becomes the largest gap for the structure. It lies at lower frequencies and so, it becomes more robust to imperfections generated by the fabrication. When β increases, the width of the G2 gap approaches its value for the case of honeycomb lattice comprising germanium rods rather than silicon rods in air. Our structure consisting of silicon rods with Ge coating is therefore mainly seen as a structure formed of germanium rods, even for thin interfacial layers. This claim is justified in the Fig. 3.13, which plots the optimum widths of the absolute gaps against the shell layer thickness. The lower (β=0) and upper (β=1) limits of the parameter β represent the two special cases, i.e. shell-less structure and structure where the rods are made of the shell material, respectively. When SiO_2 and Si_3N_4 layers are considered, the width of the G1 gap decreases, but for the Si_3N_4 layer the gap width

UNIVERSITAT ROVIRA I VIRGILI
PHOTONIC BANDGAP ANALYSIS AND FABRICATION OF MACROPOROUS SILICON BY ELECTROCHEMICAL ETCHING
Trifon Todorov Tirfonov
ISBN:978-84-693-0270-9/DL:T-1376-2010

does not fall below 2.4% at β=1. Indeed, this is the width of the G1 gap for the honeycomb lattice of Si_3N_4 rods embedded in air. Because of the low dielectric contrast, this lattice does not exhibit any other absolute PBG's. The honeycomb structure consisting of SiO_2 rods in air has no absolute PBG's for the same reason. In the case of Ge rods in air, the width of the G1 gap is about 9%, so the G1 gap for silicon rods with Ge cladding stands near this value as β increases. The G2 gap behaves in a similar way, i.e. it increases towards the value $\Delta\omega/\omega_g$=15.6%, which is the gap width for the special case of Ge rods embedded in air.

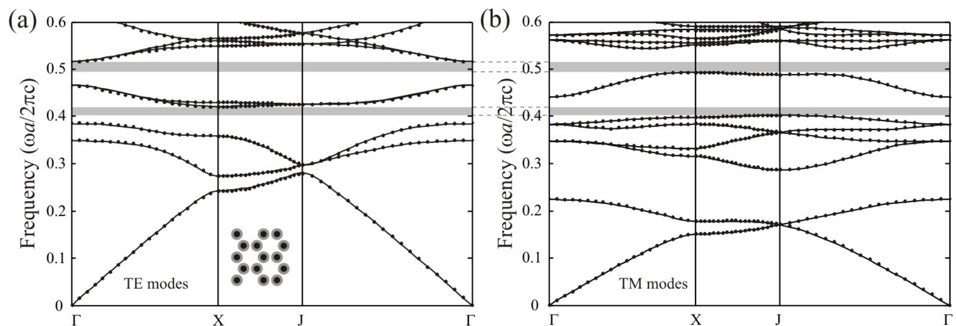

Fig. 3.14. Photonic band structure for the honeycomb lattice of silicon rods in air for r_1=0.29*a* and β=0.1 (SiO_2 shell layer), (a) TE modes and (b) TM modes. The solid lines represent the bands calculated by using MIT software package. The dispersion curves from the FDTD method are shown by dots. The shaded areas indicate G1 and G2 absolute gaps.

Finally, in order to verify the accuracy of the FDTD method we also computed the photonic bands of the considered structures by using a freely available MIT software package [84]. The MIT software uses an iterative eigensolver to calculate the fully-vectorial eigenmodes of Maxwell's equations with periodic boundary conditions. The basic principle can be characterized as a preconditioned conjugate-gradient minimization of the block Rayleigh quotient [156]. Figure 3.14 shows the dispersion relation for the honeycomb lattice of silicon rods in air at r_1=0.29*a* and β=0.1 in the case of SiO_2 shell layer. The lattice unit cell was defined using the same computational grid of 64×64 points, which ensures sufficient convergence for both MIT and FDTD programs. The G1 and G2 absolute gaps are shown (shaded area) which co-exist in the structure for the given physical parameters. The normalized widths of the G1 (G2) gaps are $\Delta\omega/\omega_g$=4.51% (4.58%) calculated from the FDTD band structure compared to $\Delta\omega/\omega_g$=4.56% (4.65%) calculated from the MIT bands. As can be seen, the agreement between both methods is very good.

UNIVERSITAT ROVIRA I VIRGILI
PHOTONIC BANDGAP ANALYSIS AND FABRICATION OF MACROPOROUS SILICON BY ELECTROCHEMICAL ETCHING
Trifon Todorov Tirfonov
ISBN:978-84-693-6270-9/DL:T-1376-2010

To conclude, it is worth pointing out that the honeycomb arrangement of dielectric rods is suitable for the fabrication of PBG materials because the largest absolute gaps are attainable for reasonable rod diameters, which avoids the tricky achievement of thin dielectric voids. In addition, our results provide further flexibility in the realization of these materials. For example, in certain cases we may not be able to obtain pillars (rods) of the required diameter or of the particular material we need, because of technological limitations. However, we are enabled to grow the rods of materials with lower dielectric constants, for which a well-developed technology exists. The rods can then be covered with the required dielectric by some depositing technique, thus achieving almost the same gap properties as those of the ideal shell-less structure.

3.4. Conclusions

We have performed a detailed quantitative analysis of the absolute PBGs in 2D triangular and honeycomb lattices considering that an interfacial layer is present between the rods and the background matrix. Both complementary structures, i.e. air rods in a dielectric and dielectric rods in air have been studied. The properties of the photonic gaps are strongly affected by the thickness and the dielectric constant of this interfacial layer. The following general conclusions about the absolute PBG evolution can be drawn:

1. For structures consisting of air rods in a dielectric background, the existence of an interfacial layer always entails a reduction in the absolute PBG width and should therefore be avoided. The decrease in the gap width depends mainly on whether the dielectric constant of the interfacial layer is greater or less than that of the background matrix. Higher dielectric constant of the shell layer entails gaps which are practically unattainable. If for any reasons an interfacial layer is desired, small thicknesses and low dielectric constants should be chosen because the gap properties will be only slightly affected.

2. For structures formed of dielectric rods in air, interfacial layers with lower dielectric constants yield gaps with smaller widths than in the shell-less case. The rate of decrease is as high as the dielectric constant of the shell material is low. However, shell layers whose dielectric constants are higher than that of the rod material lead to larger absolute photonic gaps. The gap size is increased up to values that are typical for the structure consisting of rods made only of the shell dielectric.

The interfacial layer can be treated as hollow ring-shaped rods included at the

UNIVERSITAT ROVIRA I VIRGILI
PHOTONIC BANDGAP ANALYSIS AND FABRICATION OF MACROPOROUS SILICON BY ELECTROCHEMICAL ETCHING
Trifon Todorov Tirfonov
ISBN:978-84-693-6270-9/DL:T-1376-2010

center of each basic rod of the lattice unit cell. However, we notice that the concept of including an interfacial layer into the basic unit cell does not deal at all with the symmetry reduction approach because this inclusion does not modify the symmetry properties of the lattice or those of the scatterers. The gap behavior is ruled by the dielectric constant and the filling fraction of the included material and reflects the induced changes in the effective dielectric constant of the crystal. Although we have considered here a few 2D lattices, nevertheless, the given approach is not essential and can be applied to other 2D as well 3D photonic structures.

ISBN:978-84-693-6270-9/DL:T-1376-2010

Chapter 4

Electrochemical etching of silicon. Experimental

This chapter is devoted to the experimental technique for fabricating 2D photonic crystals by light-assisted electrochemical etching of n-type silicon. Firstly, the physics of macropore formation and the properties of electrochemically etched macropore arrays are briefly outlined. The phenomenological model that describes the influence of experimental parameters like light intensity, doping level, HF concentration or temperature on the pore formation process is discussed. Secondly, the developed electrochemical etching set-up used for the macroporous silicon fabrication is described. Finally, the main process sequence and process parameters for sample preparation are detailed.

4.1. Introduction and historical overview of porous silicon

In this and in the next two chapters we shall focus our attention on the electrochemical etching of silicon as a technique for fabricating 2D photonic crystals operating in the infrared spectrum. As already mentioned in Chapter 1, the electrochemical etching of silicon in hydrofluoric acid (HF) solutions gives rise to porous material. This material was called “macroporous silicon”, in contrast to its “microscopic” relative. The existing nomenclature, adopted by the International Union

UNIVERSITAT ROVIRA I VIRGILI
PHOTONIC BANDGAP ANALYSIS AND FABRICATION OF MACROPOROUS SILICON BY ELECTROCHEMICAL ETCHING
Trifon Todorov Tirfonov
ISBN:978-84-693-0270-9/DL-T-1376-2010

of Pure and Applied Chemistry (IUPAC), distinguishes three categories with regard to the pore dimensions [157]: *micropores*, *mesopores* and *macropores* with average pore diameters of < 2 nm, 2-50 nm and > 50 nm, respectively. This categorization is related only to the pore diameter, but does not contain much information about the *pore morphology*. The term *pore morphology* is used as the collective identifier for properties like shape (smooth, branched, facetted, etc.), orientation, interconnection of pores, and so on. The morphology is the least quantifiable aspect of *porous silicon* (PS). It is very difficult to systematically characterize the morphology of PS, which has extremely rich details with respect to variations in pore size, shape and spatial distribution. In terms of the pore morphology, it can be summarized that microporous and mesoporous silicon exhibit typically a sponge-like structure with densely and randomly branched pores, which do not show a clear orientation. The tendency to branch increases with decreasing pore diameter. In contrast, macroporous silicon can have discrete pores with smooth walls, with short branches or with dendritic branches. The pores grow preferentially along <100> directions and towards the source of positive carriers (holes), which are involved in the electrochemical dissolution reaction. Pores with smooth walls tend to be aligned to the source of holes, while dendritic pores are aligned in the <100> direction. In this thesis we are concerned only with macroporous silicon and more precisely, with the ordered macropore growth, which in optimal conditions exhibits pores perpendicular to the surface for (100) substrate and with very smooth pore walls. It is worth mentioning that the pore walls are rough at atomic scale for all types of porous silicon. Under certain conditions, two different pore distributions can co-exist in the structure. For example, the macropores can be partially or fully filled by microporous silicon, as will be shown later.

Porous silicon has been known for more than forty years. Figure 4.1 summarizes the progress which has been made so far in this field. The first report of porous silicon dates back to 1956. In this article [158], Uhlir found matte black, brown or red deposits on anodized silicon samples. He thought porous silicon was something deposited on a substrate during electropolishing. Anodically formed films were studied in more details by Turner [159]. Turner found electropolishing of silicon to occur above a critical current density, which increased with HF concentration and temperature. Below the critical current density he observed a thick film with an orange-red color and a glassy appearance and speculated that it was a silicon subfluoride $(SiF_2)_x$ grown on the surface during the anodic dissolution. Subsequently, Memming and Schwandt proposed that the brown film was a result of redeposition of silicon from SiF_2 (two-step disproportionation reaction) [160]. The porous nature of electrochemically formed films

UNIVERSITAT ROVIRA I VIRGILI
PHOTONIC BANDGAP ANALYSIS AND FABRICATION OF MACROPOROUS SILICON BY ELECTROCHEMICAL ETCHING
Trifon Todorov Tirfonov
ISBN:978-84-693-6270-9/DL:T-1376-2010

on silicon was first reported by Watanabe and Sakai [161] in 1971. The number of publications dealing with porous silicon has increased rapidly since 1971. Theunissen [162] proposed the first model for pore formation in n-type silicon, postulating that the large current observed at some anodic potentials was due to barrier breakdown. Using electron diffraction, Arita and Sunohara [163] proved that porous silicon is a single crystalline with the same orientation as the substrate. They concluded that localized dissolution generates pores in the silicon electrode and the remaining substrate forms the porous silicon. In 1983 Bomchil *et al.* [164] demonstrated that the pore diameter can be as small as 2 nm. Etching of macropores in an arbitrary pattern using a pre-structured n-type silicon electrode was first reported in 1990 by Lehman and Föll [60].

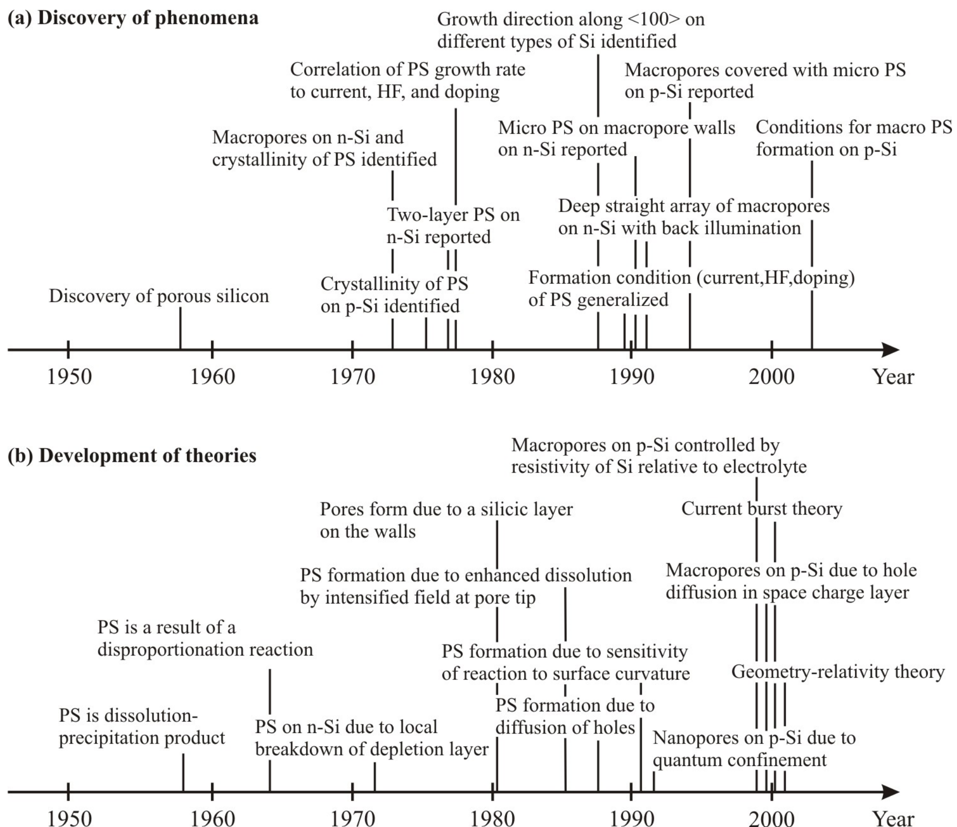

Fig. 4.1. Progress in the discovery of morphological phenomena (a) and in the development of theories (b) on formation mechanisms of porous silicon (PS). After [184].

Several theories have been proposed to explain the formation mechanism of

UNIVERSITAT ROVIRA I VIRGILI
PHOTONIC BANDGAP ANALYSIS AND FABRICATION OF MACROPOROUS SILICON BY ELECTROCHEMICAL ETCHING
Trifon Todorov Tirfonov
ISBN:978-84-693-0270-9/DL-T-1376-2010

porous silicon. Beale *et al.* [165] postulated that the material in the PS is depleted of carriers and the presence of a depletion layer is responsible for current localization at pore tips where the field is enhanced. Smith and co-workers [166-168] proposed the diffusion limited model. They described the morphology of PS based on the hypothesis that the rate of pore formation is limited by the diffusion of holes from the bulk silicon to the pore tips. Unagami [169] postulated that the formation of PS is promoted by the deposition of a passive silicic acid on the pore walls, which finally results in preferential dissolution at the pore tips. Alternatively, Parkhutik *et al.* [170] suggested that a passive film composed of silicon fluoride and silicon oxide is between the PS and the substrate and that the formation of PS is similar to that of porous alumina. To explain the formation of straight, smooth and well spaced macropore arrays on low doped n-Si using backside illumination and surface patterning, Lehman and Föll [60] postulated that the dissolution rate at pore tips is limited by mass transfer in the electrolyte and that the relative rates of carrier transport in the silicon and mass transport in the electrolyte determine PS morphology. They supposed that the critical current density found by Turner [159] is reached at the pore tips so that the mass transfer in the electrolyte and charge supply in the semiconductor are in steady-state condition at the tips. For the micropores formed on p-Si, Lehmann and Gösele [171] proposed a quantum confinement model. They assumed that in very thin pore walls, the band gap is increased due to quantum charge confinement. The increase in the band gap prevents the electronic holes from penetrating the pore walls. The pore walls become depleted and do not dissolve during the anodization. In the same year (1991), Zhang [172] proposed the surface curvature model, which postulates that not only the rate but also the distribution of reactions on a curved pore bottom can be greatly affected by the surface curvature. In the late 1990s, Föll and co-workers [173-175] proposed the current burst theory. The basic hypothesis is that the electrochemical reactions involved in the dissolution of silicon surface operate in microscopic units. These reaction units have a temporal and a spatial distribution in the number and in the state of activity. The formation of pores is due to the synchronization of these units at certain time and spatial length.

The formation of two-layer PS, consisting of a micro-PS on a surface of macro-PS in n-type silicon under front illumination, had been reported in the late 1970s but it was little investigated until 1990s [176-178]. It appeared that while the formation of a macro-PS layer under front illumination follows the same mechanism as the macro-PS formed in the dark, the formation of micro-PS is due to the effect of the photogenerated carriers. Clement *et al.* [176] suggested that micro-PS formed under

UNIVERSITAT ROVIRA I VIRGILI
PHOTONIC BANDGAP ANALYSIS AND FABRICATION OF MACROPOROUS SILICON BY ELECTROCHEMICAL ETCHING
Trifon Todorov Tirfonov
ISBN:978-84-693-6270-9/DL:T-1376-2010

illumination could result from shattering of the macro-PS into fine filaments due to residual stress. Formation of macro-PS and two-layer PS on low doped p-Si in organic HF solution was reported by Propst and Kohl [179] in 1994. They thought the formation of macro-PS was related to the chemistry of organic solvent. Macropores on low doped p-Si were later found to also form in aqueous HF solution. As described by Wehrspohn *et al.* [180] a necessary condition for the formation of macro-PS on low doped p-Si is a higher resistivity of the substrate than that of the electrolyte. This idea was later invalidated as macro-PS was also found to occur in electrolytes with much higher resistance than that of silicon substrate [181]. In this work, Lehmann and Rönnebeck [181] postulated that the formation of macro-PS on low doped p-Si is due to the dominant effect of thermionic emission which is sensitive to the barrier height rather than barrier width. Alternatively, Lust and Clement [182] reported a study of the conditions for macropore formation on p-Si in different aqueous and nonaqueous solutions, and pointed out the role of the interface chemistry in the formation process of macropores.

It should be pointed out that most theories deal only with certain aspects of the complex PS morphology and formation. No single theory is yet close to a globally coherent description of the extremely rich and complex nature of the reactions and the resulting morphological evolution of the silicon electrode surface. A complete description of the diverse morphological features of porous silicon requires the integration of all morphological aspects as well as the fundamental electrochemical reactions involved at silicon/electrolyte interface. Such a global and accurate model that can fully characterize all morphological features of PS is yet to come. Detailed and comprehensive reviews on all aspects related to PS and electrochemistry of the silicon/electrolyte interface can be found in Ref. [183-186], and also in the excellent book by Lehmann [187].

4.2. Electrochemical etching of silicon

Semiconductor-electrolyte system shows a behavior, which at first approximation is similar to that of a Schottky contact [155] (semiconductor-metal contact). In the electrochemical cell, the silicon-electrolyte interface forms an electrode-electrolyte barrier system. The potential barriers and electric field distributions depend on the doping characteristics of the semiconductor and the chemical composition of the electrolyte. The major feature of this barrier system is its *double layer* attribute. There exist finite regions of space over which the electric field is spread and potential barrier

UNIVERSITAT ROVIRA I VIRGILI
PHOTONIC BANDGAP ANALYSIS AND FABRICATION OF MACROPOROUS SILICON BY ELECTROCHEMICAL ETCHING
Trifon Todorov Tirfonov
ISBN:978-84-693-0270-9/DL-T-1376-2010

evolves: these are the Helmholtz layer in the electrolyte and the depletion layer in the semiconductor. For example, if a metal electrode is immersed in an electrolyte, a double layer is formed at the interface to the electrode. An excess of ions of charge opposite to that on the electrode is found on the solution side of this interface. The simplest view of the interface is to imagine that these ions approach the surface of the electrode as closely as possible. The double layer then consists of two parallel layers of charge, one on the metal surface and one comprising ions at the distance of closest approach. This simple possible model is known as Helmholtz layer model. Owing to the very high concentration of charge carriers both in the electrolyte and in the metal, the potential drop across the double layer is accommodated over extremely small thickness (approximately 3-10 Å). Any charge transfer across the Helmholtz layer involves a chemical reaction. If the metal electrode is replaced by a semiconductor one, the number of free charge carriers is reduced, depending on the doping density. The charge on the semiconductor side may be due to majority carriers, ionized dopants or minority carriers. The corresponding charge states are called accumulation, depletion and inversion, respectively. In contrast to the electrons and holes, which are free charge carriers, the ionized doping atoms are not mobile. If the sign of the potential applied to the semiconductor is such that the majority carriers are drawn away from the interface and into the semiconductor bulk, the maximum charge density on the semiconductor side will be equal to the density of doping atoms. They therefore will form a space charge region (SCR) that may extend up to several tens of microns into the bulk of the semiconducting electrode, depending on doping concentration [187]. In the physics literature, this is termed the *reverse bias* situation. Obviously, the reverse bias situation may happen if we apply positive potential at n-type silicon electrode and negative for p-type one. It should be noticed that under *forward bias* (for example, a negative potential applied to n-type silicon), the semiconductor electrode will have a potential distribution at the interface more reminiscent to that of metal. The thickness of the accumulation and inversion layers is in the order of nanometers. This is because the allowed concentration, for example of electrons for n-type silicon, is determined by the density of states in the conduction band, which may be comparable to that in a metal.

The current-voltage (I-V) characteristic of the semiconductor-electrolyte contact is determined by both the semiconducting nature of the electrode and the ionic species present in the electrolyte. The current density at the electrode for a certain potential is limited by the reaction kinetic at the interface, or by the charge supply from the electrode or the electrolyte [187]. If the charge transfer is limited by charge supply from the silicon electrode the basic I-V characteristic of the Si-electrolyte junction is

UNIVERSITAT ROVIRA I VIRGILI
PHOTONIC BANDGAP ANALYSIS AND FABRICATION OF MACROPOROUS SILICON BY
ELECTROCHEMICAL ETCHING
Trifon Todorov Tirfonov
ISBN:978-84-693-6270-9/DL:T-1376-2010

very similar to that of a Schottky diode (Fig. 4.2). An n-type silicon, for example, is reversely biased under anodic conditions. Therefore the current is minimal in the dark and increases upon provision of minority carriers (generated by illumination) or for a bias high enough to initiate breakdown (Fig. 4.2a). In cathodic regime the junction is under forward conditions and the current is described by the diode equation [155]. The case of p-type Si is only different insofar as the forward and the reverse regime are exchanged in the I-V curve (Fig. 4.2b).

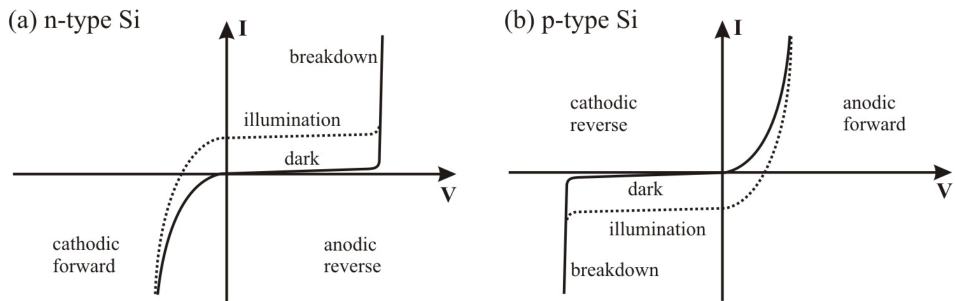

Fig. 4.2. Current-voltage (I-V) characteristics of (a) n-type and (b) p-type silicon electrode under the assumption that the current is dominated by the properties of semiconductor and is not limited by interface reactions or by diffusion in the electrolyte. The solid line indicates the dark response and the dotted line shows a response under illumination. The I-V characteristic resembles that of a Schottky diode. After [187].

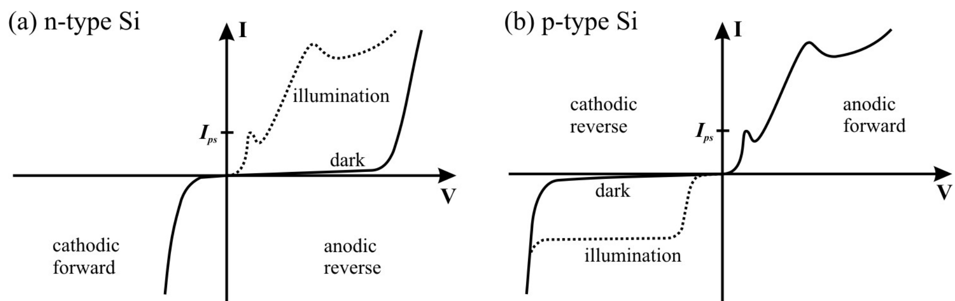

Fig. 4.3. Typical current-voltage (I-V) characteristics for (a) n-type and (b) p-type silicon under the assumption that current is not limited by charge supply from the electrode. The solid and dotted lines indicate the dark response and response under illumination, respectively. The first (lower) current peak I_{ps} corresponds to the formation of a surface anodic oxide formed during, and required for, electropolishing. The second (higher) current peak marks the beginning of stable current (potential) oscillations with the possible formation of a second type anodic oxide. After [168].

UNIVERSITAT ROVIRA I VIRGILI
PHOTONIC BANDGAP ANALYSIS AND FABRICATION OF MACROPOROUS SILICON BY ELECTROCHEMICAL ETCHING
Trifon Todorov Tirfonov
ISBN:978-84-693-0270-9/DL-T-1376-2010

A Schottky diode models the silicon-electrolyte interface accurately as long as the charge transfer is limited by the electrode rather than by the reaction or diffusion in the electrolyte. The I-V characteristic of the real silicon-electrolyte interface exhibits features unlike any solid-state device, as shown in Fig. 4.3. For simplicity, the I-V curves can be divided into four distinct regions depending on the sign of the applied potential and whether n- or p-type silicon is used.

In the cathodic regime for both n- and p-type material, silicon is normally stable: that is, it does not dissolve. The only important cathodic charge transfer reaction is the reduction of water with the subsequent liberation of hydrogen gas. This usually occurs only at significantly high cathodic overpotentials* for p-type silicon, i.e. when the electrical breakdown is reached (Fig. 4.3b). Under cathodic conditions the p-type silicon is reversely biased, so that the reverse current will be proportional to the light intensity. The n-type silicon under same conditions is forward-biased. That is why there are no apparent illumination effects in the I-V characteristic. The silicon dissolution occurs only under anodic polarization. Under anodic conditions we can see that I-V curves for p-type and strongly illuminated n-type silicon show the same behavior. The current increases exponentially with increasing potential from the open-circuit potential [188]. It breaks off from the exponential behavior at larger overpotentials, exhibiting a peak I_{ps} in the I-V curve. This characteristic current peak is assumed to divide the experimental conditions into two domains: porous silicon formation and electropolishing. At anodic potentials below the peak potential silicon is considered to dissolve through direct transfer of Si atoms into the electrolyte. It is this region where porous silicon formation occurs. Although the resulting pore structure can be quite complicated, the silicon remaining between the pores retains its original crystallinity [189], indicating that pore formation occurs by direct dissolution of the bulk material and not by some re-deposition or re-structuring process. At anodic potentials above the potential of the current peak the dissolution is thought to proceed through the formation of an intermediate oxide layer. The chemical reaction proceeds in two steps, first the electrode is anodically oxidized, and then the oxide is chemically dissolved in the

---

* The overpotential in electrochemistry is the difference between the equilibrium potential (often referred to as *open circuit potential* OCP) and the potential at an electrode at which an appreciable current flows. The open circuit potential is the potential of an electrode measured to some reference electrode when no current flows to or from it. It should be pointed out that the potential of a single electrode cannot be measured; only the difference between two electrodes is measurable. The standard reference electrode in electrochemistry is the *standard hydrogen electrode* (SHE) whose equilibrium potential is considered the zero point for measuring electrode potentials. The SHE is a platinum electrode with an electrolyte containing unit concentration of hydrogen ions and saturated with hydrogen gas at unit atmosphere pressure.

UNIVERSITAT ROVIRA I VIRGILI
PHOTONIC BANDGAP ANALYSIS AND FABRICATION OF MACROPOROUS SILICON BY ELECTROCHEMICAL ETCHING
Trifon Todorov Tirfonov
ISBN:978-84-693-6270-9/DL:T-1376-2010

electrolyte [60,160,188]. This finally results in electropolishing of the silicon surface; the surface retains relative smooth and planar morphology. Porous silicon formation is not found to occur at these potentials. In the exponential region (i.e. the region of PS formation) a visible hydrogen evolution is found to occur. The rate of hydrogen evolution substantially decreases as the potential approaches the current peak potential. Hydrogen evolution ceases above the current peak. Also, the valence of the dissolution reaction is found to vary from 2 in the exponential region to near 4 in the electropolishing region. A valence of two is due to chemical reactions responsible for hydrogen evolution.

Little is known about the second current peak in the I-V characteristics at high anodic potentials. Above this peak, the silicon/HF system undergoes current-voltage oscillations (not shown in Fig. 4.3). These oscillations are well defined with a specific current (potential) dependent frequency that increases monotonically with the potential until random noise eventually sets in. The oscillatory behavior has been reported by Lehmann [190], Stumper *et al.* [191], Föll [192], Eddowes [193]. Föll [192] speculated that the oscillatory mechanism is related to competing growth, dissolution and dielectric breakdown of the formed insulating anodic oxide. Under constant current conditions, oxide growth increases the formation potential until it exceeds the oxide breakdown field strength and short circuits the oxide formation mechanism. The oxide is then chemically etched by HF to a reasonable thickness while the short circuit disappears. The potential drops during this time, returning the system to its original state where the cycle repeats. This mechanism is not the only possible explanation which adequately describes the oscillatory electrochemical behavior. Eddowes [193] attributed the second current peak to a change in the stoichiometry or state of the anodic oxide being formed during electropolishing. If a change in stoichiometry of the oxide does occur at the second current peak, then the stable current-voltage oscillations can be explained by the formation of two oxides, “hard” and “soft”. The terms “hard” and “soft” are descriptive and refer to the slightly different etching and optical properties of the two oxides due to a change in either the chemical composition (SiO_x) or density. Oxide formation will occur only at the silicon/oxide interface, and oxide dissolution occurs only at the oxide/solution interface. The oxide thickness is determined solely by the relative rates between oxide formation and removal. Therefore, a time delay between oxide formation and its removal is present since the outer oxide is exposed to the HF solution. When a “hard” oxide reaches the oxide/solution interface, the oxide film etches slowly, increases the thickness and lowers the current. The potential across the silicon/oxide interface decreases because a greater fraction of the applied voltage drops across the

UNIVERSITAT ROVIRA I VIRGILI
PHOTONIC BANDGAP ANALYSIS AND FABRICATION OF MACROPOROUS SILICON BY ELECTROCHEMICAL ETCHING
Trifon Todorov Tirfonov
ISBN:978-84-693-0270-9/DL:T-1376-2010

thicker "hard" oxide layer. As the potential is lowered, then a "soft" faster-etching oxide layer is generated at the silicon/oxide interface. When this "soft" oxide reaches the oxide/solution interface, the oxide thickness decreases, the current correspondingly increases, the potential at silicon/oxide interface also increases giving rise to a "hard" oxide, and thus the cycle starts again. The oscillatory behavior of the Si/HF system has recently found another explanation in the scope of the developed current-burst theory [174, 194].

4.3. Electrochemical dissolution reaction

In the previous section, we have already mentioned that there are two regions in the current-voltage characteristic where anodic dissolution of silicon occurs. One is the formation of porous silicon which is associated with direct dissolution of silicon atoms and reaction valence of 2. The other region is the electropolishing which has been associated with an indirect dissolution of silicon through the formation of an anodic oxide film and reaction valence of 4. Figure 4.4 illustrates the reaction scheme proposed by Memming and Schwandt [160] for the anodic dissolution of silicon. The involved chemical reactions are given in more precise form by the Eq. 4.1 for path (1) (divalent dissolution) and Eq. 4.2 for path 2 (tetravalent dissolution). The subscript "ad" in these equations stands for adsorbed ions, while the symbols h^+ and e^- denote electronic hole and electron, respectively.

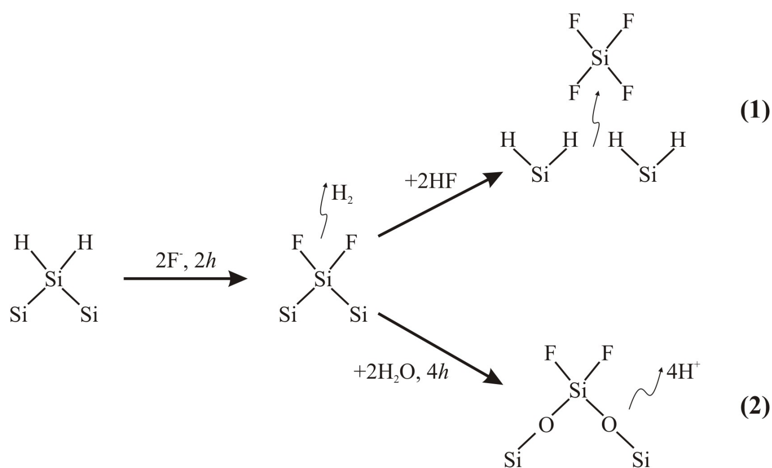

Fig. 4.4. Proposed dissolution mechanism of silicon electrodes in hydrofluoric acid (HF) solutions. The two different reaction paths illustrate the possible divalent (path 1) and tetravalent (path 2) chemical dissolution associated with two different experimental regimes: porous silicon formation and electropolishing, respectively. After [184].

UNIVERSITAT ROVIRA I VIRGILI
PHOTONIC BANDGAP ANALYSIS AND FABRICATION OF MACROPOROUS SILICON BY ELECTROCHEMICAL ETCHING
Trifon Todorov Tirfonov
ISBN:978-84-693-6270-9/DL:T-1376-2010

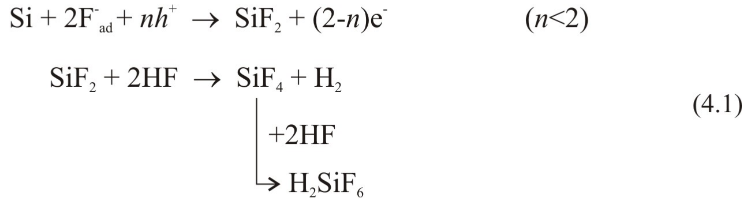

$$\begin{aligned} &Si + 2F^{-}_{ad} + nh^{+} \rightarrow SiF_2 + (2-n)e^{-} \qquad (n<2) \\ &SiF_2 + 2HF \rightarrow SiF_4 + H_2 \\ &SiF_4 \xrightarrow{+2HF} H_2SiF_6 \end{aligned} \tag{4.1}$$

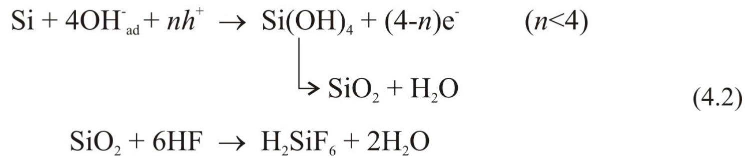

$$\begin{aligned} &Si + 4OH^{-}_{ad} + nh^{+} \rightarrow Si(OH)_4 + (4-n)e^{-} \qquad (n<4) \\ &Si(OH)_4 \rightarrow SiO_2 + H_2O \\ &SiO_2 + 6HF \rightarrow H_2SiF_6 + 2H_2O \end{aligned} \tag{4.2}$$

It is now commonly accepted that the surface of silicon immersed in the HF solution is terminated by hydrogen with or without active dissolution [195,196]. The dissolution of a surface silicon atom involves first the replacement of a surface hydrogen atom with a fluoride ion F^{-} (Fig. 4.4). The replacement of hydrogen (H) with F^{-} requires an electronic hole which results in a neutralized Si-F bonding. Because holes are only available at a certain anodic bias, the dissolution rate becomes almost zero at open circuit potential and the surface remains Si-H covered. If the Si-F bond is established due to the polarizing effect of the bonded F, another ion F^{-} can attack and bond under generation of an H_2 molecule and injection of one electron into the electrode. An important feature of this step is that no carriers from the solid are involved, and it therefore is a chemical reaction in nature. The silicon backbonds between the silicon atoms are weakened due to the large electronegatives of fluorine, so that the backbonds can be broken by reacting with HF (path 1). At this stage, the silicon atom is removed from the surface. The reaction product SiF_4 is unstable; it reacts with 2HF and becomes H_2SiF_6 (Eq. 4.1), which dissociates into SiF_6^{2-} in the solution. The remaining surface silicon atoms are again hydrogenated (path 1).

The backbonds of Si-SiF can also be broken by reacting with H_2O, resulting in Si-O-Si bonds, which are not stable in HF and the dissolution of which results in an indirect dissolution path (path 2) through the formation of anodic oxide [184]. One proposal for the electrochemistry of this oxidation/oxide-dissolution process is the reaction shown in Eq. 4.2 [188]. The first reaction in Eq. 4.2 leads to oxide formation. The oxide formation rate is in competition with its dissolution rate, governed by the second reaction in Eq. 4.2. Thus, while the reaction path 1 (see Fig. 4.4 and Eq. 4.1) results in the direct dissolution of silicon, path 2 results in an indirect dissolution. Note also the difference in the dissolution valence; it is 2 for reaction path 1 and 4 for path 2.

UNIVERSITAT ROVIRA I VIRGILI
PHOTONIC BANDGAP ANALYSIS AND FABRICATION OF MACROPOROUS SILICON BY ELECTROCHEMICAL ETCHING
Trifon Todorov Tirfonov
ISBN:978-84-693-0270-9/DL-T-1376-2010

At high potentials the coverage of the surface by Si-O-Si bonds increases, i.e. the oxide formation is enhanced and surpasses the oxide dissolution rate, resulting in electropolishing. At low potentials, the oxide formation is too low to compete with the direct dissolution of silicon, so that porous silicon formation occurs. Thus, the occurrence of different regions during the anodization of silicon in HF solutions is associated with the two competing reaction paths: direct dissolution of silicon and indirect dissolution through the formation and dissolution of a silicon oxide.

It should be noted that the exact chemistry of the silicon anodic dissolution is not yet completely understood. From all available data it appears that the reaction path 1 discussed above or some modifications of it, is the main chemistry behind the formation of porous silicon. However, while this simplified chemistry can explain the dissolution of silicon atoms, it does not account for the spatial selectivity of the reaction, which results in porous formation. In fact, the resulting pore morphology does depend on the type of silicon electrode, its doping level, process conditions, etc. and several models (some of which we have already reviewed in the previous sections) have been proposed to explain this rich and complex morphology of porous silicon. In the next section we shall describe in greater detail the phenomenological model developed by Lehmann and co-workers [60,125,187] to explain the formation of straight and regular macropores by light-assisted electrochemical etching of low doped n-type silicon. The model offers a set of empirical equations that allows us to make quantitative and measurable predictions for the resulting pore geometry. The experimental data is found to fit quite well with the predictions of the model.

4.4. The physics of macropore formation in n-type silicon

The basic assumption of the Lehmann's model is that the macropore formation in low doped n-type silicon involves two rate-determining processes. The exact dissolution mechanism and hence the surface morphology depend critically on whether the diffusion of reactants in the electrolyte or charge supply from the electrode is the rate-limiting step. For example, at current densities J[*] higher than the critical current value J_{ps} the dissolution reaction is limited by the supply of reagents through diffusion in the electrolyte. Then, a surface charge of excessive holes builds up. Convex parts of the silicon electrode are more exposed to the electrolyte and will therefore dissolve

[*] At this point forward we shall refer to the current going through the n-Si/electrolyte system by the quantity *current density* measured in A/cm^2, which is the ratio between the current in A and the contact area in cm^2.

UNIVERSITAT ROVIRA I VIRGILI
PHOTONIC BANDGAP ANALYSIS AND FABRICATION OF MACROPOROUS SILICON BY ELECTROCHEMICAL ETCHING
Trifon Todorov Tirfonov
ISBN:978-84-693-6270-9/DL:T-1376-2010

faster, which results in smoothening of the electrode surface (electropolishing).

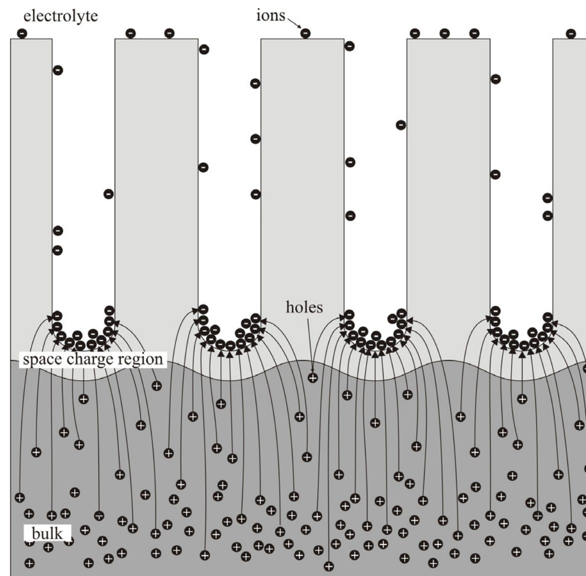

Fig. 4.5. Schematic illustration of the macropore formation in low doped n-type Si. The backside illumination generates electron-hole pairs in the bulk of the semiconductor. The holes diffuse through the wafer and reach the silicon/electrolyte interface where they are consumed in the dissolution reaction. The holes do not penetrate the area between the pores; they are focused by the space charge region mainly at the pore tips. Thus, the macropore walls become passivated against dissolution and pores grow in vertical direction. After [60].

At current densities below the critical value J_{ps} the reaction of the localized Si dissolution is limited by the hole supply from the electrode. Every hole reaching the surface will be immediately consumed in the dissolution reaction. As the electric field lines are focused at surface depressions, the dissolution is enhanced there, leading to a pore formation. The pore formation mechanism is schematically illustrated in Fig. 4.5. Since the system n-Si/electrolyte is reversely biased, a space charge region (SCR) is formed in the silicon electrode by the ionized doping impurities. Any bending of this SCR by deviations in the silicon surface would focus some of the holes, generated by light illumination in the bulk of silicon electrode (backside illumination). Surface defects therefore act as seeding points for macropore growth. Therefore, by pre-patterning the silicon surface with defect sides it is possible to determine where macropores will form and thus, to obtain strongly ordered pore arrays. As the etch process progresses, the electric field still concentrates at the pore tips. The electronic

UNIVERSITAT ROVIRA I VIRGILI
PHOTONIC BANDGAP ANALYSIS AND FABRICATION OF MACROPOROUS SILICON BY ELECTROCHEMICAL ETCHING
Trifon Todorov Tirfonov
ISBN:978-84-693-0270-9/DL-T-1376-2010

holes will be collected by the tips and will promote dissolution there. The pore walls become passivated against dissolution because of the hole depletion in the SCR between the pores. Only the pore tips are electrochemically active.

The fundamental assumption in the Lehmann's model is that the current density at the pore tips J_{tip} equals for stable pore growth the critical value J_{ps}, so that the ionic transfer from the electrolyte and charge supply from the electrode are in steady-state condition at the tips of the pores. Stable pore growth is achieved when the current density is limited by hole generation and not by the applied bias, which for higher potentials can yield electrical breakdown. Thus, the mechanism ensuring the equality of propagation rates and remarkable homogeneity in depth for an array of pores could be explained as follows. The growth rate ν of the pores can be calculated through the expression [125]

$$\nu = \frac{J_{tip}}{nqN_{Si}} \tag{4.3}$$

where n is the dissolution valence (number of charge carriers per dissolved silicon atom), q is the elementary charge (1.602×10^{-19} C), and N_{Si} is the atomic density of silicon (5×10^{22} cm^{-3}). If one pore is somewhat longer than the other pores in the array, it becomes more efficient in collecting the holes. Thus, it will hold current density J_{tip} somewhat higher than the critical value J_{ps}. Slight increase of the current density at values close to J_{ps} produces a large increase of the dissolution valence n. The dissolution valence n exhibits a step-wise increase at $J=J_{ps}$ (see Fig. 5 from Ref. 125). Since the growth rate ν is proportional to J_{tip}/n, it will be reduced for this particular pore, allowing to the others to overtake it.

Based on the assumption $J_{tip}=J_{ps}$, Lehmann proposed a simple formula (Lehmann's formula) that relates the diameter d of the pores with the applied current density J. All charge transfer occurs via the pore tips, and the tip current density is J_{ps}. Therefore, the total etching current equals the sum of the cross-sectional areas of all pores A_{pores} multiplied by J_{ps}. The total etching current divided by the initial surface area A (the contact area between the silicon electrode and the electrolyte) gives the overall current density J:

$$J_{ps} \cdot A_{pores} = A \cdot J \tag{4.4}$$

If stable macropores form and grow, all current must flow through the macropores and the current density in a pore J_{ps} can be expressed as:

UNIVERSITAT ROVIRA I VIRGILI
PHOTONIC BANDGAP ANALYSIS AND FABRICATION OF MACROPOROUS SILICON BY ELECTROCHEMICAL ETCHING
Trifon Todorov Tirfonov
ISBN:978-84-693-6270-9/DL:T-1376-2010

$$J_{ps} = J \frac{A_{cell}}{A_{pore}} \tag{4.5}$$

where A_{pore} is the cross-sectional area of the pore, and A_{cell} is the cross-sectional area of a unit cell of the pore lattice. Note that the relation A_{pore}/A_{cell} determines the porosity p of the structure. If the initial pattern is a square lattice with lattice constant a, the relation (4.5) can be written as

$$\frac{J}{J_{ps}} = \frac{\pi}{4}\left(\frac{d}{a}\right)^2 = p \tag{4.6}$$

assuming that the cross-sectional shape of the pores is circular. In fact, the macropores may have all shapes between a circle and a square. Experiments have proven that the above relation is still applicable. It holds also if the two areas A_{pore} and A_{cell} are interpreted as the averages of many individual pores, which could be the case of "random" pores obtained without pre-structuring of the wafer or non-orthogonal lattices [197].

An important parameter in the above relations is the critical current density J_{ps}, which divides the current-voltage characteristic into two experimental regions: pore formation and electropolishing. We need to known its value beforehand in order to calculate the current density that must be applied to obtain a desired pore pattern. The J_{ps} depends on the HF concentration c and absolute temperature T. Moreover, the J_{ps} depends also on crystal direction; it is largest for silicon electrodes of (100) orientation, independently of the electrolyte concentration used. This indicates that the dissolution process has an anisotropic component. Lehmann [125,187] gives the following empirically determined relationship, which holds for aqueous HF solutions:

$$J_{ps} = C_{ps}\, c^{1.5} \exp\left(-\frac{E_a}{kT}\right) \tag{4.7}$$

where the constant C_{ps}=3300 A/cm^2 (wt.% HF)$^{-1.5}$, c is the HF concentration in wt.%, the activation energy E_a=0.345 eV, k is the Boltzmann constant (8.618×10^{-5} eV/K) and T is the absolute temperature in K. The critical current density J_{ps} is then obtained in A/cm^2. The growth rate of the macropores can be calculated from Eq. 4.3 assuming an average dissolution valence of n=2.6. These values are found to fit well with the experimental results and can be used to model the macropore formation.

The diameter (or size) of the pores is mainly dependent on the applied current J, as shown in Fig. 4.6. By adjusting the applied potential and the backside illumination intensity every point of the hatched region can be reached. Note that the

ISBN:978-84-693-0270-9/DL-T-1376-2010

electropolishing is never reached even though the applied potential is greater than the potential V_{ps} corresponding to critical current peak. This is because the illumination intensity is still low to generate enough minority carriers and the reaction is limited by charge supply from the electrode and not by the ionic transfer from the electrolyte. The current-voltage characteristic for this regime is similar to that of illuminated Schottky diode (Fig. 4.2) and is shown by dotted lines in Fig. 4.6. For certain applied potentials the overall current saturates because all photogenerated holes are collected by the pores and this saturation occurs always below the critical current peak J_{ps}. Stable formation of well-defined macropores is found solely for this saturation regime. This is what we have meant by noticing that stable macropore formation only occurs when the current is limited by the hole generation and not by the applied bias.

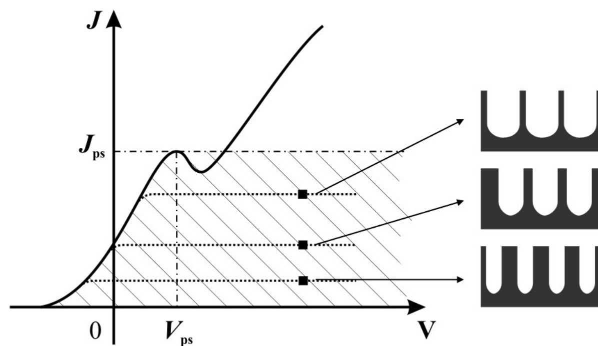

Fig. 4.6. Current-voltage characteristic of illuminated n-type silicon electrode in aqueous HF solution. The solid line represents the I-V curve of strongly illuminated electrode. Stable pore growth is observed for current densities within the hatched area and for applied potentials above the potential V_{ps} corresponding to the critical current peak. The dependence of pore diameter on the applied current density J is shown for three different values of J. After [198].

The Lehmann's formula is only applicable for macropore formation in n-type silicon with backside illumination and when the applied potentials is significantly larger than V_{ps}, but it is not valid for macropores formed in p-type silicon, especially when organic (like dimethylformamide (DMF), dimethylsulfoxide (DMSO), etc. [199]) and not aqueous solvents are used, because the relevant I-V characteristics do not contain a critical current peak J_{ps}. Also, the validity of Lehmann's formula is severely limited by the substrate resistivity (or doping level). A basic premise of the Lehmann's model was that the SCR must be bent around the pore tip, but not penetrate between the pores. This means that stable pore growth can be expected if the space charge regions between the pores overlap, so that $a \approx 2L_{SCR}$ where L_{SCR} is the width of the space charge region. The

UNIVERSITAT ROVIRA I VIRGILI
PHOTONIC BANDGAP ANALYSIS AND FABRICATION OF MACROPOROUS SILICON BY
ELECTROCHEMICAL ETCHING
Trifon Todorov Tirfonov
ISBN:978-84-693-6270-9/DL:T-1376-2010

pore diameter d should also match the L_{SCR}. This is illustrated schematically in Fig. 4.7. Stable pore growth is achieved for the case (a), i.e. L_{SCR} matched to d and a. If a is too small (Fig. 4.7b) some pores cease to grow (dying of the pores), and if a is too large (Fig. 4.7c), the pore surface becomes rough or some pores divide into two pores (branching of the pores). However, it has been shown [200,201] that stable pore growth is still achieved at distances larger than $2L_{SCR}$, for which the carriers can easily penetrate the area between the pores (Fig. 4.7c). This is a clear indication that something else besides the diversion of the carriers to the pore tips by the SCR must passivate the pore walls against further dissolution. Contrariwise, it is not clear from the Lehmann's model alone, why it is not possible to make thin pores at a relatively large spacing (Fig. 4.7d) even though $a \approx 2L_{SCR}$. A rule of thumb has been proposed for selecting an appropriate substrate resistivity: having the desired pore density (in μm^{-2}), the appropriate doping level (in cm^{-3}) is found as a product of the pore density and the number 10^{16} [187].

Fig. 4.7. Possible effects of the mismatch between space charge region (SCR) width L_{SCR} and the pore pattern on the stable macropore growth in n-type silicon. (a) L_{SCR} matched to pore spacing a and diameter d; (b) $a \ll L_{SCR}$ – some pores can cease to grow; (c) $a \gg L_{SCR}$ – branching of pores can occur; (d) $a \approx L_{SCR}$, $d \ll L_{SCR}$ – stable pore growth not possible (strong branching or spiking of the pore walls). After [183].

Lehmann's model also does not take into consideration the possible change of

UNIVERSITAT ROVIRA I VIRGILI
PHOTONIC BANDGAP ANALYSIS AND FABRICATION OF MACROPOROUS SILICON BY ELECTROCHEMICAL ETCHING
Trifon Todorov Tirfonov
ISBN:978-84-693-0270-9/DL-T: 1376-2010

the dissolution reaction at J_{ps} from direct dissolution of silicon atoms to that employing the formation of an anodic oxide film. This transition seems to be very probable, especially in the case of aqueous electrolytes, and allows a reasonable explanation of the pore propagation within some of the models discussed in Section 4.1.

4.5. Experimental

Having outlined the theoretical background of the porous silicon formation and electrochemical etching process, we shall now turn to describe in greater detail different experimental aspects of the etching process, which are important for the realization and the success of any real experiment. The electrochemical etching apparatus we have developed and used in our investigation was elaborated in collaboration with the Group for Semiconductor Devices at Technical University of Catalonia, Barcelona. The sample preparation and all experiments were realized using the clean room facilities of the Department of Electronics, Technical University of Catalonia.

4.5.1. Set-up

The experimental set-up is schematically depicted in Fig. 4.8. The wafer (or the sample) as a working electrode, together with counter and reference electrodes, is incorporated in a custom-built electrochemical etching cell. The electrochemical cell is a part of specialized in-house constructed etching rig that also comprises a computer controlled backside illumination and a heat exchanger with thermostat for temperature control. The pre-structured front side of the wafer (where macropores will grow) is in contact to the electrolyte, while the wafer backside is illuminated by a 100 W halogen lamp. To achieve a stable pore grow the minority carriers should be generated deep within the bulk or near the backside surface of the wafer. The electronic holes must diffuse through the wafer in order to be focused by the SCR at the tips of the pores. This imposes special restrictions to the spectral characteristics of the lamp used for the backside illumination. Light of wavelengths greater than 900 μm (of course, up to 1.1 μm) may provoke hole generation near the front side surface of silicon wafer or in the area between the pores, which would cause a dissolution of the pore walls. (For simulations of hole generation rate as a function of the wavelength and the wafer thickness see Ref. [187], p. 213). Therefore, the infrared emission of the used halogen lamp must be blocked, which is achieved by an IR cut-off filter (SIR dielectric heat reflecting mirror, Präzisions Glas & Optik GmbH). The backside illumination intensity

UNIVERSITAT ROVIRA I VIRGILI
PHOTONIC BANDGAP ANALYSIS AND FABRICATION OF MACROPOROUS SILICON BY
ELECTROCHEMICAL ETCHING
Trifon Todorov Tirfonov
ISBN:978-84-693-0270-9/DL:T-1376-2010

is regulated via a computer-controlled power supply (HP E3631A, Agilent Technology). A digital multimeter (HP 34401A, Agilent Technology) connected to a computer is used to measure and record the total current going through the system. The wafer (working electrode) is positively biased through an AMMT (Advanced Micromachining Tools GmbH) MEMS potentiostat, which is also controlled by a computer. A cryostat (Heto, Denmark) was used to establish and maintain a desired constant temperature of the electrolyte during the etching. The electrolyte is continuously stirred by a simple Teflon-covered magnetic stirrer. Some nice photographs of the etching apparatus in operation are given in Appendix A.

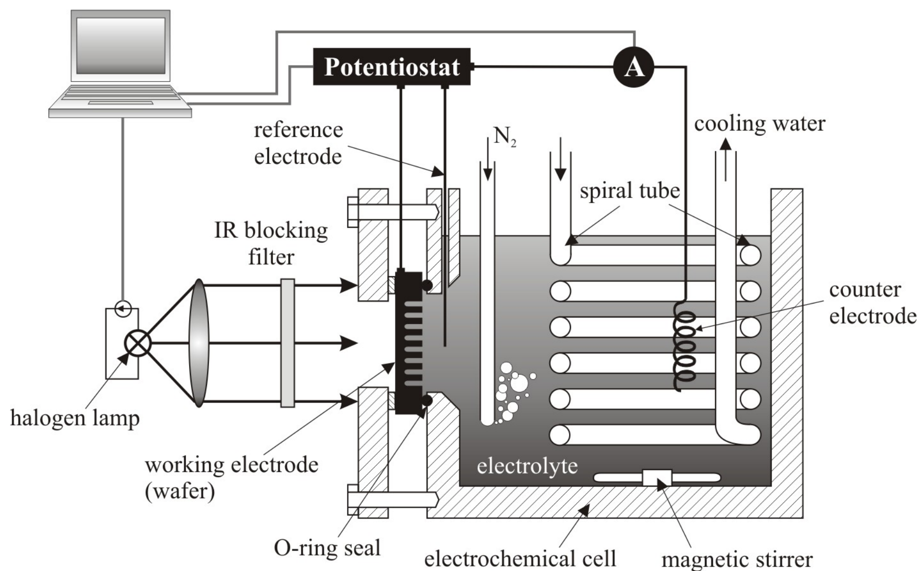

Fig. 4.8. Schematic illustration of the developed electrochemical etching set-up. The wafer is mounted onto an electrochemical etching cell with the pre-structured front side in contact to the electrolyte. The etching cell is Teflon-made and uses three-electrode configuration: working (wafer), platinum reference and counter electrodes. The wafer is mechanically pressed by screws against an O-ring (Viton) seal in order to seal the cell. The wafer backside is illuminated through a 100 W computer-regulated halogen lamp, coupled to an IR cut-off filter.

- Electrochemical cell

The electrochemical cell is the main part of the experimental set-up. Our cell was made of polytetrafluoroethylene (PTFE or Teflon), because it is resistant to HF even at high concentrations, e.g. 50 wt.%. The total amount of liquid that can be contained is about 800 ml, which is well enough to ensure a constant HF concentration

UNIVERSITAT ROVIRA I VIRGILI
PHOTONIC BANDGAP ANALYSIS AND FABRICATION OF MACROPOROUS SILICON BY ELECTROCHEMICAL ETCHING
Trifon Todorov Tirfonov
ISBN:978-84-693-0270-9/DL-T-1376-2010

during the etching process. The cell was prepared to support 2-inch wafers or smaller samples with dimensions of about 10×10 mm. In order to seal the cell, the wafer is mechanically pressed by screws against a vinylidene fluoride-hexafluoropropylene (Viton®) O-ring (Lidering, Spain). The O-ring seal defines the sample area which will be exposed to the electrolyte. In our case, the total area in contact for 2-inch wafers was about 12.44 cm^2, while for the smaller samples it was 0.52 cm^2. It should be noted that near the O-ring the current flow is not normal to the surface and the current density is slightly enhanced there [202]. This means that stable macropore growth (as will be shown in the next chapter) cannot be achieved over the whole exposed area. We used a standard three-electrode configuration for the electrochemical cell: working (the wafer), reference and counter electrodes. The reference and counter electrodes are made of platinum Pt (Aldrich, 99.9%) because it is chemically inert in HF. The counter electrode was coiled in order to increase its surface immersed in the electrolyte, while the reference electrode was a simple wire positioned close (about 3 mm) to the wafer. The reference electrode is needed to discount the voltage drop across the electrolyte and the voltage offset introduced by the counter electrode, because these are of no importance in the etching process.

The present design of the electrochemical cell however has a big disadvantage. We have already discussed that the porous silicon formation proceeds with a hydrogen gas evolution. Since the hydrogenated silicon surface is strongly hydrophobic, the H_2 bubbles stick to the wafer surface and prevent the fresh electrolyte from reaching the pores. This bubble sticking is a source of significant current noise and generally results in worsen spatial homogeneity of the fabricated macropore arrays. In our case, the wafer is laterally mounted onto the cell. The electrolyte can therefore access the wafer through a circular window drilled in one of the vertical walls of the cell, as shown in Fig. 4.8. Depending on the cell wall thickness this window resembles a short horizontal tube, which additionally obstructs the free escape of H_2 bubbles. The bubbles therefore accumulate near the top of the wafer (in the area where is the opening for the reference electrode) and hide some considerable part of the wafer surface. In the case of small samples, the bubbles can even fully hinder the sample area, which is exposed to the electrolyte. This problem was indeed a real source of frustration because many carefully prepared experiments have failed due to the bubble sticking. It was partially circumvented by enhanced stirring of the solution and by beveling the inner edge of the drilled window, as shown in Fig. 4.8. Probably, the most suitable design is the one based on pumping of the electrolyte through the cell. The circulation of the electrolyte reduces concentration gradients at the electrode surfaces, easily removes the bubbles

UNIVERSITAT ROVIRA I VIRGILI
PHOTONIC BANDGAP ANALYSIS AND FABRICATION OF MACROPOROUS SILICON BY ELECTROCHEMICAL ETCHING
Trifon Todorov Tirfonov
ISBN:978-84-693-0270-9/DL:T-1376-2010

and allows for better temperature control [187]. However, this cell design is much more complex and expensive, and also requires a long elaboration time because many safety aspects should be taken into account before handling such extremely hazardous and corrosive compound like the hydrofluoric acid.

- Electrolyte

Unless otherwise noted, the electrolyte was prepared by diluting 50 wt.% HF (Electronic grade, Honeywell Specialty Chemicals Seelze GmbH) in de-ionized (17-18 MΩ) water up to a desired concentration. Some of the experiments were performed with the addition of surfactants[*] to the electrolyte. A surfactant is usually used as a wetting agent. It reduces the surface tension and thus, the sticking probability of the hydrogen bubbles. Two surfactants have been used in our study: a nonionic surfactant, i.e. TritonX-100® (polyethylene glycol tert-octylphenyl ether, Fluka Chemie AG) and an anionic one, i.e. sodium dodecyl sulfate (SDS) (Panreac Química SA). The electrochemical etching was found to be affected not only by the type, but also by the amount of surfactants added to the electrolyte [203,204]. The effect of surfactants on macroporous silicon formation will be discussed in the next chapter.

Part of the experiments was conducted with bubbling of the electrolyte by nitrogen (N_2). There are various factors that can influence the stable macropore growth and the geometry of the resulting pore structure. One of these factors is the small reverse current at the silicon-electrolyte interface without illumination (dark current), which can be understood as caused by carrier generation in the depletion region or at defects (Fig. 4.2a). Note that we are not speaking about the current caused by electrical breakdown, shown with an abrupt line in Fig. 4.2a. Even small, for long anodization times this dark current cannot be neglected. It increases with increasing the total pore surface during the etching and is usually responsible for obtaining somewhat conical pores with decreasing diameters in depth [206]. Furthermore, the dark current density is found to depend on temperature, added surfactants and on the concentration of oxygen

[*] Surfactants are substances whose molecules bear both a polar and an apolar part. They are also called amphiphiles. An amphiphile is a chemical substance that possesses some affinity for both polar and nonpolar solvents. These affinities are referred to as hydrophilic and hydrophobic respectively since the polar solvents are in most cases aqueous solutions and the nonpolar phases are organic "oils". The surfactants are mainly classified according to their behavior in aqueous solutions, as ionic or nonionic surfactants. The ionic surfactants are those which dissociate in water to yield a charged surfactant ion. The charge of the surfactant ion can be positive or negative, in which case the surfactant is called to be cationic or anionic, respectively. Those surfactants that are not dissociated in water are labeled as nonionic surfactants [205].

UNIVERSITAT ROVIRA I VIRGILI
PHOTONIC BANDGAP ANALYSIS AND FABRICATION OF MACROPOROUS SILICON BY ELECTROCHEMICAL ETCHING
Trifon Todorov Tirfonov
ISBN:978-84-693-0270-9/DL:T-1376-2010

diluted in the electrolyte [207]. The nitrogen bubbling of the electrolyte during the etch helps to reduce the dark current density and to obtain straight pores with almost constant pore diameter in depth. This effect will also be discussed in the next chapter of the present thesis.

- Software

Besides the dark current density, there are other effects that should be taken into account in order to obtain macropore arrays with good structural characteristics. For example, with increasing pore depth the distance between the pore tips and hole generation area decreases. The pore tips become then more effective in collecting the photo-generated holes which leads to an increase in the total current, depending on the minority carrier diffusion length of the sample. If the backside illumination is kept constant, the increasing in the current will lead to an increase in the pore diameters in depth [197]. Another effect is related to a decrease of the HF concentration at the pore tips due to diffusional limitations in the narrower and deeper pores [208]. The decrease of the HF concentration leads to a decrease in the critical current density J_{ps} and in the etch rate with increasing pore depth. All these factors imply that a precise control of the etching parameters, at least of the etching current, is needed to achieve a stable macropore growth. We have developed a program, running on a LabVIEW (National Instruments) environment to control the current during the etch by adjusting the backside illumination. The main feature of the program is that it allows for an automated control of the etching process so that it can be left unattended. This becomes a very important aspect when deep pores are desired, because a long anodization time (5-6 hours) is usually required. The program needs the desired current profile and the total duration of the process to be specified as input parameters. Current profile can be generated by each of the commercially available software for processing and visualizing graphical data (like MATLAB, Microcal Origin, Microsoft Excel), or even can be manually written by using a simple text editor. This offers the possibility to easily introduce current variations which will result in macropore arrays with modulated pore diameter in depth [209]. Furthermore, different current profiles can be applied without changing the program. When the current profile is specified, the program proceeds with measuring the total current going through the system and with adjusting (if needed) the intensity of backside illumination to match the input current profile at each iteration step. The measured current is also recorded each 0.5 sec so that it can be further analyzed and compared to the resulting macropore structure.

UNIVERSITAT ROVIRA I VIRGILI
PHOTONIC BANDGAP ANALYSIS AND FABRICATION OF MACROPOROUS SILICON BY ELECTROCHEMICAL ETCHING
Trifon Todorov Tirfonov
ISBN:978-84-693-0270-9/DL:T-1376-2010

4.5.2. Sample preparation

If a flat, polished silicon wafer is anodized in HF electrolyte the pores will grow randomly across the sample surface, with average pore diameters and spacing depending on the applied current and substrate resistivity. To get ordered pores we need first to prepare the sample, marking the sites where pores should grow. We have adopted the sample preparation procedure proposed by Lehmann [60,125] in his first works, although some modifications were made. The simplified process sequence is given in Fig. 4.9. First, the wafers were oxidized in order to grow a thin oxide film [Fig. 4.9a]. The oxide film only serves as a mask and as a protective layer in the subsequent anisotropic etch of silicon in alkaline (e.g., KOH) or tetramethyl ammonium hydroxide (TMAH) solutions. The oxidation step cannot be avoided because the normal resists used in the lithography are easily dissolved by TMAH. Next, a standard photolithography was used to pattern the oxide layer [Fig. 4.9b]. The lithography step determines the arrangement and period of the resulting pore lattice. It is clear, that if we want to downscale the lattice period below micrometer we should use a high resolution lithography. The lithographic pattern was then transferred into the oxide layer by etching the silicon oxide in buffered hydrofluoric acid (BHF) [Fig. 4.9c]. Next, the silicon wafers were immersed in a TMAH solution to make the defect sites onto the wafer surface [Fig. 4.9d]. The TMAH etch is an anisotropic process; the resulting structure is a lattice of pyramidal notches (as shown in [Fig. 4.9h]) that will serve as seeds for the pore growth. It should be noted that the dimensions of these inverted pyramids do not determine the diameter of the pores. The pore diameter is mainly dependent on the applied etching current and to some extent on the wafer resistivity. Neither the pore shape is affected by the pyramids. The pyramids determine only the positions of the pores and thus, the lattice constant of the resulting pore structure. After the TMAH etch, the oxide layer is no longer needed. It was removed by a short HF 5% dip.

The second main step of the sample preparation is the formation of an ohmic contact on the wafer backside. At the first stage of our work, the backside ohmic contact was prepared by an aluminum sputtering deposition [Fig. 4.6e], photolithography patterning [Fig. 4.9f] and subsequent etching [Fig. 4.9g] of the aluminum to form a mesh electrode. The mesh is needed to achieve a uniform electric field distribution across the entire wafer surface (the current must flow perpendicularly to the surface) and at same time to open the wafer backside for illuminating. Some illumination, however, was reflected by the mesh electrode, which resulted in an unstable pore

ISBN:978-84-693-0270-9/DL-T-1376-2010

growth just behind the aluminum lines. For this reason, we replaced the aluminum mesh electrode by an *Indium Tin Oxide* (ITO) film, deposited by sputtering [Fig. 4.9i]. The ITO film is transparent to the light and has good conductance properties. Moreover, the use of ITO electrode simplified considerably the sample preparation because the lithography and etching steps to form the aluminum mesh were no longer necessary. In what follows we shall give some concrete details about the optimized process parameters for the sample preparation.

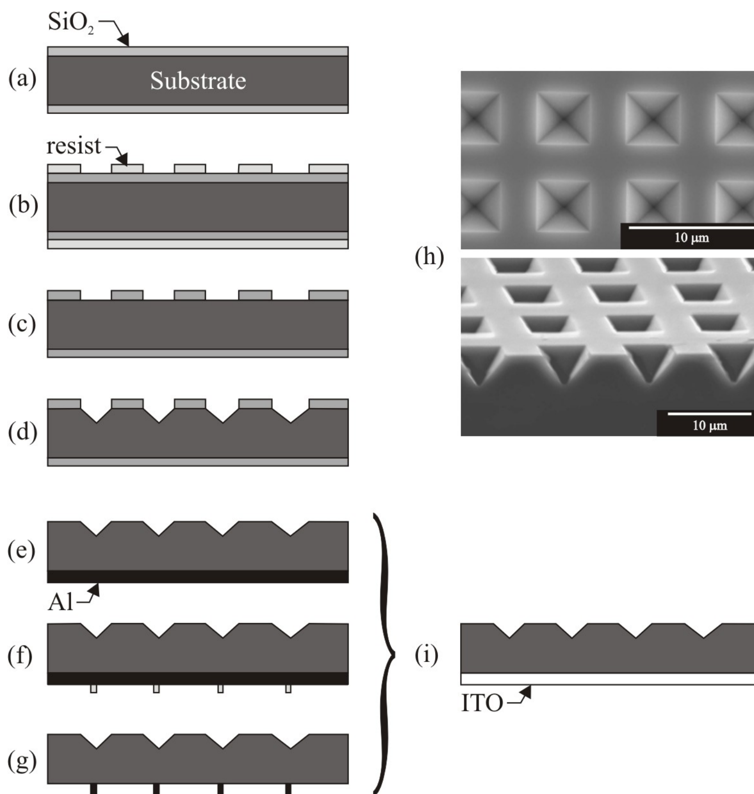

Fig. 4.9. Main process sequence for sample preparation. (a) wafer oxidation; (b) photolithography; (c) window opening in the oxide film by BHF etch; (d) TMAH etch of the silicon to form pyramidal notches; (e) aluminum sputtering; (f) and (g) photolithography and patterning of the aluminum film to form a mesh electrode; (h) SEM micrographs of the formed pyramidal notches which will serve as nucleation centers for the macropore growth; (i) the steps (e), (f) and (g) were later replaced by an ITO sputtering deposition.

UNIVERSITAT ROVIRA I VIRGILI
PHOTONIC BANDGAP ANALYSIS AND FABRICATION OF MACROPOROUS SILICON BY ELECTROCHEMICAL ETCHING
Trifon Todorov Tirfonov
ISBN:978-84-693-0270-9/DL:T-1376-2010

- Starting material

The starting material was n-type (phosphorus doped) 2-inch Si wafers with orientation (100) and resistivity 1-10 Ωcm. The nominal resistance provided by the suppliers in some cases was not accurate enough. For these reason, the actual resistance of each wafer was measured with a four-point probe. Both CZ (Czochralski grown) and FZ (Float zone) wafers were used. It is worth mentioning that the use of FZ wafers is preferred, because of the higher minority carrier lifetime in these wafers. The wafer thickness was between 280 and 300 μm.

- Oxidation

The wafers were oxidized in dry O_2 at 1100°C for 20-25 min. The thickness of the obtained oxide layer was about 600-700 Å. This thickness was found to be more than sufficient to protect the silicon in the TMAH etch because of the smaller etching rate of the TMAH to SiO_2 compared to that of KOH (potassium hydroxide) [210]. Thicker oxide layers can also be used but two factors should be taken into account. First, the duration and the temperature of the oxidation process were found to affect in some way the formation of stable macropores. CZ wafers oxidized for more than 30 min presented a problem when were electrochemically etched. The problem consisted in that the etching current required for stable pore growth could not be reached at all, even though the 100 W halogen lamp was replaced by 500 W one. The most probable explanation of this effect is that the oxidation process has killed the minority carrier lifetime, so no holes could diffuse through the whole wafer thickness to reach the front side. Second, thicker oxide layers somehow harmed the lithography and the subsequent BHF oxide etching, resulting in spatially inhomogeneous pyramidal patterns. Thinner oxide layers (of about 200-300 Å) should be also carefully processed mainly in the BHF etch step, used for window opening in the oxide film. Our BHF etching mixture (Ammonium fluoride etching mixture HF (6 %)+NH_4F (35 %), Honeywell Specialty Chemicals Seelze GmbH) has an etching rate of about 680 Å/min. Therefore, a few seconds are needed to etch the oxide which can result in an over-etching if very thin oxide layers are used.

- Photolithography

The lithography is the most critical step in the sample preparation, since any defect in the lithographic pattern will be reflected and moreover, will be extended over one or two lattice periods in the resulting pore pattern. We followed the standard

UNIVERSITAT ROVIRA I VIRGILI
PHOTONIC BANDGAP ANALYSIS AND FABRICATION OF MACROPOROUS SILICON BY ELECTROCHEMICAL ETCHING
Trifon Todorov Tirfonov
ISBN:978-84-693-0270-9/DL:T-1376-2010

procedure for making a photolithography, which consisted of resist spinning, soft baking, exposition, developing and hard baking of the resist. A positive photoresist HPR504 with a developer HPRD (Arch Chemicals Inc.), and a Karl Suss MA4 mask aligner were used for the photolithography. Two masks were designed and used at different stages of our work. The mask design and elaboration were possible thanks to the collaboration with the Nanophotonics Group, Institute of Photonic Sciences (ICFO). Both masks provide patterns with square, triangular and honeycomb arrangements of the holes with lattice constant ranging from 4 to 15 μm. Linear and point defects were introduced in the second mask, as shown in Fig. 4.10. Detailed specification of the two masks employed for the macroporous silicon formation is given in Appendix B.

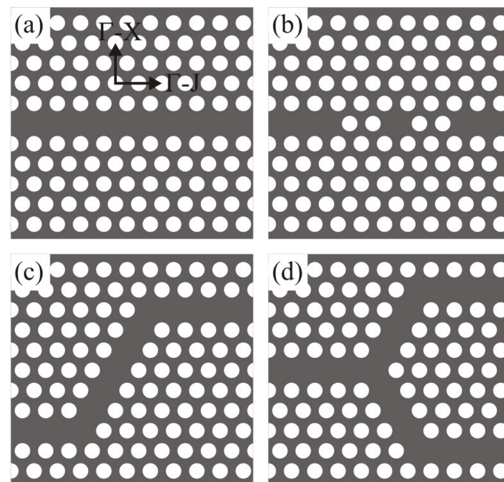

Fig. 4.10. Defects of different types included in the photolithography mask employed for macroporous silicon fabrication. (a) line defects (waveguides); (b) point defects (resonant microcavities); (c) branches and (d) Y-junctions. The directions corresponding to the edges of the irreducible Brillouin zone are also shown.

- TMAH etching of the silicon

The etching of silicon for making the nucleation centers needed for ordered macropore growth was performed in 8% TMAH solutions at 80°C temperature for 7-9 min. An important factor should be taken into account when performing the TMAH etching. The inverted pyramids after etching should have well-formed tips (vertex). If they appear like a truncated pyramid, the macropore growth will then start at the four vertices, experiencing some initial nucleation phase followed by a redistribution phase [201], and will finally give rise to a macropore with rough walls and somewhat complex

UNIVERSITAT ROVIRA I VIRGILI
PHOTONIC BANDGAP ANALYSIS AND FABRICATION OF MACROPOROUS SILICON BY ELECTROCHEMICAL ETCHING
Trifon Todorov Tirfonov
ISBN:978-84-693-0270-9/DL:T-1376-2010

shape, which is formed by joining of four or more individual pores. Although it has been shown that stable macropore formation can be achieved after forming the nucleation pits by an isotropic or dry etching of the silicon or even without nucleation pits [211], our experience showed that macropore arrays with better structural characteristics were only obtained when the initial nucleation centers had been well defined. The time for the TMAH etching to form non-truncated pyramids will depend on the size of the holes in the lithographic pattern. The nine minutes used for the TMAH etch were more than sufficient to obtain non-truncated pyramids with size of the square base of about 5×5 μm. This time was found to have no destructive effect on the finest hole regions of the lithographic pattern, i.e. 2×2 μm (see Appendix B).

- Sputtering

The aluminum and the ITO layers for the backside electrode were deposited by means of an rf-magnetron sputtering system (Edwards ESM100). The parameters used for aluminum sputtering deposition were as follows. The used target material was Al/1%-Si with a diameter of 100 mm and thickness of 3.18 mm. The target-substrate distance was fixed at 70 mm. The sputtering atmosphere consisted of Ar gas at pressure 0.5 Pa (5×10^{-3} mbar). The rf-forward input power was maintained at 200 W with zero reflected power. The deposition was performed for 30 min at room temperature. Under these conditions the thickness of the sputtered Al film was in-between 0.6 and 0.65 μm (measured by a Sloan DEKTAK 3030 profilometer). After patterning, the Al mesh electrode was annealed at 400°C in forming gas (N_2/H_2) atmosphere for 20 min.

The ITO sputtering was performed under the following conditions: ITO 99.99% purity target with a diameter 100 mm, 50 mm target-substrate distance, Ar plasma with pressure 5×10^{-3} mbar, 50 W forward power, 12 min deposition time at room temperature. The thickness and the refractive index of the obtained ITO films were characterized by a TELSTAR ellipsometer. Under these conditions the ITO thickness was in the range 150-170 nm and the ITO refractive index ranged in between 1.97-1.99. The resistance of the ITO films was in the order of $3\text{-}5\times10^{-4}$ Ωcm (measured by a four-point probe).

Other processes involved in the sample preparation, including the initial and intermediate wafer cleaning procedures, were performed under standard conditions.

UNIVERSITAT ROVIRA I VIRGILI
PHOTONIC BANDGAP ANALYSIS AND FABRICATION OF MACROPOROUS SILICON BY ELECTROCHEMICAL ETCHING
Trifon Todorov Tirfonov
ISBN:978-84-693-6270-9/DL-T:1376-2010

ISBN:978-84-693-6270-9/DL:T-1376-2010

Chapter 5

Fabrication of 2D photonic crystals based on macroporous silicon. Technological aspects

This chapter deals with the fabrication of macroporous silicon structures that can be suitable for applications as 2D infrared photonic crystals. First, a preliminary study is made of the electrochemical etching process in order to provide a basic understanding of how the process parameters affect the pore morphology, and to determine the optimal etching conditions that ensure stable macropore growth. After the etching parameters had been optimized, several ordered macroporous structures were fabricated by means of light-assisted electrochemical etching of n-type silicon. In this chapter, we put particular emphasis on the most important etching parameters that have to be taken into account if large-area macropore arrays, with high aspect ratio and good structural characteristics are to be obtained. We describe some of the critical effects of the etching process that act as sources of imperfections in the otherwise perfect pore pattern. We also discuss several technological aspects of macropore fabrication and how the pore uniformity and quality of the fabricated microstructures can be improved.

UNIVERSITAT ROVIRA I VIRGILI
PHOTONIC BANDGAP ANALYSIS AND FABRICATION OF MACROPOROUS SILICON BY ELECTROCHEMICAL ETCHING
Trifon Todorov Tirfonov
ISBN:978-84-693-6270-9/DL:T-1376-2010

5.1. Pore morphology and process parameters

Making porous silicon in any one of its numerous manifestations demands specific sets of parameters and appropriate control of the etching process. Different pore morphologies could result not only from different etching conditions, but also from differences in the preparation conditions and the design of the electrochemical etching set-up. In addition, while some pore morphologies are attainable only for a specific parametric set, others can be obtained for many and sometimes very different conditions. Clearly, everything could be important in the formation of porous silicon: type of substrate, doping concentrations, crystal orientation, chemical composition of the electrolyte, anodization regime, temperature, specific construction of the electrochemical cell, sample preconditioning and so on. Although a lot of experimental data are available, samples produced by different research groups are often not comparable even if the experimental and preparation conditions are apparently the same. Moreover, our experience shows that carefully prepared experiments conducted under apparently identical conditions can lead to somewhat different results, proving that the samples are sometimes difficult to reproduce even in the same laboratory. These are probably the main reasons why electrochemical methods are viewed with some suspicion by the hard-core silicon community ("it is not only chemistry, but – even worse – electrochemistry") [192]. In this context, we believe that a preliminary study of the etching process is needed to account for some particular aspects of the experimental set-up developed. In what follows we shall describe the experimental results obtained in the first stage of our study on macroporous silicon formation.

5.1.1. Random macropore formation in n-type silicon

At the beginning of our study our aim was to make the silicon porous. This may not sound very serious bearing in mind that a considerable amount of research has already been done worldwide in this field. However, making porous silicon was not so straightforward for us because we had almost no experience at this stage. It is also worth mentioning our fruitless and time-consuming efforts to fix continuously emerging problems with the cell design, which resulted in numerous broken samples, leaks from the etching cell, bubbles sticking, contaminated electrolytes and corroded electrodes. However, we are not going to describe this aspect of our work. In this section, we shall briefly describe some experimental evidence on how the etching parameters, and specific features of the sample preparation and cell design influenced the resulting pore morphology.

UNIVERSITAT ROVIRA I VIRGILI
PHOTONIC BANDGAP ANALYSIS AND FABRICATION OF MACROPOROUS SILICON BY ELECTROCHEMICAL ETCHING
Trifon Todorov Tirfonov
ISBN:978-84-693-6270-9/DL:T-1376-2010

It has been already mentioned that when a flat pattern-free silicon wafer is anodized in HF solution, a porous silicon layer (PSL) can then form on the wafer surface if the appropriate anodization regime is matched. This means that the etching current should not exceed the critical current density J_{ps}, which divides the I-V characteristics of the Si/HF-electrolyte system into two anodization regimes, i.e. porous silicon formation and electropolishing. This is illustrated in the two figures below. Figure 5.1 shows SEM* micrographs of the surface and cross-section of an n-type silicon wafer anodized in 2.5 wt.% aqueous HF solution at an applied voltage of 2.4 V (with respect to the reference electrode). The experiment was conducted at room temperature (RT≈22°) for 345 min. The supplied voltage between the working and counter electrode was approximately 4.5 V. Note the large voltage difference between the potentials measured with respect to the reference and counter electrodes. Only the potential against the reference electrode is meaningful, since it determines the real anodic potential at which the wafer is biased. The voltage drop across the electrolyte or at the ohmic contacts is of less importance for the process. By adjusting the backside illumination, the etching current density was fixed at 16.08 mA/cm^2. For the HF concentration used and room temperature, the value of critical current density J_{ps} calculated by the parameter set given in Chapter 4 is J_{ps}=15.17 mA/cm^2. Therefore, the applied etching current exceeds the critical current J_{ps} and an electropolishing effect should be expected. Indeed, this is what we have observed in this case. The porous (macroporous or microporous) silicon layer was not seen at any point on the entire wafer surface. After the sample had been removed from the etching cell and dried in a N_2 stream, the wafer surface presented the bright gray metallic appearance typical of a clean silicon wafer. Commonly, the microporous silicon layer covering the wafer surface is colored and its color depends on the thickness and porosity of the layer because the light reflected at the interfaces between the substrate, PS-layer and air interferes [212]. On the other hand, the wafer surface has a pitch-black appearance if a thick macroporous layer is formed because light is trapped inside the pores.† However, this does not mean that the resulting pore morphology can be deduced simply with the naked eye. It is worth mentioning that the wafer was perforated at some local positions (which can be caused by a local enhancement of the current density because of inhomogeneous illumination, defect sites or inhomogeneous electric field distribution due to bad backside contact) and crashed when it was removed from the etching cell.

* After etching, all samples were examined under scanning electron microscope (SEM) JEOL JSM6400 at the Service of Scientific Resources, Rovira i Virgili University, Tarragona

† Microporous and mesoporous silicon layers have been found to absorb light to an extremely high degree and have been proposed as anti-reflective coatings for solar cells [213-216]

UNIVERSITAT ROVIRA I VIRGILI
PHOTONIC BANDGAP ANALYSIS AND FABRICATION OF MACROPOROUS SILICON BY ELECTROCHEMICAL ETCHING
Trifon Todorov Tirfonov
ISBN:978-84-693-6270-9/DL:T-1376-2010

From Fig. 5.1 it can be seen that no macropores have been formed even though the etching was performed for about 6 hours, which, despite including the initial nucleation phase is more than sufficient to initiate macropore growth. Lehmann's model may be used to provide the explanation for this. At current densities higher than the critical value J_{ps} the rate of electrochemical dissolution is no longer limited by hole diffusion in the silicon electrode but by mass-transfer in the electrolyte. So an excess of holes is formed at the pore tips. These holes penetrate the interpore area and promote dissolution there, which completely destroys the pore walls. The remaining surface roughness that is observed in Fig. 5.1a confirms this hypothesis. It seems that only the pore tips have survived. The surface resembles a close-packed hexagonal-like structure, which is what is left of the macropore tips after the pore walls have been dissolved (see also Fig. 5.1b). We also notice that the applied etching current is very close to the critical current peak. Although no porous silicon was formed, this indicates that the wafer surface was probably not electropolished. According to Ref. [177], at current densities only slightly greater than the critical value J_{ps} numerous small pits are observed on the wafer surface and it appears as if it had been sand blasted. At somewhat greater current densities the surface exhibits the "orange peel" appearance that is often observed on chemically etched surfaces. It has also been reported that the silicon surface can be partly covered with a PS layer and partly electropolished [188].

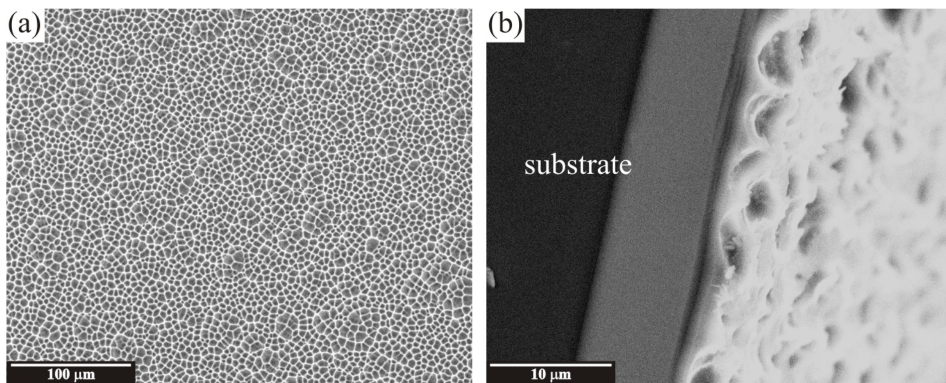

Fig. 5.1. SEM micrographs of the surface (a) and in cross-section (b) of an n-type silicon wafer anodized in 2.5 wt.% aqueous HF solution. Porous silicon formation is not observed since the applied etching current J exceeded the current density J_{ps} peak, which is the critical value separating the porous silicon formation and electropolishing anodic regimes.

However, the situation described so far was not observed when current densities were below J_{ps}. Figure 5.2 shows SEM micrographs of an n-type wafer etched

UNIVERSITAT ROVIRA I VIRGILI
PHOTONIC BANDGAP ANALYSIS AND FABRICATION OF MACROPOROUS SILICON BY ELECTROCHEMICAL ETCHING
Trifon Todorov Tirfonov
ISBN:978-84-693-6270-9/DL:T-1376-2010

with an applied current density J=8.04 mA/cm^2. The electrolyte composition was 2.5 wt.% aqueous HF as in the case described above. The applied voltage was 2.1 V and the experiment was performed at room temperature for 360 min. Let us say that in this experiment the wafer was not perforated and did not crash after it was removed from the etching cell. The wafer surface was also deep black, indicating very low light reflectance.

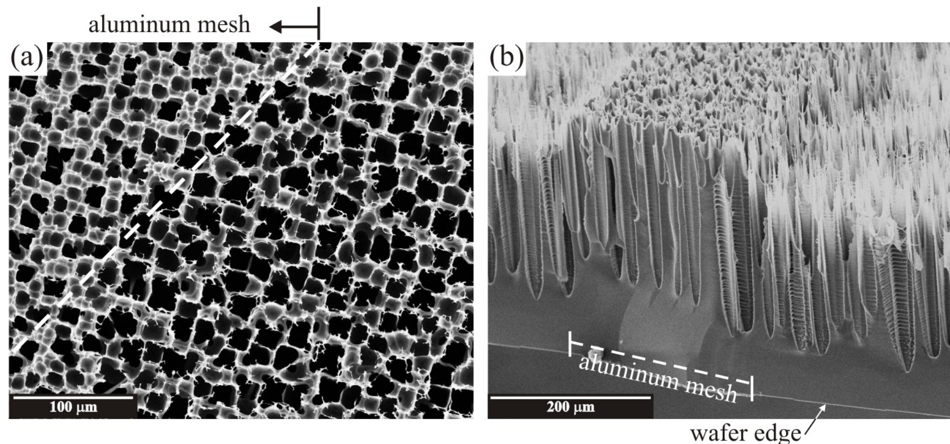

Fig. 5.2. SEM micrographs of the surface (a) and cross-section (b) of an n-type silicon wafer etched in 2.5 wt.% aqueous HF with current density $J<J_{ps}$. Deep macropores were formed in this case, which have grown in the <100> direction. The screening effect of the aluminum wires forming the backside mesh electrode can be observed.

Figure 5.2 shows that deep macropores were formed in this case. The macropores have big diameters and are mostly the result of various smaller pores joining together. The pore walls are very thin and are mostly destroyed near the front side of the wafer. The screening effect of the aluminum mesh used for the backside electrode can be seen clearly. Behind the aluminum wires the macropores are less dense because part of the backside illumination is reflected from the aluminum mesh. These differences in the density of the macropores are detectable by the naked eye. As shown in Appendix A, the lower pore density is seen as light-gray lines just behind the aluminum wires so it seems that the aluminum mesh is projected onto the front wafer surface. Figure 5.2 suggests that the macropore length is not so easily defined. Some macropores in the bulk of the electrode have very different lengths and also smaller macropores that “died” in the initial stages of the etching process. It has been demonstrated that the nucleation of macropores on polished defect-free wafer surfaces

UNIVERSITAT ROVIRA I VIRGILI
PHOTONIC BANDGAP ANALYSIS AND FABRICATION OF MACROPOROUS SILICON BY
ELECTROCHEMICAL ETCHING
Trifon Todorov Tirfonov
ISBN:978-84-693-6270-9/DL:T-1376-2010

is preceded by prolonged nucleation and redistribution phases [176,197]. In the nucleation phase the silicon dissolves homogeneously, which results in a step between the original surface and the surface of the etched silicon. At the end of this nucleation phase, shallow macropores with relatively high density are formed. Then, a redistribution phase starts, because the initial density of the macropores is not yet the equilibrium density. During the redistribution phase some pores stop growing, whereas other pores continue to grow with increased diameters. As soon as the redistribution process finishes, the phase of stable pore growth starts and yields a stable arrangement of macropores. Unlike the polished wafer surface, such nucleation and redistribution phases do not head the stable macropore growth if the surface is pre-structured with nucleation sites. This effect is illustrated in Fig. 5.3 and 5.4.

Fig. 5.3. Interface between random and ordered macropore formation. A step of specific height *h* is observed between the etched surface where macropores have grown randomly and the surface with pre-structured nucleation sites. This indicates that macropore growth on polished wafer surfaces is preceded by a nucleation phase in which silicon dissolves homogeneously. The first row of the pre-structured surface is laterally etched because on the side of random macropore formation there is no hole depletion near the pore wall. This effect cannot be avoided.

Figure 5.3 shows a SEM micrograph of the interface region between the lithographically pre-structured wafer surface where macropore formation is ordered and the polished wafer surface where it is random. The wafer was etched under conditions that ensure stable macropore growth for the patterned area, i.e 2.5 wt.% aqueous HF, 1.4 V, current density increased from 3.38 to 4.98 mA/cm^2, RT, 240 min. The ordered pore grow will be discussed in greater detail in the next sections. A step of specific height *h* is clearly seen between the pre-structured surface and the surface of random pore formation. This indicates that an initially polished wafer surface is first

UNIVERSITAT ROVIRA I VIRGILI
PHOTONIC BANDGAP ANALYSIS AND FABRICATION OF MACROPOROUS SILICON BY ELECTROCHEMICAL ETCHING
Trifon Todorov Tirfonov
ISBN:978-84-693-6270-9/DL:T-1376-2010

homogeneously etched. The height *h* of the "crater" was found to depend on the substrate resistivity and on the temperature, but it is almost independent of the etching potential [197]. For the given case, the wafer resistivity was 2.15 Ωcm. The height *h* of the step between the two surfaces was about 4.4 μm (measured by Sloan DEKTAK 3030 profilometer). Similar steps between the patterned and polished wafer surfaces (although of different heights) were observed for all the pre-structured wafers we have used in our work.

Another effect that can be seen in Fig. 5.3 is the side branching of the first row (or column) of the patterned region. The pore walls on the random-macropore-formation side are not depleted of holes, as they are on the ordered-macropore side because of the overlapping SCRs. Consequently, the macropores at the boundaries between patterned and non-patterned surfaces will always be "badly" etched. Although it has been reported that this effect can be minimized by shading the backside illumination over the non-patterned areas [211], it cannot be completely avoided. This is important because if the patterned area contains defects (e.g. waveguide), these defects will be badly defined near the boundary.

Turning back to our discussion, we have pointed out that random macropore formation is preceded by a nucleation phase. This is also confirmed in Fig. 5.4, where the wafer was etched only for 12 min. The electrolyte composition was the same as in the previous case, and the applied etching current (3.22 mA/cm^2) is comparable to the one used previously. Other parameters were optimal so that stable macropore growth could be ensured in the patterned regions. Clearly, random macropores were not formed for this short etching time. Where nucleation sites exist, however, well-defined macropores with a pore length of about 6.37 μm (excluding the depth of the pyramidal notches) have grown. It can also be seen that the size of the pores at the random-ordered boundary is enhanced at the very beginning of the etching process. Figure 5.4a also reveals the formation of a two-layer structure, i.e. a microporous layer covering the macropore walls [125,163]. The existence of such a microporous layer has been reported for macropores in n-type silicon formed under front-side illumination [60,176,178], as well as for macropores in p-type silicon [179]. There are no doubts about whether this layer is indeed a microporous layer with nanometric feature size because of the following experimental observations: (*i*) room-temperature photoluminescence originates in this layer and the luminescence spectrum shifts as the doping changes [217]; (*ii*) this layer is considerably more resistive than the bulk silicon [169,218]; and (*iii*) it is easily dissolved in alkaline etching solutions [60] such as potassium hydroxide (KOH), which is known to etch the silicon but not the silicon

ISBN:978-84-693-6270-9/DL:T-1376-2010

oxide. However, the reason why this layer forms and covers the entire wafer surface even inside the macropores is poorly understood. We shall focus our attention on the microporous layer later on in this chapter.

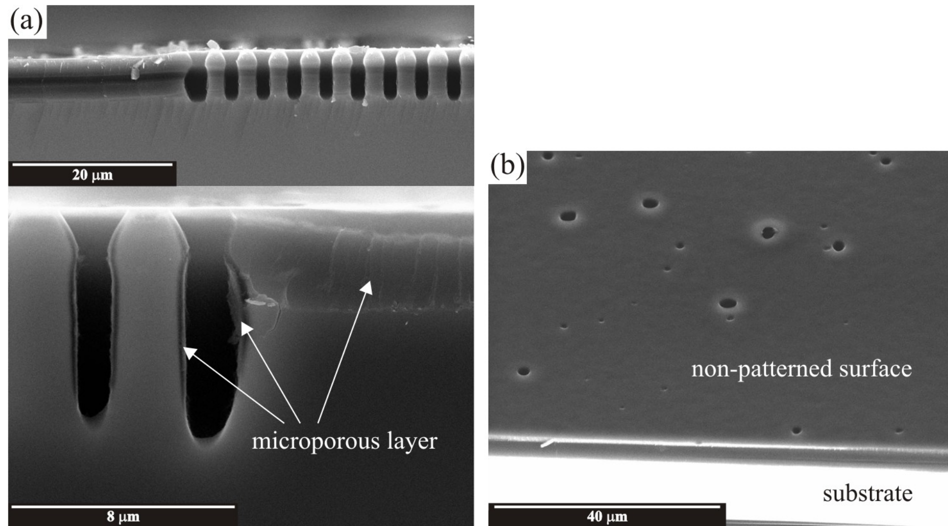

Fig. 5.4. SEM micrographs of an n-type Si wafer anodically etched in 2.5 wt.% aqueous HF for 12 min. (a) Cross-sections showing the boundary between patterned and polished surfaces. The two pictures are taken from different regions in the wafer. (b) Cross section of the polished surface. The sample is tilted to allow better observation of the wafer surface. Well-defined macropores are grown at the nucleation sites but no macropores are observed on the non-patterned area. A microporous silicon layer is formed and covers the macropore walls and the wafer surface.

Figure 5.5 shows the macropores that form after a polished n-type silicon wafer is etched for 285 min in 5 wt.% aqueous HF solution with an etching current density of 12.06 mA/cm^2. The critical current density for the given HF concentration is 42.92 mA/cm^2, calculated with the same set of parameters as for the case in Fig. 5.1. Macropores are therefore expected to form and this is clearly observed in Fig. 5.5. What is important here is that some macropores cross the whole thickness of the wafer. This indicates that the etching rate is strongly dependent on the HF concentration. For example, in the wafer etched in 2.5 wt.% HF for 360 min the macropores did not reach the wafer backside (see Fig. 5.2). When the HF concentration was doubled, the macropores crossed the wafer thickness for 285 min. This time is 75 min shorter than in the previous case in which no through pores are observed. Although the current density (12.06 mA/cm^2) is greater than one (8.04 mA/cm^2) used in Fig. 5.2, experiments with

UNIVERSITAT ROVIRA I VIRGILI
PHOTONIC BANDGAP ANALYSIS AND FABRICATION OF MACROPOROUS SILICON BY ELECTROCHEMICAL ETCHING
Trifon Todorov Tirfonov
ISBN:978-84-693-6270-9/DL:T-1376-2010

2.5 wt.% HF and current densities of about 12 mA/cm^2 showed that the wafer was not perforated for etching times shorter than 360 min. However, it is difficult to make a precise quantitative evaluation of the etching rate because nucleation and redistribution phases are present in the random macropore formation, and the macropore length is badly defined. For these reasons, the etching rate can be determined better in case of ordered macropore growth. Nevertheless, a comparison between Fig. 5.5 and 5.3, and between the etching conditions used clearly suggests that the etching rate strongly depends on the HF concentration in the electrolyte.

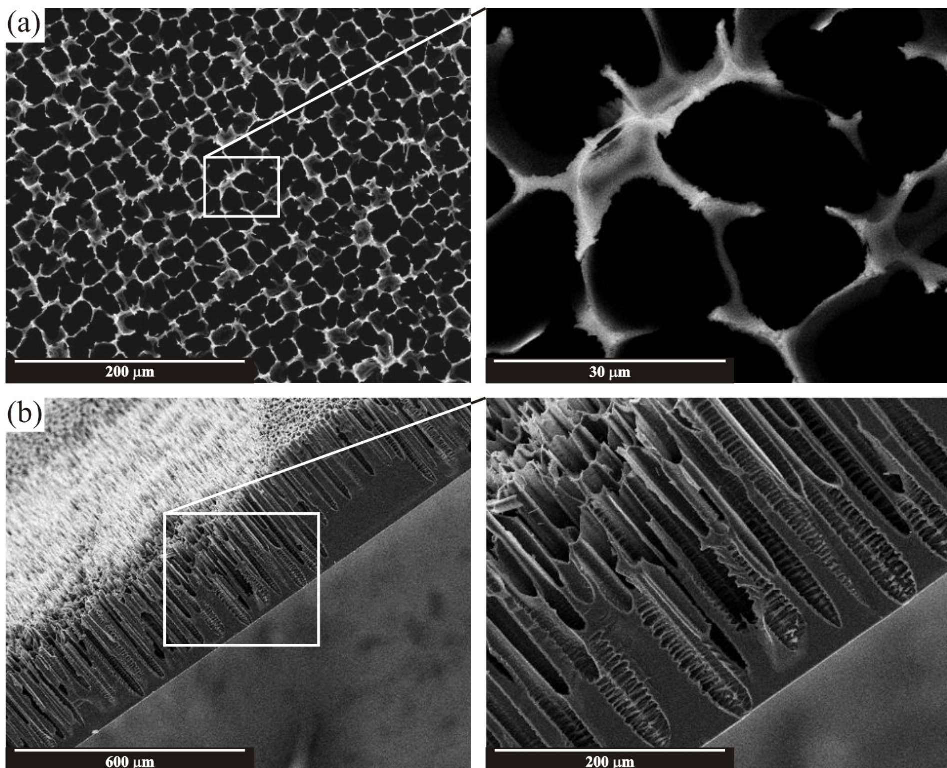

Fig. 5.5. SEM micrographs of the surface (a) and cross-section (b) of an n-type wafer etched in 5 wt.% HF solution for 285 min. The micrographs on the right-hand side were taken with higher magnification over the regions indicated by squares. The figure shows through-pores which pierce the entire wafer.

A porous membrane can be obtained by making through-wafer pores. It should be pointed out that this way for producing porous membrane is not the best way. First, because the HF leaks could destroy some of the metallic elements used to connect the

wafer backside to the external circuit, and be a safety hazard. Second, the electrochemical etching is unstable in the vicinity of the wafer backside. Thus, the best way is to etch pores of a particular length and then remove the backside silicon by chemical etching or mechanical polishing until the pores are revealed.

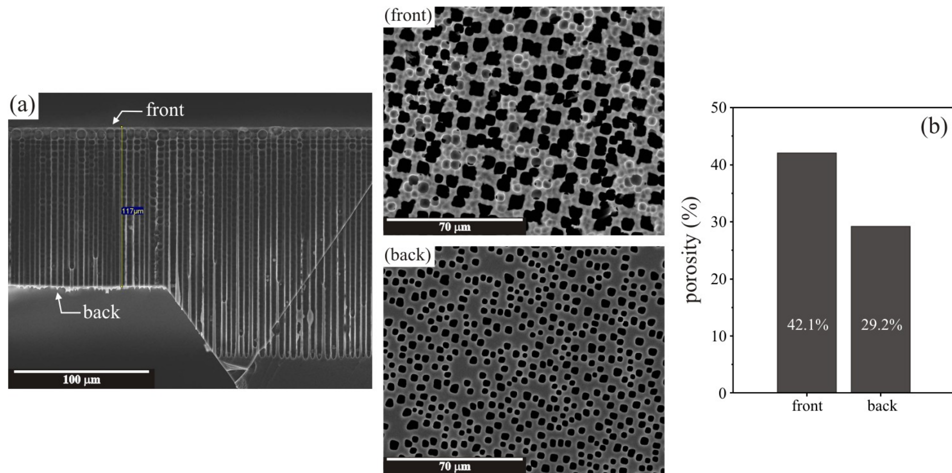

Fig. 5.6. (a) SEM micrographs of the front side (front) and backside (back) surfaces of a porous membrane; (b) porosity calculated at different macropore depths. Although the etching conditions are kept constant, considerable changes are observed in the porosity in depth. The present effect is assumed to be caused by higher dark current densities because of the greater inner pore surface.

Figure 5.6a shows a porous membrane, which has been produced by etching the backside silicon in TMAH solution. The process sequence for obtaining through-pores or silicon dioxide pillars is fully described in Chapter 6. Here, we shall pay particular attention to the porosity of the resulting macroporous structure. The micrographs on the right-hand side in Fig. 5.6 were taken from the front surface (the surface in contact with the electrolyte) and from the back surface of the membrane after the silicon had been removed. (The arrows in Fig. 5.6a only label the front and backside membrane surfaces and do not indicate the exact positions from which the SEM micrographs were taken). The membrane is 117 µm thick, while the total pore length is about 171 µm. This ensures that the backside TMAH etching is deep enough to exclude the possibility that eventually only the pore tips have been revealed. The electrochemical etching was performed for 300 min in 2.5 wt.% aqueous HF with a current density of 4.98 mA/cm^2. The current was kept constant during the etching by adjusting the backside illumination intensity. The constant applied potential was 1.7 V.

UNIVERSITAT ROVIRA I VIRGILI
PHOTONIC BANDGAP ANALYSIS AND FABRICATION OF MACROPOROUS SILICON BY ELECTROCHEMICAL ETCHING
Trifon Todorov Tirfonov
ISBN:978-84-693-6270-9/DL:T-1376-2010

At first glance, it can be seen that the pore diameter is much greater on the frontside than on the backside. The calculated porosity* (Fig. 5.6b) confirms this observation. The porosity of the macroporous structure in this case was defined as the area occupied by all holes divided by the total area of the image. The two micrographs from the front and backside surfaces were taken with the same magnification so that the total area is identical in both images. The overall porosity (Fig. 5.6b) clearly decreases during the etching. One mechanism that can explain this effect is the pure chemical dissolution of the pore walls due to increased dark current because of the increased pore surface area for long anodization times. This effect is known to be more pronounced for microporous silicon layers, because of their large inner surface [220,221]. For meso- and macroporous layers another effect is known to affect the porosity and to produce depth inhomogeneities in the resulting porous structure. This effect is caused by the HF concentration decreasing with pore depth because of diffusional limitations. It leads to an increase in the porosity with pore depth and is more pronounced for higher HF concentrations and higher current densities. For long anodization times, both effects – the higher dark current and the decrease in HF concentration- can develop. It is therefore difficult to quantify the changes in porosity with the penetration depth.

Another effect which appears at long anodization times is the formation of spiking pores with diameters in the order of a few tens of nanometers on the macropore walls. The formation of such spiking pores is greater at higher anodic potentials. The spiking effect is illustrated in Fig. 5.7. The etching was performed again in 2.5 wt.% aqueous HF solution for 240 min with a current density of 4.02 mA/cm^2. In contrast to the samples discussed previously, the applied anodic potential in this case was fixed at 2.5 V. In Fig. 5.7a, the spiking pores can hardly be seen because of their smaller dimensions even for an SEM. Note that the spiking pores are different from the side branching pores, which are seen, for example, as side undulations on macropore walls. The branching pores are still macropores etched by the photo-generated current, while the spiking pores are mostly mesopores formed by electrical breakdown. The morphology of the spiking pores becomes visible by forming an oxide replica and subsequently etching off the remaining silicon [125]. Such an oxide replica is shown in Fig. 5.7b where the silicon was completely removed by TMAH etching from the backside. The spiking structure can clearly be seen in the magnified inset. Spiking pores are found to grow always along <100> directions and the spikes are at right angles to

* The image processing and the calculation of porosity was performed by using freely available software NIH Image/J developed at the Research Services Branch of the National Institutes of Health, USA [219].

ISBN:978-84-693-6270-9/DL:T-1376-2010

the main pore. For a substrate resistivity of about 2-3 Ωcm, the formation of spiking pores increased at anodic potentials greater than 2 V. However, the reason why they form only at the beginning of the macropores is still unclear. One mechanism that may account for this effect invokes changes in the doping level distribution and/or changes in the surface potential with the pore propagation.

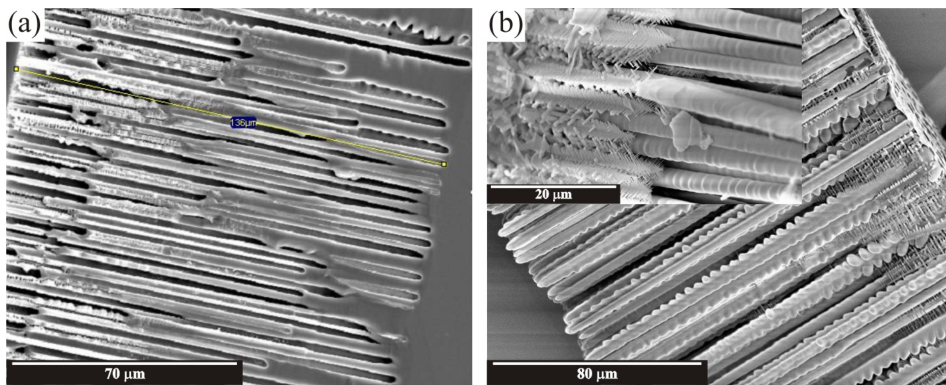

Fig. 5.7. Formation of spiking breakdown-type pores on the macropore walls at higher anodic potentials. (a) Macropores etched in 2.5 wt.% aqueous HF with an applied voltage of 2.5 V. Spiking pores are observable on the macropore walls near the surface. (b) Oxide replica (formed by oxidation and subsequent etching of the remaining silicon) of the macropores reveals more details of the spiking pore morphology.

At much higher anodic potentials (e.g. 27 V) the formation of breakdown pores is considerably enhanced. Figure 5.8 shows an example of an n-type wafer etched in 5 wt.% aqueous HF for 100 min with a 27 V anodic bias. The etching current (11.25 mA/cm^2) was kept constant by adjusting the backside illumination. The pores at the wafer surface (Fig. 5.8a) are cross-shaped with strong spiking in depth. Note that the observed porous structure is still formed of macropores growing towards the source of photo-generated carriers. However, after the illumination was switched off at the end of the etching process the current going through the system was 9.65 mA/cm^2, which is a clear indication that the pore formation mechanism was governed by electrical breakdown and not by the backside illumination. The pore morphology is similar to that obtained when mesopores are grown in highly doped n- and p-type silicon wafers without illumination [187,222], or mesopores formed in low-doped n-type silicon at high anodic potentials also without illumination [187,125]. The growth of mesopores is strongly anisotropic and mesopores in low-doped n-type substrates are found to grow exclusively along <100> directions of the crystal [60,223-225]. This orientation

UNIVERSITAT ROVIRA I VIRGILI
PHOTONIC BANDGAP ANALYSIS AND FABRICATION OF MACROPOROUS SILICON BY ELECTROCHEMICAL ETCHING
Trifon Todorov Tirfonov
ISBN:978-84-693-6270-9/DL:T-1376-2010

dependence has been ascribed to the anisotropy of the critical current density J_{ps} [125], which is found to show a maximum for (100) substrates independently of the HF concentration used. Nowadays, there seems to be no conceptual problem with the formation of n-type mesopores. Avalanche breakdown is thought to be the only source of electronic holes needed for the dissolution reaction, so the resulting pores must be small (which it is) to allow high field strength at the tips. However, some questions are still unanswered. For example, why are the n-type mesopores always heavily branched? If the pores are close enough to each other (and they usually are), there should be no sizeable electrical field between them and thus no inducement to branching [183]. At present, there is no convincing model for the formation of mesopores, although the model of current bursts makes some suggestions [173-175].

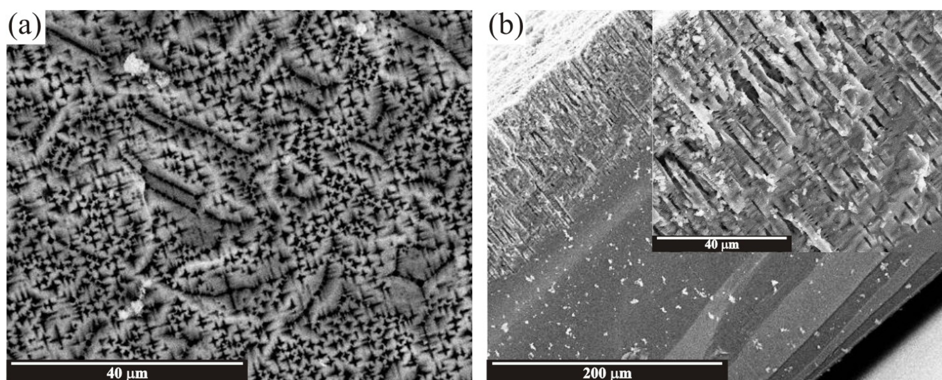

Fig. 5.8. Formation of breakdown pores at higher anodic potentials. SEM micrographs of the surface (a) and the cross-section (b) of an n-type wafer etched in 5 wt.% aqueous HF for 100 min at 27 V anodic bias.

The next effect that is worth mentioning here is related to the specific construction of the electrochemical cell. At some distance from the O-ring used to seal the cell, the current flow is not normal to the wafer surface. The current density is slightly enhanced near the O-ring, which results in inhomogeneities in the thickness of the porous layer (Fig. 5.9). This effect also appears on the borders of structures if a masking layer (for example, silicon nitride Si_3N_4) is used to perform a selective anodization [202]. Strong undercutting was found below the masking layer on the borders of the patterned structures. This is caused by the higher local current density, which in turn is due to the inhomogeneous distribution of the electric field in the substrate. These inhomogeneities in the porous layer near the O-ring seal show that samples that are too small (e.g., smaller than 10x10 mm [187]) cannot be etched

UNIVERSITAT ROVIRA I VIRGILI
PHOTONIC BANDGAP ANALYSIS AND FABRICATION OF MACROPOROUS SILICON BY ELECTROCHEMICAL ETCHING
Trifon Todorov Tirfonov
ISBN:978-84-693-6270-9/DL:T-1376-2010

uniformly. This effect can be reduced if the O-ring seal has a diameter in excess of a centimeter and a section thickness as small as possible.

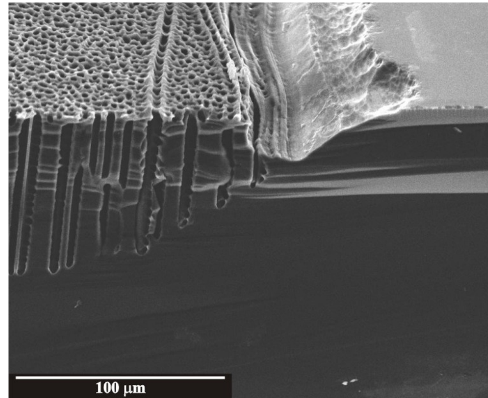

Fig. 5.9. SEM micrograph of the area near the O-ring seal showing inhomogeneities in the porous layer due to inhomogeneous distribution of the electric field in the substrate.

From what has been discussed above it is clear that it is difficult to establish explicit and unambiguous relations between the pore morphologies and process parameters. What is more, many experimental factors should be taken into account if homogeneous etching and reproducible results are required.

5.1.2. Ordered macropore growth in n-type silicon

All the results discussed in the section above were obtained from experiments that were part of a trial-and-error period, which we had needed to acquire a basic understanding of the electrochemical process and to improve the etching set-up. Although these results are not directly related to the fabrication of ordered macropore arrays, we think they are helpful as an introduction to the mechanism of macropore formation and also because they shed light on some etching effects, which (as will be shown) are critical if perfectly grown macropore arrays are to be obtained. In this section and in the rest of the chapter we shall focus solely on the fabrication of ordered macropore arrays by electrochemical etching of n-type samples with pre-structured surfaces.

The wafer front side was pre-structured by applying the sample preparation procedure already described in Chapter 4. The cases, for which the use of aluminum

UNIVERSITAT ROVIRA I VIRGILI
PHOTONIC BANDGAP ANALYSIS AND FABRICATION OF MACROPOROUS SILICON BY ELECTROCHEMICAL ETCHING
Trifon Todorov Tirfonov
ISBN:978-84-693-6270-9/DL:T-1376-2010

mesh or ITO layer that form the backside electrode is critical, will be specially noted. Also, in order to avoid constant repetition we should mention at this point that most of the experiments were conducted at room temperature in 2.5 wt.% aqueous HF electrolyte. The conditions for the experiments that were not carried out at room temperature or for which the electrolyte composition was changed will be explicitly stated.

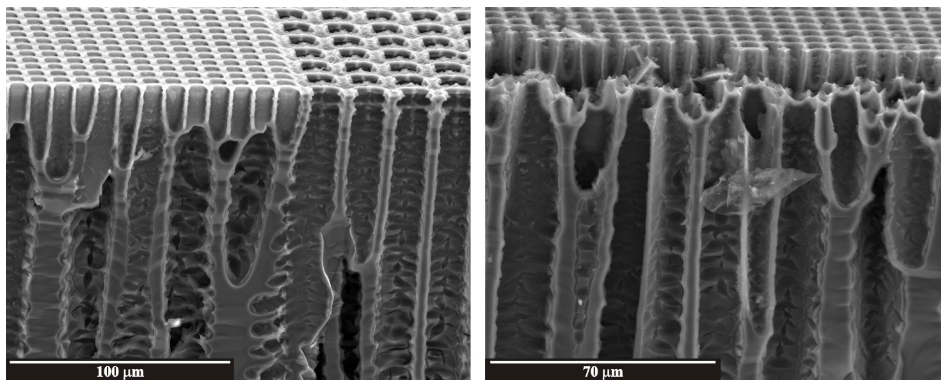

Fig. 5.10. SEM micrographs (taken from regions with different patterning) of a pre-structured n-type silicon wafer etched in 10 wt.% aqueous HF solution for 250 min. No stable macropore growth was found in any experiments at this particular HF concentration.

It should be noted that such a low (2.5 wt.%) HF concentration was not chosen arbitrarily. The HF concentrations reported in the literature* range between 2 and 6 wt.%. According to Ref. 183, it is very difficult, if not impossible, to obtain smooth macropores in n-type wafers with backside illumination for HF concentrations above about 10%. Although the Lehmann's formula should apply to all HF concentrations (which essentially define the critical current peak J_{ps}), diffusional limitations in the narrow pores have been found to limit the obtainable pore length and to yield degradations in the stable pore growth. The maximum obtainable pore length decreases

* We would like to mention here to the research groups that are actively working in the field of ordered macropore growth, namely Lehmann's group at Infineon Technologies AG, Germany [60,125,187,208]; Föll's group at the Christian-Albrechts-University of Kiel, Germany [60,183]; Gösele's group at the Max-Planck Institute of Microstructure Physics, Halle, Germany [209,228-230]; the Italian groups at the University of Pisa [201] and at the University of Trento [231]; V. Starkov and co-workers at the Institute of Microelectronics Technology, Moscow, Russia [227,232]; H. Ohji and co-workers at Mitsubishi Electric Corporation, Japan [211,226]; P. Kleimann and co-workers at the Royal Institute of Technology, Stockholm, Sweden [200]; and many others.

ISBN:978-84-693-6270-9/DL:T-1376-2010

rapidly as the HF concentration increases [187,208]. This effect has been ascribed to a poisoning of the dissolution reaction by the diffusion-limited transport of the etching products (e.g. H_2SiF_6). The rate of H_2SiF_6 production is proportional to J_{ps}, which depends exponentially on the HF concentration (see Eq. 4.7), while the diffusion of H_2SiF_6 shows a slight dependence on the concentration. Therefore, the etching of deep, straight macropores requires low HF concentrations. Figure 5.10 provides experimental evidence for the discussion so far. The electrochemical etching was performed in 10 wt.% aqueous HF solution for 250 min with an applied etching current of 12.06 mA/cm^2. We believe that these SEM micrographs require little further comment.

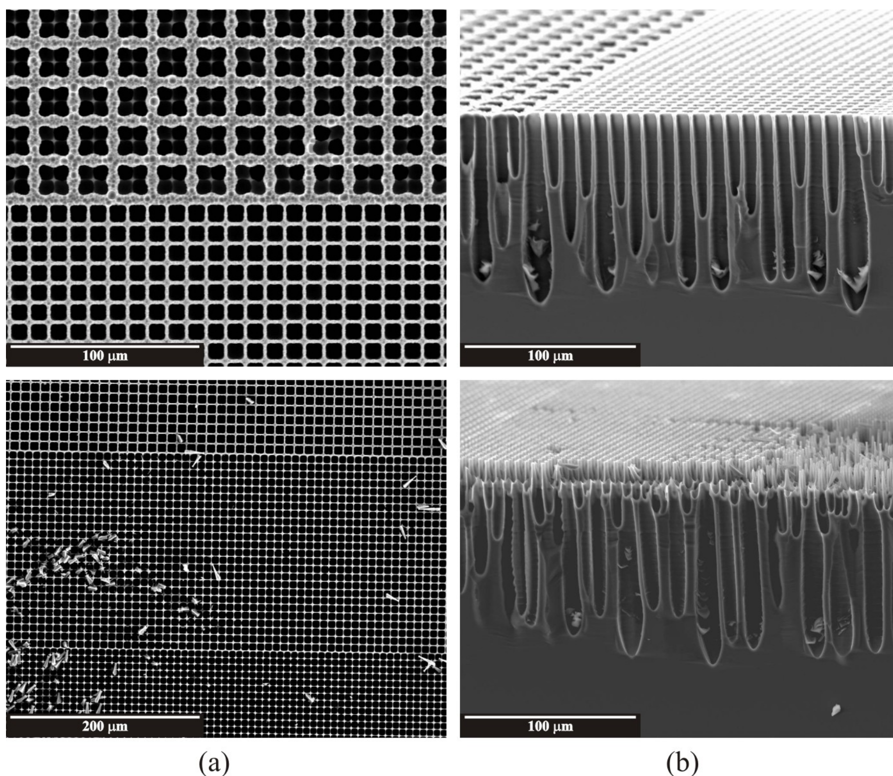

Fig. 5.11. SEM micrographs of the surface (a) and cross-section (b) of an n-type silicon wafer etched in 2.5 wt.% aqueous HF for 300 min with an initial current density of 4.02 mA/cm^2. Patterns with different lattice constants are shown. Since the current is not controlled by adjusting the backside illumination no stable macropore growth can occur.

As has been mentioned above, macropore growth can only be stable if the etching parameters (HF concentration, applied voltage, etching current, temperature,

UNIVERSITAT ROVIRA I VIRGILI
PHOTONIC BANDGAP ANALYSIS AND FABRICATION OF MACROPOROUS SILICON BY ELECTROCHEMICAL ETCHING
Trifon Todorov Tirfonov
ISBN:978-84-693-6270-9/DL:T-1376-2010

etc.) are properly adjusted. Moreover, if very perfect, deep pores are required, precise control of the etching conditions is essential. Precise control of the etching current is of particular importance for stable pore growth. As the pores penetrate deeper and deeper into the substrate, the pore tips become more effective in collecting the photo-generated holes, and this increases the etching current. If the current is not reduced by adjusting the backside illumination, the pore pattern in depth will be imperfect. This effect is illustrated in Fig. 5.11. The wafer was etched at room temperature for 300 min with an applied bias of 1 V. The etching current was initially fixed at 4.02 mA/cm^2 and was unlimited during the etching.

The increase in the current density with the pore growth leads to an increase in the pore diameter, according to Lehmann's formula (Eq. 4.6). Since the spacing between the pores is not a free parameter (because it is limited by the lithographic pattern) some of the pores must die to enable other pores to grow with greater diameters. Note that the increase in diameter will not always destroy the pore walls and will not always result in the growth of overlapping pores in depth. We have observed that the most probable thing that will happen is that some pores must die so that the porosity of the resulting structure will adjust to match the increased current. As can be seen from Fig. 5.11, no region contains straight pores, although the lithography provided initial patterns with different pore spacing (with lattice constants between 5 and 20 μm). The regions in which the lithographic mask defines patterns with smaller pore distances (e.g. 7 μm in the second row of the Fig. 5.11) are destroyed near the surface. This indicates that the initial current was too high to match the given porosity and/or there was a mismatch between the substrate resistivity and pore spacing, according to Lehmann's rule of thumb [187] (discussed in Chapter 4).

Keeping the current constant by decreasing the backside illumination intensity during etching resulted in stable, straight pores with an almost constant pore diameter in depth (Fig. 5.12). The etching was conducted at room temperature for 240 min with a constant anodic potential of 1.5 V. The current density was fixed at 2.41 mA/cm^2. Figure 5.12b shows SEM micrographs taken at various magnifications to reveal the remarkable uniformity of the resulting macroporous structure. The initial lithographic pattern was a square lattice with a center-to-center distance between the holes of 5 μm and a hole size of 2.5 μm. Note that the obtained pore diameter is somewhat larger than the predicted one. For example, the pore diameter measured near the bottom of the pores is about 3.44 μm. If we consider that the pores are circular then from Lehmann's formula (Eq. 4.6) for the applied etching current density of 2.41 mA/cm^2, the calculated porosity is about 0.16, which results in a predicted pore diameter of 2.25 μm. The

UNIVERSITAT ROVIRA I VIRGILI
PHOTONIC BANDGAP ANALYSIS AND FABRICATION OF MACROPOROUS SILICON BY ELECTROCHEMICAL ETCHING
Trifon Todorov Tirfonov
ISBN:978-84-693-6270-9/DL:T-1376-2010

critical current density J_{ps} (i.e. 15.17 mA/cm^2) was calculated from Eq. 4.7 and assuming a room temperature RT=20°C and an HF concentration of 2.5 wt.%. The set of parameters given in Chapter 4 were used.

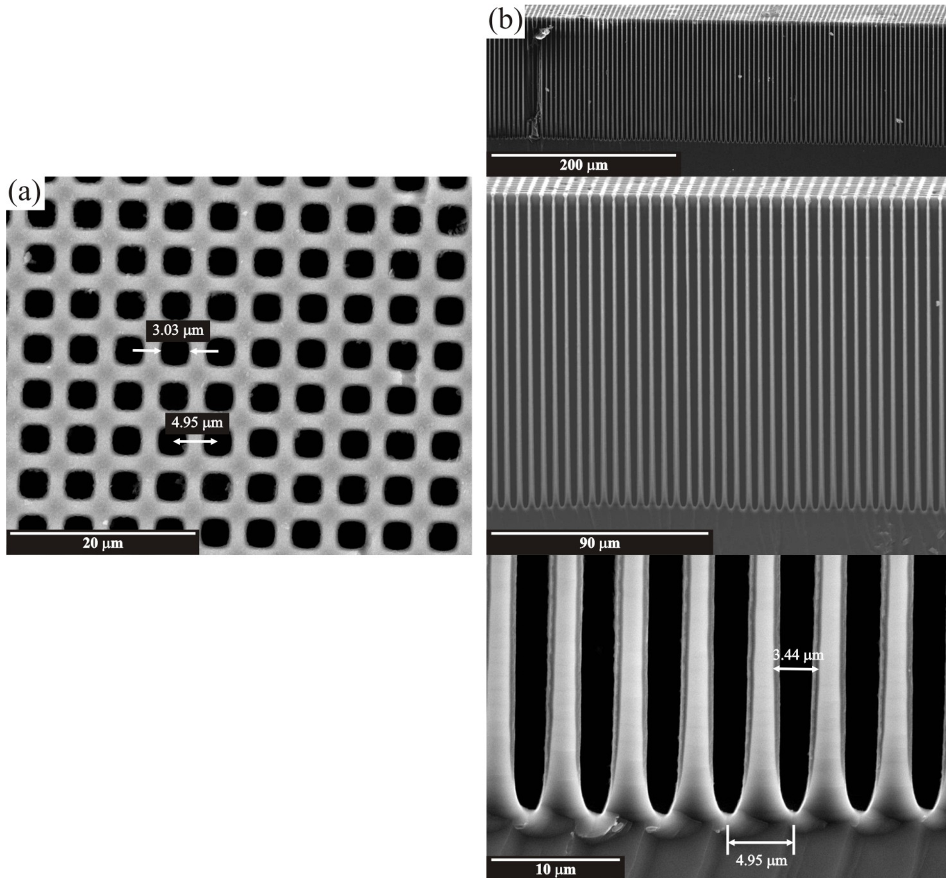

Fig. 5.12. SEM micrographs of the surface (a) and cross section (b) of an n-type wafer etched in 2.5 wt.% aqueous HF for 240 min. The applied etching current (2.41 mA/cm^2) was kept constant during the etching by adjusting the backside illumination. The micrographs show stable, uniform pores with almost constant pore diameter in depth.

The shape of the pores is somewhere between a circle and a square. For constant porosity, the calculated diameter of the pores is therefore somewhat different for circular and square shapes (see Appendix C). For both shapes, however, the obtained diameter exceeds the predicted one. The difference could arise from errors in the assumed and the real HF concentration and/or temperature, as well as from the fact that

UNIVERSITAT ROVIRA I VIRGILI
PHOTONIC BANDGAP ANALYSIS AND FABRICATION OF MACROPOROUS SILICON BY ELECTROCHEMICAL ETCHING
Trifon Todorov Tirfonov
ISBN:978-84-693-6270-9/DL:T-1376-2010

the current distribution was not uniform over the entire surface area due to inhomogeneous backside illumination. The measured pore size (about 3.03 μm) at the pore entrance (Fig. 5.12a) is smaller than the one (3.44 μm) near the pore bottom. However, we should note that measuring the pore diameter on the wafer surface can sometimes give wrong results because of the bottleneck effect (see Fig. 5.19). Of course, if the wafer front side is polished after etching to remove the remaining pyramidal notches and the bottleneck, the measurements will then be accurate.

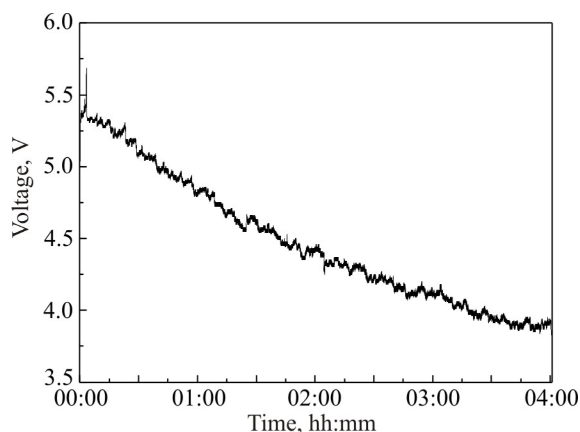

Fig. 5.13. Recorded profile of the voltage source controlling the backside illumination circuit. Higher voltages correspond to higher illumination intensities. In order to keep the current constant the illumination intensity should be reduced with the etching time.

Figure 5.13 shows the recorded voltage profile of the voltage source (HP E3631A) controlling the lamp circuit for backside illumination. Higher voltages correspond to higher illumination intensities. Note that the illumination intensity decreases over time in order to keep the current constant. The noise that can be seen in the curve is due to H_2 bubble formation and sticking to the surface. It is worth pointing out that this profile is of little importance and is given here solely as an illustration. For the etching experiment only the current profile is meaningful. This is because the illumination intensity does not depend linearly on the voltage supply. Neither is the current going through the n-Si/HF system proportional to the illumination intensity. The quantum efficiency (defined as the ratio of the number of exchanged holes and electrons to the number of incident photons) can be above unity for n-type silicon electrodes anodized in HF solutions [187]. The reason for this is that for every hole generated by an incident photon that reaches the HF/silicon interface, up to three electrons may be injected from the electrolyte into the substrate [192]. The total current can therefore be

ISBN:978-84-693-6270-9/DL:T-1376-2010

four times the light-generated hole current. The electron injection current is not constant either, but depends on the absolute current density [160,233].

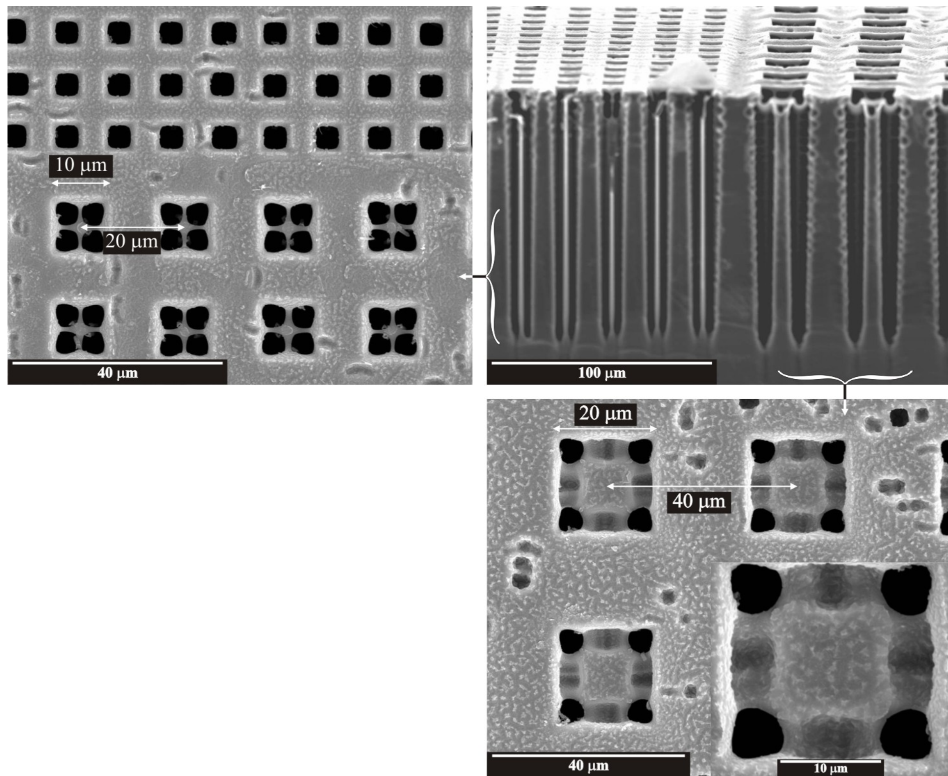

Fig. 5.14. SEM micrographs of pore patterns with large spacing between the pores (i.e. 20 and 40 μm) etched under conditions optimized for etching patterns of smaller pitch (2.5 μm, shown in Fig. 5.12). Four macropores grow at the four vertices of truncated pyramidal notches. The macropore walls are side-branched only on the side where the pore spacing is large.

The porosity can be identical for different lithographic patterns. For example, square patterns with pore diameters 2.5, 10 and 20 μm and center-to-center pore distances 5, 20 and 40 μm, respectively, all have the same porosity of 0.25. However, this does not mean that all these patterns can be etched under the same conditions. Although Lehmann's formula can be used to calculate the required current density, it does not take into account the substrate resistivity. The requirement $a \approx 2L_{SCR}$ (a=pitch of the pattern, L_{SCR}=SCR width) should be fulfilled if pore growth is to be stable. Since the SCR width depends on the applied potentials and doping level, patterns of larger pitch can be etched if substrates of higher resistivities are used. For example, according to Lehmann's rule of thumb [187] the following substrate resistivities are appropriate for

UNIVERSITAT ROVIRA I VIRGILI
PHOTONIC BANDGAP ANALYSIS AND FABRICATION OF MACROPOROUS SILICON BY
ELECTROCHEMICAL ETCHING
Trifon Todorov Tirfonov
ISBN:978-84-693-6270-9/DL:T-1376-2010

the patterns described above: 11, 177 and 706 Ωcm, respectively. The pattern shown in Fig. 5.12 is 2.5×5 μm (hole diameter × pitch) and it was etched quite well even though the substrate resistivity was 2-3 Ωcm. However, the pore walls are very thin. We think that unsuitable substrate resistivity is largely responsible for the difference between the predicted and the obtained pore diameters. In order to etch pores with smaller diameters, we performed various tests with current densities lower than the value given above (2.41 mA/cm^2), but they all resulted in somewhat unstable pore growth. Although the example given (Fig. 5.12) shows that straight pores can also be etched in substrates whose resistivities are lower than recommended, we think that the results will be better if the resistivity and the lithographic pattern are properly adjusted.

Figure 5.14 shows experimental evidence for the above discussion. The etched wafer is the same as in the example in Fig. 5.12, but now SEM micrographs of other initial patterns (i.e. 10×20 μm and 20×40 μm) are presented. As can be seen, four macropores have grown at the four vertices of the truncated pyramids created by the TMAH etching step in the sample preparation procedure. The macropore walls are not smooth but side-branched, which indicates that the area between the pores is not fully depleted of electronic holes. In conclusion, there is no easy way to etch patterns of different sizes simultaneously. As stated by Lehmann [187], the pitch of a pattern across the sample surface can be enlarged or shrunk by a maximum factor of about three. However, the optimized current density that provides the best results for a particular pattern cannot hold so well for the other patterns. It is better to optimize the etching conditions solely for a single pattern and then see if it works for the others or not.

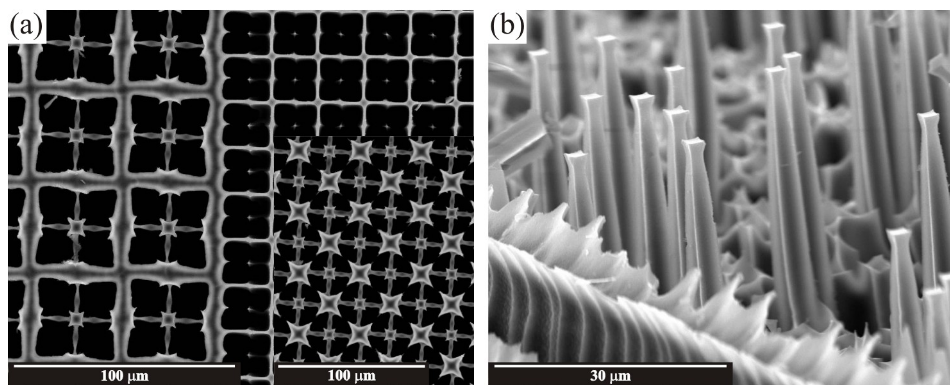

Fig. 5.15. Top view (a) and side view (b) of over-etched patterns achieved by higher current density. The higher current means that the pores that are grown should overlap so that only the thinnest walls between the pores are dissolved, leaving behind silicon pillars with strange shapes.

ISBN:978-84-693-6270-9/DL:T-1376-2010

The growing of four pores inside a single pyramidal notch can be used to over-etch the pattern so that silicon pillars are formed instead of pores. Figure 5.15 shows an example. The etching current was fixed at 7.23 mA/cm^2. This current density was too high. It caused dissolution of the thinnest walls between adjacent pores because the close-packing condition had been reached. If done properly, this effect can be exploited to fabricate several new structures. For example, a similar procedure has been used by Lau *et al.* [128] and Meerakker *et al.* [234] to produce silicon nanowires by electrochemical etching of n-type and p-type silicon wafers, respectively. Barillaro *et al.* [235] have used the growing of four macropores inside a single truncated pyramid to fabricate highly uniform micropillar and microtip arrays.

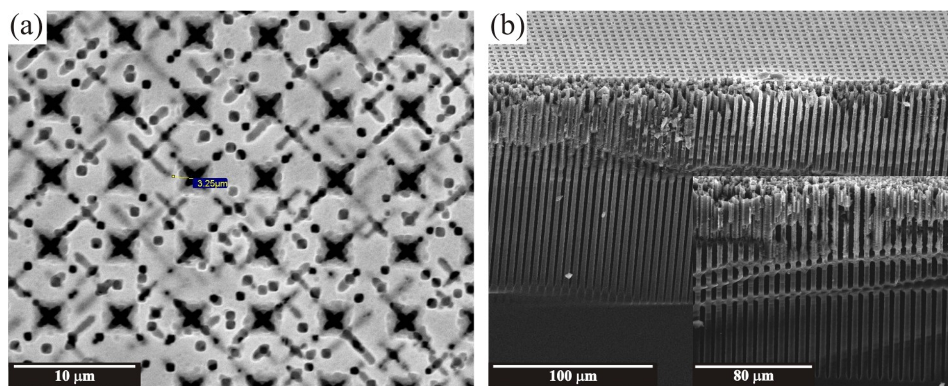

Fig. 5.16. Surface (a) and cross-section views (b) of an n-type wafer etched with an applied bias of 2.5 V. Strong spiking of the macropores near the surface is observed although the etching current ensured stable macropore growth.

The formation of side branching and spiking pores at the beginning of the macropores has been discussed in the previous section. This effect is also present in the case of ordered macropore growth at slightly higher anodic potentials (Fig. 5.15). Figure 5.16 shows an example of an n-type wafer (resistivity 2-3 Ωcm) etched at 2.5 V anodic bias for 240 min. The etching current density was kept constant at 4.02 mA/cm^2 by adjusting the backside illumination, thus ensuring stable pore growth for the patterning given in Fig. 5.16. The formation of cross-shaped pores at the front side surface of the wafer can be seen clearly. It is worth pointing out that all the experiments that resulted in the macropores being spiked were characterized with relatively high dark currents, which were measured after the backside illumination had been switched off at the end of the etching. For example, the measured dark current density for the sample presented was about 72 μA/cm^2 and 418 μA/cm^2 at the beginning and at the end

UNIVERSITAT ROVIRA I VIRGILI
PHOTONIC BANDGAP ANALYSIS AND FABRICATION OF MACROPOROUS SILICON BY ELECTROCHEMICAL ETCHING
Trifon Todorov Tirfonov
ISBN:978-84-693-6270-9/DL:T-1376-2010

of the etching, respectively. Well-etched samples had dark currents below 80 μA/cm^2 after the etching had finished. The dark current density depends on the temperature, oxygen concentration in the electrolyte, added surfactants and the total area of the pores [187,207,208]. Its effect on the uniformity of macropore arrays is somewhat difficult to quantify. However, high dark currents during or at the end of the etching are an almost certain indication that something has gone wrong.

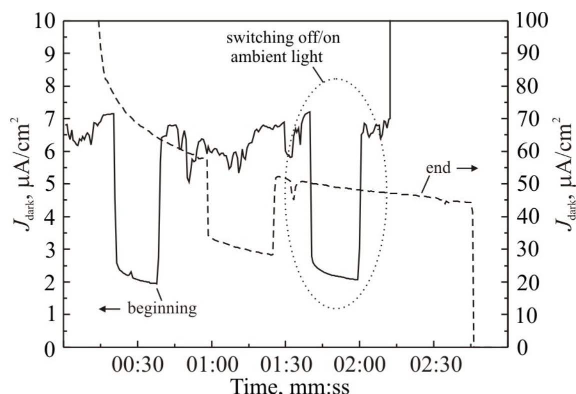

Fig. 5.17. Recorded profile of the dark current density at the beginning and the end of the etching process. Note the different scales. The effect of the ambient lighting is clearly seen.

We shall go on to discuss one aspect of the electrochemical etching that has been dealt with very little in the literature but we believe it is important for all experiments. Figure 5.17 shows the dark current density recorded for about 3 min at the beginning and at the end of the etching. The etching was carried out at room temperature for 240 min. The macropore arrays obtained were well etched, with high uniformity and good structural characteristics. The dark current density at the end of the etching is slightly higher than at the beginning, which is expected because of the higher inner surface of the porous structure formed. What is interesting here are the step variations in the current profiles. These variations are due to switching on/off the ambient light in the room where the experiment took place. Note that the electrochemical cell is opaque and closed from all sides (see Appendix A). Only the wafer backside is exposed to the ambient light. All of our experiments took place in ambient light conditions. We found that ambient lighting has little effect on the stable macropore growth, but we think it will be very important if finer structures with dimensions below 1 μm are to be produced. Etching in dark ambient conditions is advisable in this case. Because of the ambient light, our measurements of the dark

UNIVERSITAT ROVIRA I VIRGILI
PHOTONIC BANDGAP ANALYSIS AND FABRICATION OF MACROPOROUS SILICON BY ELECTROCHEMICAL ETCHING
Trifon Todorov Tirfonov
ISBN:978-84-693-6270-9/DL:T-1376-2010

current density were not accurate. Such measurements are, however, important because they provide additional information that can help in optimizing the etching conditions and obtaining more reproducible results.

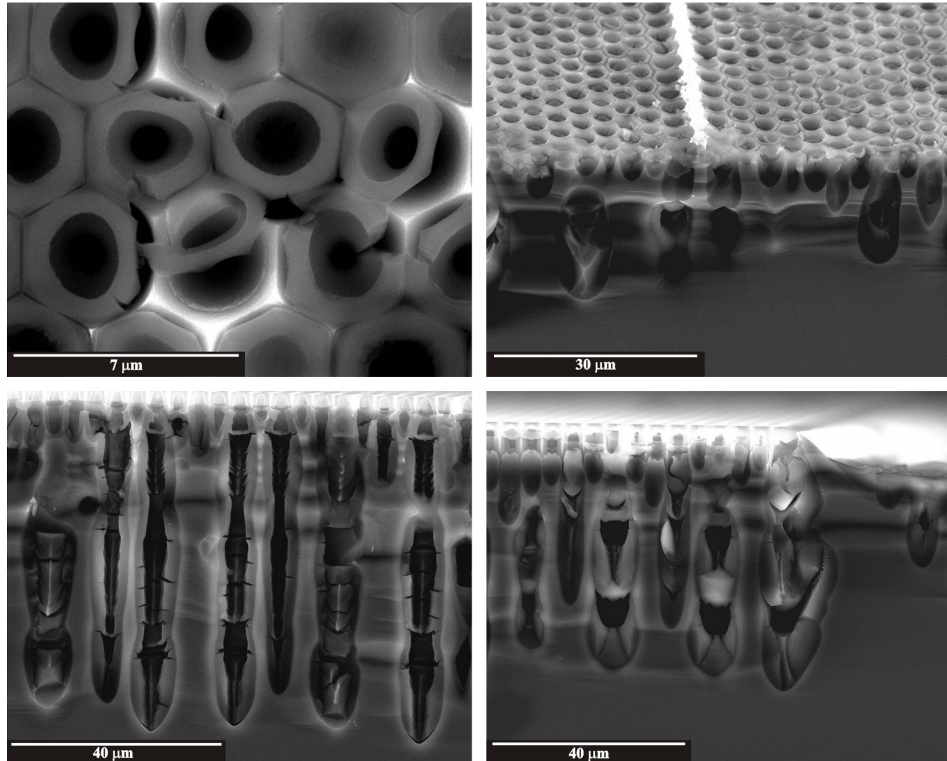

Fig. 5.18. Examples of "fat" macropores etched at low anodic potentials (0.2-0.3 V). Stable macropore growth has not been achieved. The macropores are almost entirely filled by a thick microporous layer.

We have already pointed out that there is an upper voltage limit for a given substrate resistivity above which the formation of spiking pores increases. However, relatively low anodic potentials can also have a detrimental effect on the stable macropore formation. Figure 5.18 shows an example of this. The wafer was etched in conditions that ensure stable pore growth, with the only exception that the anodic potential was about 0.2-0.3 V. The etching was performed at room temperature for 218 min. At such a low anodic potential, pore growth was unstable. Some "fat" macropores were formed but the most interesting fact is that they were almost fully covered by a thick microporous layer. Lehmann (see Ref. 125, Fig. 8) reported that at

ISBN:978-84-693-6270-9/DL:T-1376-2010

low anodic potentials the current density at the pore tips J_{tip} can be smaller than the critical current density J_{ps} (remember that the onset of stable macropore formation is given by the steady-state condition $J_{tip}=J_{ps}$). Clear indication for this is the microporous silicon which still covers the pore tips. This is particularly evident in the first SEM micrograph in Fig. 5.18 where the microporous silicon appears as rings detached from the substrate.

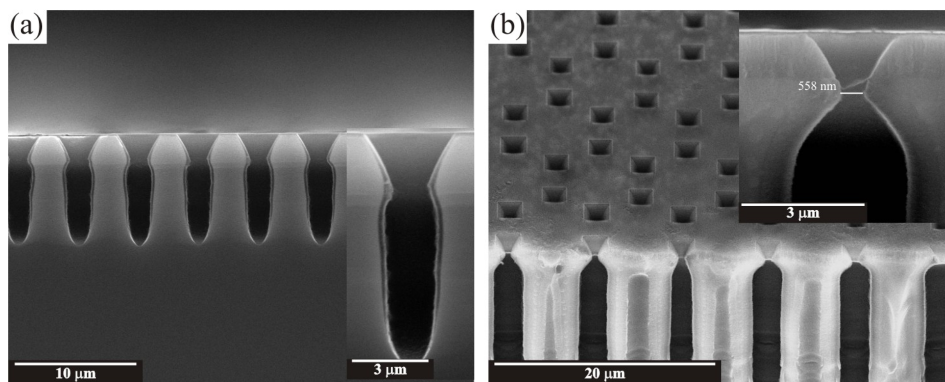

Fig. 5.19. SEM micrographs illustrating the bottleneck at the pore entrance. (a) The bottleneck usually results from the transition of the pyramidal etch pit into a pore tip (etching time 12 min); (b) Very narrow bottlenecks can be formed even for long etching times.

Another effect that could be a source of trouble is the bottleneck at the pore entrance. The pore starts growing at the tip of a pyramidal notch, the diameter increases to match the porosity determined by the etching current and then the pore continue growing in depth. The pyramidal notch is not completely etched, which results in a bottleneck at the pore entrance. This is shown in Fig. 5.19a where the etching was performed for only 12 min. The macropores are already formed and the etching proceeds in depth without any further increase in the pore diameter (of course, if the chemical dissolution of pore walls due to the dark current is not considered). Figure 5.19b shows another example of a bottleneck for a longer etching time (165 min). The mass transport inside the pores should be carried out through a 558 nm aperture, which means that some unwanted effects due to diffusional limitations could appear. Also, the pyramidal notches and bottlenecks may cause problems when the reflectivity of the photonic structure formed has to be measured. Any variations in the pore diameter due to the inverted pyramids and the bottlenecks generate considerable noise in the reflectivity spectrum so the information related to the photonic lattice is somewhat difficult to reveal [236]. In this case it is recommended that the wafer surface

ISBN:978-84-693-6270-9/DL:T-1376-2010

be polished after etching. Bottlenecks can be avoided by increasing the current during the first minutes of pore array fabrication [187].

Finally, to conclude this section, we point out that most of the examples given here are illustrations of problems that are commonly encountered in the electrochemical etching technique for macroporous fabrication. In order to produce arrays of "perfect" macropores all etching parameters have to be just right. Changing one parameter without properly readjusting the others tends to result in less perfect pore patterns. This requires carefully prepared experiments with plenty of fine tuning, as well as meticulous design of the electrochemical etching apparatus. Some examples of well etched macropore arrays together with the etching conditions are presented in the sections below. We shall turn now to more specific aspects of the fabrication of perfect macropore arrays.

5.2. Microporous silicon covering the pore walls

Following the discussion on the ordered macropore formation, we shall go on to describe some general aspects of the microporous silicon layer, which under certain conditions is formed on the macropore walls. This two-layer PS structure only forms on low-doped p-Si and illuminated n-Si electrodes. For low-doped and illuminated n-Si samples, the formation of a microporous silicon layer inside the macropores increases under lower light intensities (lower currents) and lower anodic potentials [184]. The macropores can be fully or partially filled with microporous silicon (see for example Fig. 5.18). At the moment, no model can satisfactorily explain this. It has been suggested that a two-layer PS forms because the reaction is sensitive to the surface curvature [172,184]. For moderately or highly doped wafers, this sensitivity is associated only with the space charge layer because the potential drop in the semiconductor is very small. For lightly doped substrates, a significant amount of potential can drop in the semiconductor and cause the current flow inside the semiconductor to be sensitive to the curvature of the surface also. The electric field in the space charge layer is greatly increased, which results in a higher current flow through a surface with smaller radius of curvature than that with larger one. The current is greatest at the pore tip because that is where the radius of the curvature is smallest. The current decreases from the pore tip to the pore walls as the radius of curvature increases. In particular, Zhang [172] postulated that the current distribution over the pore surface should obey a cosine law, because of the almost hemispherical shape of the pore. Thus, there is a distribution of the kind of the reactions along the pore bottom. At

UNIVERSITAT ROVIRA I VIRGILI
PHOTONIC BANDGAP ANALYSIS AND FABRICATION OF MACROPOROUS SILICON BY ELECTROCHEMICAL ETCHING
Trifon Todorov Tirfonov
ISBN:978-84-693-6270-9/DL:T-1376-2010

the pore tips the reaction may fall in the onset of electropolishing and therefore at the pore tips the silicon dissolution may proceeds through the formation and dissolution of an anodic oxide layer. When the tip area of the macropores is partially covered with an oxide film, the macropores are partially filled with microporous silicon only in the area that is not covered by oxide. Thus, the macropore walls become covered with microporous silicon film, while the tip area is not (Fig. 5.20a). Figure 5.20b shows the pore tips after the current has been increased to enlarge the pore diameter. The etching was performed for 180 min with a constant current density of 4.82 mA/cm^2. At the end of the etching the current density was increased to 9.65 mA/cm^2 and was kept constant at this value for 5 min. The higher current causes the critical current density J_{ps} to be reached not only at the center of the pore tips but over a larger area. The electropolishing condition is met also at the pore walls so the electrochemical dissolution there leads to an increase in the pore diameter. Consequently, no microporous silicon layer can be observed on the walls of the enlarged pores. If the current density at the pore tips is lower than required for the formation of an oxide film, then the entire tip area is not covered with oxide film and the macropores are completely filled with microporous silicon (Fig. 5.19).

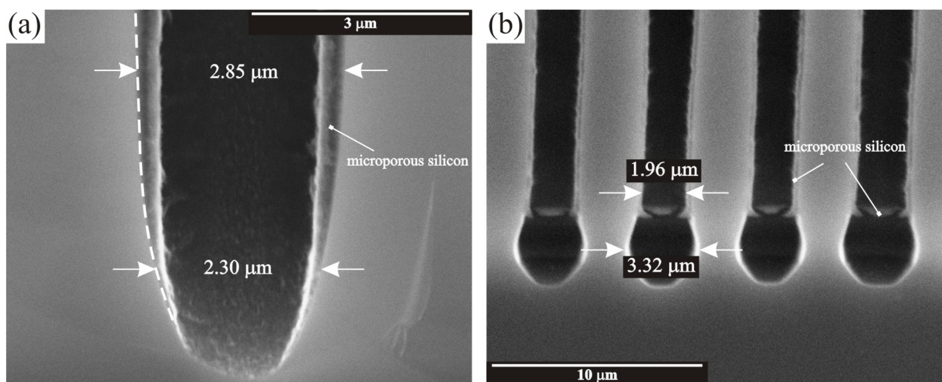

Fig. 5.20. SEM micrographs showing that the pore tips are free of microporous silicon. (a) Microporous silicon layer covering the pore walls (dashed line). (b) Pore tips after the current is increased for few minutes at the end of the etching. The electropolishing condition is met for a larger area of the tips, which leads to an increase in the pore diameter. The regions where electropolishing occurs are free of microporous silicon.

Microporous silicon was not observed at higher potentials and lower currents. Under these conditions, the formation of spiking pores due to electrical breakdown was greater. Figure 5.21 shows macropores etched at an anodic bias of 2 V and a current

ISBN:978-84-693-6270-9/DL:T-1376-2010

density of 0.72 mA/cm^2. Large spiking pores growing out of the macropore walls have not developed but the macropore walls are rather rough. The spikes are probably too small to be easily seen with the SEM magnifications used. From the inset micrograph, which shows a patterned and non-patterned wafer surface, it could be deduced that breakdown pores had formed.

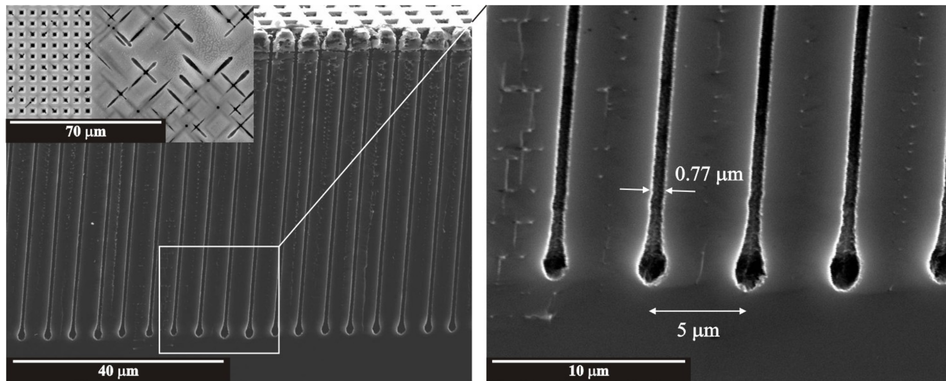

Fig. 5.21. SEM micrographs showing macropores without a microporous silicon layer. The surface roughness of the macropore walls is an indication of the existence of small breakdown-type pores. The inset shows the wafer surface with patterned and non-patterned areas.

In Chapter 3 we discussed that a microporous layer covering the pore walls can be regarded as an interfacial layer between the host dielectric and air rods. The thickness and the dielectric constant of such an interfacial layer has a strong influence on the photonic gap parameters and in some cases (high dielectric constants, thicker layers) can even lead to a complete closure of the absolute band gap. Microporous silicon can be seen as an effective medium, with a refractive index somewhere between that of bulk silicon and air. The effective refractive index of microporous silicon has been shown to be dependent on the degree of porosity attained [237] and can be obtained from Bruggeman effective medium approximation [238]. The porosity itself depends on the etching conditions: current density, doping, HF concentration, etc. However, finding clear relations between the etching conditions and the properties of the microporous silicon layer covering the pore walls is a highly complex problem. The thickness and the porosity of the resulting microporous layer can hardly be known beforehand and so it should be avoided.

Fortunately, the microporous layer can be dissolved easily, for example, by a short dip in TMAH solutions. This is shown in Fig. 5.22. After the electrochemical etching, the sample was immersed in 25 % TMAH solution for 1 min at room

UNIVERSITAT ROVIRA I VIRGILI
PHOTONIC BANDGAP ANALYSIS AND FABRICATION OF MACROPOROUS SILICON BY ELECTROCHEMICAL ETCHING
Trifon Todorov Tirfonov
ISBN:978-84-693-6270-9/DL:T-1376-2010

temperature (Fig. 5.22a). Because of its large surface area, microporous silicon is dissolved almost immediately as is shown in the magnified SEM micrographs. If the TMAH etching is not done properly (as in Fig. 5.22b where the sample was etched for 10 sec) the microporous silicon can only be removed to a certain depth. The SEM micrographs from the right-hand side of Fig. 5.22b suggest that the microporous silicon layer covering the pore walls can have different porosities because the TMAH etching has proceeded with different etching rates. Logically, microporous silicon of higher porosity should be etched more rapidly by the TMAH. Performing the TMAH etch in a vacuum makes it possible to remove the microporous silicon in shorter times and to obtain better results.

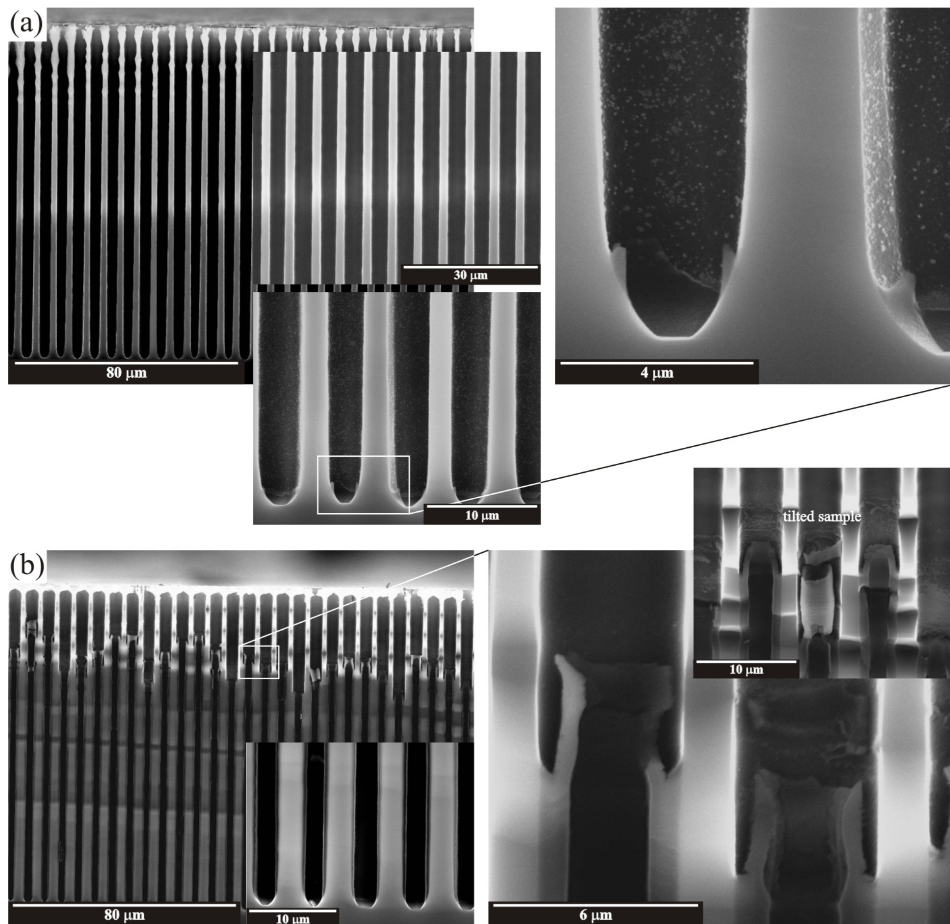

Fig. 5.22. Removing the microporous silicon layer by TMAH etching at room temperature. (a) Sample immersed for 60 sec in 25 % TMAH solution. (b) Sample immersed for 10 sec in 25 % TMAH solution. All SEM micrographs show a single pattern of the same wafer.

UNIVERSITAT ROVIRA I VIRGILI
PHOTONIC BANDGAP ANALYSIS AND FABRICATION OF MACROPOROUS SILICON BY
ELECTROCHEMICAL ETCHING
Trifon Todorov Tirfonov
ISBN:978-84-693-6270-9/DL:T-1376-2010

5.3. Conical pores. Rules for improving pore uniformity.

In Section 5.1.2 we have shown that precise control of the applied current during the etching is required to obtain a stable pore growth and straight pores. A logical conclusion after looking at Eq. 4.5 and 4.6 is that the applied etching current must be kept constant during etching in order for the pore diameter to be constant in depth. However, this argument no longer holds for long anodization times, which are usually required to etch deep pores.

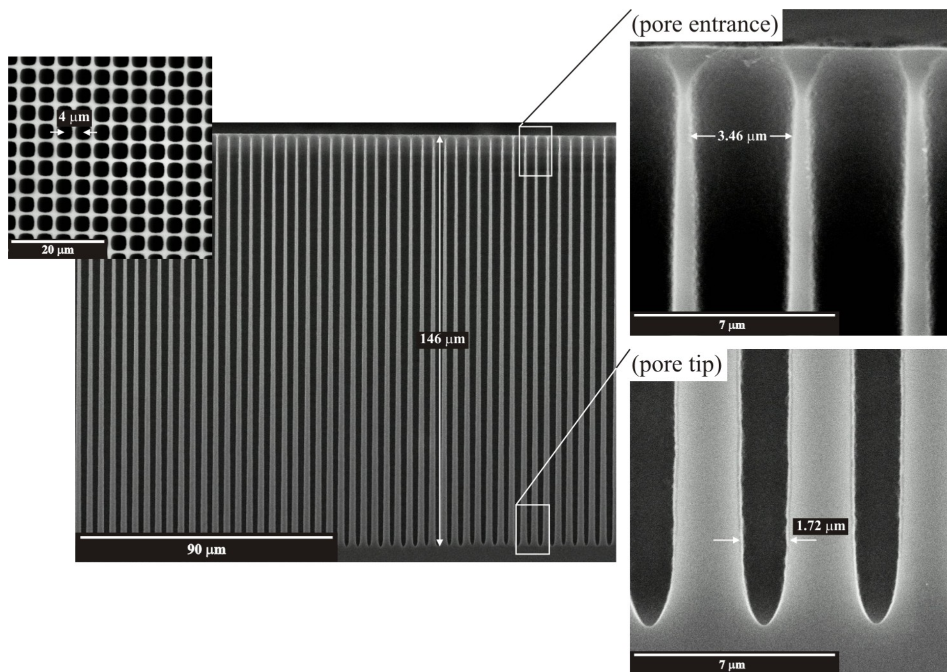

Fig. 5.23. Constant current density during the etching yields conical pores. The structure shown is a square lattice with a 4 μm pitch (inset micrograph) as defined by lithography. The magnified micrographs on the right-hand side are taken from regions around the pore entrance and the pore tip. The diameter near the pore tips is approximately twice as small as the diameter near the entrance. Both diameters are measured 3 μm from the pore entrance and pore tip, respectively.

For example, Fig. 5.23 shows a macropore structure etched by keeping the etching current density constant. A whole 2-inch wafer was pre-structured using the photolithography mask shown in Fig. B.1 (Appendix B) and etched under the following conditions: 2.5 wt.% aqueous HF electrolyte, 1.3 V applied bias, room temperature, 240 min. The SEM micrographs shown are taken from the region with initial **C/4-2**

UNIVERSITAT ROVIRA I VIRGILI
PHOTONIC BANDGAP ANALYSIS AND FABRICATION OF MACROPOROUS SILICON BY
ELECTROCHEMICAL ETCHING
Trifon Todorov Tirfonov
ISBN:978-84-693-6270-9/DL:T-1876-2010

patterning, which defines a square lattice with a 4 µm pitch and 2 µm pore diameter (as shown in the inset micrograph). The etching current was set at 5.23 mA/cm^2 and was kept constant throughout the anodization by adjusting the backside illumination. If we use the equations of Lehmann's model (Eq. 4.6 and 4.7), we can see that this current density should produce pores with a diameter of about 2.65 µm if the cross-section is circular, or pores with a diameter of 2.35 µm if the cross-section is square. As can be seen from the figure, the pore diameter obtained is different from the calculated one whatever the cross section may be. What is more, the macropores are conical in shape and their diameter decreases with depth. The diameter near the pore entrance is about 3.46 µm, while near the pore tip it is about 1.72 µm (i.e. two times smaller).

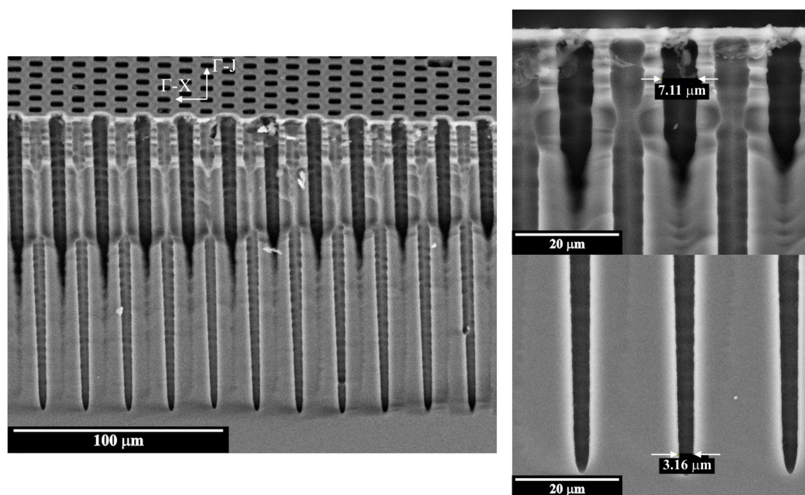

Fig. 5.24. SEM micrographs from the region with the lithographic pattern **T/11.6-5** (triangular lattice with a 11.6 µm period), which was etched simultaneously with the square pattern shown in Fig. 5.23. The diameter near the pore tip is about 2.25 times smaller than the diameter near the pore entrance. The sample is badly cleaved along the **Γ-X** direction of the triangular lattice.

The electrochemical etching in the other regions of the pre-structured wafer with different lithographic patterns also resulted in conical pores. The pore conicity was even slightly enhanced. For example, for the region with the patterning **T/11.6-5** (triangular lattice with a 11.6 µm period) the diameter near the entrance is about 7.11 µm, while near the pore tip it is 3.16 µm (Fig. 5.24). The diameter near the tip is approximately 2.25 times smaller than near the entrance. It should be noted that according to Lehmann's model, the current density used (5.23 mA/cm^2) should provide pore diameters of 6.33 µm or 7.15 µm for the given triangular lattice if the pore cross-

UNIVERSITAT ROVIRA I VIRGILI
PHOTONIC BANDGAP ANALYSIS AND FABRICATION OF MACROPOROUS SILICON BY ELECTROCHEMICAL ETCHING
Trifon Todorov Tirfonov
ISBN:978-84-693-6270-9/DL:T-1376-2010

section is square or circular, respectively. The fact that the pores are conical for all the patterned regions suggests that conical pores are not formed by a possible misadjustment between the initial pattern and the etching conditions. Therefore, a constant etching current is not sufficient to obtain straight pores.

The decrease of the pore diameter as the pore depth increases cannot be ascribed to diffusional limitations because the diffusion-related phenomenon usually leads to an increase in the pore diameter with increasing pore depth [239]. Indeed, the diffusion of the electrolyte is more difficult into deeper pores. This leads to a decrease in the HF concentration towards the pore tips and to a concomitant decrease in the critical current density J_{ps}. According to Eq. 4.6, if the applied current density J is kept constant during the etching the decrease in J_{ps} would result in an increase in the porosity and, thus, in increasing pore diameters in depth, which has not been observed in our samples. The formation of conical pores, the diameter of which decreases with depth, can be attributed to an increase in the dark current density because of the increased pore surface area during the etching. Indeed, the total etching current J flowing through the system will be a sum of the real pore tip current J_{tip} and the dark current J_{dark}: that is, $J = J_{tip} + J_{dark}$. If the applied current J is kept constant, the real pore tip current J_{tip} gets smaller because J_{dark} increases with anodization time. This means that the steady state condition $J_{tip}=J_{ps}$ is reached for smaller and smaller areas of the pore bottom during the etching, which finally results in a reduced pore diameter at depth. In order to obtain a constant pore diameter at depth we must search for ways of compensating for the effect of the increased dark current density, as well as for ways of reducing the higher dark current.

5.3.1. Nitrogen bubbling of the electrolyte

The reverse current at an n-type silicon electrode anodized in dark was found to depend on the temperature and the oxygen concentration in the electrolyte (see Ref. 187, fig. 4.11 on page 65). The dark current increases significantly with increasing the concentration of the diluted oxygen. Since all electrolytes dissolve some oxygen from the air, displacing the dissolved oxygen by bubbling of the electrolyte with nitrogen is necessary to reduce the dark current to some extent. Figure 5.25 shows SEM micrographs taken from the region with the **C/4-2** patterning. The wafer was etched at room temperature in 2.5 wt.% aqueous HF solution for 240 min. The applied voltage was 1.3 V. The current density was kept constant at 4.98 mA/cm^2. The major difference with the case discussed above is that the electrolyte was bubbled by nitrogen for 30 min

UNIVERSITAT ROVIRA I VIRGILI
PHOTONIC BANDGAP ANALYSIS AND FABRICATION OF MACROPOROUS SILICON BY ELECTROCHEMICAL ETCHING
Trifon Todorov Tirfonov
ISBN:978-84-693-6270-9/DL:T-1876-2010

before and during the anodization. The pore diameters near the entrance and the tip of the pores are 3.42 and 2.22 μm, respectively. Therefore, the pore diameter near the tip is about 1.54 times smaller than the diameter near the entrance, which is much better than in the previous case. Since there is no way of knowing what the amount of diluted oxygen will be for different electrolytes, the electrolyte must be bubbled with nitrogen before and during the etching to obtain more reproducible results.

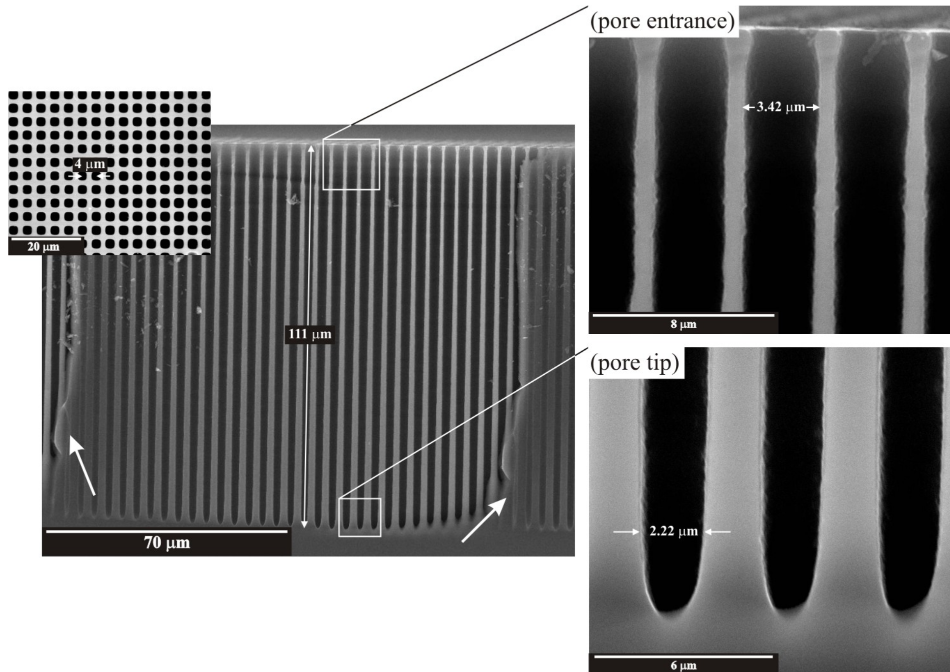

Fig. 5.25. Bubbling the electrolyte with nitrogen during the etching helps to reduce the pore conicity by lowering the dark current density. The SEM micrographs are taken from the region with the **C/4-2** patterning. The diameter near the pore tip is now 1.54 times smaller than the diameter near the pore entrance. Both diameters are measured 3 μm from the pore entrance and pore tip, respectively. The artifacts indicated by arrows were caused by the wafer being cleaved into different rows of pores.

5.3.2. Etching at lower temperatures

At lower temperatures the electrochemical dissolution rate slows down. As can be seen from Eq. 4.7, the critical current density J_{ps} has an Arrhenius-type dependency on the electrolyte temperature [125]. Lowering the temperature reduces the critical current density J_{ps}. Therefore, the electrochemical dissolution rate determined from

ISBN:978-84-693-6270-9/DL:T-1376-2010

Eq. 4.3 also decreases since the current density at the pore tips J_{tip} equals the critical current J_{ps} under conditions of stable pore growth. Arrhenius type of behavior with respect to the temperature has also been observed for the reverse current at an n-type electrode anodized without illumination [187]. It is advisable to perform the etching at lower temperatures to inhibit the formation of conical pores.

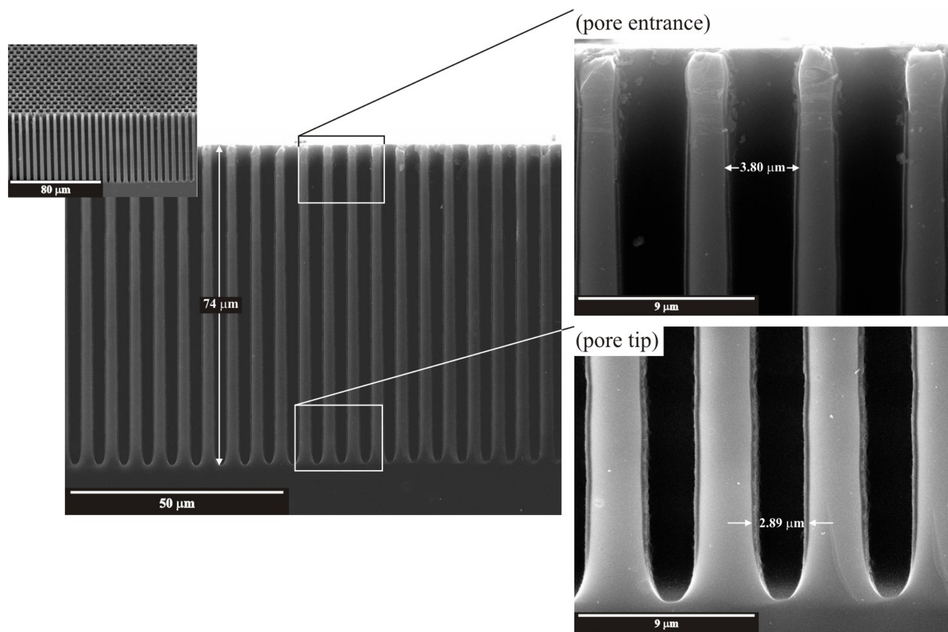

Fig. 5.26. An example of macropores etched at an electrolyte temperature of 10°C. The dark current at lower temperatures is reduced because of the lower concentration of thermally generated carriers. The pore depth is 74 µm even though the anodization time (240 min) was similar to that of the previous cases. This indicates that the dissolution rate has slowed down. The ratio between the pore diameters near the entrance and near the tip is 1.32. The micrographs are taken from the region with the **T/5.8-3** patterning.

Figure 5.26 shows an example of macropores etched at 10°C. At this temperature, the critical current density (calculated using the empirical relation from Lehmann's model - Eq. 4.7) is reduced from J_{ps}=15.17 mA/cm^2 to J_{ps}=9.45 mA/cm^2. This means that the etching current should be lower so that the porosity is the same as in the previous cases. An n-type wafer (patterned using the lithographic mask in Fig. B.1) was etched with an applied bias of 1.3 V and a constant current density of 2.57 mA/cm^2. Although the anodization time was 240 min, the pore depth was 74 µm, which indicates that the dissolution rate slows down because of reduced J_{ps}. The micrographs in

UNIVERSITAT ROVIRA I VIRGILI
PHOTONIC BANDGAP ANALYSIS AND FABRICATION OF MACROPOROUS SILICON BY ELECTROCHEMICAL ETCHING
Trifon Todorov Tirfonov
ISBN:978-84-693-6270-9/DL:T-1376-2010

Fig. 5.26 are taken from the region with **T/5.8-3** patterning (triangular lattice with a 5.8 μm period and a 3 μm diameter). For this lattice period and for the etching current used, the pore diameter according to Lehmann's model should be 2.82 μm (3.18 μm) assuming the pore shape is square (circular). The pore diameter obtained is 3.80 μm and 2.89 μm near the pore entrance and tip, respectively. Again, the pore diameter matches the calculated values only for the "bulk" of the structure, which is a consequence of the pore conicity. Nevertheless, the diameter near the tip is approximately 1.32 times smaller than near the pore entrance, which is a more promising result.

Lower temperatures are also recommended when macropores with modulated pore diameters at depth are to be etched [183]. At room- and higher temperatures the etching process becomes rather unstable. The dark currents are higher because of thermally generated carriers and can easily drive the system out of the stable pore-growth regime. For macropores with a modulated pore diameter, diffusional limitations can give rise to inhomogeneities in the modulation period if the frequency of the current variations is kept constant. Indeed, diffusional limitations entail a steady decrease in the HF concentration with pore depth, which in turns reduces the dissolution rate. Thus, if the current variations are applied at a linear time scale the changes in the dissolution rate will give rise to non-equidistant variations in the pore diameter.

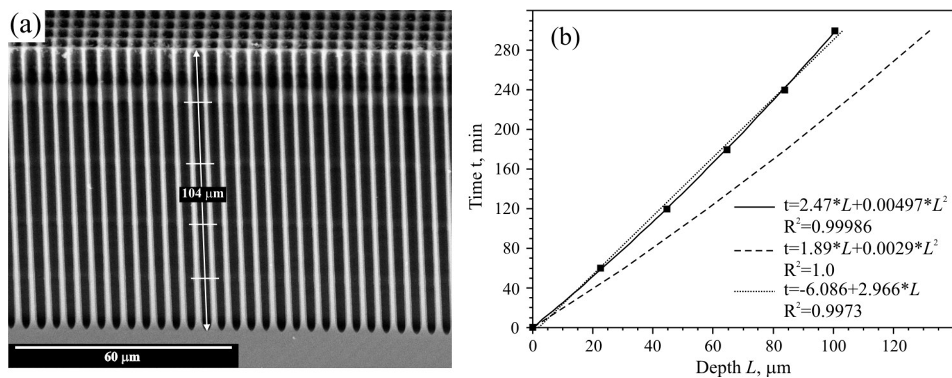

Fig. 5.27. The dependence of the macropore diameter on the etching current provides a perfect tool for setting depth markers (a) by controlling the light source. The SEM micrograph shows macropores arranged in a square lattice with a 5 μm period. The pore diameter was decreased every hour by reducing the etching current (by 33%) from its initial value (2.65 mA/cm^2). These depth markers are used to measure the pore depth as a function of the etching time (b). The filled squares represent the experimental results. The solid curve is a parabolic fit of the results, where R^2 denotes the coefficient of determination. The linear fit (dotted line), which would account for a constant growth rate, is given only for purposes of comparison. The dashed line represents the results after [125].

ISBN:978-84-693-6270-9/DL:T-1376-2010

To find how the growth rate changes with pore depth and also to see what is the effect of limited diffusion in deeper pores, we used the possibility of modulating the pore diameter by controlling the light source. The wafer was etched at 10°C for 300 min. The current density was periodically kept at 2.65 mA/cm^2 for 55 min and then reduced to 1.77 mA/cm^2 for 5 min. This current reduction resulted in a slight decrease of the pore diameter, which can be easily detected by SEM (Fig. 5.27a). The results of measuring the pore depth between each of those depth markers are shown in Fig. 5.27b where the etching time t is plotted versus the pore depth L. The results fit with a parabolic curve very well (see figure legend). We also give the coefficient of determination R^2, which is a measure of how well the fitting curve represents the data. A linear fit of the data (dotted line) is given only for purposes of comparison. We also plot the results (dashed line) found by Lehmann (Ref. 125, Fig. 9). There could be two reasons for the discrepancy in the results. First, we performed the etching at a lower temperature. One of the consequences of this is the lower etch rate observed for our results, although the HF concentration used by Lehmann is the same (2.5 wt.% HF). Second, the dissolution of the pore walls in our case may have been greater, which accounts for the formation of conical pores and also for the higher non-linear coefficient in our fit. If the HF is also consumed at the pore walls, the concentration gradient is nonlinear and pore growth is delayed [187], which is what we observed in our case.

Looking at the empirical data given in Fig. 5.27b, we can conclude that the pore growth rate decreases with the etching time because of diffusional limitations in the deeper pores. This data can be used to make the necessary correction to the current profile in order to compensate for the reduced growth rate and to obtain equidistant changes in the pore diameter with depth. Similar studies for different temperatures and HF concentrations must also be made.

5.3.3. Compensation of pore conicity by increasing etching current

Increasing the applied current density during the etching is an effective way of preventing conical pores form forming. As we have already discussed at the beginning of this section, the dark current J_{dark} increases because of the larger pore surface area and leads to a decrease in the real pore-tip current J_{tip} if the applied etching current J is kept constant (from the relation $J = J_{tip} + J_{dark}$). Therefore, if we increase the etching current in such a way that the real tip current J_{tip} remains constant during the etching, no conical pores will be formed regardless of the increasing J_{dark}. What we actually have to do is to etch pores with the reverse conical shape: that is, pores with increasing diameter

UNIVERSITAT ROVIRA I VIRGILI
PHOTONIC BANDGAP ANALYSIS AND FABRICATION OF MACROPOROUS SILICON BY ELECTROCHEMICAL ETCHING
Trifon Todorov Tirfonov
ISBN:978-84-693-6270-9/DL:T-1876-2010

with depth, in order to compensate for the initial pore conicity we have discussed above. The increment in the etching current can be found from the following considerations. Let J_{const} be the constant current density which, if applied, yields conical pores with diameter d_{tip} near the pore tip. If d_{wanted} is the desired pore diameter near the tip, the new current J_{new} to which we have to increase during the etching can be found from the relation [239]:

$$J_{new} = J_{const}\left(\frac{d_{wanted}}{d_{tip}}\right)^2 \tag{5.1}$$

Note that the values of J_{const} and d_{tip} are known from the experiment. Of course, this optimization should be applied for a few etching runs in order to get more "perfect" pores.

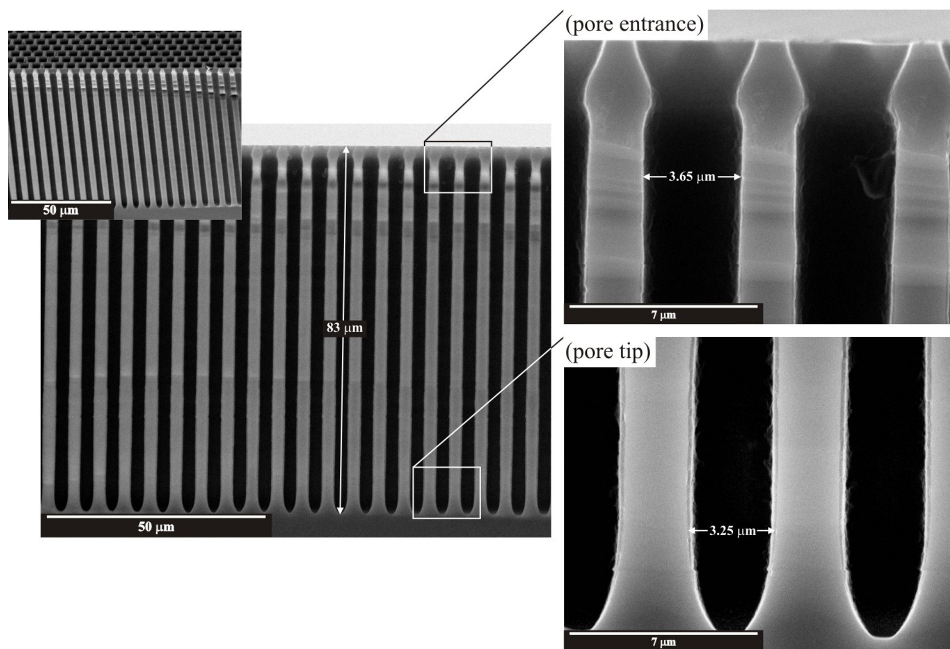

Fig. 5.28. Increasing the etching current density with the anodization time could be an effective way of reducing the pore conicity. The SEM micrographs are taken from the region with the **T/5.8-3** patterning. The pore diameter near the tip is now 1.12 times smaller than the diameter near the entrance. The diameters are measured at 4 μm and 5 μm from the pore tip and entrance, respectively.

Figure 5.28 shows macropores that were etched at room temperature for

ISBN:978-84-693-6270-9/DL:T-1376-2010

150 min. The etching current density was increased linearly from 4.18 mA/cm^2 to 6.43 mA/cm^2. Assuming the pores to be square (circular), the pore diameters pre-determined with Lehmann's model are 2.83 μm (3.20 μm) for the initial current density and 3.51 μm (3.96 μm) for the current density at the end of the etching. As can be seen from the magnified micrographs, the pore diameters obtained roughly match the values calculated for the square pore section. However, the most important fact here is that the difference between the diameters near the pore entrance and near the tip is minimized. The pore diameter near the tip is now only 1.12 times smaller than the diameter near the entrance. However, a lot still remains to be done if the pore uniformity is to be further improved. For example, if we look more carefully at the SEM micrographs, we will see that the pore diameter near the tip is somewhat greater than the diameter half way along the pore. This means that a linear increase in the current may not be the best choice. For deeper pores, diffusional limitations will also be important and will affect not only the growth rate but also the pore diameter. Therefore, perfect macropore arrays can be obtained if the applied current density is adjusted in such a way that the effects of diffusional limitations and high dark currents can be compensated for. Clearly, a great deal of empirical data is needed to achieve this.

It is worth mentioning that the measured pore diameters and lengths given in this section must be considered only as roughly accurate. Some errors inevitably arise from difficulties in determining the exact pore diameter from the SEM micrographs. SEM micrographs do not always show the true size of a pore due to secondary electrons which are backscattered from the inside of the pores [197].

5.4. Effects of surfactants on macropore growth

So far we have only discussed the formation of macropore arrays after etching in aqueous HF electrolytes. Hydrogen bubbles are the main source of degeneration in the spatial homogeneity of the fabricated macropore arrays. Since the hydrogenated silicon surface is strongly hydrophobic, the H_2 bubbles stick to the wafer surface and prevent a fresh electrolyte from reaching the pores. As a result, the macropores degenerate in the spatially limited region corresponding to the bubble diameter (Fig. 5.29). The SEM micrographs are taken from the region with **H/4.8-2.3** patterning, which corresponds to a honeycomb lattice with a center-to-center distance of 4.8 μm between two neighboring holes. In the regions where bubbles have stuck to the wafer surface, the macropores have grown in an unstable fashion. In contrast, outside these regions (right SEM micrograph) the macropore formation is stable. The electrochemical

ISBN:978-84-693-6270-9/DL:T-1376-2010

etching was performed at room temperature for 240 min. The electrolyte was bubbled by nitrogen and the etching current was linearly increased throughout the etching from 3.38 mA/cm^2 to 4.98 mA/cm^2. Under these conditions, the macropores obtained are 115 μm deep and have diameters of about 3.8 μm near the entrance and 2.9 μm near the tip. This indicates that the macropores are still slightly conical in shape.

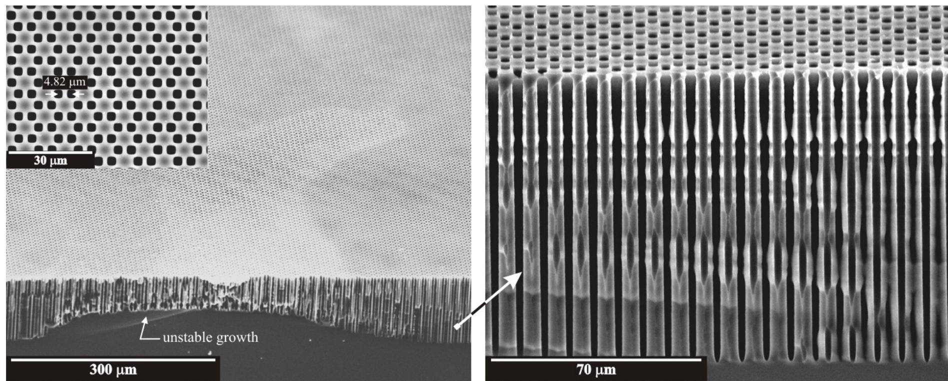

Fig. 5.29. Bubbles sticking to the wafer surface degenerate the macropores in the spatially limited region of the bubble diameter (left micrograph). Outside these regions macropore growth is stable (right micrograph). The **H/4.8-2.3** patterning shown corresponds to a honeycomb lattice with a center-to-center distance of 4.8 μm between neighboring holes (Fig. B.2 from Appendix B).

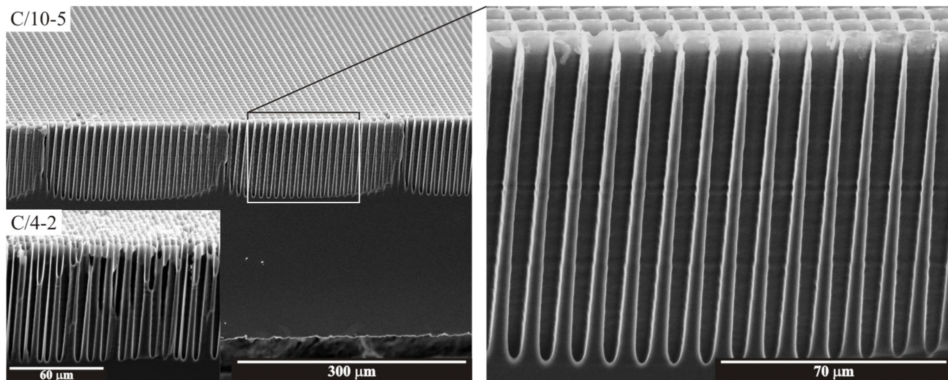

Fig. 5.30. Adding ethanol improves the spatial homogeneity of the macropore arrays because it reduces the surface tension and, therefore, the sticking probability of hydrogen bubbles. However, the electrolyte composition of 1:9:10 (HF:EtOH:H_2O volume ratio) gave rise to enhanced lateral etching along the pore walls, which produced macropores with a strong conical shape at depth. With the exception of the inset, the SEM micrographs are taken from a region with **C/10-5** patterning. Some macropores died for all patterns with a pitch less than 10 μm (e.g. region **C/4-2** of the inset micrograph).

ISBN:978-84-693-6270-9/DL:T-1376-2010

To prevent the problem of bubble sticking, ethyl alcohol (EtOH) is usually added to the electrolyte to reduce the surface tension at the silicon/solution interface and therefore to reduce the sticking probability of the hydrogen bubbles. Adding ethanol helps to improve the spatial homogeneity of the etched macropore arrays. This is shown in Fig. 5.30, where the electrolyte composition was set at 1:9:10 (volume ratio) of HF:EtOH:H_2O. The electrochemical etching was performed at room temperature for 240 min. The applied current density was set at 4.42 mA/cm^2 and was kept constant throughout the etching. The macroporous structures formed were thoroughly inspected under scanning electron microscope and no degeneration of the macropores due to bubble sticking was observed. Experimental evidence can be seen in the left SEM micrograph, taken at very low magnification. However, changes in the electrolyte composition led to changes in the conditions that identify the onset of stable macropore growth. The current density used was good enough to provide stable macropore growth when aqueous HF electrolytes were used. In the present case, however, pore growth was unstable in the regions with a lattice period less than 10 μm. The micrographs in Fig. 5.30 are taken from the region with **C/10-5** patterning. The electrochemical etching for the **C/4-2**, **C/5-3**, **T/4.6-2**, and **T/5.8-3** patterns resulted in many dead pores. For example, the inset micrograph in Fig. 5.30 is taken from the region with **C/4-2** patterning. The pore walls are very thin and even destroyed close to the surface, which is an indication of a high formation current. Nevertheless, this current density was found to work very well for aqueous HF electrolytes. Besides, the macropores formed in ethanoic HF etchant were much more conical than those formed in aqueous HF. More experiments are needed to gain clear insights into the problem.

Ethanol is added to the electrolyte as a wetting agent. However, the quantity of ethanol required to obtain the “bubble-removing” effect is rather large (tens of a percent). The surface tension can be similarly reduced in solutions containing small concentrations of surfactants. By using surfactants instead of ethanol it is possible to prevent variation of solution composition with temperature. What is more, surfactant-containing solutions are cheaper than ethanoic ones [203]. However, electrochemical etching was found to be affected not only by the type, but also by the amount of surfactant added to the electrolyte [203,204]. The amphiphilic surfactants consist of a polar head group and an apolar tail. In HF solutions, the silicon surface is H-terminated and exhibits hydrophobicity so, at low concentrations, surfactant molecules are expected to absorb quickly onto the silicon surface with their apolar tails attached to the surface and their polar heads sticking out. This may affect not only the kinetics of silicon dissolution but also the local electrostatic properties and, in turn, the electrochemical

UNIVERSITAT ROVIRA I VIRGILI
PHOTONIC BANDGAP ANALYSIS AND FABRICATION OF MACROPOROUS SILICON BY
ELECTROCHEMICAL ETCHING
Trifon Todorov Tirfonov
ISBN:978-84-693-6270-9/DL:T-1376-2010

behavior at the interface [204]. We tested two types of surfactants: a nonionic surfactant TritonX-100 and an anionic one – sodium dodecyl sulfate (SDS). In what follows, we shall discuss how the type and the concentration of these surfactants affect macropore morphology.

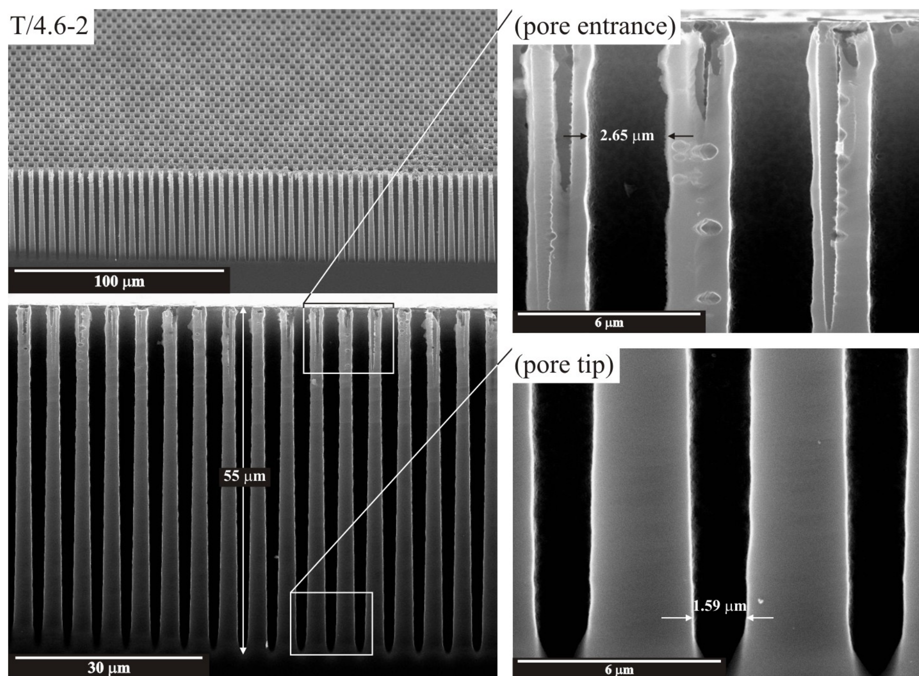

Fig. 5.31. The nonionic surfactant TritonX-100 (0.18 mM concentration) improves the spatial homogeneity of the macropore arrays by reducing the surface tension and, therefore, the probability of H_2 bubbles sticking. However, it increases the dark current, which leads to greater pore conicity. The pore diameter near the tip is 1.67 times smaller than near the entrance, which indicates that the pores are not as straight as in the surfactant-less case.

Figure 5.31 shows macropores formed after anodization in 2.5 wt.% HF electrolyte containing TritonX-100 surfactant at a concentration of about 0.18 mM. The wafer, which was patterned using the mask from Fig. B.1, was etched at room temperature for 105 min. The applied etching current of 4.18 mA/cm^2 was kept constant during the anodization. The SEM micrographs shown are taken from the region with **T/4.6-2** patterning, which defines a triangular lattice with a 4.6 μm pitch. As can be deduced from the upper left micrograph, pore degeneration due to bubble sticking is minimized. Therefore, the use of surfactants even at such low concentrations favors the formation of spatially homogeneous macropore arrays. The surfactants modify the

wetting properties of the silicon surface and thus reduce the probability of H_2 bubble sticking. However, we have observed that the nonionic TritonX-100 surfactant leads to the formation of strongly conical pores, as shown by the right-hand micrographs. The pore diameter near the tip (1.59 μm) is 1.67 times smaller than the diameter near the entrance (2.65 μm) even after such a short anodization time (shallow pores). The reason for this may be that the addition of TritonX-100 increases the dark current density, which we have blamed for the formation of conical pores. Recently, it has turned out that conical carrot-shaped pores are obtained because the applied current contributes less to the pore growth and more to the dark current [240]. Cationic and nonionic surfactants give rise to a higher dark current density, which increases with increasing surfactant concentration. On the other hand, anionic surfactants reduce the dark current by increasing the surface potential barrier at the silicon-electrolyte interface [240]. The TritonX-100 is a nonionic surfactant and it is possible that the dark current density was greater in the present case than when no surfactant was used. One indication for this is the presence of unwanted breakdown-type pores which grew on the walls between the macropores of the intended structure (upper right micrograph in Fig. 5.31). For the surfactant-less case under similar etching conditions, such pores were not observed. The higher dark current may eventually initiate the formation of breakdown-type pores, which in turn causes a further increase in the dark current by local breakdown at the pore tips [187]. We think that this effect is observed here.

Higher concentrations of the TritonX-100 surfactant led to higher dark current densities and increased the formation of breakdown-type pores near the surface. Figure 5.32 shows SEM micrographs taken from the region with the same **T/4.6-2** patterning as in the previous case. The wafer was etched in 2.5 wt.% HF containing TritonX-100 at a concentration of about 0.4 mM. The anodization time was 240 min. The current density was increased linearly from 4.34 mA/cm^2 to 5.95 mA/cm^2 during the etching in an attempt to reduce the pore conicity. This approach was found to work quite well as has been demonstrated in the previous section. Despite the increased etching current, the macropores obtained were strongly conical. The ratio of the pore diameter near the entrance to the diameter near the tip is about 1.73. This value could be wrong because the pore walls near the wafer surface are almost completely destroyed and it is difficult to determine the pore diameter exactly. The macroporous structure resembles one formed after etching at higher anodic potentials (Fig. 5.16) with high-density spiking pores at the beginning. In the present case, however, the anodic potential was set at 1.2 V which generally produced no spiking pores for electrolytes without surfactants even at very long anodization times.

UNIVERSITAT ROVIRA I VIRGILI
PHOTONIC BANDGAP ANALYSIS AND FABRICATION OF MACROPOROUS SILICON BY ELECTROCHEMICAL ETCHING
Trifon Todorov Tirfonov
ISBN:978-84-693-6270-9/DL:T-1376-2010

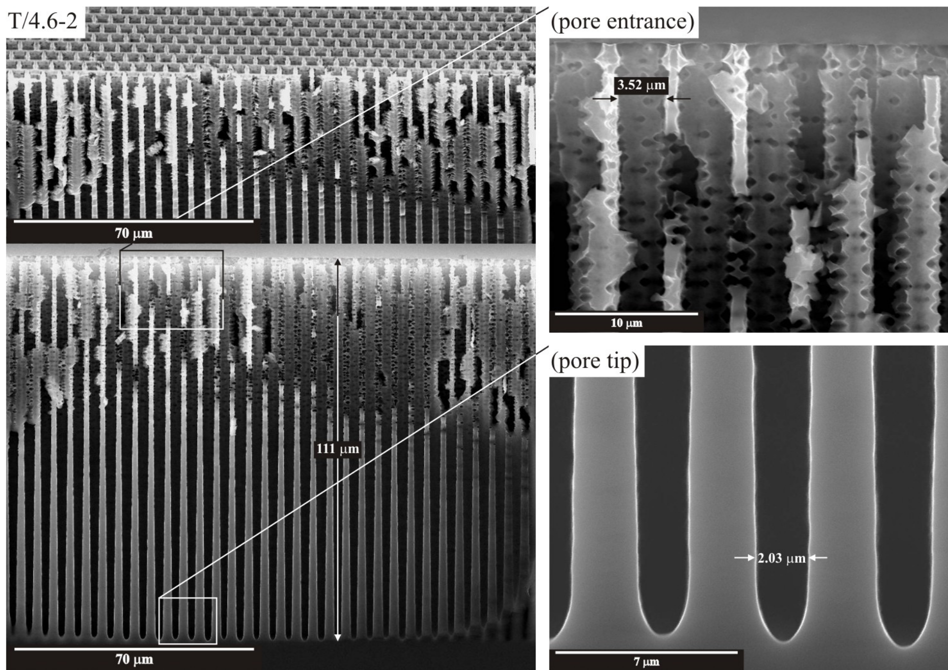

Fig. 5.32. Macropores etched in HF electrolyte containing TritonX-100 surfactant at a concentration of 0.4 mM. The higher concentration of the surfactant increased the dark current density and the formation of high-density spiking pores near the surface. The macropores have a strong conical shape although the etching current was increased in an attempt to reduce the pore conicity.

The measurements of the dark current density after the backside illumination had been switched off at the end of the etching revealed the following. For the first of the two cases mentioned above (i.e. a concentration of 0.18 mM TritonX-100) the dark current density was measured to be about 0.56 mA/cm^2. This means that the dark current was about 13% of the total etching current. When TritonX-100 was used at concentration of 0.4 mM, the measured dark current (1.21 mA/cm^2) was 28 % of the total current (4.34 mA/cm^2 for the etching current is used as a reference). Any further increase in the TritonX-100 concentration increases the contribution of the dark current to the total etching current. Figure 5.33 shows macropores etched with a 1.1 mM concentration of the surfactant in the electrolyte. The etching was performed for 240 min with a constant current density of 3.50 mA/cm^2. After switching off the backside illumination, the dark current was about 1.36 mA/cm^2, which is 39% of the total etching current. As can be seen from the figure, there are a lot of dead pores, but interestingly many of these are terminated by narrow microcracks. It can be speculated that the dark current density is high enough to move the system in the transition regime

between the stable pore growth and the growth of breakdown-type pores because of the enhanced electric field strength at local defects. The macropore tips can be considered as local defect sites. Also, macropores die after a certain depth is reached, which can be explained with the enhanced contribution of the dark current because of continuously increasing pore surface area with increasing pore depth.

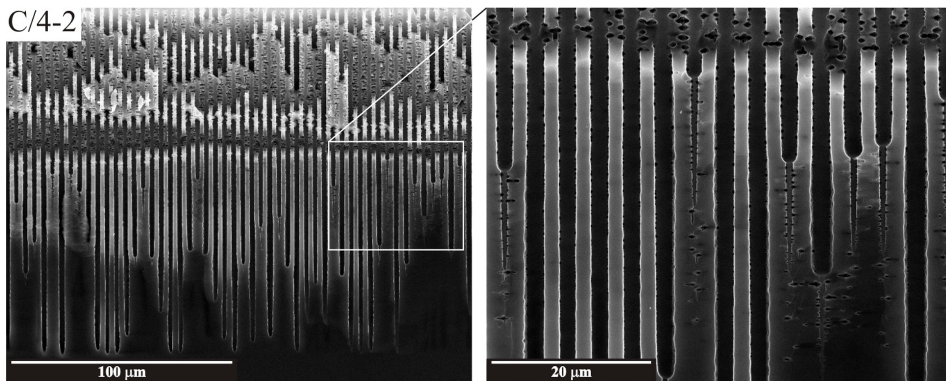

Fig. 5.33. Macropores etched in HF electrolyte with a 1.1 mM concentration of TritonX-100 surfactant. The macropores are arranged in a square lattice with a 4 μm pitch as defined by the initial **C/4-2** pattern. The pore growth becomes unstable because of the higher dark current, which draws the system out of the stable growth regime.

From the results discussed above, it can be concluded that adding TritonX-100 to the electrolyte helps to improve the regularity of the macropore arrays produced because it makes the hydrophobic silicon surface wettable by water and, therefore, favors the removal of hydrogen bubbles from the surface. However, very low concentrations (well below 0.18 mM) should be used because TritonX-100 increases the dark current density and enhances the formation of conical pores. The dark current density increases with increasing TritonX-100 concentration and could even draw the system out of stable pore growth for concentrations as high as 1 mM.

Having discussed the use of the TritonX-100 surfactant, we now go on to study how adding the SDS, which is an anionic surfactant, affects the etching process. Figure 5.34 shows the macropores obtained after etching in 2.5 wt.% HF containing SDS surfactant at a concentration of about 1.02 mM. The wafer was etched at room temperature for 247 min with a constant etching current of 4.82 mA/cm^2. Under these conditions, regular 110 μm-deep pores were obtained for the region with a **T/4.6-2** initial patterning. The ratio of the pore diameter measured near the entrance to the diameter measured near the pore tip is about 1.06. Note that the microporous layer

UNIVERSITAT ROVIRA I VIRGILI
PHOTONIC BANDGAP ANALYSIS AND FABRICATION OF MACROPOROUS SILICON BY
ELECTROCHEMICAL ETCHING
Trifon Todorov Tirfonov
ISBN:978-84-693-6270-9/DL:T-1376-2010

formed on the pore walls was not taken into account for the measurements. It is difficult to measure the thickness of the microporous layer in the region near the surface from the present micrographs. The microporous layer must be removed and then the diameter must be measured again. We lack such information at this time. One of the reasons why the microporous layer is thicker could be that the etching proceeded in the onset of currents limited by the applied bias (see Section 5.2). The applied bias was set at 1.4 V and measured against the reference electrode. Adding the anionic surfactant SDS might change the electrolyte conductivity and the current-voltage characteristic of the system, so the real anodic potential at the HF/silicon interface will be different from the measured one.

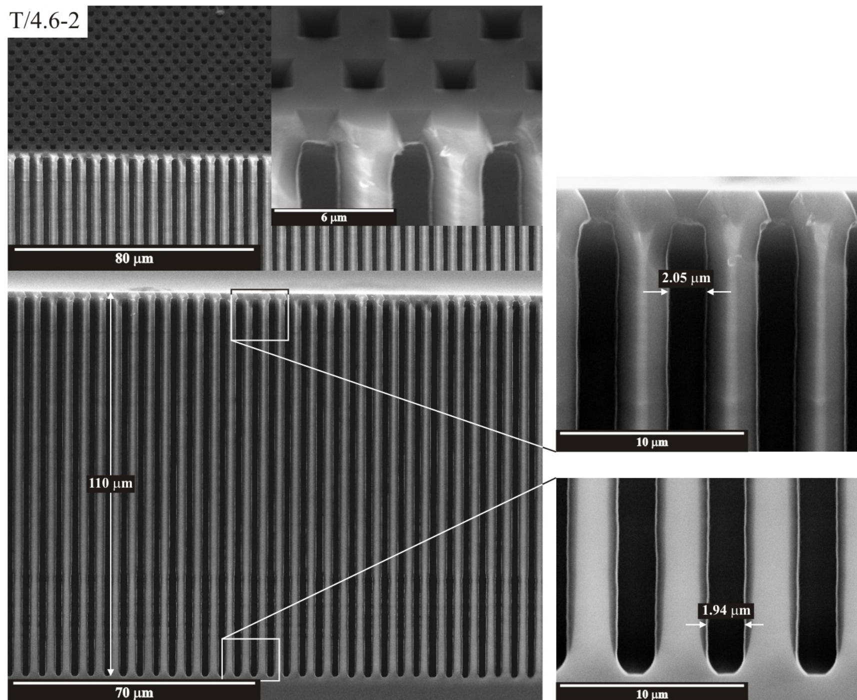

Fig. 5.34. Macropores formed after etching in SDS containing electrolyte. The concentration of anionic surfactant was about 1.02 mM. Keeping the applied current constant during the etching was sufficient to produce almost straight pores. The microporous layer was not taken into account when measuring the pore diameter. No spiking pores are observed despite the long anodization time and relatively high SDS concentration.

The dark current density at the end of the etching was measured to be 0.1 mA/cm^2, which is about 2% of the total etching current. This reduction in the dark current is reflected in the quality of the macropore arrays produced. The macropores are

now less conical than those etched without a surfactant or those etched with TritonX-100. The reason why different types of surfactants have different effects on the anodization process has not yet been clarified. During the anodization process, the surfactant molecules are adsorbed at the silicon electrode with their apolar tails attached to the surface. As suggested by Chao *et al.* [204], the density of the surfactant adsorbed on the sidewall of macropores could be higher than at the tip because of geometric constraints. The anionic surfactants (e.g. SDS) have a polar head group that carries a negative charge so they may hinder the diffusion of anionic fluoride ions/silicon fluoride complexes at the interface. In turn, this may protect the sidewalls against dissolution, which is the effect observed here. Experimental evidence for this notion is shown in Fig. 5.35. The SEM micrographs are taken from the region with **C/10-5** patterning. No stable pore growth was expected for this region because of the mismatch between the wafer resistivity (2-3 Ωcm) and the initial pattern, which defined pores spaced at large distances (10 μm). Therefore, the lattice constant a is greater than the width of the space charge region L_{SCR}, i.e. $a \gg L_{SCR}$, which can induce branching of the macropores as discussed in Chapter 4 (Fig. 4.7). In the case of the TritonX-100 surfactant, the macropores are strongly branched on the sidewalls (Fig. 5.35a), whereas in the case of SDS, branching occurs only at the pore bottom (Fig. 5.35b) – the macropores divide into two or more pores to adjust the porosity. It seems therefore that the anionic SDS surfactant protects the macropore walls against further dissolution.

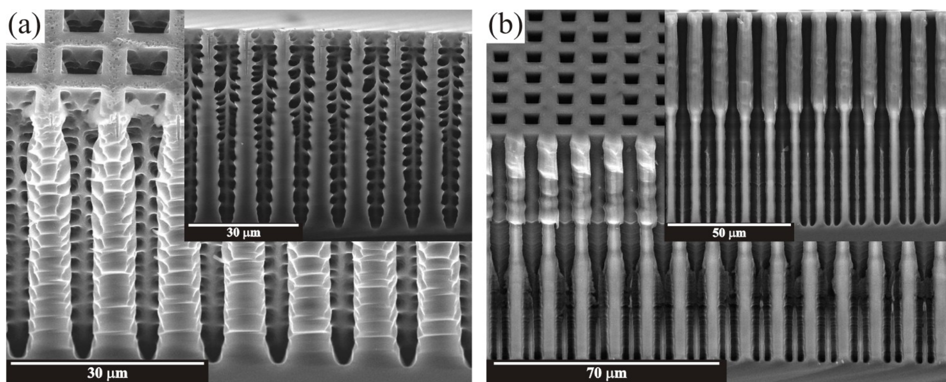

Fig. 5.35. Macropores etched in 2.5 wt.% HF electrolyte containing (a) 0.18 mM TritonX-100 and (b) 1.02mM SDS surfactants. The micrographs in both cases are taken from the region with initial **C/10-5** patterning. The mismatch between the wafer resistivity (2-3 Ωcm) and the initial pattern gives rise to branching of the macropores. For the electrolyte containing TritonX-100, the macropores are strongly branched on the sidewalls, whereas for the SDS surfactant the macropores divide into two or more pores at depth. This indicates that the SDS surfactant has a passivation effect on the macropore walls.

UNIVERSITAT ROVIRA I VIRGILI
PHOTONIC BANDGAP ANALYSIS AND FABRICATION OF MACROPOROUS SILICON BY
ELECTROCHEMICAL ETCHING
Trifon Todorov Tirfonov
ISBN:978-84-693-6270-9/DL:T-1376-2010

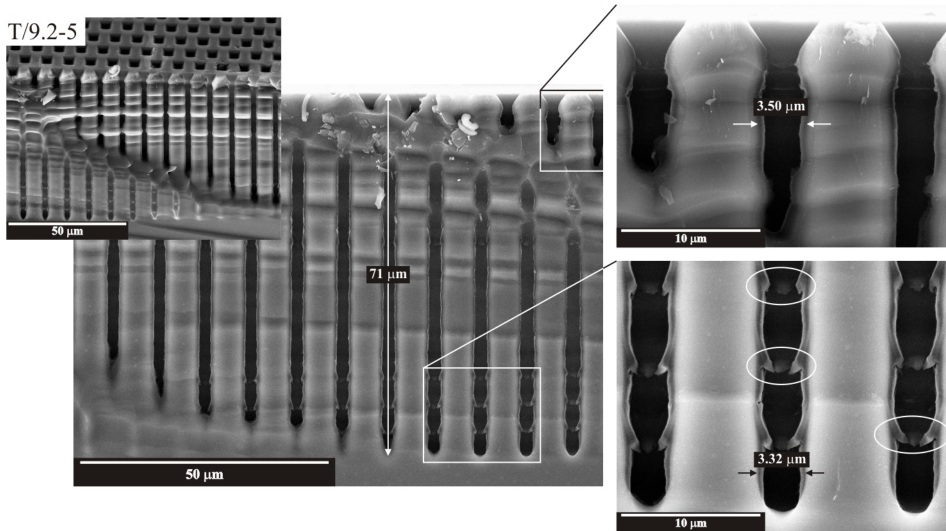

Fig. 5.36. Macropores etched in 2.5 wt.% HF electrolyte containing 0.21 mM of SDS anionic surfactant. The addition of SDS affected the etching process in the same way as 1.02 mM did (see Fig. 5.34). Some distinctive effects of the changed concentration were not noticed. The contribution of the dark current to the total etching current is reduced by adding SDS, which yields straight pores. The cleaving is along different rows of pores. The artifacts enclosed by white ellipses were caused by a periodic decrease in the applied etching current, which was intentionally induced.

The electrochemical etching performed by adding the SDS surfactant at lower concentrations (0.21 mM) produced similar results. The wafer was etched at room temperature for 160 min by keeping the etching current constant (4.82 mA/cm^2). Figure 5.36 shows macropores etched under these conditions. The SEM micrographs are taken from the region with **T/9.2-5** patterning. The shown edge of the sample is the result of an unlucky cleaving along the **Γ-J** direction (i.e. the cleaving is along different rows of pores). The artifacts enclosed by ellipses were caused by a decrease in the applied etching current every 15 min, which we intentionally induced in an attempt to establish depth markers by modifying the pore diameter. This experiment failed because the current variations were applied for a very short time – the current was reduced to 60% of its constant value for only 3 min. Nevertheless, the micrographs are good enough to measure the pore diameters at different depths. The diameter near the pore tip is only 1.05 times smaller than the diameter near the entrance. The dark current measured after the backside illumination had been switched off at the end of the etching was less than 1% of the total etching current. All these findings suggest that the problem of producing conical pores, which we have discussed above, can be effectively avoided

UNIVERSITAT ROVIRA I VIRGILI
PHOTONIC BANDGAP ANALYSIS AND FABRICATION OF MACROPOROUS SILICON BY ELECTROCHEMICAL ETCHING
Trifon Todorov Tirfonov
ISBN:978-84-693-6270-9/DL:T-1376-2010

by adding SDS surfactant to the electrolyte. A more systematic study of the effects of SDS on the etching process at different surfactant concentrations and electrolyte temperatures is required.

5.5. Conclusions

Ordered macropore formation achieved by lithography and light-assisted electrochemical etching of n-type silicon is proven to be a valuable approach for studying the optical properties of 2D and even 3D photonic crystals. Regularly arranged macropores with high aspect ratios and high geometric accuracies can only be obtained if all the parameters of the etching process (doping level, HF concentration, etching current, anodic potential and temperature) are properly adjusted. In fact, the parametric set that identifies the stable pore-growth regime occupies a very narrow range of the total parametric space associated with the formation of porous silicon. For example, HF concentrations higher than 10 wt.%, which are commonly used for growing micro- and mesoporous films, are not suitable for growing deep, straight macropores. Relatively high anodic potentials (e.g. even higher than 2 V for our samples) inevitably enhance the formation of spiking breakdown-type pores on macropore walls. On the other hand, low anodic potentials (less than 1 V) usually lead to unstable pore growth with macropores that are partially or fully filled with microporous silicon. The substrate resistivity should be adjusted to the required initial pattern. The condition that the lattice period should be twice the SCR width, which depends on resistivity and applied potential, is a good rule of thumb for choosing a suitable substrate.

Of all the etching parameters, the applied etching current is the most critical. Current densities greater than the critical current density J_{ps}, which depends on the temperature and HF concentration, will move the system into the electropolishing regime. Lehmann’s model provides a perfect tool for calculating the etching currents required for the formation of macropores with a specific diameter. For almost all the samples, discussed in this chapter, the macropores obtained were somewhat bigger than the pre-defined ones. One of the reasons for this could be the enhanced dissolution of macropore walls because of higher dark currents.

Controlling the etching current during the process is a key issue. Keeping the etching current constant was found not to be sufficient to grow deep, straight macropores. Two effects that influence the pore shape at depth were identified. First, the decrease in HF concentration towards the pore tips because of diffusional limitations leads to an increase in the pore diameter close to the tip. Second, the higher dark current

UNIVERSITAT ROVIRA I VIRGILI
PHOTONIC BANDGAP ANALYSIS AND FABRICATION OF MACROPOROUS SILICON BY
ELECTROCHEMICAL ETCHING
Trifon Todorov Tirfonov
ISBN:978-84-693-6270-9/DL:T-1376-2010

due to the high surface area leads to conical pores whose diameter decreases with depth because the applied current contributes less to the pore growth and more to the dark current. Our samples showed conical, carrot-shaped pores with, in some cases, a difference of more than 1 μm between the diameters near the pore entrance and pore tip. The dark current depends on the temperature and on the concentration of oxygen diluted in the electrolyte. Performing the etching at lower temperatures and bubbling the electrolyte with nitrogen can reduce the dark current and produce less conical pores. By increasing the applied current during the etching, we were able to compensate for the effects of the higher dark current and, therefore, to reduce the pore conicity.

Bubbles caused by the evolution of hydrogen gas are known to generate imperfections in regular macropore arrays. Macropores degenerate in a spatially limited region corresponding to a sticking bubble. The problem is usually avoided by adding surfactants to the electrolyte. Two surfactants of different types (nonionic TritonX-100 and anionic SDS) were used. It was found that the etching process is affected not only by the type but also by the amount of surfactant added to the electrolyte. Dark currents are higher for electrolytes containing TritonX-100 surfactant and, as a consequence, the pore conicity is greater than when no surfactants were used. On the other hand, the addition of SDS surfactant reduces the dark current, so straight, regular pores can be etched without difficulty.

The etching conditions discussed in this chapter were optimized for etching macropores with diameters in the range 2-3 μm, arranged in a triangular lattice with a period of 4.6 μm. Therefore, the optical effects associated with the photonic bandgap should be expected in the far infrared spectrum (i.e. about 8-10 μm wavelength). The lattice dimension was limited by the resolution of our photolithography equipment. Downscaling of the lattice parameter and etching of sub-micrometer pores, although possible in principle, proved to be extremely difficult in practice [183,242-244].

UNIVERSITAT ROVIRA I VIRGILI
PHOTONIC BANDGAP ANALYSIS AND FABRICATION OF MACROPOROUS SILICON BY
ELECTROCHEMICAL ETCHING
Trifon Todorov Tirfonov
ISBN:978-84-693-6270-9/DL:T-1376-2010

ISBN:978-84-693-6270-9/DL:T-1376-2010

Chapter 6

Applications of macroporous silicon

Macroporous silicon has proven to be a promising material for a multitude of novel devices. It offers a number of attractive features for many kinds of applications. Some of the most prominent features of macroporous silicon are that it is possible to make perfect periodic (or with defects) pore arrays of different arrangements, it can attain extremely large aspect ratios, its internal surface area is large, it is fully compatible with the silicon microtechnology, and many others. Applications of macroporous silicon have been proposed in the fields of micromachining, gas sensing, photonic crystals, biotechnology, etc. and are also continuously emerging. In this chapter, we shall briefly review some of the most interesting examples and present new structures based on macroporous silicon formation. Since our work on macroporous silicon applications is still at an early stage, we shall restrict ourselves to suggesting some particular innovative uses of the structures presented.

6.1. Brief overview

The perfect periodicity and straightness of the macropores has been exploited for the fabrication of 2D IR photonic crystals [59,61,126,127,242-244], as has already been outlined in Chapter 1. However, the post-treatment of the as-etched macropore arrays for fabricating the final PC devices and even the preparation of the samples for

UNIVERSITAT ROVIRA I VIRGILI
PHOTONIC BANDGAP ANALYSIS AND FABRICATION OF MACROPOROUS SILICON BY ELECTROCHEMICAL ETCHING
Trifon Todorov Tirfonov
ISBN:978-84-693-6270-9/DL:T-1376-2010

transmission measurements, involve a rather sophisticated procedure developed by Ottow *et al.* [241]. It consists of covering the macropore arrays with a lithographically structured mask and subsequently etching off the macroporous silicon in the unmasked area. In this way, deep bars consisting of one, two, three or more macropore rows have been fabricated with a very high precision so that the transmission properties of 2D PC based on macroporous silicon can be studied [242-244]. Similar samples have been investigated in terms of diffraction from the surface of such 2D PC structures. It has been shown that the diffraction properties are not determined by the photonic band structure alone but also by the surface termination of the crystal [245]. Possible applications of 2D macroporous photonic crystals as diffraction gratings in Raman and photoluminescence spectroscopy have been proposed.

A unique feature of the electrochemical etching technique is that it makes it possible to modify the pore diameter in the growing direction, efficiently providing 3D-like photonic structures [209,230]. This feature also makes it possible to fabricate waveguides embedded in the "bulk" of the macropore arrays [246,247]. Such structures are comparable to photonic crystal slabs, which guide light in the third dimension by total internal reflection. The waveguides are formed when the pore diameter is decreased at a certain depth. The region in which the pore diameter is decreased will have a higher effective refractive index than the regions with a constant (and large) pore diameter. Therefore, the structure resembles a photonic crystal slab with core and cladding layers of different effective indexes.

Macropores have also been found to exhibit interesting optical properties for light traveling in the pore direction. Roughly speaking, photons with wavelengths that are smaller than the pore diameter pass through, while the others are blocked. This is due to the fact that blue light is less diffracted at the entrance of an aperture with small diameter and large length (such as the macropore) than red light. The macropore acts as a filter, absorbing all the light which has been diffracted to hit the macropore walls. While the mechanism is actually more complicated than this, the general behavior is that the macropore arrays of through-pores have the characteristics of an optical shortpass filter when are illuminated in the pore direction. Lehmann *et al.* [248] produced an optical shortpass filter based on macroporous silicon and showed that by adjusting the pore diameter, pore length and porosity the cut-off wavelength could be easily modified. Unlike Bragg or glass filters, macropore filters are true shortpass filters because the light is transmitted in empty space not in matter, which is advantageous for many applications.

Besides being used in optical devices, macroporous silicon has several other

UNIVERSITAT ROVIRA I VIRGILI
PHOTONIC BANDGAP ANALYSIS AND FABRICATION OF MACROPOROUS SILICON BY ELECTROCHEMICAL ETCHING
Trifon Todorov Tirfonov
ISBN:978-84-693-0270-9/DL:T-1376-2010

unique applications. A novel proposal is that macropores can be used as anti-scatter grids in medical X-ray imaging. All inelastically scattered photons that reach the photographic plate will blur the image. A collimator, known as an anti-scatter grid, is placed between the patient and the film to absorb the scattered radiation and, therefore, to improve the resolution of the X-ray image. Recently, Lehmann and Rönnebeck [249] have proposed a technique for fabricating a new silicon anti-scatter grid based on macroporous silicon. They used macroporous silicon as a mold to produce free-standing lead pillars with defined arrangements. The macropores were filled by a lead casting process in a chamber under pressure in order to overcome the capillary forces of the liquid lead in the micrometer-size pores. Then, the silicon was etched back and the lead pillars were fixed by an epoxy resin. It is believed that a fully optimized anti-scatter grid filter could reduce the X-ray dose by a factor of three with no loss in resolution, or allow better images, respectively [183].

Macroporous silicon has also been used as a template for the production of metal barcodes, as described by Matthias *et al.* [229]. The authors filled diameter-modulated macropores with gold by autocatalytic electroless deposition. After the silicon template was etched off, metal rods with modulated diameter (between 1 and 1.35 μm) were obtained. The metal rods can be optically identified because the reflectivity is considerably enhanced in the areas with large diameters and also because different profiles for the fabrication can be used. These modulated microwares have many uses as a kind of label, e.g. in biotechnology.*

It has been suggested that macropores can be filled with copper to make through-wafer electrical interconnections for 3D integrated circuits [251]. In this study, through-wafer macropores were filled by the copper electroplating technique to form a very high-density matrix of plugs for chip-to-chip interconnections.

Sensors based on optimized macropore arrays are also being developed. Angelucci *et al.* [252] developed a sub-ppm benzene sensor for air quality monitoring. The key part of this device is a permeable macroporous silicon membrane, a few tens of microns thick, and the pore walls are coated by a semiconductor SnO_2 film. The resistivity of this film changes in the presence of benzene, and the large surface together with the optimized gas flow pattern through the pores allows extreme sensitivities.

It has also been suggested that macroporous silicon can be used in electron

* A similar approach was used by Nicewarner-Peña *et a*l. [250] to produce optically identifiable "stripes". However, the used template was porous alumina. A succession of different metals (gold and silver) was used to fill the pores, taking advantage of the different reflectivities of these materials.

UNIVERSITAT ROVIRA I VIRGILI
PHOTONIC BANDGAP ANALYSIS AND FABRICATION OF MACROPOROUS SILICON BY ELECTROCHEMICAL ETCHING
Trifon Todorov Tirfonov
ISBN:978-84-693-6270-9/DL:T-1376-2010

devices. Lehmann *et al.* [253] developed a capacitor based on macroporous silicon. After etching, the porous silicon was doped using a phosphorus diffusion process to increase the conductivity of the remaining walls between the pores. Then, the macropores were coated with a standard high-quality dielectric, an oxide-nitride-oxide layer a few nm thick. The second electrode is formed by depositing highly doped poly-Si inside the pores. Specific capacities of 4 μF.V/mm^3 were attained, but optimized designs showed that values of up to 12 μF.V/mm^3 could be achieved. These values are comparable to those of the best Ta_2O_5 and Al_2O_3 capacitors; all other properties are better than those of all competitors. Porous silicon capacitors are naturally fully compatible with silicon technology and, because of their extremely good dielectric, of very high quality [183]. Astrova *et al.* [254] studied the diffusion of boron and phosphorus into the walls of macroporous silicon with applications for power devices in mind. Diode structures based on n-Si/n$^+$-PS have been fabricated using this technique. However, as yet little has been published on this issue.

A particularly innovative use of macroporous silicon is the ratchet-type membrane, which is potentially suitable for large-scale particle separation [255,256]. Two reservoirs with particles of two different sizes suspended in some liquid are separated by a silicon wafer, which is pierced by a huge number of identical, ratchet-shaped pores (that is to say, periodic but asymmetric, variation of pore diameter). Pumping the carrier liquid back and forth through the membrane separates the small from the large particles into the basins at both sides of the membrane. Theoretical simulations [256] indicate that for particles in the 0.1-1 μm range strong variations of the direction of transport on particle size is likely to occur, and that the ratchet-type membrane might act as a massively parallel one-dimensional Brownian separator for particle separation applications. This system is thought to be suitable for an efficient and selective continuous separation of sensitive biological materials like viruses or cell fragments.

Many other applications of macroporous silicon in biotechnology have been proposed. Ohji *et al.* [211,257] suggested using macroporous silicon to fabricate deoxyribose nucleic acid (DNA) sequencing microchips. After etching, the macropores were oxidized in order to obtain silicon dioxide pillars. The separation between the pillars can be controlled by the thickness of the oxide layer formed. Thus, SiO_2 pillar structures with spaces of 100 nm (less than the photolithography resolution) have been fabricated although the initial pattern was defined by standard photolithography. It is thought that these closely spaced structures will replace the use of gels in electrophoretic DNA sieving. It has been suggested that ordered macropore arrays can

UNIVERSITAT ROVIRA I VIRGILI
PHOTONIC BANDGAP ANALYSIS AND FABRICATION OF MACROPOROUS SILICON BY ELECTROCHEMICAL ETCHING
Trifon Todorov Tirfonov
ISBN:978-84-693-6270-9/DL:T-1376-2010

be used to fabricate biochips for molecular-binding recognition events [187,258]. Loosely speaking, these biochips look like a matrix of tiny tubes in a regular array each of which is coated with a biochemical (recognition element) that reacts only with specific molecules or DNA sequences. Absence or presence of a reaction can be monitored optically (e.g. by luminescence) or electronically, and the position in the matrix identifies the chemical, which is present in the solution to be analyzed. Pumping the solution through the pores guarantees close contact with the recognition elements and reduces the time required for molecular binding. This allows for quick and fully automated detection of thousands of molecules simultaneously. Work on these devices has progressed to the point that the first prototypes have been made and the technique may see product applications in the near future [183].

Below we shall describe our work on novel applications of macroporous silicon.

6.2. Silicon dioxide pillars

As described above, small silicon dioxide pillars fabricated on the front side of a silicon wafer have been proposed for DNA separation [211,257]. In this section, starting from macroporous silicon fabrication we describe a technique that makes it possible to obtain high-aspect-ratio silicon dioxide pillars on the backside of a silicon wafer. The uniformity and the dimensions of these pillar arrays depend exclusively on the etching conditions, which ensure a stable growth of high-aspect-ratio macropores.

The key technique in silicon dioxide pillar fabrication is the formation of macropore by electrochemical etching of n-type silicon in HF solutions. The experimental technique and the fabrication of macropore arrays have already been described in Chapters 4 and 5. Here, we shall describe the post-etching treatment of the wafer that is necessary to obtain silicon dioxide pillars. The simplified process sequence is given in Fig. 6.1 and should be seen as complementary to the process sequence given in Fig. 4.9.

After straight regular pores have been formed by electrochemical etching (Fig. 6.1a), the backside electrode (ITO layer) should be removed. This was done by a short 5% HF dip. Next, the wafer was thermally oxidized in dry O_2 at 1100°C for about 190 min (Fig. 6.1b). This oxidation time results in an oxide layer with thickness about 2100 Å thick. It should be noted that the oxide-induced stress could cause the wafer to bend significantly, which makes any subsequent processing impossible. The wafer can

UNIVERSITAT ROVIRA I VIRGILI
PHOTONIC BANDGAP ANALYSIS AND FABRICATION OF MACROPOROUS SILICON BY ELECTROCHEMICAL ETCHING
Trifon Todorov Tirfonov
ISBN:978-84-693-6270-9/DL:T-1376-2010

even be broken quite easily when handling. It has been found that the bending curvature depends linearly on the specific area of macroporous silicon [259]. Our experience showed that thinner oxide layers and shallower pores should be used to minimize this problem. Noticeable wafer bending was not observed for the given oxide thickness and pores as long as 140 μm. Following the oxidation, the backside oxide layer was patterned by a standard lithography and BHF etch to open the windows where silicon should be removed (Fig. 6.1c). Finally, the backside silicon was etched off in 25 % TMAH solution at 85°C (Fig. 6.1d). The oxide within the pores is resistant to the TMAH etch. Consequently, when the membrane is thin enough, silicon dioxide tips begin to appear on the backside of the wafer.

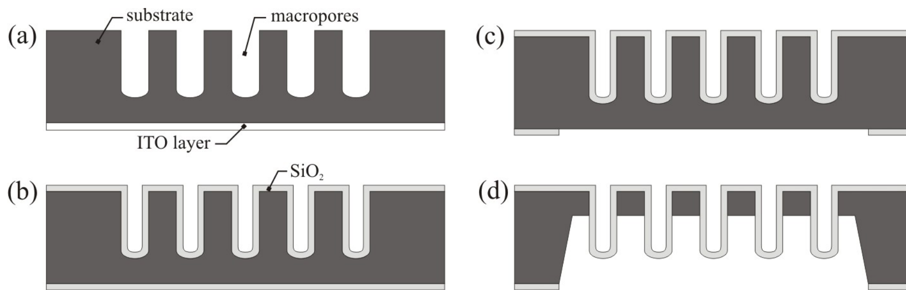

Fig. 6.1. Process flow for silicon dioxide pillar fabrication: (a) electrochemical etching to form deep macropore arrays; (b) thermal oxidation of the macropores; (c) backside lithography of the oxide layer; (d) TMAH etching of backside silicon to release the pillars

Figure 6.2 shows examples of SiO_2 pillars released after the silicon has been etched back. In Fig. 6.3a the etching was stopped just when the pillar tips were reached. The geometry of the pillar tips is almost hemispherical. The pillar cross section is not an ideal circle, but rather slightly faceted because of the anisotropic nature of the etching process. However, if circular pillars are desired the pore cross section can first be tuned by successive oxidation/oxide-removal steps before the process steps described above are performed. Figures 3b and 3c show higher pillars obtained through longer silicon etching. Some pillars broke when the wafer was cleaved for SEM inspection. The samples have been tilted to allow better SEM observation of the pillars. The length of the pillars depends on the backside silicon etching and of course on the total length of the macropores. In Fig. 3b the pillars are 14 μm high, while in Fig. 3c they are 48 μm. The TMAH etching of silicon is a well-known process in micromachining [210] so that the total depth required to etch the silicon can be easily calculated in order to release pillars of certain height. Problems may arise from difficulties in predicting the

UNIVERSITAT ROVIRA I VIRGILI
PHOTONIC BANDGAP ANALYSIS AND FABRICATION OF MACROPOROUS SILICON BY ELECTROCHEMICAL ETCHING
Trifon Todorov Tirfonov
ISBN:978-84-693-6270-9/DL:T-1376-2010

macropore length with etching time, as discussed in Chapter 5. Precise control of the etching parameters and a large amount of experimental data are therefore needed in order to optimize the etching process and gain control on the pore geometry.

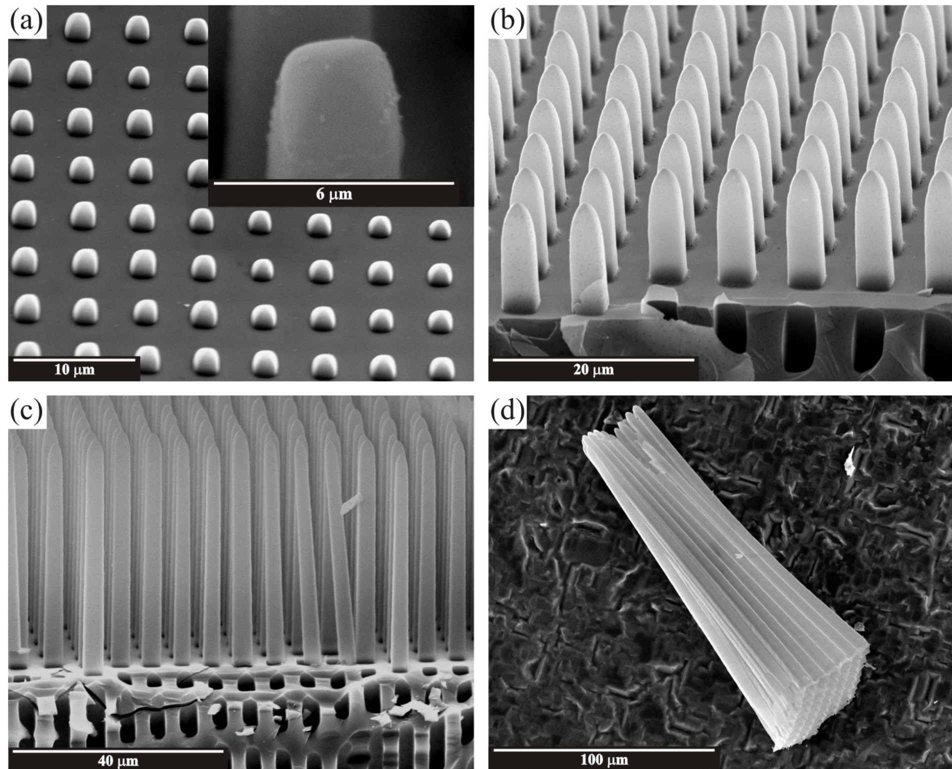

Fig. 6.2. SEM micrograph of silicon dioxide pillars after TMAH etching of backside silicon: (a) only the pillar tips have been released (the inset micrograph is a magnified view of the pillar tip showing the faceted cross section of the pillars); (b) 14 μm high pillars; (c) 48 μm high pillars; (d) 150 μm high pillars (the backside silicon has been completely removed to release pillars with the total macropore length).

The silicon can be completely removed and the pillar height is then the same as the macropore depth, as shown in Fig. 6.2d. However, a problem emerges that can be deduced from the shown micrograph. The unsupported pillars inevitably stick together because of capillary forces at the liquid-gas interface. This can be clearly seen in Fig. 6.3. The pillars are still supported by the remaining oxide layer on the front side of the wafer (Fig. 6.1), so they stick together and form bundles that break in an uncontrolled manner. If silicon is to be completely removed, some way of fixing the

ISBN:978-84-693-6270-9/DL:T-1376-2010

pillars should be invented. We were not able to avoid this problem.

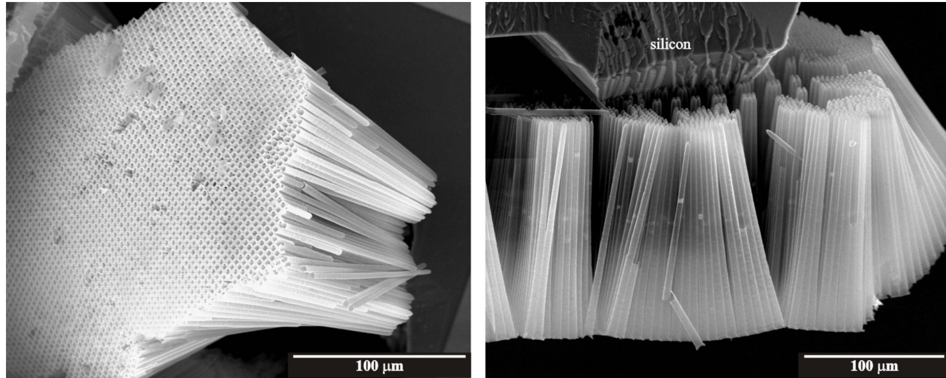

Fig. 6.3. Sticking of the completely released pillars because of capillary forces at the liquid-gas interface. The right micrograph shows part of the silicon rib which was not etched in TMAH because of the patterning. Note that some of the pillar bundles are still supported by the oxide layer on the front side of the wafer.

The pillar arrangement is determined by the pre-etching pattern. By adjusting such etching conditions as wafer resistivity and photogenerated current, a wide variety of pore and therefore, pillar arrangements can be achieved. Figure 6.4a shows two square patterns of pillar arrays with different dimensions, which were obtained in a single etching step. Figure 4b shows silicon dioxide pillars ordered in a triangular lattice.

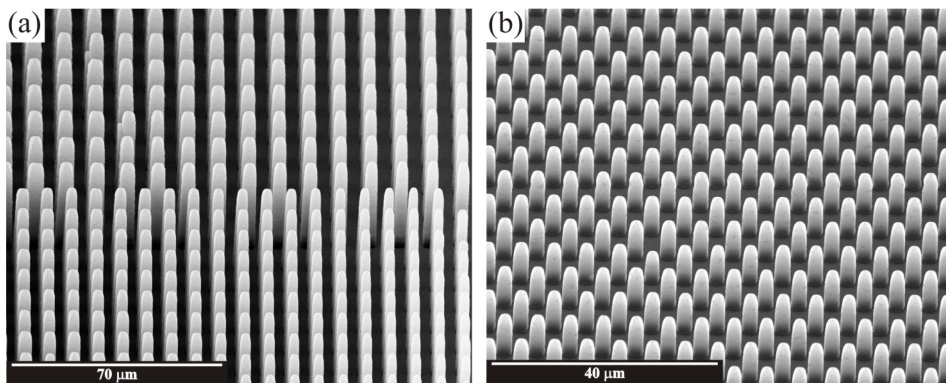

Fig. 6.4. SEM micrographs showing SiO_2 pillars of different arrangements: (a) two square patterns of pillar arrays with different dimensions; (b) pillar arrays in a triangular arrangement

The proposed technique enlarges the designer's toolbox in several fields and

UNIVERSITAT ROVIRA I VIRGILI
PHOTONIC BANDGAP ANALYSIS AND FABRICATION OF MACROPOROUS SILICON BY ELECTROCHEMICAL ETCHING
Trifon Todorov Tirfonov
ISBN:978-84-693-6270-9/DL:T-1376-2010

new applications can be envisaged. For instance, Fig. 6.5 shows SiO_2 pillar arrays inside a set of truncated pyramids. The fabrication procedure is the same as the one described above, selecting smaller mask for the back silicon etch. Because TMAH etching is an anisotropic process, the size of the mask together with the etching time determines the dimensions of the pyramids. Thus, extremely precise 3D structures can be fabricated by releasing different numbers of pillars (even 9 as shown in Fig. 6.5b). Each one of these truncated pyramids can be used to detect different molecular binding events [259], increasing at the same time the contact area between probe and target molecules due to the presence of pillars. The probe molecules can be immobilized on the pillar surface. In this way, the third dimension (pillar height) is exploited which can improve the intermixing between the molecules because of the closer contact between the analyte and probe. We note that the contact area can be further increased by downscaling the pillar dimensions (diameter and separation) to the submicrometer range.

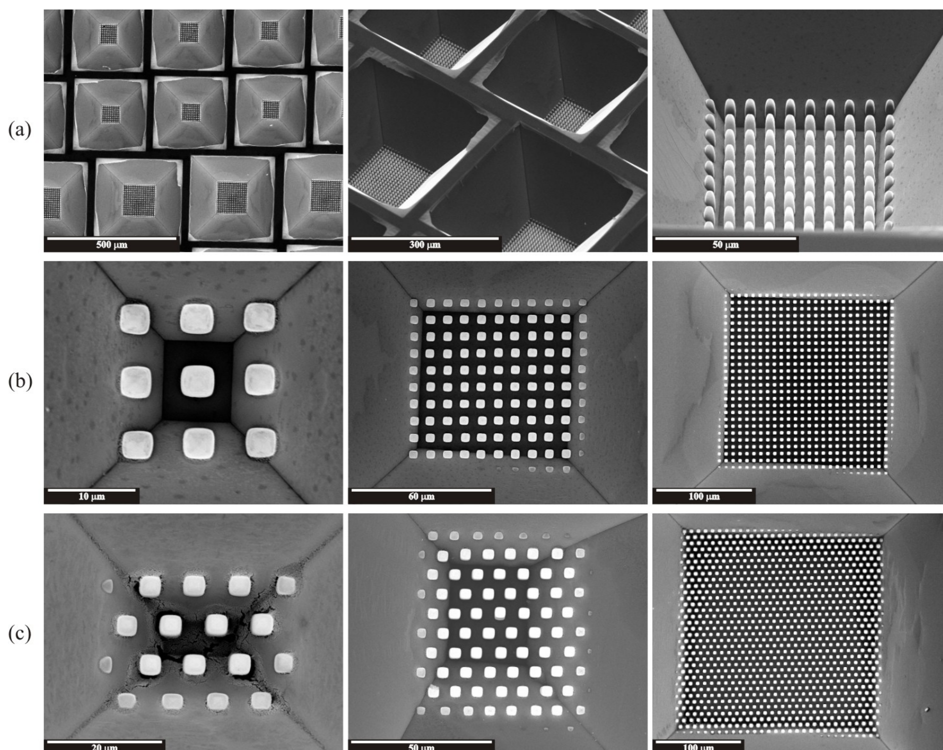

Fig. 6.5. Micro-pillars in truncated pyramids which can be used as a 3D sensor platform: (a) micrographs showing surface and 40° views of a set of pyramids; (b) and (c) surface views of pyramids with different dimensions releasing different numbers of pillars and different arrangements (i.e. square and triangular).

ISBN:978-84-693-6270-9/DL:T-1376-2010

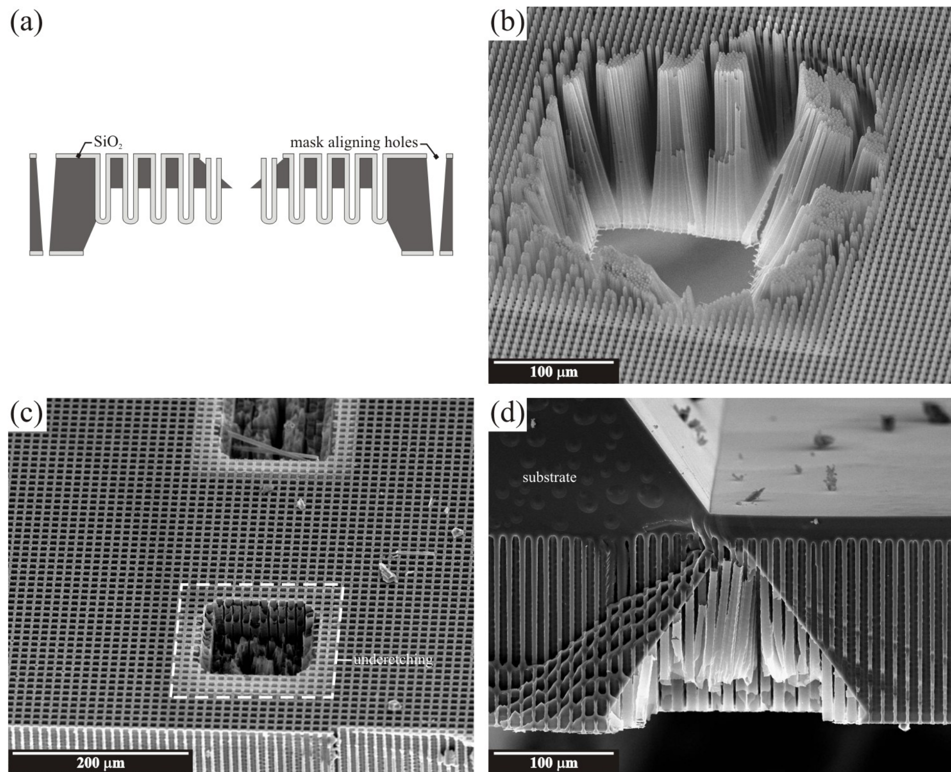

Fig. 6.6. Creating through holes inside the pyramids filled with SiO_2 pillars: (a) schematic representation of the structure (the through-wafer holes on both sides of the porous area are necessary for mask aligning); (b) example of a badly etched hole; (c) structuring of the front side of the wafer; (d) cross section view showing details of the structures formed (the macropores have not been reached by the backside TMAH etching).

The anisotropic properties of TMAH etching can be used to make holes inside each of these pyramids, thus producing a pierced membrane through which the solution can be pumped. The procedure for optimizing the fabrication of such a membrane is currently being studied. Some preliminary results are given in Fig. 6.6. The front side lithography was made using a high viscosity photoresist that is usually used for lift-off processing (Microposit SJR5740, Shipley Co.). Spinning a resist layer of about 7 µm thickness was sufficient to completely cover the pores. The fabrication is sketched in Fig. 6.6a. By adjusting the dimensions of the windows opened in the oxide for the TMAH etch on the front and back side of the wafer, it is even possible to remove only one pillar. Actually, the fabrication sequence is more complicated than the picture shows. The TMAH etching on both sides of the wafer should not be performed in a single step. First, the front side of the wafer has to be lithographically patterned and

UNIVERSITAT ROVIRA I VIRGILI
PHOTONIC BANDGAP ANALYSIS AND FABRICATION OF MACROPOROUS SILICON BY ELECTROCHEMICAL ETCHING
Trifon Todorov Tirfonov
ISBN:978-84-693-6270-9/DL:T-1376-2010

etched. The backside is protected from the TMAH by the oxide layer. Next, the oxide layer should be completely removed and then the wafer has to be oxidized again to grow protective oxide on the patterned areas of the front side. Afterwards, the backside oxide film is patterned and the wafer is TMAH etched until the front side structures are reached. Note that a set of through-wafer holes should also be created to allow mask aligning for the front and backside lithography. When the TMAH etching is performed in a single step, the macropores may not be reached (Fig. 6.6d).

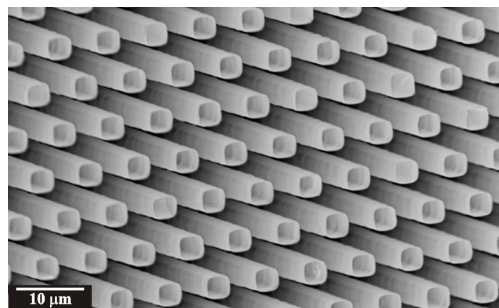

Fig. 6.7. SEM micrograph of an array of microneedles released after TMAH etch of backside silicon. (Courtesy of D. Molinero and E. Valera, UPC, Barcelona)

Opening a hole in the pillar tip makes it possible to convert the silicon dioxide pillars (remember they are hollow) into arrays of microcapillaries or microsyringes, which can be potentially useful as microchannels for fluid delivery or for precisely located chemical-reaction stimulation [260]. Figure 6.7 shows an example of such microtubes made of silicon dioxide. The TMAH etching was stopped just when the macropore tips were reached. Then, the pore tips were opened by a short (and carefully performed) BHF etching. Next, the wafer was immersed again in TMAH solution to further release the tubes. The diameter of the microtubes is mainly determined by the electrochemically etched pores. Downscaling the pore diameter will enable narrower tubes to be fabricated. The inner tube diameter can be further reduced by oxidation. The growth of thicker oxide layer can reduce the inner diameter to below 1 µm and is also good for strengthening the tubes. Care should be taken with the oxide-induced stress in this case. Another way to make sharper microtubes is to reduce the current density during electrochemical etching in order to form conical carrot-shaped pores. These conical pores have already been discussed in Chapter 5, where the pore conicity was considered as an unwanted result of the macropore formation. Here, it can be exploited to reduce the pore diameter near the tips.

ISBN:978-84-693-6270-9/DL:T-1376-2010

In other applications, the silicon dioxide pillar arrays can be filled from the front side and the silicon dioxide can be easily eliminated. This will result in pillar arrays of different materials. Alternatively, the pillar arrays can be used as a mold and high-aspect-ratio macropores in unusual materials can be obtained after etching.

6.3. Optical short-pass filters

As was first proposed by Lehmann *et al.* [248], it was envisaged that macroporous silicon would be useful for fabricating optical shortpass filters. In this section, we shall describe our work on this subject. However, we would like to note that the results presented here should be seen solely as a preliminary investigation, because a lot of work has yet to be done to achieve samples of perfect quality.

Figure 6.8 shows SEM micrographs taken from the front and back surfaces of a macroporous membrane, fabricated by electrochemical etching and subsequent post-processing of the wafer by applying the process sequence depicted in Fig. 6.1. In order to obtain through-wafer pores, one additional step should be added. After the TMAH etching that releases the silicon dioxide pillars (Fig. 6.1d), the wafer was immersed in 5% HF solution to completely dissolve the oxide. The backside silicon was TMAH etched in 25% TMAH solution at 85°C for 360 min. The remaining silicon membrane was about 160 µm thick. The electrochemical etching was conducted at room temperature for 300 min with an applied bias of 1.4 V and a constant current density of 4.98 mA/cm^2. The wafer was pre-structured using the photo-lithographic mask depicted in Fig. B.1 from Appendix B. It should be noted that the etching conditions were optimal for obtaining a stable pore growth for the regions **C/4-2** and **T/4.6-2**. The porosity defined by J/J_{ps} ratio was about 0.33, which if circular pore shape is considered (see Appendix C) yields pore diameters of 2.59 µm and 2.77 µm for both regions, respectively. The obtained pore diameters (on the back side of the membrane) are slightly different from the predefined ones. It should be pointed out that the pore cross section is not exactly a circle but rather resembles a rounded square, which makes it difficult to determine the diameter accurately. Growing an oxide layer and subsequently removing the oxide also changes the original pore shape and diameter and introduces additional ambiguity. The obtained pore diameter measured on the backside of the membrane is less than the diameter on the front side which indicates conical carrot-shaped pores in depth. Higher dark current densities are mainly responsible for this effect, as discussed in Chapter 5. The different porosities on the front and the back sides of the membrane lead to different spectral characteristics, if the filter is illuminated from

UNIVERSITAT ROVIRA I VIRGILI
PHOTONIC BANDGAP ANALYSIS AND FABRICATION OF MACROPOROUS SILICON BY
ELECTROCHEMICAL ETCHING
Trifon Todorov Tirfonov
ISBN:978-84-693-6270-9/DL:T-1376-2010

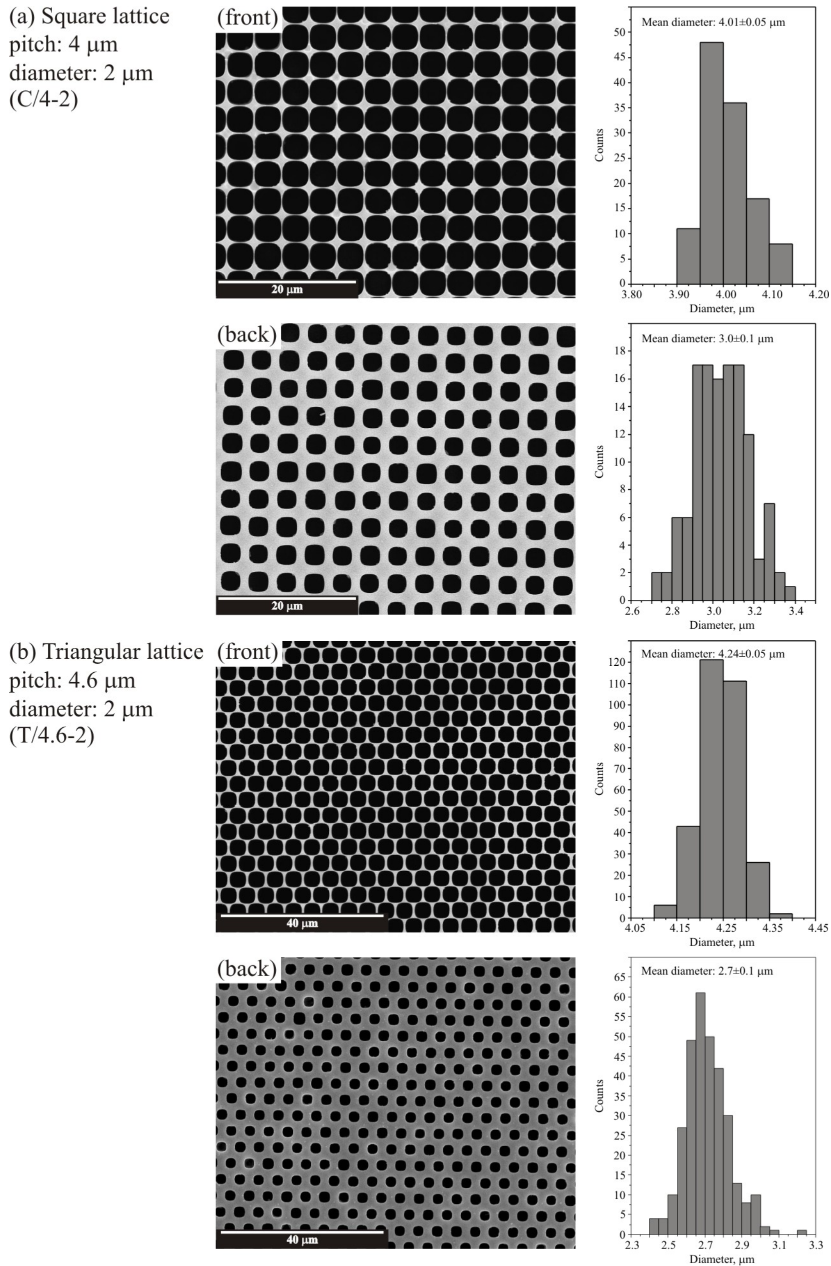

Fig. 6.8. Histograms showing the dispersion of pore diameter on the front and the backside of a macroporous silicon membrane with (a) square and (b) triangular pore arrangements. The dimensions of the predefined patterns are also given. The membrane is 160 µm thick. For all histograms, the total number of counts is greater than 100, and the bin size is identical (0.05 µm). Note the greater diameter dispersion on the backside of the membrane for both arrangements. The edge pores were excluded from the analysis.

ISBN:978-84-693-6270-9/DL:T-1376-2010

the front or back side, respectively.

The histograms of the pore diameter distribution were obtained by analyzing the corresponding SEM micrographs using the freely available software Image/J [219]. This program, and most of the software for similar image processing, measures the so-called *Feret diameter*, which can be defined as the largest distance between any two points along the boundary of the region of interest (in this case the pore). In a square, for example, the longest distance between two end points will be the diagonal of the square. Therefore, the exact pore size will be found if the Feret diameter is divided by a factor $\sqrt{2}$. In the present histograms, the values obtained were not corrected in this way, mainly because the pore shape is not a well-defined square. The results are therefore roughly accurate. The mean diameter is found by averaging the values of all counts, and the standard deviation *SD* is calculated using $SD = \sqrt{\frac{1}{N-1}\sum_{i=1}^{N}(x_i - \overline{x})^2}$, where *N* is the number of counts and $\overline{x}$ is the mean diameter.

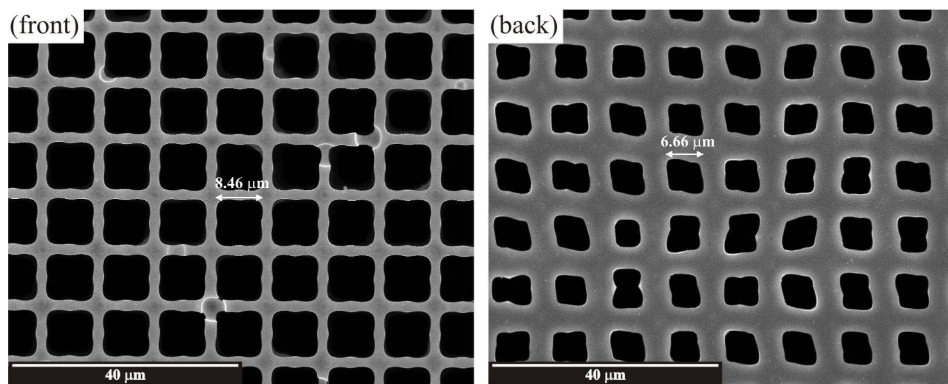

Fig. 6.9. SEM micrographs of the front and back sides of the macroporous silicon membrane taken from the **C/10-5** region (square lattice with 10 µm pitch and 5 µm diameter) of the initial patterning. The etching conditions were not properly adjusted to yield stable pore growth for the given patterning. The macropores formed are the result of growing two or four pores inside a pyramidal notch of the predefined pattern.

However, the results are accurate in that the dispersion of the pore diameter is greater on the back side. This means that macropores are not identical in size. The standard deviation of the statistics for the front side image is 0.05 µm, while for the backside image it is 0.1 µm. These differences in the pore size can be seen by simply looking at the backside SEM micrographs. This lack of uniformity in size may be

UNIVERSITAT ROVIRA I VIRGILI
PHOTONIC BANDGAP ANALYSIS AND FABRICATION OF MACROPOROUS SILICON BY ELECTROCHEMICAL ETCHING
Trifon Todorov Tirfonov
ISBN:978-84-693-6270-9/DL:T-1376-2010

because of inhomogeneous backside illumination, inhomogeneous doping density distribution across the wafer, or many other reasons, which need not be specified here. Problems with the backside electrical contact or even problems with the stirring could also give rise to differences in the pore size.

Figure 6.9 shows SEM micrographs taken from the front and the back sides of the fabricated silicon membrane for the region with **C/10-5** patterning (see Appendix B). Straight pores were not obtained for this region under the etching conditions given above. Both micrographs suggest that the rare pore cross section is a result of growing two or four joined pores. Obviously, there is no point in making an analysis like the one above.

Figures 6.8 and 6.9 illustrate to the major shortcomings of the macroporous filter fabricated. An aluminum mesh, not an ITO layer, was used to make the backside ohmic contact. This resulted inevitably in suppressing the pore growth behind the aluminum wires. The porous membrane is formed actually of porous compartments separated by an opaque silicon grid. This can be seen in Fig. 6.10b, which shows a digital photograph of a small piece (10×10 mm) of the porous membrane. The membrane is illuminated from the back side with white light. The blue appearance of the sample is a clear indication of a shortpass spectral characteristic.

The measured spectral transmittance shown in Fig. 6.10a, however, does not promise so much. The measurements were performed on a SpectraPro-150i (Acton Research Co.) grating spectrometer. The light transmitted through the sample (10×10 mm) with the pores parallel to the light beam was collected by a lens and projected onto a silicon photodiode. To discard the emission spectra of the light source, the spectral characteristics of the detector and the influence of the optical set-up the transmittance data with a sample was normalized to a reference spectrum taken without sample. The shown spectra exhibit very low transmission. We think that the remaining silicon grid together with spatial inhomogeneities in the pore arrays (caused by H_2 bubble sticking) could be the reason for this higher absorption. It should be noted that the data presented were not corrected for the porosity of macropore arrays mainly because the porosity was different on either side of the membrane. Such correction is necessary only for purposes of comparison, i.e. to estimate the effect of the pore diameter by itself and not of the spacing between the pores [239]. Nevertheless, the shortpass characteristics of the filter can be qualitatively estimated. The cut-off wavelength is blue-shifted as the pore diameter decreases (see Ref. 248). The increased transmission for wavelengths greater than 900 nm is due to a reduced absorption in silicon close to the indirect band gap at 1.1 eV. It is not understood why transmission

ISBN:978-84-693-6270-9/DL:T-1376-2010

decreases for wavelengths below 350 nm. Such behavior has not been reported by Lehmann *et al.* [248].

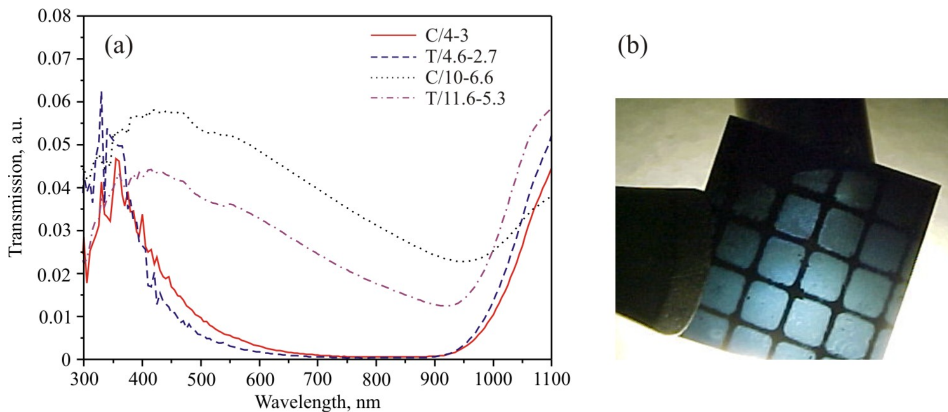

Fig. 6.10. (a) Measured transmittance of macropore arrays with different arrangements and pore diameters. The labeling convention is as follows: C/*x*-*y* stands for a square lattice with a center-to-center distance of *x* μm between the pores and a pore diameter of *y* μm; T/*x*-*y* means the same but for a triangular lattice. The pore length is 160 μm in all cases. The data has not been corrected for porosity. (b) Digital photograph of a sample (10×10 mm) illuminated with white light from the back. The opaque grid is the result of dead-end pores in the silicon because aluminum mesh was used as the backside electrode.

The results presented in this section are not the best that can be achieved. The etching process needs to be optimized further if good quality samples are to be obtained. It is worth mentioning that growing straight and very deep pores that are required for the shortpass filter behavior is not an easy task. It involves plenty of fine tuning, as well as fine control of the etching parameters for long anodization times (5-6 hours).

6.4. Ratchet-type macropores

Macropores with periodic but asymmetric variations in the pore diameter with depth have been used to fabricate a novel ratchet-type particle separation device [228,255,256]. It has been demonstrated both theoretically [256] and experimentally [255] that the asymmetric pore profile in conjunction with the far-from-equilibrium situation created by periodically pumping the solution through the pores gives rise to a ratchet effect: that is to say, there is a net directional motion of the particles along the pore axis but the liquid itself does not move. The asymmetry of the pore profile plays a critical role in the ratchet effect. The pore diameter can be periodically and

UNIVERSITAT ROVIRA I VIRGILI
PHOTONIC BANDGAP ANALYSIS AND FABRICATION OF MACROPOROUS SILICON BY
ELECTROCHEMICAL ETCHING
Trifon Todorov Tirfonov
ISBN:978-84-693-6270-9/DL:T-1379-2010

asymmetrically modulated by controlling the backside illumination intensity, which, in turn, changes the total etching current. Applying a sawtooth-like current profile yields strong asymmetrically varying pore shapes [228]. According to Lehmann's model for macropore formation, the current density at the pore tips is always equal to the critical current density J_{ps}. For a regular pore arrangement (e.g. square lattice), the porosity of the macropore array is determined by the ratio of the total current density to the critical current density (see Eq. 4.5 and 4.6). Increasing the backside illumination intensity causes a higher hole generation rate. This results in an increased total current density, which flows over the whole sample. Since J_{ps} remains fixed at the pore tips, the increased total current will lead to a larger pore cross section and thus to a bigger pore diameter. The variations in the backside illumination intensity are therefore reflected in the pore diameter (with some limitations). In this section, we present some of the preliminary results of our work on the fabrication of 3D microstructures obtained by applying the approach described.

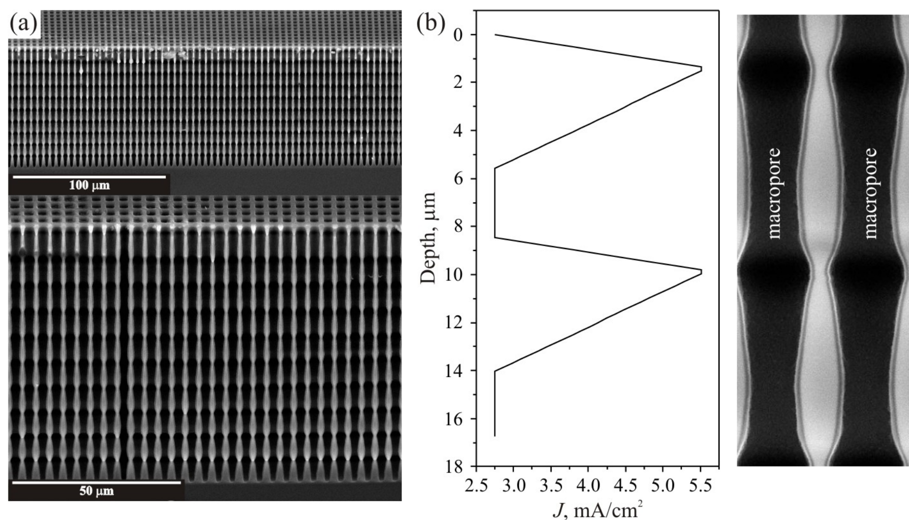

Fig. 6.11. (a) Cross section SEM micrographs (40° view) of electrochemically etched macropores with periodic asymmetric modulation of the pore diameter. The upper micrograph is taken with lower magnification to show the high uniformity of the pore array. (b) Fragment (two periods) of the applied etching current profile together with a cross section SEM image showing the modulation of the pore diameter. Ten periods were etched using the given current profile.

Figure 6.11a shows an example of macropores with asymmetric and periodic variation of the pore diameter. The wafer was etched in 2.5 wt.% aqueous HF solution with an applied bias of 1.2 V. A fragment (two periods) of the etching current profile

UNIVERSITAT ROVIRA I VIRGILI
PHOTONIC BANDGAP ANALYSIS AND FABRICATION OF MACROPOROUS SILICON BY ELECTROCHEMICAL ETCHING
Trifon Todorov Tirfonov
ISBN:978-84-693-6270-9/DL:T-1376-2010

used together with a cross section image of the pores formed is shown in Fig. 6.11b. Macropores with ten modulation periods were etched according to the given profile. The etching was performed at 11°C temperature for 280 min. It should be noted that the control of the temperature is essential to obtain deep and perfectly modulated pores. Not only must the temperature be kept constant but room temperature must also be avoided in the present case. Some of the advantages of etching at lower temperatures have already been discussed in Chapter 5.

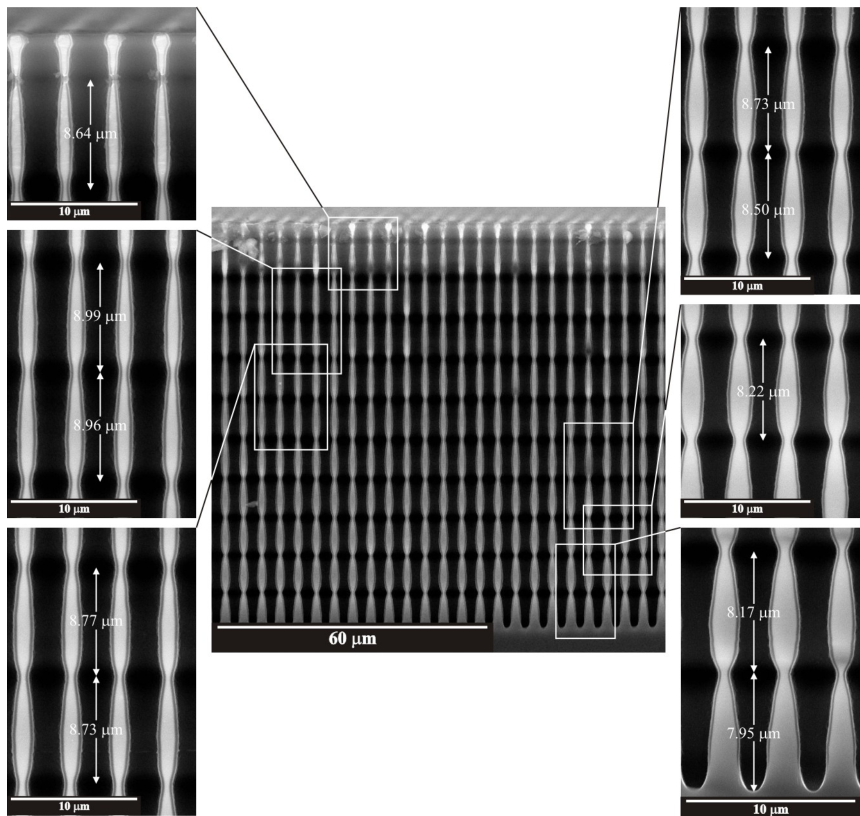

Fig. 6.12. SEM micrographs showing deviations in the length of the modulation period as the pore depth increases. The deviations are due to a decrease in the pore growth rate because of diffusional limitations. All ten periods are shown. The white rectangles indicate the corresponding period and do not show the exact positions of the magnified micrographs.

Although the micrographs shown suggest that an asymmetric periodic modulation has been achieved, there are some deviations from the constant modulation length and pore diameter in depth, which we shall discuss here. Figure 6.12 shows SEM

UNIVERSITAT ROVIRA I VIRGILI
PHOTONIC BANDGAP ANALYSIS AND FABRICATION OF MACROPOROUS SILICON BY
ELECTROCHEMICAL ETCHING
Trifon Todorov Tirfonov
ISBN:978-84-693-6270-9/DL:T-1378-2010

micrographs of higher magnification taken from different periods of the modulated pores as shown with white rectangles. The distance between two maximum diameters is considered to be the length of a period. It is clearly seen that the length of the period decreases slightly as the pore depth increases. This effect is known to be caused by diffusional limitations in deeper pores. With increasing pore depth, the HF concentration at the pore tips and therefore the critical current density J_{ps} and also the growth rate ν (see Eq. 4.3) are reduced. If the sawtooth-like current density is applied on a linear time scale, the period length from top to bottom for 100 μm deep pores can vary by about 20% [228]. For the given example, we have tried to compensate for this variation in the length of the period by reducing the frequency as defined in the applied current profile. Actually, the length of the period determined by the current profile was linearly increased by a total of 26% over the ten periods. If we plot the measured lengths against the period number (Fig. 6.13) a good linear fit is obtained, with a deviation of about 3.4% from the mean period length. The mean period length 8.63 μm was calculated by averaging the first nine periods. The last (tenth) period was not included in the statistic because it was not completed. Although the deviation in the period length is really very low, we think that the method used to compensate for the effect of diffusional limitations is not the best one. The linear decrease in the modulation frequency of the applied current profile is not a good choice because the growth rate has a non-linear (approximately parabolic) dependence on the pore length, as described by Lehmann [125,187]. Therefore, to produce equidistant changes in the pore diameter there must be a non-linear decrease in the modulation frequency. The good results achieved in the present case are probably due to the fact that the pores are not so deep (89 μm) and diffusional limitations are therefore less pronounced.

Figure 6.13 shows the position of the diameter maxima for each period (filled squares) plotted together with a linear fit. The measured values of the period length, and the maximal and minimal pore diameters are plotted. The variations in the maximal pore diameter are about 3% with a mean diameter of 3.55 μm, while the variations in the minimal pore diameter are 11% with a mean diameter of 2.66 μm. It can be clearly seen (it is even noticeable by simply looking at the SEM micrographs in Fig. 6.12) that the pore diameter tends to decrease as the pore depth increases: that is, the pores have a conical shape. This effect has already been discussed in Chapter 5, where some approaches to reduce the pore conicity have been presented. Actually, the structures presented were etched by linearly increasing the etching current with the etching time in an attempt to reduce the pore conicity. The linear increase was superimposed on the sawtooth-like current profile shown in Fig. 6.11b. Clearly, further optimization of the

UNIVERSITAT ROVIRA I VIRGILI
PHOTONIC BANDGAP ANALYSIS AND FABRICATION OF MACROPOROUS SILICON BY ELECTROCHEMICAL ETCHING
Trifon Todorov Tirfonov
ISBN:978-84-693-6270-9/DL:T-1376-2010

etching conditions is needed in order to surmount this problem.

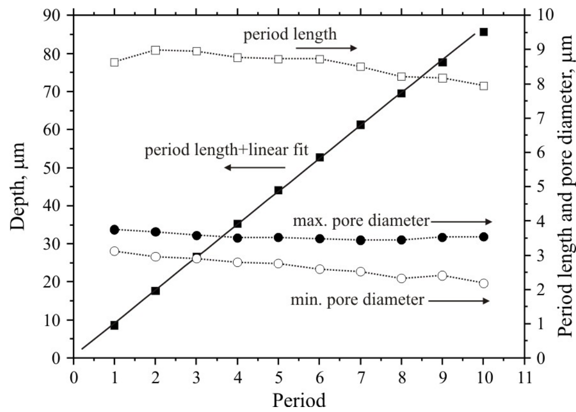

Fig. 6.13. Positions of the diameter maxima (filled squares) together with a linear fit (solid line) plotted against the period. Period length (unfilled squares), maximal pore diameter (filled circles) and minimal pore diameter (unfilled circles) are also shown. The dotted lines are drawn as guides for the eyes.

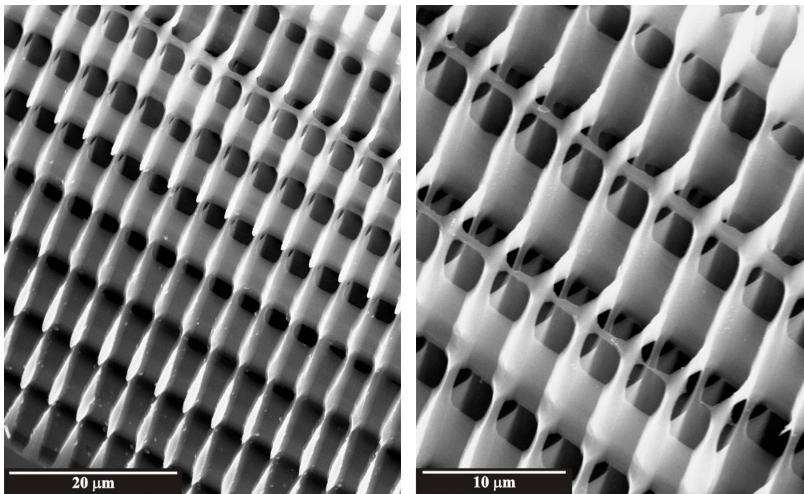

Fig. 6.14. A fully 3D network of interconnected voids in silicon obtained after a few oxidation/oxide-removal cycles of the structure with modulated macropores (Fig. 6.11). The oxidation and the subsequent etching of the oxide led to the dissolution of thinnest silicon walls only at the positions of diameter maxima.

The post-processing of the modulated macropores arrays led to the structure shown in Fig. 6.14. It is a fully 3D network of interconnected voids separated by thin

UNIVERSITAT ROVIRA I VIRGILI
PHOTONIC BANDGAP ANALYSIS AND FABRICATION OF MACROPOROUS SILICON BY ELECTROCHEMICAL ETCHING
Trifon Todorov Tirfonov
ISBN:978-84-693-6270-9/DL:T-1376-2010

silicon walls. This was achieved by a few oxidation/oxide-removal steps of the asymmetric macropores to dissolve the thin silicon walls only at the positions of diameter maxima. Very recently, Matthias *et al.* [261] reported the fabrication of a 3D microstructure in a similar way (that is to say, by periodic and symmetric modulation of the macropores and subsequent oxidation/oxide-removal cycles). The authors obtained a fully 3D cubic photonic lattice, which resembles a 3D photonic crystal of air spheres embedded in silicon. The pore diameter was modulated in depth by varying not only the applied etching current but also the applied anodic potential. This made it possible to optimally focus the charge carriers and therefore achieve sharper variations in the pore diameter. This sharp periodic modulation is required if the 3D cubic lattice is to be accurately represented. Sawtooth-like modulation of the etching current leads solely to a sinusoidal variation in the pore diameter [209] or ratchet-type pores [255]. The micrographs in Fig. 6.12 show that the sharp peaks in the current profile are smoothed in the pore diameter. As described in Ref. 261, this problem can be overcome by varying the anodic potential in accordance with the applied sawtooth-like current profile.

6.5. Summary

In short, we have presented here some preliminary results of our work on the novel applications of macroporous silicon. The structural features of the electrochemically etched macropore arrays have been used to fabricate high-aspect-ratio silicon dioxide pillars, which can have possible applications in biotechnology as a 3D sensor platform for molecular recognition detections or as dense arrays of microsyringes for fluid delivery or precise chemical reaction stimulation. The silicon dioxide pillar arrays can be used as a mold for fabricating ordered macropore arrays in materials other than silicon. We have also measured the optical characteristics of a macroporous filter with 160 μm-long through-wafer pores. For light incidence parallel to the pores, a shortpass spectral behavior has been observed but the results are only qualitative and suggest that further optimization of the etching process is needed to produce higher quality samples. We were also able to modulate the pore diameter periodically in depth and to fabricate ratchet-type macropore arrays, which have been envisioned as ratchet devices for large-scale particle separation [255]. We have shown that by a few post-etching steps the modulated macropore arrays can be converted into microstructures consisting of interconnected voids in all three dimensions. The technique can be used to fabricate fully 3D photonic crystals.

UNIVERSITAT ROVIRA I VIRGILI
PHOTONIC BANDGAP ANALYSIS AND FABRICATION OF MACROPOROUS SILICON BY ELECTROCHEMICAL ETCHING
Trifon Todorov Tirfonov
ISBN:978-84-693-6270-9/DL:T-1376-2010

UNIVERSITAT ROVIRA I VIRGILI
PHOTONIC BANDGAP ANALYSIS AND FABRICATION OF MACROPOROUS SILICON BY ELECTROCHEMICAL ETCHING
Trifon Todorov Tirfonov
ISBN:978-84-693-6270-9/DL:T-1376-2010

Chapter 7

Summary and conclusions

The work presented in this thesis has dealt with the following subjects: photonic band structure simulations and analysis of 2D photonic crystals, and the fabrication of macroporous silicon structures suitable for application as 2D infrared photonic crystals.

Since many potential applications of photonic crystals are based on their photonic band gaps, it is of interest to design photonic crystals with an absolute band gap that is as large as possible. We began the thesis by describing a way to enlarge the absolute photonic band gap, and showing the role that symmetry plays in designing optimal photonic structures. We have examined how reducing symmetry by inserting additional elements into the lattice unit cell or by changing the shape of the scatterers alters the dispersion behavior of the *TM*- and *TE*-polarization modes in 2D photonic crystals. Our goal was to maximize the absolute PBG width by breaking the symmetry of the simple square and triangular lattices and thus constructing new structures, the so-called *hybrid lattices.* Using the FDTD method for photonic band structure calculations, we performed a detailed numerical analysis of the photonic dispersion relation in 2D hybrid lattices consisting of air holes drilled in silicon.

For square lattices, we successfully applied the symmetry reduction approach to maximize the absolute PBG width. In the case of square lattices of circular air rods, including an additional rod increases the absolute PBG threefold. In the case of square

ISBN:978-84-693-6270-9/DL:T-1376-2010

lattices of square air rods, the rotation of the rods plays a critical role in the opening of an absolute PBG. No absolute PBG is found if the square rods are not rotated. The size of the absolute PBG is improved most significantly by a combination of including an additional rod and rotating the square rods. Moreover, a new absolute PBG is generated that persists over a wide range of rotation angles and filling fractions far from the closed-packed condition. This greatly favors the fabrication of photonic crystals.

The largest absolute PBG is the one for the triangular lattice of circular air rods. Our results have shown that modifying the triangular structure by adding interstitial rods or using square rods (even though the rods are rotated) is not a good way of achieving a larger absolute PBG, at least for the special case of air/silicon structures. Adding more rods to the lattice unit cell cannot further enlarge the absolute PBG width.

In Chapter 3 we made a detailed quantitative analysis of the absolute PBGs in 2D triangular and honeycomb lattices considering that there is an interfacial (shell) layer between the rods and the background dielectric matrix. This interfacial layer may be the unwanted result of the fabrication process itself or created intentionally. The properties of the photonic gaps are strongly affected by the thickness and the dielectric constant of the shell layer. The results of band structure simulation show that for structures consisting of air rods embedded in a dielectric background this layer reduces the absolute photonic gap. A surprising result is that for structures consisting of dielectric rods in air, an interfacial layer can yield larger photonic gaps if the dielectric constant of the layer is greater than that of the rods. This provides further flexibility for the fabrication of 2D photonic crystals. For example, in certain cases we may not be able to obtain dielectric rods of the required diameter or of the particular material we need because of technological limitations. However, we are enabled to grow the rods of materials with lower dielectric constants, for which a well-developed technology exists. The rods can then be covered with the required dielectric by deposition, thus achieving almost the same gap properties as those of the ideal shell-less structure.

In the subsequent chapters, we described the electrochemical etching process and the etching set-up we developed for fabricating 2D periodic structures based on macroporous silicon formation. We made a detailed study of how the electrochemical etching parameters influenced the pore morphology and found the optimal conditions for stable macropore growth. Straight and stable macropores can only be etched if the etching conditions are properly adjusted. The optimal conditions are only a very tiny part of the total parametric space, which requires a fine control of the process. Some intrinsic effects of the etching process have been found to generate imperfections in the

UNIVERSITAT ROVIRA I VIRGILI
PHOTONIC BANDGAP ANALYSIS AND FABRICATION OF MACROPOROUS SILICON BY
ELECTROCHEMICAL ETCHING
Trifon Todorov Tirfonov
ISBN:978-84-693-6270-9/DL:T-1370-2010

otherwise perfect pore pattern. At long anodization times, the pore surface area increases, which leads to an increase in the dark current density and yields conical pores, the diameter of which decreases with depth. Increasing the etching current accordingly, which means to etch pores with the reverse conical shape is one of the methods to reduce the pore conicity. Another effective way is to use appropriate surfactants. Surfactants are commonly used to prevent degeneration caused by bubbles sticking to the sample surface. We found that the addition of nonionic surfactants increases the dark current contribution and thus enhances the formation of conical pores. The use of anionic surfactants considerably reduces the dark current and straight pores can be formed without difficulty. Highly uniform macropore arrays with different arrangements and dimensions were obtained by applying these “compensation” rules.

Finally, we have also presented some of the preliminary results of our work on novel applications of macroporous silicon. The structural features of the etched macropore arrays have been exploited to fabricate high-aspect-ratio silicon dioxide pillars, which may have applications in biotechnology as a 3D sensor platform for molecular recognition detections or as dense arrays of microsyringes for fluid delivery or precise chemical reaction stimulation. We have also fabricated a macroporous filter consisting of through-wafer pores and measured its optical characteristics. For light incidence parallel to the pores, a shortpass spectral behavior has been observed. The obtained results are only qualitative and suggest that further optimization of the etching process is needed in order to produce higher quality samples. We were also able to introduce periodic modulations of the pore diameter in depth and to fabricate ratchet-type macropore arrays, which have been envisioned for applications as ratchet devices for large-scale particle separation. We have shown that by a few post-etching steps the modulated macropore arrays can be converted into microstructures consisting of interconnected voids in all three dimensions. The technique used can be exploited for the fabrication of fully 3D photonic crystals.

Outlook

There are many possibilities for future work to extend upon the results presented here.

Optical characterization of the fabricated structures is required in order to reveal their photonic properties. Currently, we are working on an optical set-up based on a Fourier transform infrared (FTIR) spectrometer that will enable us to perform variable-angle specular reflectance measurements. They would be helpful to extract the

UNIVERSITAT ROVIRA I VIRGILI
PHOTONIC BANDGAP ANALYSIS AND FABRICATION OF MACROPOROUS SILICON BY ELECTROCHEMICAL ETCHING
Trifon Todorov Tirfonov
ISBN:978-84-693-6270-9/DL:T-1376-2010

photonic dispersion and compare it with the simulated photonic bands. To perform transmission measurements in a plane perpendicular to the pore axis, further three-dimensional micro-structuring of the etched samples is required. We hope that this optical characterization will be attempted in the near future.

Further optimization of the etching set-up and process is necessary if it is to be possible to downscale the lattice dimensions to 1 μm or less. Clearly, this will expand the potential applications of the fabricated macroporous structures. Optimizations are also needed to make it possible to fabricate 3D periodic structures by modulating the pore diameter with depth.

Greater effort must be made in simulations to take into account the disorder introduced by imperfections and to study the effects of the finite-size and material absorption.

ISBN:978-84-693-6270-9/DL:T-1376-2010

Appendixes

UNIVERSITAT ROVIRA I VIRGILI
PHOTONIC BANDGAP ANALYSIS AND FABRICATION OF MACROPOROUS SILICON BY
ELECTROCHEMICAL ETCHING
Trifon Todorov Tirfonov
ISBN:978-84-693-6270-9/DL:T-1376-2010

Appendix A

Electrochemical etching set-up

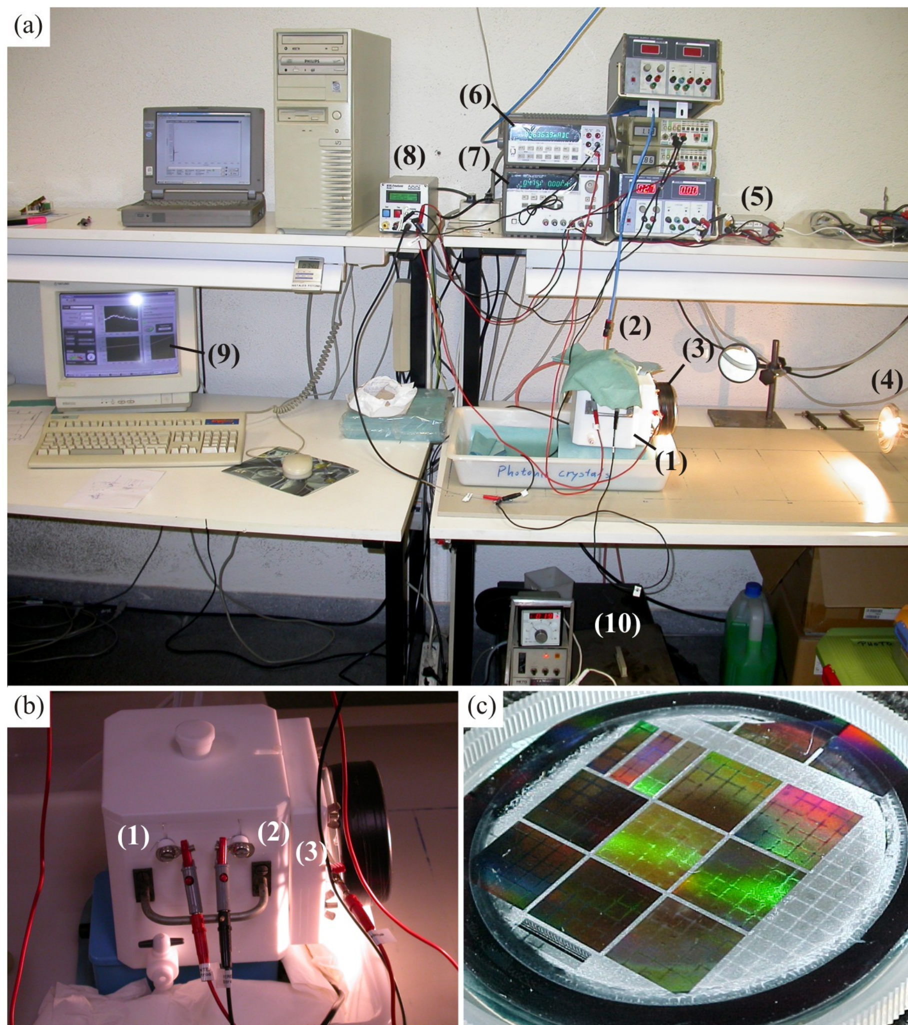

Fig. A.1. (a) photograph of the developed electrochemical etching apparatus in operation; (b) closer view of the electrochemical etching cell; (c) an example of etched 2-inch silicon wafer.

UNIVERSITAT ROVIRA I VIRGILI
PHOTONIC BANDGAP ANALYSIS AND FABRICATION OF MACROPOROUS SILICON BY ELECTROCHEMICAL ETCHING
Trifon Todorov Tirfonov
ISBN:978-84-693-6270-9/DL:T.1376-2010

Figure A.1a shows a photograph of the developed electrochemical etching set-up in operation. The etching apparatus comprises: (1) in-house made electrochemical cell for 2-inch wafers; (2) circuit for nitrogen bubbling; (3) IR blocking filter; (4) 100 W halogen lamp; (5) custom-built voltage-to-voltage transformer for controlling the backside illumination circuit; (6) HP 34401A digital multimeter; (7) HP E3631A power supply; (8) MEMS potentiostat; (9) LabVIEW based software for automatic control of the process parameters; (10) cryostat for temperature control.

Figure A.1b shows a closer view of the electrochemical etching cell with three-electrode configuration, as follows: (1) counter electrode (coiled Pt wire); (2) reference electrode (Pt wire positioned closely to the wafer); (3) working electrode (wafer).

Figure A.1c is a photograph of an electrochemically etched 2-inch wafer. The colored squares represent the regions where ordered macropores have grown, as defined by the sample preparation procedure. The white (or light grey) area indicates the region of random macropore formation. The observed white lines are the projection of the backside aluminum mesh electrode because of lower illumination intensity behind the aluminum wires. Due to diffraction, the ordered macropore regions present spectacular iridescence, which is a prominent feature of every periodic photonic media.

UNIVERSITAT ROVIRA I VIRGILI
PHOTONIC BANDGAP ANALYSIS AND FABRICATION OF MACROPOROUS SILICON BY ELECTROCHEMICAL ETCHING
Trifon Todorov Tirfonov
ISBN:978-84-693-6270-9/DL:T-1376-2010

Appendix B

Specifications of the lithographic masks employed for the macroporous silicon fabrication

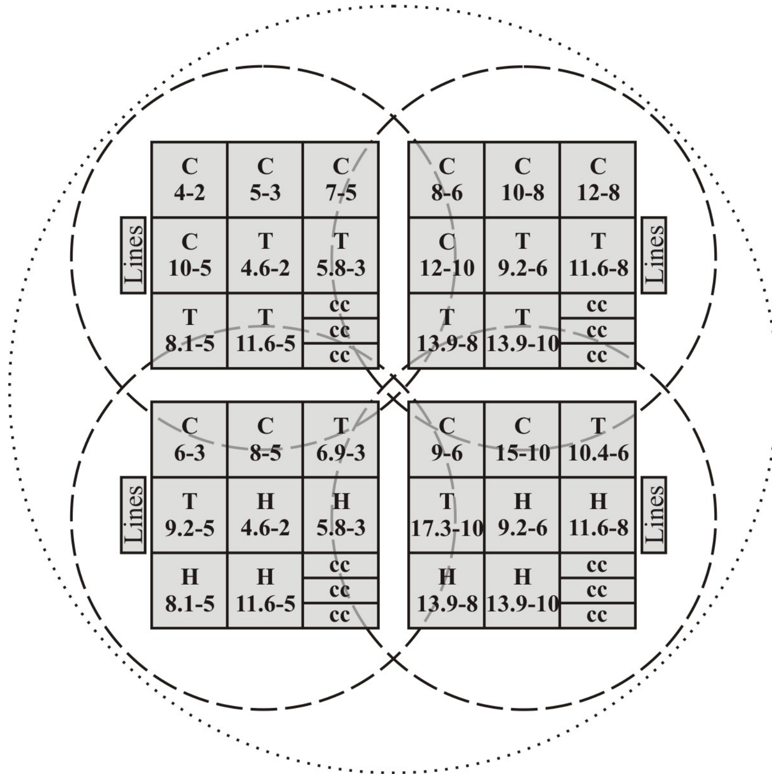

Fig. B.1. Photolithographic mask used in the electrochemical etching for ordered macropore formation. The areas where periodic microstructures exist are shaded. The doted circle denotes the diameter of a full 4-inch wafer. The diameter of a 2-inch wafer is represented by dashed circles. The dimensions of the figure are representative for the real dimensions of the structures.

The first lithographic mask we have used in our work is shown in Fig. B.1. It was prepared for making lithography on a full 4-wafer. There are four regions (shaded areas) with lithographic patterns, which have been used for making lithography on individual 2-inch wafers by appropriate aligning, as shown by dashed circles. The convention used for labeling the arrangements and the dimensions of the different periodic structures is as follows. Characters **C**, **T**, and **H** denote the lattice arrangement

UNIVERSITAT ROVIRA I VIRGILI
PHOTONIC BANDGAP ANALYSIS AND FABRICATION OF MACROPOROUS SILICON BY ELECTROCHEMICAL ETCHING
Trifon Todorov Tirfonov
ISBN:978-84-693-6270-9/DL:T-1376-2010

as square, triangular, and honeycomb, respectively. (The characters **CC** label regions, where the square lattice was distorted. These regions were not prepared for photonic applications and are beyond the scope of this thesis.) The numbers *x*-*y* label the dimensions of the lattice. The first number *x* stands for the lattice constant, i.e. the center-to-center distance between adjacent holes, while the second number *y* denotes the hole diameter. All numbers are in μm. For example, the label **C/4-2** denote a square lattice of holes with center-to-center distance of 4 μm and hole diameter 2 μm. Each of the ordered regions has a size of 10×10 mm approximately. Just from curiosity, the region **C/4-2** with 10×10 mm size contains approximately 6.25×10^6 holes.

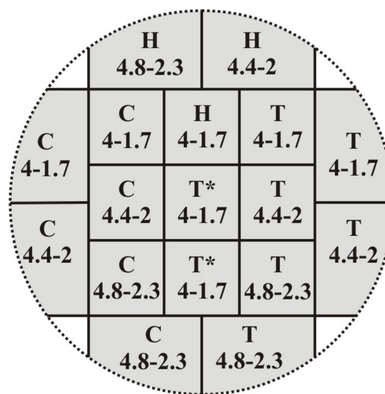

Fig. B.2. Photolithographic mask used for ordered macropore formation. The shaded area represent the regions with periodic microstructures. The dotted circle denotes the diameter of a 2-inch wafer. The dimensions of the figure are representative for the real dimensions of the microstructures.

The second mask we have used in our work is shown in Fig. B.2. It was designed for making photolithography on a single 2-inch wafer. Again, the shaded areas denote the regions where lithographic pattern exists. The used naming convention is the same as for the mask from Fig. B.1. As can be seen, the new mask design makes better use of the whole wafer surface in comparison to the first lithographic mask. Also, new features have been added. The triangular structures labeled by asterisk contain intentionally introduced point and line defects. Every lithographic pattern is provided with some alignment marks, which facilitates the future microstructuring of the fabricated macropore arrays.

UNIVERSITAT ROVIRA I VIRGILI
PHOTONIC BANDGAP ANALYSIS AND FABRICATION OF MACROPOROUS SILICON BY ELECTROCHEMICAL ETCHING
Trifon Todorov Tirfonov
ISBN:978-84-693-6270-9/DL:T-1376-2010

Appendix C

Porosity as a function of the pore diameter to pore pitch ratio for different pore shapes and patterns

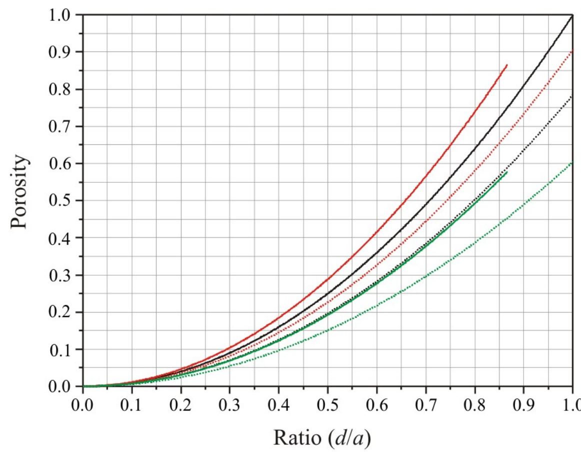

Legend:

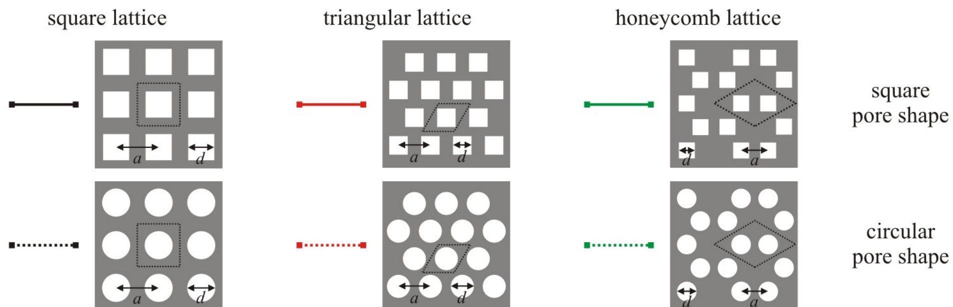

Fig. C.1. Dependence of the porosity on the ratio between the pore diameter *d* and center-to-center pore distance *a* for different pore shapes and pore patterns. The dotted line inside the lattice figures denotes the unit cell used for the calculations.

The porosity *p* of the pattern is defined as

$$p = \frac{A_{pore}}{A_{cell}}$$

where A_{pore} and A_{cell} denote the area occupied by the pores and the total area of the unit

UNIVERSITAT ROVIRA I VIRGILI
PHOTONIC BANDGAP ANALYSIS AND FABRICATION OF MACROPOROUS SILICON BY ELECTROCHEMICAL ETCHING
Trifon Todorov Tirfonov
ISBN:978-84-693-6270-9/DL:T-1376-2010

cell, respectively. Note that the center-to-center distance *a*, termed the pitch of the pattern, is not equal to the lattice constant for the honeycomb lattice. Also, the unit cell for the honeycomb lattice comprises two pores. The expressions for A_{pore} and A_{cell} for the different patterns are given in Table C.1. Note that the close-packed condition (when the pores begin to touch) for the triangular and honeycomb lattice of square-shaped pores is d=0.866a, while it is $d=a$ for other patterns.

From Fig. C.1 it can be seen that for a fixed porosity the diameter (or size) of the pores is different if circular or square shapes are considered. Since the pores may have all shapes between a circle and a square, an average porosity should be considered when calculating the required etching currents.

Table C.1. Expressions used to calculate the porosity of different pore patterns. The close-packed condition (when the pores begin to touch) is also given.

Lattice	Pore area, A_{pore}	Unit cell area, A_{cell}	Close-packing condition, d/a
1. Square lattice			
square shape	d^2	a^2	1
circular shape	$\frac{\pi d^2}{4}$		1
2. Triangular lattice			
square shape	d^2	$\frac{\sqrt{3}}{2}a^2$	0.866
circular shape	$\frac{\pi d^2}{4}$		1
3. Honeycomb lattice			
square shape	$2d^2$	$\frac{3\sqrt{3}}{2}a^2$	0.866
circular shape	$\frac{\pi d^2}{2}$		1

UNIVERSITAT ROVIRA I VIRGILI
PHOTONIC BANDGAP ANALYSIS AND FABRICATION OF MACROPOROUS SILICON BY ELECTROCHEMICAL ETCHING
Trifon Todorov Tirfonov
ISBN:978-84-693-6270-9/DL:T-1376-2010

UNIVERSITAT ROVIRA I VIRGILI
PHOTONIC BANDGAP ANALYSIS AND FABRICATION OF MACROPOROUS SILICON BY ELECTROCHEMICAL ETCHING
Trifon Todorov Tirfonov
ISBN:978-84-693-6270-9/DL:T-1376-2010

References

[1] J. Bardeen and W. H. Brattain, "The Transistor, A Semi-Conductor Triode", *Phys. Rev.* **74**, (1948), 230.

[2] D. Miller, "Rationale and challenges for optical interconnects to electronic chips", *Proc. IEEE* **88**, (2000), 728.

[3] R. W. Keyes, "Physical limits in digital electronics", *Proc. IEEE* **63**, (1975), 740.

[4] L. Pavesi, "Will silicon be the photonic material of the third millenium?" *J. Phys.: Condens. Matter* **15**, (2003), R1169.

[5] L. C. Kimerling, "Silicon microphotonics", *Appl. Surf. Sci.* **159-160**, (2000), 8.

[6] G. Massini, L. Colace and G. Assanto, "Si based optoelectronics for communications", *Mater. Sci. Eng. B* **89**, (2002), 2.

[7] J. D. Joannopoulos, P. R. Villeneuve and S. Fan, "Photonic crystals: putting a new twist on light", *Nature* **386**, (1997), 143.

[8] J. D. Joannopoulos, P. R. Villeneuve and S. Fan, "Photonic crystals", *Solid State Commun.* **102**, (1997), 165.

[9] E. Yablonovitch, "Photonic band-gap structures", *J. Opt. Soc. Am. B* **10**, (1993), 283.

[10] E. Yablonovitch, "Photonic band-gap crystals", *J. Phys.: Condens. Matter* **5**, (1993), 2443.

[11] C. López, "Materials aspects of photonic crystals", *Adv. Mater.* **15**, (2003), 1679.

[12] T. F. Krauss and R. M. de la Rue, "Photonic crystals in the optical regime - past, present and future", *Prog. Quantum Electron.* **23**, (1999), 51.

[13] J. D. Joannopoulos, R. D. Meade and J. N. Winn, in "Photonic crystals. Molding the flow of light", (Princeton University Press, Princeton, NJ, 1995).

[14] E. Yablonovitch, "Inhibited spontaneous emission in solid-state physics and electronics", *Phys. Rev. Lett.* **58**, (1987), 2059.

[15] S. John, "Strong localization of photons in certain disordered superlattices", *Phys. Rev. Lett.* **58**, (1987), 2486.

[16] N. W. Ashcroft and N. D. Mermin, in "Solid State Physics", (Saunders College, Philadelphia, USA, 1976).

[17] K. Sakoda, in "Optical Properties of Photonic Crystals", (Springer-Verlag, Berlin, 2001).

[18] R. G. Hulet, E. S. Hilfer and D. Kleppner, "Inhibited spontaneous emission by a Rydberg atom", *Phys. Rev. Lett.* **55**, (1985), 2137.

[19] J. Martorell and N. M. Lawandy, "Observation of inhibited spontaneous emission in a periodic dielectric structure", *Phys. Rev. Lett.* **65**, (1990), 1877.

ISBN:978-84-693-6270-9/DL:T-1376-2010

[20] P. W. Anderson, "Absence of diffusion in certain random lattices", *Phys. Rev.* **109**, (1958), 1492.

[21] P. A. Lee and T. V. Ramakrishnan, "Disordered electronic systems", *Rev. Mod. Phys.* **57**, (1985), 287.

[22] E. N. Economou and M. M. Sigalas, "Classical wave propagation in periodic structures: Cermet versus network topology", *Phys. Rev. B* **48**, (1993), 13434.

[23] M. M. Sigalas and E. N. Economou, "Band structure of elastic waves in two dimensional systems", *Solid State Commun.* **86**, (1993), 141.

[24] M. S. Kushwaha, P. Halevi, L. Dobrzynski and B. Djafari-Rouhani, "Acoustic band structure of periodic elastic composites", *Phys. Rev. Lett.* **71**, (1993), 2022.

[25] M. S. Kushwaha, P. Halevi, G. Martinéz, L. Dobrzynski and B. Djafari-Rouhani, "Theory of acoustic band structure of periodic elastic composites", *Phys. Rev. B* **49**, (1994), 2313.

[26] R. Mártinez-Sala, J. Sancho, J. V. Sánchez, V. Gómez, J. Llinares and F. Meseguer, "Sound attenuation by sculpture", *Nature* **378**, (1995), 241.

[27] J. V. Sánchez-Pérez, D. Caballero, R. Mártinez-Sala, C. Rubio, J. Sánchez-Dehesa, F. Meseguer, J. Llinares and F. Gálvez, "Sound attenuation by a two-dimensional array of rigid cylinders", *Phys. Rev. Lett.* **80**, (1998), 5325.

[28] F. Meseguer, M. Holgado, D. Caballero, N. Benaches, C. López, J. Sánchez-Dehesa and J. Llinares, "Two-dimensional elastic bandgap crystal to attenuate surface waves", *IEEE J. Lightwave Technol.* **17**, (1999), 2196.

[29] A. Yariv and P. Yeh, in "Optical Waves in Crystals: Propagation and Control of Laser Radiation", (Wiley, New York, 1983).

[30] K. M. Ho, C. T. Chan and C. M. Soukoulis, "Existence of a photonic gap in periodic dielectric structures", *Phys. Rev. Lett.* **65**, (1990), 3152.

[31] E. Yablonovitch, T. J. Gmitter and K. M. Leung, "Photonic band structure: the face-centered-cubic case employing nonspherical atoms", *Phys. Rev. Lett.* **67**, (1991), 2295.

[32] S.-Y. Lin and J. G. Fleming, "A three-dimensional optical photonic crystal", *IEEE J. Lightwave Technol.* **17**, (1999), 1944.

[33] J. G. Fleming and S.-Y. Lin, "Three-dimensional photonic crystal with a stop-band from 1.35 to 1.95 micrometers", *Opt. Lett.* **24**, (1999), 49.

[34] S. Noda, N. Yamamoto, M. Imada, H. Kobayashi and M. Okano, "Alignment and stacking of semiconductor photonic bandgaps by wafer-fusion", *IEEE J. Lightwave Technol.* **17**, (1999), 1948.

[35] J. E. G. J. Wijnhoven and W. L. Vos, "Preparation of photonic crystals made of air spheres in titania", *Science* **281**, (1998), 802.

[36] A. Blanco, E. Chomski, S. Grabtchak, M. Ibisate, S. John, S. W. Leonard, C. López, F. Meseguer, H. Miguez, J. P. Mondia, G. A. Ozin, O. Toader and H. M. van Driel, "Large-scale synthesis of a silicon photonic crystal with a complete three-dimensional bandgap near 1.5 micrometres", *Nature* **405**, (2000), 437.

[37] A. Chutinan and S. Noda, "Spiral three-dimensional photonic-band-gap structure", *Phys. Rev. B* **57**, (1998), R2006.

[38] O. Toader and S. John, "Proposed square spiral microfabrication architecture for large three-dimensional photonic band gap crystals", *Science* **292**, (2001), 1133.

[39] S. G. Johnson and J. D. Joannopoulos, "Three-dimensionally periodic dielectric layered structure with omnidirectional photonic band gap", *Appl. Phys. Lett.* **77**, (2000), 3490.

[40] M. Notomi, T. Tamamura, T. Kawashima and S. Kawakami, "Drilled alternating-layer three-dimensional photonic crystals having a full photonic band gap", *Appl. Phys. Lett.* **77**, (2000), 4256.

[41] S. Y. Chou, P. R. Krauss and P. J. Renstrom, "Imprint lithography with 25-nanometer resolution", *Science* **272**, (1996), 85.

[42] S. Noda, K. Tomoda, N. Yamamoto and A. Chutinan, "Full three-dimensional photonic bandgap crystals at near-infrared wavelengths", *Science* **289**, (2000), 602.

[43] R. B. Wehrspohn and J. Schilling, "A model system for photonic crystals: macroporous silicon", *Phys. Stat. Sol. A* **197**, (2003), 673.

[44] M. Plihal, A. Shambrook, A. A. Maradudin and P. Sheng, "Two-dimensional photonic band structures", *Opt. Commun.* **80**, (1991), 199.

[45] W. M. Robertson, G. Arjavalingam, R. D. Meade, K. D. Brommer, A. M. Rappe and J. D. Joannopoulos, "Measurement of photonic band structure in a two-dimensional periodic dielectric array", *Phys. Rev. Lett.* **68**, (1992), 2023.

[46] R. D. Meade, K. D. Brommer, A. M. Rappe and J. D. Joannopoulos, "Existence of a photonic band gap in two dimensions", *Appl. Phys. Lett.* **61**, (1992), 495.

[47] P. R. Villeneuve and M. Piche, "Photonic band gaps in two-dimensional square lattices: Square and circular rods", *Phys. Rev. B* **46**, (1992), 4973.

[48] M. Plihal and A. A. Maradudin, "Photonic band structure of two-dimensional systems: the triangular lattice", *Phys. Rev. B* **44**, (1991), 8565.

[49] D. Cassagne, C. Jouanin and D. Bertho, "Hexagonal photonic-band-gap structures", *Phys. Rev. B* **53**, (1996), 7134.

[50] C. M. Anderson and K. P. Giapis, "Larger two-dimensional photonic band gaps", *Phys. Rev. Lett.* **77**, (1996), 2949.

[51] X.-H. Wang, B.-Y. Gu, Z.-Y. Li and G.-Z. Yang, "Large absolute photonic band gaps created by rotating noncircular rods in two-dimensional lattices", *Phys. Rev. B* **60**, (1999), 11417.

[52] R. Padjen, J. M. Gerard and J. Y. Marzin, "Analysis of the filling pattern dependence of the photonic bandgap for two-dimensional systems", *J. Mod. Opt.* **41**, (1994), 295.

[53] M. Agio and L. C. Andreani, "Complete photonic band gap in a two-dimensional chessboard lattice", *Phys. Rev. B* **61**, (2000), 15519.

[54] T. Baba and T. Matsuzaki, "Theoretical calculation of photonic gap in

ISBN:978-84-693-6270-9/DL:T-1376-2010

semiconductor 2-dimensional photonic crystals with various shapes of optical atoms", *Jpn. J. Appl. Phys.* **34**, (1995), Part 1 4496.

[55] M. Qiu and S. He, "Large complete band gap in two-dimensional photonic crystals with elliptic air holes", *Phys. Rev. B* **60**, (1999), 10610.

[56] P. L. Gourley, J. R. Wendt, G. A. Vawter, T. M. Brennan and B. E. Hammons, "Optical properties of two-dimensional photonic lattices fabricated as honeycomb nanostructures in compound semiconductors", *Appl. Phys. Lett.* **64**, (1994), 687.

[57] T. Krauss, Y. P. Song, S. Thoms, C. D. W. Wilkinson and R. M. de la Rue, "Fabrication of 2-D photonic bandgap structures in GaAs/AlGaAs", *Electron. Lett.* **30**, (1994), 1444.

[58] K. Inoue, M. Wada, K. Sakoda, A. Yamanaka, M. .Hayashi and J. W. Haus, "Fabrication of two-dimensional photonic band structure with near-infrared band gap", *Jpn. J. Appl. Phys.* **33**, (1994), Part2 L1463.

[59] U. Grüning, V. Lehmann, S. Ottow and K. Busch, "Macroporous silicon with a complete two-dimensional photonic band gap centered at 5 μm", *Appl. Phys. Lett.* **68**, (1996), 747.

[60] V. Lehmann and H. Föll, "Formation mechanism and properties of electrochemically etched trenches in n-type silicon", *J. Electrochem. Soc.* **137**, (1990), 653.

[61] J. Schilling, A. Birner, F. Müller, R. B. Wehrspohn, R. Hillebrand, U. Gösele, K. Busch, S. John, S. W. Leonard, H. M. van Driel, "Optical characterisation of 2D macroporous silicon photonic crystals with bandgaps around 3.5 and 1.3 μm", *Opt. Mater.* **17**, (2001), 7.

[62] H. Masuda, H. Yamada, M. Satoh, H. Asoh, M. Nakao and T. Tamamura, "Highly ordered nanochannel-array architecture in anodic alumina", *Appl. Phys. Lett.* **71**, (1997), 2770.

[63] S. G. Johnson, S. Fan, P. R. Villeneuve, J. D. Joannopoulos and L. A. Kolodziejski, "Guided modes in photonic crystal slabs", *Phys. Rev. B* **60**, (1999), 5751.

[64] A. Chutinan, M. Okano and S. Noda, "Wider bandwidth with high transmission through waveguide bends in two-dimensional photonic crystal slabs", *Appl. Phys. Lett.* **80**, (2002), 1698.

[65] A. Chutinan and S. Noda, "Waveguides and waveguide bends in two-dimensional photonic crystal slabs", *Phys. Rev. B* **62**, (2000), 4488.

[66] O. Painter, T. Vuckovic and A. Scherer, "Defect modes of a two-dimensional photonic crystal in an optically thin dielectric slab", *J. Opt. Soc. Amer. B* **16**, (1999), 275.

[67] T. Baba, N. Fukaya and J. Yonekura, "Observation of light propagation in photonic crystal optical waveguides with bends", *Electron. Lett.* **35**, (1999), 654.

[68] T. F. Krauss, R. M. de la Rue and S. Brand, "Two-dimensional photonic-bandgap structures operating at near-infrared wavelengths", *Nature* **383**, (1996), 699.

UNIVERSITAT ROVIRA I VIRGILI
PHOTONIC BANDGAP ANALYSIS AND FABRICATION OF MACROPOROUS SILICON BY ELECTROCHEMICAL ETCHING
Trifon Todorov Tirfonov
ISBN:978-84-693-6270-9/DL:T-1376-2010

[69] S. Kuchinsky, D. C. Allan, N. F. Borrelli and J.-C. Cotteverte, "3D localization in a channel waveguide in a photonic crystal with 2D periodicity", *Opt. Commun.* **175**, (2000), 147.

[70] A. Shinya, M. Notomi, I. Yokohama, C. Takahashi, J.-I. Takahashi and T. Tamamura, "Two-dimensional Si photonic crystals on oxide using SOI substrate", *Opt. Quantum Electron.* **34**, (2002), 113.

[71] M. Loncar, D. Nedeljkovic, T. Doll, J. Vuckovic, A. Scherer and T. P. Pearsall, "Waveguiding in planar photonic crystals", *Appl. Phys. Lett.* **77**, (2000), 1937.

[72] M. Loncar, T. Doll, J. Vuckovic and A. Scherer, "Design and fabrication of silicon photonic crystal optical waveguides", *IEEE J. Lightwave Technol.* **18**, (2000), 1402.

[73] M. Notomi, A. Shinya, K. Yamada, J.-I. Takahashi, C. Takahashi and I. Yokohama, "Structural tuning of guiding modes of line-defect waveguides of silicon-on-insulator photonic crystal slabs", *IEEE J. Quantum Electron.* **38**, (2002), 736.

[74] M. Imada, S. Noda, A. Chutinan, T. Tokuda, M. Murata and G. Sasaki, "Coherent two-dimensional lasing action in surface-emitting laser with triangular-lattice photonic crystal structure", *Appl. Phys. Lett.* **75**, (1999), 316.

[75] S. Fan, P. R. Villeneuve, J. D. Joannopoulos and E. F. Schubert, "High extraction efficiency of spontaneous emission from slabs of photonic crystals", *Phys. Rev. Lett.* **78**, (1997), 3294.

[76] J. C. Knight, J. Broeng, T. A. Birks and P. S. J. Russell, "Photonic band gap guidance in optical fibers", *Science* **282**, (1998), 1476.

[77] Y. Ohtera, T. Sato, T. Kawashima, T. Tamamura and S. Kawakami, "Photonic crystal polarisation splitters", *Electron. Lett.* **35**, (1999), 1271.

[78] S. Fan, P. R. Villeneuve, J. D. Joannopoulos, M. J. Khan, C. Manolatou and H. A. Haus, "Theoretical analysis of channel drop tunneling processes", *Phys. Rev. B* **59**, (1999), 15882.

[79] A. Chutinan, M. Mochizuki, M. Imada and S. Noda, "Surface-emitting channel drop filters using single defects in two-dimensional photonic crystal slabs", *Appl. Phys. Lett.* **79**, (2001), 2690.

[80] A. R. Parker, R. C. McPhedran, D. R. McKenzie, L. C. Botten and N. A. Nicorovici, "Photonic engineering: Aphrodite's iridescence", *Nature* **409**, (2001), 36.

[81] R. D. Meade, K. D. Brommer, A. M. Rappe and J. D. Joannopoulos, "Photonic bound states in periodic dielectric materials", *Phys. Rev. B* **44**, (1991), 13772.

[82] E. Yablonovitch, T. J. Gmitter, R. D. Meade, A. M. Rappe, K. D. Brommer and J. D. Joannopoulos, "Donor and acceptor modes in photonic band structure", *Phys. Rev. Lett.* **67**, (1991), 3380.

[83] R. D. Meade, A. M. Rappe, K. D. Brommer and J. D. Joannopoulos, "Nature of the photonic band gap: some insights from a field analysis", *J. Opt. Soc. Am. B* **10**, (1993), 328.

[84] S. G. Johnson and J. D. Joannopoulos, The MIT Photonic-Bands Package home page http://ab-initio.mit.edu/mpb/.

[85] P. R. Villeneuve, S. Fan and J. D. Joannopoulos, "Microcavities in photonic crystals: Mode symmetry, tunability, and coupling efficiency", *Phys. Rev. B* **54**, (1996), 7837.

[86] R. D. Meade, A. Devenyi, J. D. Joannopoulos, O. L. Alerhand, D. A. Smith and K. Kash, "Novel applications of photonic band gap materials: low-loss bends and high Q cavities", *J. Appl. Phys.* **75**, (1994), 4753.

[87] J. Vuckovic, M. Loncar, H. Mabuchi and A. Scherer, "Design of photonic crystal microcavities for cavity QED", *Phys. Rev. E* **65**, (2002), 016608.

[88] H. Benisty, C. Weisbuch, D. Labilloy, M. Rattier, C. J. M. Smith, T. F. Krauss, R. M. de la Rue, R. Houdre, U. Oesterle, C. Jouanin and D. Cassagne, "Optical and confinement properties of two-dimensional photonic crystals", *IEEE J. Lightwave Technol.* **17**, (1999), 2063.

[89] S. G. Johnson, P. R. Villeneuve, S. Fan and J. D. Joannopoulos, "Linear waveguides in photonic-crystal slabs", *Phys. Rev. B* **62**, (2000), 8212.

[90] A. Mekis, J. C. Chen, I. Kurland, S. Fan, P. R. Villeneuve and J. D. Joannopoulos, "High transmission through sharp bends in photonic crystal waveguides", *Phys. Rev. Lett.* **77**, (1996), 3787.

[91] S.-Y. Lin, E. Chow, V. Hietala, P. R. Villeneuve and J. D. Joannopoulos, "Experimental demonstration of guiding and bending of electromagnetic waves in a photonic crystal", *Science* **282**, (1998), 274.

[92] H. Benisty, M. Rattier and S. Olivier, "Two-dimensional photonic crystals: new feasible confined optical systems", *C. R. Physique* **3**, (2002), 89.

[93] T. K. Krauss, "Planar photonic crystal waveguide devices for integrated optics", *Phys. Stat. Sol. A* **197**, (2003), 688.

[94] "Roadmap on Photonic Crystals", edited by S. Noda and T. Baba, (Kluwer Academic Publishers, Dordrecht, Boston, London, 2003).

[95] J. D. Jackson, in "Classical Electrodynamics", (John Wiley & Sons, New York, 1975).

[96] E. Yablonovitch and T. J. Gmitter, "Photonic band structure: the face-centered-cubic case", *Phys. Rev. Lett.* **63**, (1989), 1950.

[97] K. M. Leung and Y. F. Liu, "Photon band structures: The plane-wave method", *Phys. Rev. B* **41**, (1990), 10188.

[98] K. M. Leung and Y. F. Liu, "Full vector wave calculation of photonic band structures in face-centered-cubic dielectric media", *Phys. Rev. Lett.* **65**, (1990), 2646.

[99] W. H. Press, S. A. Teukolsky, W. T. Vetterling and B. P. Flannery, in "Numerical Recipes in Fortran 77: The Art of Scientific Computing", (Cambridge University Press, Cambridge, 1992).

[100] P.-G. Luan and Z. Ye, "Two-dimensional photonic crystals", *Condensed Matter* **1**, (2001), 0105428.

[101] H. S. Sözüer, J.W.Hans and R.Inguva, "Photonic bands: Convergence problems with the plane-wave method", *Phys. Rev. B* **45**, (1992), 13962.

[102] P. R. Villeneuve and M. Piché, "Photonic bandgaps in periodic dielectric

structures", *Prog. Quantum Electron.* **18**, (1994), 153.

[103] K. Busch and S. John, "Photonic band gap formation in certain self-organizing systems", *Phys. Rev. E* **58**, (1998), 3896.

[104] K. Busch, M. Frank, A. Garcia-Martin, D. Hermann, S. F. Mingaleev, M. Schillinger and L. Tkeshelashvili, "A solid state theoretical approach to the optical properties of photonic crystals", *Phys. Stat. Sol. A* **197**, (2003), 637.

[105] K. Sakoda, "Optical transmittance of a two-dimensional triangular photonic lattice", *Phys. Rev. B* **51**, (1995), 4672.

[106] K. Sakoda, "Transmittance and Bragg reflectivity of two-dimensional photonic lattices", *Phys. Rev. B* **52**, (1995), 8992.

[107] K. S. Yee, "Numerical solution of initial boundary value problems involving Maxwell's equations in isotropic media", *IEEE Trans. Antennas Propag.* **14**, (1966), 302.

[108] C. T. Chan, Q. L. Yu and K. M. Ho, "Order-n spectral method for electromagnetic waves", *Phys. Rev. B* **51**, (1995), 16635.

[109] A. Taflove and S. C. Hagness, in "Computational Electrodynamics: The Finite-Difference Time-Domain Method", (Artech House Publishers, Boston, London, 2000).

[110] O. Hess, C. Hermann and A. Klaedtke, "Finite-difference time-domain simulations of photonic crystal defect structures", *Phys. Stat. Sol. A* **197**, (2003), 605.

[111] A. J. Ward and J. B. Pendry, "A program for calculating photonic band structures and Green's functions using a non-orthogonal FDTD method", *Comput. Phys. Commun.* **112**, (1998), 23.

[112] S. G. Johnson, C. Manolatou, S. Fan, P. R. Villeneuve, J. D. Joannopoulos and H. A. Haus, "Elimination of cross talk in waveguide intersections", *Opt. Lett.* **23**, (1998), 1855.

[113] D. Felbacq, G. Tayeb and D. Maystre, "Scattering by a random set of parallel cylinders", *J. Opt. Soc. Am. A* **11**, (1994), 2526.

[114] L. C. Botten, N. A. Nicorovici, R. C. McPhedran, C. M. d. Sterke and A. A. Asatryan, "Photonic band structure calculations using scattering matrices", *Phys. Rev. E* **64**, (2001), 046603.

[115] J. B. Pendry and A. MacKinnon, "Calculation of photon dispesion relations", *Phys. Rev. Lett.* **69**, (1992), 2772.

[116] M. D. B. Charlton, S. W. Roberts and G. J. Parker, "Guided mode analysis, and fabrication of a 2-dimensional visible photonic band structure confined within a planar semiconductor waveguide", *Mater. Sci. Eng. B* **49**, (1997), 155.

[117] J. M. Gerard, A. Izraël, J. Y. Marzin, R. Padjen and F. R. Ladan, "Photonic bandgap of two-dimensional dielectric crystals", *Solid-State Electron.* **37**, (1994), 1341.

[118] V. Berger, O. Gauthier-Lafaye and E. Costard, "Fabrication of a 2D photonic bandgap by a holographic method", *Electron. Lett.* **33**, (1997), 425.

[119] M. Campbell, D. N. Sharp, M. T. Harrison, R. G. Denning and A. J.

UNIVERSITAT ROVIRA I VIRGILI
PHOTONIC BANDGAP ANALYSIS AND FABRICATION OF MACROPOROUS SILICON BY ELECTROCHEMICAL ETCHING
Trifon Todorov Tirfonov
ISBN:978-84-693-6270-9/DL:T-1376-2010

Turberfield, "Fabrication of photonic crystals for the visible spectrum by holographic lithography", *Nature* **404**, (2000), 53.

[120] I. Divliansky, T. S. Mayer, K. S. Holliday and V. H. Crespi, "Fabrication of three-dimensional polymer photonic crystal structures using single diffraction element interference lithography", *Appl. Phys. Lett.* **82**, (2003), 1667.

[121] J. O'Brien, O. Painter, R. Lee, C. C. Cheng, A. Yariv and A. Scherer, "Lasers incorporating 2D photonic bandgap mirrors", *Electron. Lett.* **32**, (1996), 2243.

[122] T. Baba, K. Inoshita, H. Tanaka, J. Yonekura, M. Ariga, A. Matsutani, T. Miyamoto, F. Koyama and K. Iga, "Strong enhancement of light extraction efficiency in GaInAsP 2-D-arranged microcolumns", *IEEE J. Lightwave Technol.* **17**, (1999), 2113.

[123] Y. Xia and G. M. Whitesides, "Soft lithography", *Annu. Rev. Mater. Sci.* **28**, (1998), 153.

[124] A. Rosenberg, R. J. Tonucci and E. A. Bolden, "Photonic band-structure effects in the visible and near ultraviolet observed in solid-state dielectric arrays", *Appl. Phys. Lett.* **69**, (1996), 2638.

[125] V. Lehmann, "The physics of macropore formation in low doped n-type silicon", *J. Electrochem. Soc.* **140**, (1993), 2836.

[126] U. Grüning, V. Lehmann and C. M. Engelhardt, "Two-dimensional infrared photonic band gap structure based on porous silicon", *Appl. Phys. Lett.* **66**, (1995), 3254.

[127] S. Rowson, A. Chelnokov and J. M. Lourtioz, "Two-dimensional photonic crystals in macroporous silicon: from mid-infrared (10 μm) to telecommunication wavelengths (1.3-1.5 μm)", *IEEE J. Lightwave Technol.* **17**, (1999), 1989.

[128] H. W. Lau, G. J. Parker, R. Greef and M. Hölling, "High aspect ratio submicron silicon pillars fabricated by photoassisted electrochemical etching and oxidation", *Appl. Phys. Lett.* **67**, (1995), 1877.

[129] T. Baba and M. Koma, "Possibility of InP-based 2-dimensional photonic crystal: an approach by the anodization method", *Jpn. J. Appl. Phys.* **34**, (1995), Part1 1405.

[130] J.-N. Chazalviel, R. B. Wehrspohn and F. Ozanam, "Electrochemical preparation of porous semiconductors: from phenomenology to understanding", *Mater. Sci. Eng. B* **69-70**, (2000), 1.

[131] H. Föll, S. Langa, J. Carstensen, M. Christophersen and I. M. Tiginyanu, "Pores in III-V semiconductors", *Adv. Mater.* **15**, (2003), 183.

[132] H. Masuda, M. Ohya, H. Asoh, M. Nakao, M. Nohtomi and T. Tamamura, "Photonic crystal using anodic porous alumina", *Jpn. J. Appl. Phys.* **38**, (1999), L1403.

[133] P. R. Villeneuve and M. Piché, "Photonic band gaps in two-dimensional square and hexagonal lattices", *Phys. Rev. B* **46**, (1992), 4969.

[134] W. M. Robertson, G. Arjavalingam, R. D. Meade, K. D. Brommer, A. M. Rappe and J. D. Joannopoulos, "Measurements of the photon dispersion relation in two-dimensional ordered dielectric arrays", *J. Opt. Soc. Am. B* **10**,

(1993), 322.

[135] F. Bassani and G. P. Parravicini, in "Electronic states and optical transitions in solids", (Pergamon press, Oxford, 1975).

[136] G. F. Koster, "Space groups and their representations", *Solid State Phys.* **5**, (1957), 173.

[137] H. S. Sözüer and J. W. Haus, "Photonic bands: simple-cubic lattice", *J. Opt. Soc. Am. B* **10**, (1993), 296.

[138] M. Qiu and S. He, "Optimal design of a two-dimensional photonic crystal of square lattice with a large complete two-dimensional bandgap", *J. Opt. Soc. Am. B* **17**, (2000), 1027.

[139] C. S. Kee, J. E. Kim and H. Y. Park, "Absolute photonic band gap in a two-dimensional square lattice of square dielectric rods in air", *Phys. Rev. E* **56**, (1997), R6291.

[140] C. M. Anderson and K. P. Giapis, "Symmetry reduction in group 4mm photonic crystals", *Phys. Rev. B* **56**, (1997), 7313.

[141] Z. Y. Li, B. Y. Gu and G. Z. Yang, "Large absolute band gap in 2D anisotropic photonic crystals", *Phys. Rev. Lett.* **81**, (1998), 2574.

[142] N. Malkova, S. Kim and V. Gopalan, "Symmetrical perturbation analysis of complex two-dimensional photonic crystals", *Phys. Rev. B* **66**, (2002), 115113.

[143] X. Zhang, Z.-Q. Zhang, L.-M. Li, C. Jin, D. Zhang, B. Man and B. Cheng, "Enlarging a photonic band gap by using insertion", *Phys. Rev. B* **61**, (2000), 1892.

[144] R. Hillebrand and W. Hergert, "Band gap studies of triangular 2D photonic crystals with varying pore roundness", *Solid State Commun.* **115**, (2000), 227.

[145] M. M. Sigalas, C. M. Soukoulis, R. Biswas and K. M. Ho, "Effect of the magnetic permeability on photonic band gaps", *Phys. Rev. B* **56**, (1997), 959.

[146] D. F. Sievenpiper, E. Yablonovitch, J. N. Winn, S. Fan, P. R. Villeneuve and J. D. Joannopoulos, "3D metallo-dielectric photonic crystals with strong capacitive coupling between metallic islands", *Phys. Rev. Lett.* **80**, (1998), 2829.

[147] X. Zhang and Z.-Q. Zhang, "Creating a gap without symmetry breaking in two-dimensional photonic crystals", *Phys. Rev. B* **61**, (2000), 9847.

[148] S. Kim and V. Gopalan, "Strain-tunable photonic band gap crystals", *Appl. Phys. Lett.* **78**, (2001), 3015.

[149] D. Cassagne, C. Jouanin and D. Bertho, "Photonic band gaps in a two-dimensional graphite structure", *Phys. Rev. B* **52**, (1995), R2217.

[150] J. B. Nielsen, T. Sondergaard, S. E. Barkou, A. Bjarklev, J. Broeng and M. B. Nielsen, "Two-dimensional Kagome structure, fundamental hexagonal photonic crystal configuration", *Electron. Lett.* **35**, (1999), 1736.

[151] L. Wu, F. Zhuang and S. He, "Degeneracy analysis for a supercell of a photonic crystal and its application to the creation of band gaps", *Phys. Rev. E* **67**, (2003), 026612.

[152] J. Kim and S. Lee, "Metamorphosis of photonic bandgaps", *J. Appl. Phys.* **92**,

(2002), 1185.

[153] T. Pan and Z.-Y. Li, "The effect of etching interfacial layers on the absolute photonic band gap in two-dimensional photonic crystals", *Solid State Commun.* **128**, (2003), 187.

[154] T. Baba and T. Matsuzaki, "Fabrication and photoluminescence studies of GaInAsP/InP 2-dimensional photonic crystals", *Jpn. J. Appl. Phys.* **35**, (1996), 1348.

[155] S. M. Sze, in "Physics of Semiconductor Devices", (John Wiley & Sons, NJ, 1981).

[156] S. G. Johnson and J. D. Joannopoulos, "Block-iterative frequency-domain methods for Maxwell's equations in a plane-wave basis", *Optics Express* **8**, (2001), 173.

[157] P. Müller, "IUPAC Manual of Symbols and Technology", *Pure Appl. Chem.* **31**, (1972), 578.

[158] A. Uhlir, "Electrolytic shaping of germanium and silicon", *Bell System Tech. J.* **35**, (1956), 333.

[159] D. R. Turner, "Electropolishing silicon in hydrofluoric acid solutions", *J. Electrochem. Soc.* **105**, (1958), 402.

[160] R. Memming and G. Schwandt, "Anodic dissolution of silicon in hydrofluoric acid solutions", *Surf. Sci.* **4**, (1966), 109.

[161] Y. Watanabe and T. Sakai, "Application of a thick anode film to semiconductor devices", *Rev. Electron. Commun. Labs.* **19**, (1971), 899.

[162] M. J. J. Theunissen, "Etch channel formation during anodic dissolution of n-type silicon in aqueous hydrofluoric acid", *J. Electrochem. Soc.* **119**, (1972), 351.

[163] Y. Arita and Y. Sunohara, "Formation and properties of porous silicon film", *J. Electrochem. Soc.* **124**, (1977), 285.

[164] G. Bomchil, R. Herino, K. Barla and J. C. Pfister, "Pore size distribution in porous silicon studied by adsorption isotherms", *J. Electrochem. Soc.* **130**, (1983), 1611.

[165] M. I. J. Beale, J. D. Benjamin, M. J. Uren, N. G. Chew and A. G. Cullis, "An experimental and theoretical study of the formation and microstructure of porous silicon", *J. Cryst. Growth* **73**, (1985), 622.

[166] R. L. Smith, S. F. Chuang and S. D. Collins, "A theoretical model of the formation morphologies of porous silicon", *J. Electron. Mater.* **17**, (1988), 533.

[167] R. L. Smith and S. D. Collins, "Generalized model for the diffusion-limited aggregation and Eden models of cluster growth", *Phys. Rev. A* **39**, (1989), 5409.

[168] R. L. Smith and S. D. Collins, "Porous silicon formation mechanisms", *J. Appl. Phys.* **71**, (1992), R1.

[169] T. Unagami, "Formation mechanism of porous silicon layer by anodization in HF solution", *J. Electrochem. Soc.* **127**, (1980), 476.

[170] V. P. Parkhutik, L. K. Glinenko and V. A. Labunov, "Kinetics and mechanism

UNIVERSITAT ROVIRA I VIRGILI
PHOTONIC BANDGAP ANALYSIS AND FABRICATION OF MACROPOROUS SILICON BY ELECTROCHEMICAL ETCHING
Trifon Todorov Tirfonov
ISBN:978-84-693-6270-9/DL:T-1376-2010

of porous layer growth during n-type silicon anodization in HF solution", *Surf. Technol.* **20**, (1983), 265.

[171] V. Lehmann and U. Gösele, "Porous silicon formation: A quantum wire effect", *Appl. Phys. Lett.* **58**, (1991), 856.

[172] X. G. Zhang, "Mechanism of pore formation on n silicon", *J. Electrochem. Soc.* **138**, (1991), 3750.

[173] J. Carstensen, M. Christophersen and H. Föll, "Pore formation mechanisms for the Si-HF system", *Mater. Sci. Eng. B* **69-70**, (2000), 23.

[174] H. Föll, J. Carstensen, M. Christophersen and G. Hasse, "A new view of silicon electrochemistry", *Phys. Stat. Sol. A* **182**, (2000), 7.

[175] J. Carstensen, M. Christophersen, G. Hasse and H. Föll, "Parameter dependence of pore formation in silicon within a model of local current bursts", *Phys. Stat. Sol. A* **182**, (2000), 63.

[176] C. Levy-Clement, A. Lagoubi and M. Tomkiewicz, "Morphology of porous n-type silicon obtained by photoelectrochemical etching. I. Correlations with material and etching Parameters", *J. Electrochem. Soc.* **141**, (1994), 958.

[177] C. Levy-Clement, A. Lagoubi, R. Tenne and M. Neumann-Spallart, "Photoelectrochemical etching of silicon", *Electrochim. Acta* **37**, (1992), 877.

[178] A. Albu-Yaron, S. Bastide, J. L. Maurice and C. Lévy-Clément, "Morphology of porous n-type silicon obtained by photoelectrochemical etching II: Study of the tangled Si wires in the nanoporous layer", *J. Lumin.* **57**, (1993), 67.

[179] E. K. Propst and P. A. Kohl, "The electrochemical oxidation of silicon and formation of porous silicon in acetonitrile", *J. Electrochem. Soc.* **141**, (1994), 1006.

[180] R. B. Wehrspohn, F. Ozanam and J.-N. Chazalviel, "Nano- and macropore formation in p-type silicon", *J. Electrochem. Soc.* **146**, (1999), 3309.

[181] V. Lehmann and S. Rönnebeck, "The physics of macropore formation in low-doped p-type silicon", *J. Electrochem. Soc.* **146**, (1999), 2968.

[182] S. Lust and C. Lévy-Clément, "Chemical limitations of macropore formation on medium-doped p-type silicon", *J. Electrochem. Soc.* **149**, (2002), C338.

[183] H. Föll, M. Christophersen, J. Carstensen and G. Hasse, "Formation and application of porous silicon", *Mater. Sci. Eng.* **R39**, (2002), 93–141.

[184] X. G. Zhang, "Morphology and formation mechanisms of porous silicon", *J. Electrochem. Soc.* **151**, (2004), C69.

[185] B. Hamilton, "Porous silicon", *Semicond. Sci. Technol.* **10**, (1995), 1187.

[186] V. Parkhutik, "Porous silicon-mechanisms of growth and applications", *Solid-State Electron.* **43**, (1999), 1121.

[187] V. Lehmann, in "Electrochemistry of silicon. Instrumentation, science, materials and applications", (WILEY-VCH, Weinheim, Germany, 2002).

[188] X. G. Zhang, S. D. Collins and R. L. Smith, "Porous silicon formation and electropolishing of silicon by anodic polarization in HF solution", *J. Electrochem. Soc.* **136**, (1989), 1561.

[189] K. Barla, G. Bomchil, R. Herino and J. C. Pfister, "X-ray topographic

ISBN:978-84-693-6270-9/DL:T-1376-2010

characterization of porous silicon layers", *J. Cryst. Growth* **68**, (1984), 721.

[190] V. Lehmann, "On the origin of electrochemical oscillations at silicon electrodes", *J. Electrochem. Soc.* **143**, (1996), 1313.

[191] J. Stumper, R. Greef and L. M. Peter, "Current oscillations during anodic dissolution of p-Si in ammonium fluoride: an investigation using ring disc voltammetry and ellipsometry", *J. Electroanal. Chem.* **310**, (1991), 445.

[192] H. Föll, "Properties of silicon-electrolyte junctions and their application to silicon characterization", *Appl. Phys. A* **53**, (1991), 8.

[193] M. J. Eddowes, "Anodic dissolution of p- and n-type silicon: Kinetic study of the chemical mechanism", *J. Electroanal. Chem.* **280**, (1990), 297.

[194] J. Carstensen, R. Prange and H. Föll, "A model for current-voltage oscillations at the silicon electrode and comparison with experimental results", *J. Electrochem. Soc.* **146**, (1999), 1134.

[195] V. A. Burrows, Y. J. Chabal, G. S. Higashi, K. Raghavachari and S. B. Christman, "Infrared spectroscopy of Si(111) surfaces after HF treatment: Hydrogen termination and surface morphology", *Appl. Phys. Lett.* **53**, (1988), 998.

[196] Y. Kato, T. Ito and A. Hiraki, "Initial oxidation process of anodized porous silicon with hydrogen atoms chemisorbed on the inner surface", *Jpn. J. Appl. Phys.* **27**, (1988), L1406.

[197] M. Hejjo al Rifai, M. Christophersen, S. Ottow, J. Carstensen and H. Föll, "Dependence of macropore formation in n-Si on potential, temperature, and doping", *J. Electrochem. Soc.* **147**, (2000), 627.

[198] U. Grüning and V. Lehmann, "Fabrication of 2-D infrared photonic crystals in macroporous silicon", in "Photonic Band Gap Materials", edited by C. M. Soukoulis, (Kluwer Academic Publishers, Dordrecht, 1996), 453.

[199] M. Christophersen, J. Carstensen, K. Voigt and H. Föll, "Organic and aqueous electrolytes used for etching macro- and mesoporous silicon", *Phys. Stat. Sol. A* **197**, (2003), 34.

[200] P. Kleimann, J. Linnros and S. Petersson, "Formation of wide and deep pores in silicon by electrochemical etching", *Mater. Sci. Eng. B* **69-70**, (2000), 29.

[201] G. Barillaro, A. Nannini and F. Pieri, "Dimensional constraints on high aspect ratio silicon microstructures fabricated by HF photoelectrochemical etching", *J. Electrochem. Soc.* **149**, (2002), C180.

[202] M. Krüger, R. Arens-Fischer, M. Thönissen, H. Münder, M. G. Berger, H. Lüth, S. Hilbrich and W. Theiss, "Formation of porous silicon on patterned substrates", *Thin Solid Films* **276**, (1996), 257.

[203] G. Sotgiu, L. Schirone and F. Rallo, "On the use of surfactants in the electrochemical preparation of porous silicon", *Thin Solid Films* **297**, (1997), 18.

[204] K. J. Chao, S. C. Kao, C. M. Yang, M. S. Hseu and T. G. Tsai, "Formation of high aspect ratio macropore array on p-type silicon", *Electrochem. Solid-State Lett.* **3**, (2000), 489.

UNIVERSITAT ROVIRA I VIRGILI
PHOTONIC BANDGAP ANALYSIS AND FABRICATION OF MACROPOROUS SILICON BY ELECTROCHEMICAL ETCHING
Trifon Todorov Tirfonov
ISBN:978-84-693-6270-9/DL:T-1376-2010

[205] A. W. Adamson, in "Physical Chemistry of Surfaces", (Wiley Interscience, New York, 1990).

[206] S. Matthias, (Max Planck Institute of Microstructure Physics, Halle, Germany), *private communication*.

[207] Dr. F. Müller, (Max Planck Institute of Microstructure Physics, Halle, Germany), *private communication*.

[208] V. Lehmann and U. Grüning, "The limits of macropore array fabrication", *Thin Solid Films* **297**, (1997), 13.

[209] J. Schilling, F. Müller, S. Matthias, R. B. Wehrspohn, U. Gösele and K. Busch, "Three-dimensional photonic crystals based on macroporous silicon with modulated pore diameter", *Appl. Phys. Lett.* **78**, (2001), 1180.

[210] O. Tabata, R. Asahi, H. Funabashi, K. Shimaoka and S. Sugiyama, "Anisotropic etching of silicon in TMAH solutions", *Sens. Actuators A* **34**, (1992), 51.

[211] H. Ohji, Ph. D. Thesis, (Technical University of Delft, Netherlands, 2002).

[212] S. Lazarouk, P. Jaguiro, S. Katsouba, G. Maiello, S. La Monica, G. Masini, E. Proverbio and A. Ferrari, "Visual determination of thickness and porosity of porous silicon layers", *Thin Solid Films* **297**, (1997), 97.

[213] A. Prasad, S. Balakrishnan, S. K. Jain and G. C. Jain, "Porous silicon oxide anti-reflection coating for solar cells", *J. Electrochem. Soc.* **129**, (1982), 596.

[214] K. Grigoras, A. Krotkus, V. Pacebutas, J. Kavaliauskas and I. Simkiene, "Enhanced light absorption in anodically etched silicon wafers", *Thin Solid Films* **276**, (1996), 228.

[215] R. R. Bilyalov, L. Stalmans, L. Schirone and C. Lévy-Clément, "Use of porous silicon antireflection coating in multicrystalline silicon solar cell processing", *IEEE Trans. Electron Devices* **46**, (1999), 2035.

[216] S. Strehlke, S. Bastide, J. Guillet and C. Lévy-Clément, "Design of porous silicon antireflection coatings for silicon solar cells", *Mater. Sci. Eng. B* **69-70**, (2000), 81.

[217] E. Galun, R. Tenne, A. Lagoubi and C. Lévy-Clément, "Room temperature photoluminescence of photoelectrochemically etched n-type Si", *J. Lumin.* **57**, (1993), 125.

[218] V. Lehmann, F. Hofmann, F. Möller and U. Grüning, "Resistivity of porous silicon: a surface effect", *Thin Solid Films* **255**, (1995), 20.

[219] RSB, NIH Image/J home page http://rsb.info.nih.gov/nih-image/index.html/.

[220] M. Thönissen, S. Billat, M. Krüger, H. Lüth, M. G. Berger, U. Frotscher and U. Rossow, "Depth inhomogeneity of porous silicon layers", *J. Appl. Phys.* **80**, (1996), 2990.

[221] R. Herino, G. Bomchil, K. Barla, C. Bertrand and J. L. Ginoux, "Porosity and pore size distributions of porous silicon layers", *J. Electrochem. Soc.* **134**, (1987), 1994.

[222] V. Lehmann, R. Stengl and A. Luigart, "On the morphology and the electrochemical formation mechanism of mesoporous silicon", *Mater. Sci.*

UNIVERSITAT ROVIRA I VIRGILI
PHOTONIC BANDGAP ANALYSIS AND FABRICATION OF MACROPOROUS SILICON BY ELECTROCHEMICAL ETCHING
Trifon Todorov Tirfonov
ISBN:978-84-693-6270-9/DL:T-1376-2010

Eng. B **69-70**, (2000), 11.

[223] S. Rönnebeck, J. Carstensen, S. Ottow and H. Föll, "Crystal orientation dependence of macropore growth in n-type silicon", *Electrochem. Solid-State Lett.* **2**, (1999), 126.

[224] S. F. Chuang, S. D. Collins and R. L. Smith, "Preferential propagation of pores during the formation of porous silicon: A transmission electron microscopy study", *Appl. Phys. Lett.* **55**, (1989), 675.

[225] M. Christophersen, J. Carstensen, S. Rönnebeck, C. Jäger, W. Jäger and H. Föll, "Crystal orientation dependence and anysotropic properties of macropore formation of p- and n-type silicon", *J. Electrochem. Soc.* **148**, (2001), E267.

[226] H. Ohji, S. Izuo, P. J. French and K. Tsutsumi, "Macroporous-based micromachining on full wafers", *Sens. Actuators A* **92**, (2001), 384.

[227] V. V. Starkov, "Ordered macropore formation in silicon", *Phys. Stat. Sol. A* **197**, (2003), 22.

[228] F. Müller, A. Birner, J. Schilling, U. Gösele, C. Kettner and P. Hänggi, "Membranes for micropumps from macroporous silicon", *Phys. Stat. Sol. A* **182**, (2000), 585.

[229] S. Matthias, J. Schilling, K. Nielsch, F. Müller, R. Wehrspohn and U. Gösele, "Monodisperse diameter-modulated gold microwires", *Adv. Mater.* **14**, (2002), 1618.

[230] J. Schilling, F. Müller, R. B. Wehrspohn, U. Gösele and K. Busch, "Dispersion relation of 3D photonic crystals based on macroporous silicon", *Mater. Res. Soc. Symp .Proc.* **722**, (2002), L6.8.1.

[231] M. Galli, M. Agio, L. C. Andreani, M. Belotti, G. Guizzetti, F. Marabelli, M. Patrini, P. Bettotti, L. Dal Negro, Z. Gaburro, L. Pavesi, A. Lui and P. Bellutti, "Spectroscopy of photonic bands in macroporous silicon photonic crystals", *Phys. Rev. B* **65**, (2002), 113111.

[232] A. Vyatkin, V. Starkov, V. Tzeitlin, H. Presting, J. Konle and U. König, "Random and ordered macropore formation in p-type silicon", *J. Electrochem. Soc.* **149**, (2002), G70.

[233] S. R. Morrison, "Hole injection into silicon from ions in solution", *J. Appl. Phys.* **53**, (1982), 1233.

[234] J. E. A. M. van den Meerakker, R. J. G. Elfrink, W. M. Weeda and F. Roozeboom, "Anodic silicon etching; the formation of uniform arrays of macropores or nanowires", *Phys. Stat. Sol. A* **197**, (2003), 57.

[235] G. Barillaro, A. Nannini and M. Piotto, "Electrochemical etching in HF solution for silicon micromachining", *Sens. Actuators A* **102**, (2002), 195.

[236] Dr. Z. Gaburro, (University of Trento, Trento, Italy), *private communication*.

[237] C. Pickering, "Optical properties of porous silicon (1984-1993): correlation with microstructure", in "Porous Silicon", edited by Z. C. Feng and R. Tsu, (World Scientific, Singapore, 1994), 3.

[238] D. E. Aspnes, J. B. Theeten and F. Hottier, "Investigation of effective-medium models of microscopic surface roughness by spectroscopic ellipsometry",

UNIVERSITAT ROVIRA I VIRGILI
PHOTONIC BANDGAP ANALYSIS AND FABRICATION OF MACROPOROUS SILICON BY
ELECTROCHEMICAL ETCHING
Trifon Todorov Tirfonov
ISBN:978-84-693-6270-9/DL:T-1376-2010

Phys. Rev. B **20**, (1979), 3292.

[239] Dr. V. Lehmann, (Infineon Technologies AG, Munich, Germany), *private communication*.

[240] R. B. Wehrspohn, J. Schilling, J. Choi, Y. Luo, S. Matthias, S. L. Schweizer, F. Müller, U. Gösele, S. Lölkes, S. Langa, J. Carstensen and H. Föll, "Electrochemically-prepared 2D and 3D photonic crystals", in "Photonic Crystals: Advances in Design, Fabrication, and Characterization." edited by K. Busch, S. Lölkes, R. B. Wehrspohn and H. Föll, (Wiley-VCH, Weinheim, Germany, 2004), 63.

[241] S. Ottow, V. Lehmann and H. Föll, "Processing of three-dimensional microstructures using macroporous n-type silicon", *J. Electrochem. Soc.* **143**, (1996), 385.

[242] F. Müller, A. Birner, U. Gösele, V. Lehmann, S. Ottow and H. Föll, "Structuring of macroporous silicon for applications as photonic crystals", *J. Porous Mater.* **7**, (2000), 201.

[243] J. Schilling, R. B. Wehrspohn, A. Birner, F. Müller, R. Hillebrand, U. Gösele, S. W. Leonard, J. P. Mondia, F. Genereux, H. M. van Driel, P. Kramper, V. Sandoghdar and K. Busch, "A model system for two-dimensional and three-dimensional photonic crystals: macroporous silicon", *J. Opt. A: Pure Appl. Opt.* **3**, (2001), S121.

[244] A. Birner, R. Wehrspohn, U. Gösele and K. Busch, "Silicon-based photonic crystals", *Adv. Mater.* **13**, (2001), 377.

[245] G. von Freymann, W. Koch, D. C. Meisel, M. Wegener, M. Diem, A. Garcia-Martin, S. Pereira, K. Busch, J. Schilling, R. B. Wehrspohn and U. Gösele, "Diffraction properties of two-dimensional photonic crystals", *Appl. Phys. Lett.* **83**, (2003), 614.

[246] C. Jamois, R. B. Wehrspohn, J. Schilling, F. Müller, R. Hillebrand and W. Hergert, "Silicon-based photonic crystal slabs: two concepts", *IEEE J. Quantum Electron.* **38**, (2002), 805.

[247] R. Hillebrand, C. Jamois, J. Schilling, R. Wehrspohn and W. Hergert, "Computation of optical properties of Si-based photonic crystals with varying pore diameters", *Phys. Stat. Sol. B* **240**, (2003), 124.

[248] V. Lehmann, R. Stengl, H. Reisinger, R. Detemple and W. Theiss, "Optical shortpass filters based on macroporous silicon", *Appl. Phys. Lett.* **78**, (2001), 589.

[249] V. Lehmann and S. Rönnebeck, "MEMS techniques applied to the fabrication of anti-scatter grids for X-ray imaging", *Sens. Actuators A* **95**, (2002), 202.

[250] S. R. Nicewarner-Peña, R. G. Freeman, B. D. Reiss, L. He, D. J. Peña, I. D. Walton, R. Cromer, C. D. Keating and M. J. Natan, "Submicrometer metallic barcodes", *Science* **294**, (2001), 137.

[251] N. T. Nguyen, E. Boellaard, N. P. Pham, V. G. Kutchoukov, G. Craciun and P. M. Sarro, "Through-wafer copper electroplating for three-dimensional interconnects", *J. Micromech. Microeng.* **12**, (2002), 395.

[252] R. Angelucci, A. Poggi, L. Dori, A. Tagliani, G. C. Cardinali, F. Corticelli and

UNIVERSITAT ROVIRA I VIRGILI
PHOTONIC BANDGAP ANALYSIS AND FABRICATION OF MACROPOROUS SILICON BY ELECTROCHEMICAL ETCHING
Trifon Todorov Tirfonov
ISBN:978-84-693-6270-9/DL:T-1376-2010

M. Marisaldi, "Permeated porous silicon suspended membrane as sub-ppm benzene sensor for air quality monitoring", *J. Porous Mater.* **7**, (2000), 197.

[253] V. Lehmann, W. Hönlein, H. Reisinger, A. Spitzer, H. Wendt and J. Willer, "A novel capacitor technology based on porous silicon", *Thin Solid Films* **276**, (1996), 138.

[254] E. V. Astrova, V. B. Voronkov, I. V. Grekhov, A. V. Nashchekin and A. G. Tkachencko, "Deep diffusion doping of macroporous silicon", *Phys. Stat. Sol. A* **182**, (2000), 145.

[255] S. Matthias and F. Müller, "Asymmetric pores in a silicon membrane acting as massively parallel brownian ratchets", *Nature* **424**, (2003), 53.

[256] C. Kettner, P. Reimann, P. Hänggi and F. Müller, "Drift ratchet", *Phys. Rev. E* **61**, (2000), 312.

[257] S. Izuo, H. Ohji, P. J. French, K. Tsutsumi and M. Kimata, "Silicon dioxide micropillars for sieving fabricated by macroporous silicon-based micromachining", *Sens. Mater.* **14**, (2002), 239.

[258] V. Lehmann, "Barcoded molecules", *Nature Mater.* **1**, (2002), 12.

[259] E. V. Astrova, V. V. Ratnikov, A. D. Remenyuk and I. L. Shulpina, "Strains in macroporous silicon introduced by cyclic oxidation", *Phys. Stat. Sol. A* **197**, (2003), 16.

[260] K. Chun, G. Hashiguchi, H. Toshiyoshi and H. Fujita, "Fabrication of array of hollow microcapillaries used for injection of genetic materials into animal/plant cells", *Jpn. J. Appl. Phys.* **38**, (1999), Part 2 L279.

[261] S. Matthias, F. Müller, R. Wehrspohn and U. Gösele, "Large area three-dimensional microstructuring by self-organisation and lithography", *Proceedings of 4th International Conference "Porous Semiconductors: Science and Technology"*, (14-19 March, 2004, Cullera, Valencia, Spain), 128.

UNIVERSITAT ROVIRA I VIRGILI
PHOTONIC BANDGAP ANALYSIS AND FABRICATION OF MACROPOROUS SILICON BY ELECTROCHEMICAL ETCHING
Trifon Todorov Tirfonov
ISBN:978-84-693-6270-9/DL:T-1376-2010

Publications related to this thesis

Journal articles

L. F. Marsal, **T. Trifonov**, A. Rodríguez, J. Pallarés and R. Alcubilla, "Larger absolute photonic band gap in two-dimensional air-silicon structures", *Physica E: Low-dimensional Systems and Nanostructures* **16**, (2003), p. 580.

T. Trifonov, L. F. Marsal, A. Rodríguez, J. Pallarès and R. Alcubilla, "Effects of symmetry reduction in two-dimensional square and triangular lattices", *Physical Review B* **69**, (2004), p. 235112.

T. Trifonov, L. F. Marsal, A. Rodríguez, J. Pallarés and R. Alcubilla, "Analysis of photonic band gaps in two-dimensional photonic crystals with rods covered by a thin interfacial layer", *Physical Review B* **70**, (2004), p. 195108.

T. Trifonov, A. Rodríguez, F. Servera, L. F. Marsal, J. Pallarés and R. Alcubilla, "High-aspect-ratio silicon dioxide pillars", *Physica Status Solidi C* (2004), (*submitted*).

T. Trifonov, L. F. Marsal, A. Rodríguez, J. Pallarés and R. Alcubilla, "Fabrication of two- and three-dimensional photonic crystals by electrochemical etching of silicon", *Physica Status Solidi C* (2004), (*submitted*).

A. Rodríguez, D. Molinero, E. Valera, **T. Trifonov**, L. F. Marsal, J. Pallarès and R. Alcubilla, "Fabrication of silicon oxide microneedles from macroporous silicon", *Sensors and Actuators B*, (*submitted*).

S. Cheylan, **T. Trifonov**, A. Rodríguez, L. F. Marsal, J. Pallarès, R. Alcubilla and G. Badenes, "Visible light emission from macroporous silicon", *Optical Materials, (submitted).*

Communications

L. F. Marsal, **T. Trifonov**, A. Rodríguez, J. Pallarés and R. Alcubilla, "Larger photonic band gaps in two-dimensional hybrid lattices", *European Materials Research Society E-MRS meeting*, (18-21 June 2002, Strasbourg, France).

T. Trifonov, L. F. Marsal, A. Rodríguez, J. Pallarés and R. Alcubilla, "Photonic band gaps in 2D air/silicon structures with reduced symmetry", *4a Conferencia de Dispositivos Electrónicos CDE'03*, (12-14 February 2003, Calella de la Costa, Barcelona, Spain), p. III-08-1

A. Rodríguez, **T. Trifonov**, L. F. Marsal, J. Pallarés and R. Alcubilla, "Development of macroporous silicon fabrication technology", *4a Conferencia de Dispositivos Electrónicos CDE'03*, (12-14 February 2003, Calella de la Costa, Barcelona, Spain), p. I-01-1

F. Fonthal, **T. Trifonov**, R. Cabré, A. Rodríguez, L. F. Marsal and J. Pallarès, "Electrical and optical characterization of macroporous silicon on crystalline silicon diodes", *4a Conferencia de Dispositivos Electrónicos CDE'03*, (12-14 February 2003, Calella de la Costa, Barcelona, Spain), p. V-09-1.

T. Trifonov, L. F. Marsal, A. Rodríguez, J. Pallarés and R. Alcubilla, "Effects of symmetry reduction on the photonic band gap in two-dimensional air/silicon structures", *3a Reunión Española de Optoelectrónica OPTOEL'03*, (14-16 July 2003, Leganés, Madrid, Spain), p. T5-18.

T. Trifonov, A. Rodríguez, F. Servera, L. F. Marsal, J. Pallarés and R. Alcubilla, "High-aspect-ratio silicon dioxide pillars", *4th International Conference "Porous Semiconductors: Science and Technology"*, (14-19 March 2004, Cullera, Valencia, Spain), p. 340.

F. Fonthal, **T. Trifonov**, A. Rodríguez, L. F. Marsal, X. Vilanova and J. Pallarés, "Fabrication and characterization of macroporous silicon on crystalline silicon based devices", *4th International Conference "Porous Semiconductors: Science and Technology"*, (14-19 March 2004, Cullera, Valencia, Spain), p. 218.

E. Xifré, **T. Trifonov**, J. Pallarés and L. F. Marsal, "One-dimensional porous silicon photonic crystal for visible and NIR applications", *4th International Conference "Porous Semiconductors: Science and Technology"*, (14-19 March 2004, Cullera, Valencia, Spain), p. 386.

T. Trifonov, L. F. Marsal, A. Rodríguez, J. Pallarés and R. Alcubilla, "Fabrication of 2D and 3D microstructures by electrochemical etching of silicon", *International Conference on Superlattices, Nano-structures and Nano-devices (ICSNN 2004)*, (19-23 July 2004, Cancún, Mexico).

L. F. Marsal, **T. Trifonov**, A. Rodríguez, J. Pallarés and R. Alcubilla, "Two- and three-dimensional photonic crystals based on macroporous silicon", *XX Trobades Científiques de la Mediterrània "Fotònica: ciència i tecnologia de la llum"*, (26-28 September 2004,Maó, Menorca, Spain).

J. J. Carvajal, A. Peña, M. Aguiló, F. Díaz, S. di Finizio, **T. Trifonov**, J. Pallarés, L. F. Marsal, A. Rodríguez, R. Alcubilla and J. Martorell, "2-D photonic structures of KTP grown by liquid phase epitaxy using a 2-D photonic ordered macroporous Si crystal mask", *XX Trobades Científiques de la Mediterrània "Fotònica: ciència i tecnologia de la llum"*, (26-28 September 2004, Maó, Menorca, Spain).

A. Rodríguez, D. Molinero, E. Valera, **T. Trifonov**, L. F. Marsal, J. Pallarés and R. Alcubilla, "Fabrication of silicon oxide microneedles from macroporous silicon",

UNIVERSITAT ROVIRA I VIRGILI
PHOTONIC BANDGAP ANALYSIS AND FABRICATION OF MACROPOROUS SILICON BY ELECTROCHEMICAL ETCHING
Trifon Todorov Tirfonov
ISBN:978-84-693-6270-9/DL:T-1376-2010

European Materials Research Society E-MRS meeting, (6-10 September 2004,Warsaw, Poland).

T. Trifonov, A. Rodríguez, L. F. Marsal, J. Pallarés and R. Alcubilla, "Two- and three-dimensional microstructures produced by electrochemical etching of silicon", *5a Conferencia de Dispositivos Electrónicos CDE'05*, (2-4 February 2005, Tarragona, Spain), (*accepted for poster presentation).*

T. Trifonov, L. F. Marsal, A. Rodríguez, J. Pallarès and R. Alcubilla, "Two-dimensional photonic crystals of rods with a dielectric cladding", *SPIE International Symposium "Microtechnologies for the New Millennium 2005"*, (9-11 May 2005, Sevilla, Spain), *(accepted for poster presentation).*

S. Cheylan, **T. Trifonov**, A. Rodríguez, L. F. Marsal, J. Pallarès, R. Alcubilla and G. Badenes, "Visible light emission from macroporous silicon", *SPIE International Symposium "Microtechnologies for the New Millennium 2005"*, (9-11 May 2005, Sevilla, Spain), *(accepted for poster presentation).*

UNIVERSITAT ROVIRA I VIRGILI
PHOTONIC BANDGAP ANALYSIS AND FABRICATION OF MACROPOROUS SILICON BY ELECTROCHEMICAL ETCHING
Trifon Todorov Tirfonov
ISBN:978-84-693-6270-9/DL:T-1376-2010